PHENIX

An Upgrade Proposal from the PHENIX Collaboration

July 1, 2012
Updated March 22, 2013

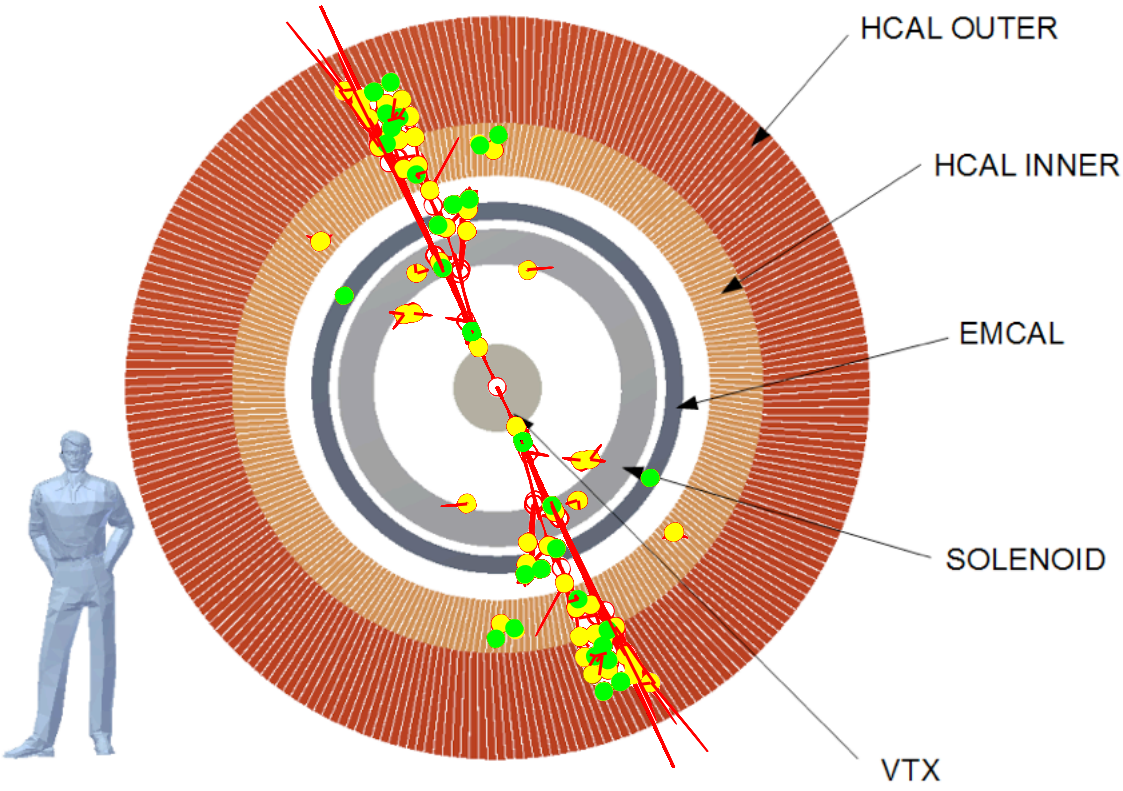

Executive Summary

The PHENIX collaboration presents in this document a proposal for a major upgrade to the PHENIX detector at the Relativistic Heavy Ion Collider. This upgrade, sPHENIX, brings exciting new capability to the RHIC program by opening new and important channels for experimental investigation and utilizing fully the luminosity of the recently upgraded RHIC facility. sPHENIX enables a compelling jet physics program that will address fundamental questions about the nature of the strongly coupled quark-gluon plasma discovered experimentally at RHIC to be a perfect fluid. Fundamental questions such as how and why the quark-gluon plasma behaves as a perfect fluid in the vicinity of strongest coupling, near 1–2 T_c, can only be fully addressed with world-class jet observables at RHIC energies. Comparing these measurements to higher temperature quark-gluon plasma measurements at the Large Hadron Collider will provide invaluable insight into the thermodynamics of QCD. Importantly, sPHENIX also provides the foundation for a future detector able to exploit the novel physics opportunities of an electron-ion collider at RHIC.

The proposed upgrade addresses specific questions whose answers are necessary to advance our understanding of the quark-gluon plasma:

1. How to reconcile the observed strongly coupled quark-gluon plasma with the asymptotically free theory of quarks and gluons?
2. What are the dynamical changes to the quark-gluon plasma in terms of quasiparticles and excitations as a function of temperature?
3. How sharp is the transition of the quark-gluon plasma from the most strongly coupled regime near T_c to a weakly coupled system of partons known to emerge at asymptotically high temperatures?

To pursue this physics we are proposing an upgrade consisting of a 2 T magnetic solenoid of radius 70 cm surrounded by electromagnetic and hadronic calorimetry with uniform coverage over $|\eta| < 1.0$. With the now completed RHIC luminosity upgrade, a 20 week run will deliver over 50 billion Au+Au collisions at $\sqrt{s_{NN}} = 200\,\text{GeV}$, and sPHENIX will thus sample over 10 million dijet events with $E_T > 20\,\text{GeV}$, along with a correspondingly large γ+jet sample. The newly developed flexibility of RHIC enabled by the Electron Beam Ion Source and the high rate capability of sPHENIX will provide critical precision control data sets in p+p, $p(d)$+A, and a full range of collision species over a wide span of

collision energies..

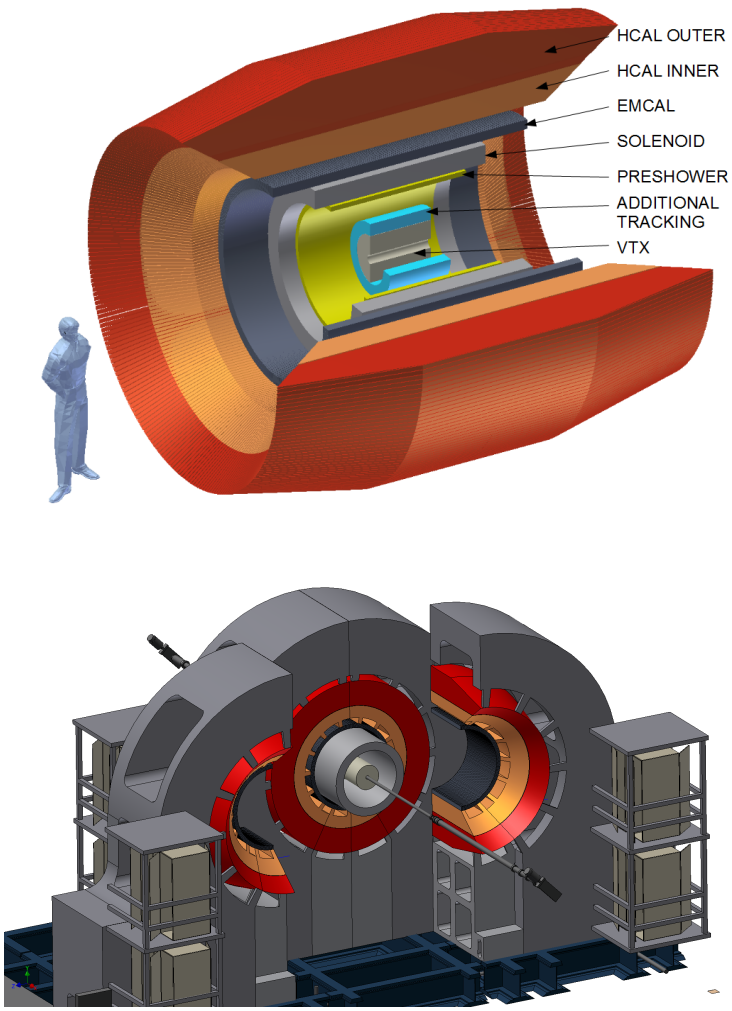

Figure 1: (top) An engineering drawing of the sPHENIX upgrade showing the inner silicon tracker (VTX), the solenoid, and the calorimeters. (bottom) A view showing how sPHENIX would fit into and be supported and serviced in the current PHENIX interaction region.

An engineering drawing of the upgraded detector and its incorporation into the PHENIX interaction region are shown in Figure 1. The design of sPHENIX takes advantage of technological developments enabling the detector to be very compact, which allows for a significantly lower cost per unit solid angle coverage. Further cost savings are achieved by reusing significant elements of the existing PHENIX mechanical and electrical infrastructure. We have obtained budgetary guidance from well-regarded vendors for the major components of sPHENIX. We have also estimated the need for engineering and installation and management. We have applied standard guidance for overhead and contingency. From this we conclude that the cost of sPHENIX is on the order of $29M, and

that designing, building and installing the detector could be done within five years.

The sPHENIX upgrade proposed in this document represents a major scientific instrument. Its physics capabilities can be augmented through modest incremental upgrades that have been an integral part of the design considerations from the outset. These additional upgrades are envisioned to be contributions of PHENIX international collaborators.

The specific options considered for installation in conjunction with the solenoid magnet are additional charged particle tracking outside the existing PHENIX silicon vertex detector (VTX) and a preshower with fine segmentation in front of the electromagnetic calorimeter. These additions will expand the sPHENIX physics program to include: (a) heavy quarkonia suppression via the three upsilon states, (b) tagging of charm and beauty jets, (c) jet fragmentation function modifications, (d) nuclear suppression of π^0 yields up to $p_T = 40\,\mathrm{GeV/c}$, and (e) a possible low mass dilepton program. The potential for extending the sPHENIX capabilities in this way has attracted significant international interest. Our goal is to have these upgrades installed and available for physics on day-one, and toward that goal we are pursuing funding through proposals to US-Japan, RIKEN and JSPS. These upgrades are described in Chapter 6.

The open geometry of the magnetic solenoid also allows for a forward angle spectrometer upgrade option aimed at measuring photon, jet, and lepton observables relevant to answering questions in $p(d) + A$ collisions about cold nuclear matter and in transversely polarized $p{+}p$ collisions about transversity. This forward upgrade is envisioned to be available on a slightly longer time scale is described in Appendix A.

The design for a future Electron Ion Collider (EIC) at RHIC consists of adding a 5–30 GeV electron beam to the current hadron and nuclear beam capabilities. The proposed initial construction would consist of a 5–10 GeV electron beam, referred to as Phase 1 of eRHIC. We have designed sPHENIX so that it would also serve as the foundation for a future EIC detector, referred to as ePHENIX. The sPHENIX proposal, covering $|\eta| < 1.0$, when combined with future upgrades in the backward ($\eta < -1.0$) and forward ($\eta > 1.0$) regions is compatible with a full suite of EIC physics measurements as described in Appendix B. Engineering drawings of the detector in the PHENIX IR at each evolutionary stage from PHENIX through ePHENIX — with each stage delivering world-class physics — are shown in Figure 2.

The document is organized as follows. In Chapter 1, we detail the physics accessible via jet, dijet, and γ+jet measurements at RHIC to demonstrate the mission need. In Chapter 2, we detail the sPHENIX detector upgrade and the subsystem requirements to achieve the physics goals. In Chapter 3, we detail the specific detector design and GEANT4 simulation results. In Chapter 4, we detail the physics performance with full detector simulations. In the Appendices we detail the additional physics capabilities gained through further upgrades. Appendix 6 describes two midrapidity detector additions, Appendix A details a forward rapidity upgrade, and Appendix B shows an evolution to an ePHENIX detector suitable for a future Electron Ion Collider at RHIC.

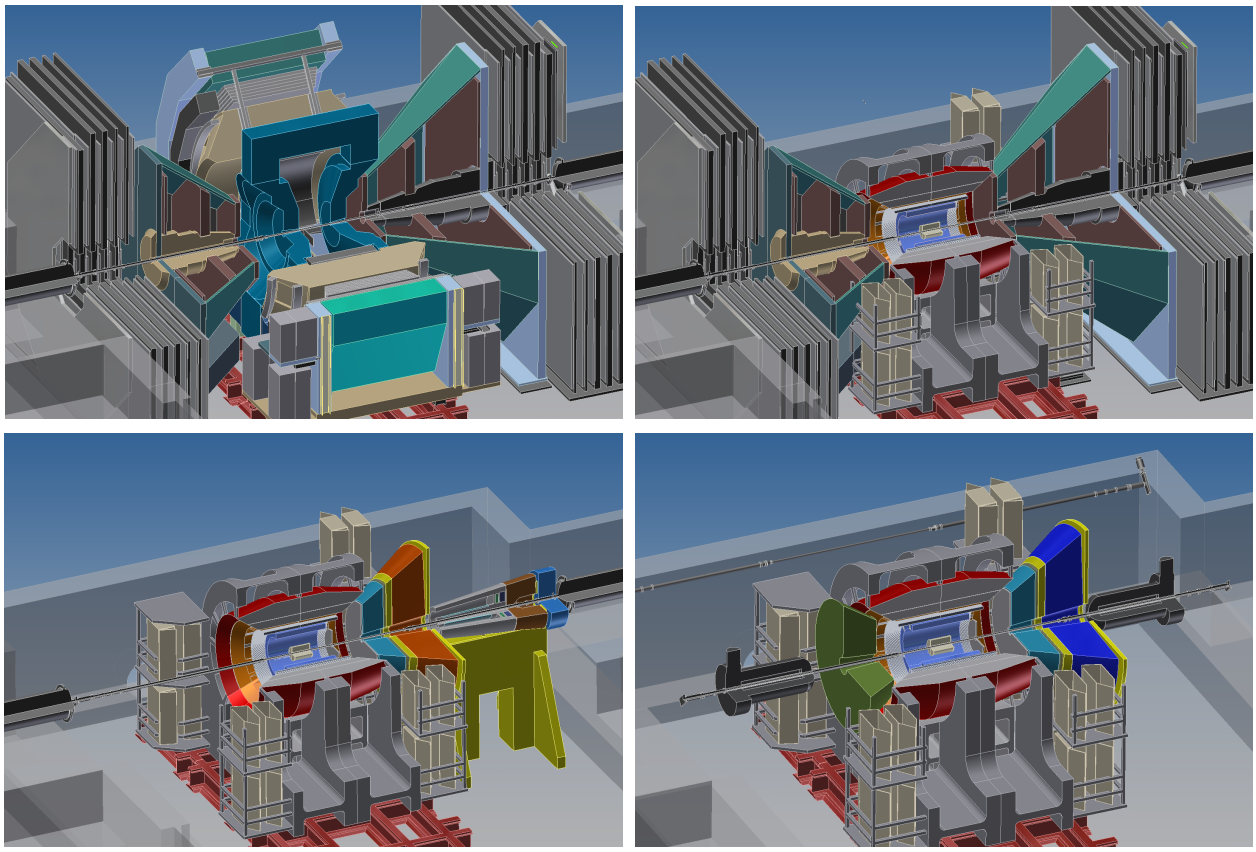

Figure 2: Engineering drawings showing the progression from current PHENIX (top left); to sPHENIX as described in the main part of this proposal (top right); to fsPHENIX, with additional forward instrumentation and capabilities (bottom left, see Appendix A); to ePHENIX, a detector capable of world-class measurements with an electron-ion collider at RHIC (bottom right, see Appendix B).

Contents

1 The Physics Case for sPHENIX . . . 1

1.1 Pushing and probing the QGP . . . 3

1.2 What is the temperature dependence of the QGP? . . . 5

1.3 What are the inner workings of the QGP? . . . 9

1.4 How does the QGP evolve along with the parton shower? . . . 10

1.5 Current jet probe measurements . . . 11

1.6 Theoretical calculations of jets at RHIC . . . 16

1.7 Measuring jets, dijets, and γ-jet correlations at RHIC . . . 22

1.8 Summary . . . 25

2 sPHENIX Detector Requirements . . . 27

2.1 Detector Overview . . . 27

2.2 Design Goals . . . 30

3 sPHENIX Detector Concept . . . 35

3.1 Magnet and Tracking . . . 36

3.2 The Electromagnetic Calorimeter . . . 37

3.3 The Hadronic Calorimeter . . . 43

3.4 Simulations . . . 47

3.5 Electronics . . . 53

3.6 Mechanical Design and Infrastructure Concept . . . 64

4 Jet, Dijet, and γ-Jet Performance . . . 69

4.1 Simulations . . . 69

4.2 Jet finding algorithm . . . 70

4.3 Jet performance in $p+p$ collisions . . . 70

4.4 Jet Performance in Au$+$Au collisions . . . 74

4.5 Summary . . . 86
5 Management, Cost, and Schedule . . . 91
5.1 Management . . . 91
5.2 Research and Development . . . 93
5.3 Cost . . . 95
5.4 Schedule . . . 99
6 Midrapidity Upgrades and Physics . . . 101
6.1 Tracking Upgrade . . . 101
6.2 Preshower Detector . . . 104
6.3 Upsilon Spectroscopy . . . 105
6.4 Tagging Charm / Beauty Jets . . . 111
6.5 Extending π^0 R_{AA} to 40 GeV/c . . . 114
6.6 High z Jet Fragmentation Functions . . . 115
6.7 Low and Intermediate Mass Dileptons . . . 116
A Forward Upgrades and Physics . . . 119
A.1 Transverse Momentum Dependent Phenomena in Nucleon Structure . . . 120
A.2 Cold Nuclear Matter Effects . . . 123
A.3 Detector Considerations . . . 124
B Evolution to ePHENIX . . . 127
B.1 ePHENIX at eRHIC . . . 128
B.2 Physics Goals of the EIC . . . 129
B.3 Detector Considerations . . . 134
C The PHENIX Collaboration . . . 143
References . . . 151

Chapter 1

The Physics Case for sPHENIX

Hadronic matter under conditions of extreme temperature or net baryon density transitions to a new state of matter called the quark-gluon plasma. Lattice QCD calculations at zero net baryon density indicate a smooth crossover transition at $T_c \approx 170$ MeV, though with a rapid change in properties at that temperature as shown in the left panel of Figure 1.1 [1]. This quark-gluon plasma dominated the early universe for the first six microseconds of its existence. Collisions of heavy nuclei at the Relativistic Heavy Ion Collider (RHIC) have sufficient initial kinetic energy that is then converted into heat to create quark-gluon plasma with an initial temperature—measured via the spectrum of directly emitted photons—of greater than 300 MeV [2]. The higher energy collisions at the Large Hadron Collider (LHC) produce an even higher initial temperature $T > 420$ MeV [3].

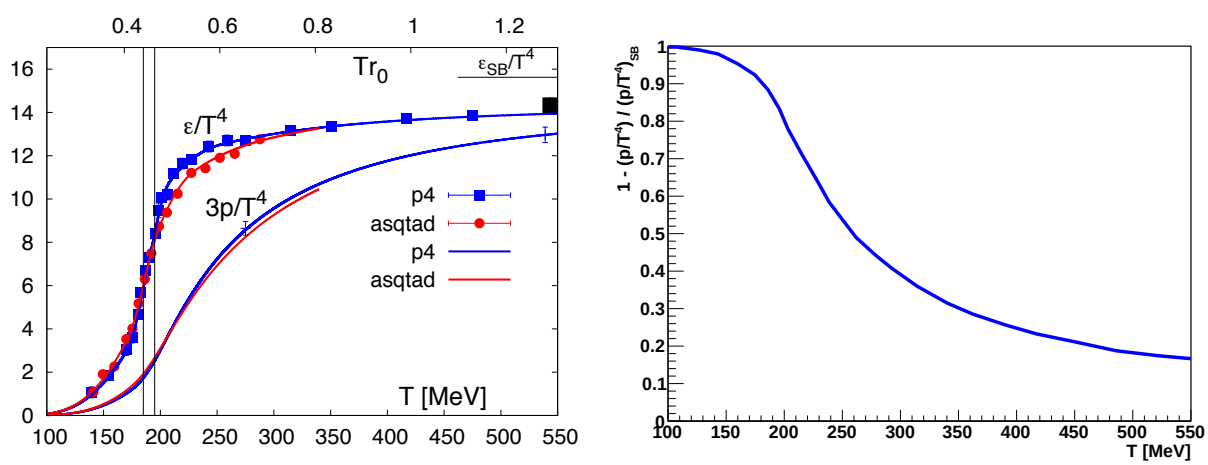

Figure 1.1: (Left) The energy density and three times the pressure normalized by $1/T^4$ as a function of temperature [1]. (Right) Deviation in p/T^4 relative to the Stefan-Boltzmann value as a function of temperature. The deviation from the Stefan-Boltzmann value is 23%, 39%, 53%, and 80% at temperatures of 420, 300, 250, and 200 MeV, respectively.

In materials where the dominant forces are electromagnetic, the coupling $\alpha_{\rm em}$ is always much less than one. Even so, many-body collective effects can render perturbative calculations non-convergent and result in systems with very strong coupling [4]. In cases where the nuclear force is dominant, and at temperature scales of order 1–3 T_c, the coupling constant α_s is not much less than one and the system is intrinsically non-perturbative. In addition, the many-body collective effects in the quark-gluon plasma and their temperature dependence near T_c are not well understood.

Lattice QCD results for the deviation of the pressure, normalized by $1/T^4$, from the Stefan-Boltzmann limit are shown in Figure 1.1. The Stefan-Boltzmann limit holds for a non-interacting gas of massless particles (i.e., the extreme of the weakly coupled limit), and as attractive inter-particle interactions grow stronger the pressure decreases. Thus, one might expect that the quark-gluon plasma would transition from a weakly coupled system at high temperature to a more strongly coupled system near T_c. However, a direct quantitative extraction of the coupling strength warrants caution as string theory calculations provide an example where the coupling is very strong and yet the deviation from the Stefan-Boltzmann limit is only 25% [5, 6]. The change in initial temperature between RHIC and LHC collisions is thus expected to be associated with important changes in the nature of the quark-gluon plasma [7]. If not, the question is why not.

The collisions at RHIC and the LHC involve a time evolution during which the temperature drops as the quark-gluon plasma expands. The real constraint on the temperature dependence of the quark-gluon plasma properties will come from calculations which simultaneously describe observables measured at both energies. Since we are studying a phase transition, it is crucial to do experiments near the phase transition and compare them with experiments done further above T_c. Typically, all the non-scaling behavior is found near the transition.

For many systems the change in coupling strength is related to quasiparticle excitations, strong coherent fields, etc., and to study these phenomena one needs to probe the medium at a variety of length scales. For example, in a superconductor probed at long length scales, one scatters from Cooper pairs; in a superconductor probed at short distance scales one observes the individual electrons. Hard scattered partons generated in heavy ion collisions that traverse the quark-gluon plasma serve as the probes of the medium. Utilizing these partonic probes, measured as reconstructed jets, over the broadest possible energy scale is a key part of unraveling the quasiparticle puzzle in the quark-gluon plasma. Jet probes at the LHC reach the highest energies and with large total energy loss probe the shortest distance scales; the lower backgrounds at RHIC will push the jet probes to lower energies thus probing the important longer distance scales in the medium.

This Chapter is organized into Sections as follows. We first describe the key ways of 'pushing' and 'probing' the quark-gluon plasma to understand its properties. We then discuss three different aspects in which the RHIC jet results are crucial in terms of (1) the temperature dependence of the QGP, (2) the microscopic inner workings of the QGP, and (3) the QGP time evolution along with the parton shower evolution. We then discuss the

current state of jet probe measurements from RHIC and LHC experiments, followed by a review of theoretical calculations for RHIC jet observables. Finally, we review the jet, dijet, and γ-jet rates relevant for measurements at RHIC.

1.1 Pushing and probing the QGP

Results from RHIC and LHC heavy ion experiments have provided a wealth of data for understanding the physics of the quark-gluon plasma. One very surprising result discovered at RHIC was the fluid-like flow of the quark-gluon plasma [8], in stark contrast to some expectations that the quark-gluon plasma would behave as a weakly coupled gas of quarks and gluons. It was originally thought that even at temperatures as low as 2–5 T_c, the quark-gluon plasma could be described with a weakly coupled perturbative approach despite being quite far from energy scales typically associated with asymptotic freedom. The quark-gluon plasma created in heavy ion collisions expands and cools, eventually passing through the phase transition to a state of hadrons, which are then measured by experiment. Extensive measurements of the radial and elliptic flow of hadrons, when compared to hydrodynamics calculations, imply a very small ratio of shear viscosity to entropy density, η/s [9]. In the limit of very weak coupling (i.e., a non-interacting gas), the shear viscosity is quite large as particles can easily diffuse across a velocity gradient in the medium. Stronger inter-particle interactions inhibit diffusion to the limit where the strongest interactions result in a very short mean free path and thus almost no momentum transfer across a velocity gradient, resulting in almost no shear viscosity. The shortest possible mean free path is of order the de Broglie wavelength, which sets a lower limit on η/s [10]. A more rigorous derivation of this limit of $\eta/s \geq 1/4\pi$ has been calculated within string theory for a broad class of strongly coupled gauge theories by Kovtun, Son, and Starinets (KSS) [11]. Viscous hydrodynamic calculations assuming η/s as temperature independent through the heavy ion collision time evolution are consistent with the experimental data where η/s is within 50% of this lower bound for strongly coupled matter [9, 12, 13, 14, 15, 16]. Even heavy quarks (i.e., charm and beauty) are swept up in the fluid flow and theoretical extractions of the implied η/s are equally small [17].

Other key measures of the coupling strength to the medium are found in the passage of a hard scattered parton through the quark-gluon plasma. As the parton traverses the medium it accumulates transverse momentum as characterized by $\hat{q} = d(\Delta p_T^2)/dt$ and transfers energy to the medium via collisions as characterized by $\hat{e} = dE/dt$. Ref. [19] has calculated $\hat{q}/T^3$ in $\mathcal{N} = 4$ supersymmetric Yang-Mills theory to be proportional to the square root of the coupling strength whereas η/s asymptotically approaches the quantum lower bound as the coupling increases. Both of these ratios are shown as a function of the inverse coupling in Figure 1.2. For large 't Hooft coupling (λ), η/s is already quite close to $1/4\pi$, whereas $T^3/\hat{q}$ is still changing. This behavior has caused the authors of Ref. [18] to comment: "The ratio $T^3/\hat{q}$ is a more broadly valid measure of the coupling strength of the medium than η/s."

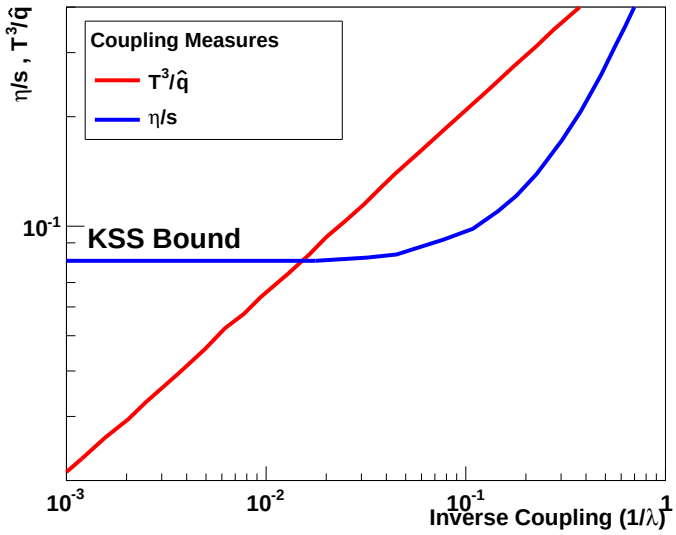

Figure 1.2: η/s (blue) and $T^3/\hat{q}$ (red) as a function of the inverse of the 't Hooft coupling[18]. For large λ (i.e., small $1/\lambda$), η/s approaches the quantum lower bound asymptotically, losing its sensitivity to further changes in the coupling strength.

In vacuum, the hard scattered parton creates a shower of particles that eventually form a cone of hadrons, referred to as a jet. In the quark-gluon plasma, the lower energy portion of the shower may eventually be equilibrated into the medium, thus giving a window on the rapid thermalization process in heavy ion collisions. This highlights part of the reason for needing to measure the fully reconstructed jet energy and the correlated particle emission with respect to the jet at all energy scales. In particular, coupling parameters such as $\hat{q}$ and $\hat{e}$ are scale dependent and must take on weak coupling values at high enough energies and very strongly coupled values at thermal energies.

The focus of this proposal is the measurement of jet probes of the medium as a way of understanding the coupling of the medium, the origin of this coupling, and the mechanism of rapid equilibration. Some of these jet probe measurements are already being carried out by the LHC experiments. The quark-gluon plasma is one form of the "condensed matter" of QCD and in any rigorous investigation of condensed matter of any type, it is critical to make measurements as one pushes the system closer to and further from a phase transition and with probes at different length scales. Substantially extending these scales with measurements at RHIC, particularly closer to the transition temperature and at longer distance scales, is the unique ability provided by this proposal.

The critical variables to manipulate for this program are the temperature of the quark-gluon plasma, the length scale probed in the medium, and the virtuality of the hard process as shown schematically in Figure 1.3. In the following three sections we detail the physics of each axis.

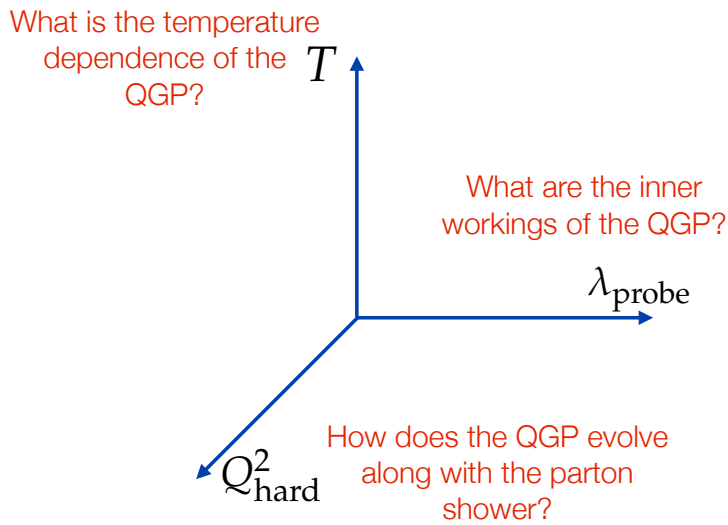

Figure 1.3: Three illustrative axes along which the quark-gluon plasma may be pushed and probed. The axes are the temperature of the quark-gluon plasma, the Q^2_{hard} of the hard process that sets of the scale for the virtuality evolution of the probe, and the wavelength with which the parton probes the medium λ_{probe}.

1.2 What is the temperature dependence of the QGP?

The internal dynamics of more familiar substances—the subjects of study in conventional condensed matter and material physics—are governed by quantum electrodynamics. It is well known that near a phase boundary they demonstrate interesting behaviors, such as the rapid change in the shear viscosity to entropy density ratio, η/s, near the critical temperature, T_c. This is shown in Figure 1.4 for water, nitrogen, and helium [20]. Despite the eventual transition to superfluidity at temperatures below T_c, η/s for these materials remains an order of magnitude above the conjectured quantum bound of Kovtun, Son, and Starinets (KSS) derived from string theory [11]. These observations provide a deeper understanding of the nature of these materials: for example the coupling between the fundamental constituents, the degree to which a description in terms of quasiparticles is important, and the description in terms of normal and superfluid components.

The dynamics of the QGP is dominated by quantum chromodynamics and any experimental characterization of the dependence of η/s on temperature will lead to a deeper understanding of strongly coupled QCD near this fundamental phase transition. Theoretically, perturbative calculations in the weakly coupled limit indicate that η/s decreases slowly as one approaches T_c from above, but with a minimum still a factor of 20 above the KSS bound [21] (as shown in the right panel of Figure 1.4). However, as indicated by the dashed lines in the figure, the perturbative calculation has a large renormalization scale dependence and results for different values of the scale parameter $(\mu, \mu/2, 2\mu)$ diverge

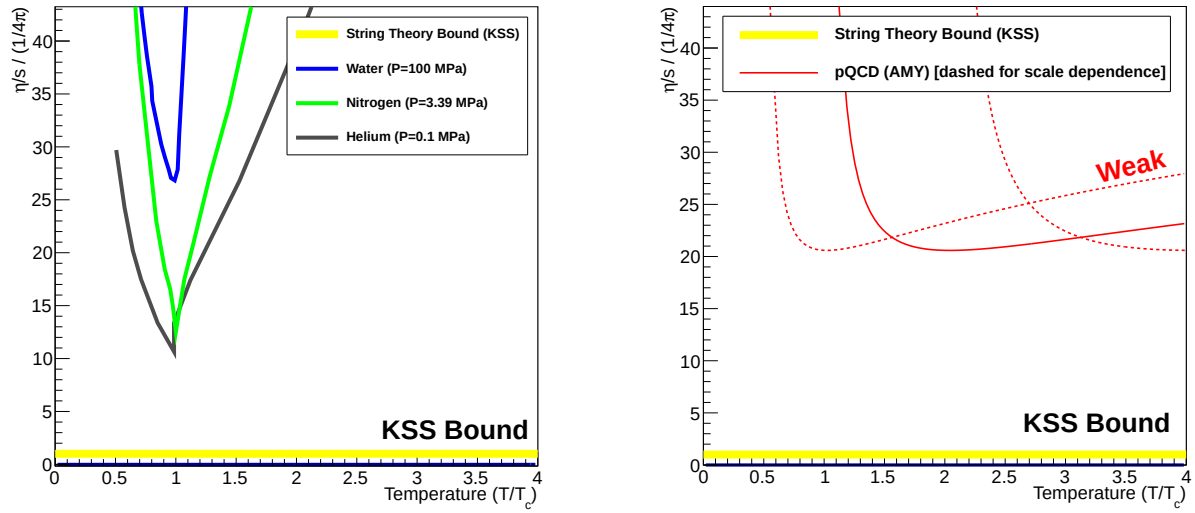

Figure 1.4: (Left) The ratio of shear viscosity to entropy density, η/s, normalized by the conjectured KSS bound as a function of the reduced temperature, T/T_c, for water, Nitrogen, and Helium. The cusp for Helium as shown corresponds to the case at the critical pressure. (Right) Calculation of hot QCD matter (quark-gluon plasma) for a weakly coupled system. Dashed lines show the scale dependence of the perturbative calculation.

from each other near T_c.

Figure 1.5 (left panel) shows several state-of-the-art calculations for η/s as a function of temperature. Hadron gas calculations show a steep increase in η/s below T_c [22], and similar results using the UrQMD model have also been obtained [23]. Above T_c there is a lattice calculation in the SU(3) pure gauge theory [24] resulting in a value near the KSS bound at $T = 1.65\,T_c$. Calculations in the semi-QGP model [25], in which color is not completely ionized, have a factor of five increase in η/s in the region of 1–2 T_c. Also shown are calculations from a quasiparticle model (QPM) with finite μ_B [26] indicating little change in η/s up to 2 T_c. There is also an update on the lower limit on η/s from second order relativistic viscous hydrodynamics [27], with values remaining near $1/4\pi$. It is safe to say that little is known in a theoretically reliable way about the nature of this transition or the approach to weak-coupling.

Hydrodynamic modeling of the bulk medium does provide constraints on η/s, and recent work has been done to understand the combined constraints on η/s as a function of temperature utilizing both RHIC and LHC flow data sets [28, 29, 30]. The results from [30] as constrained by RHIC and LHC data on hadron transverse momentum spectra and elliptic flow are shown in Figure 1.5 (left panel). These reach the pQCD weak coupled value at $20 \times 1/4\pi$ for $T = 3.4T_c$. Also shown are two scenarios, labeled "Song-a" and "Song-b", for $\eta/s(T)$ in [28] from which the authors conclude that "one cannot unambiguously determine the functional form of $\eta/s(T)$ and whether the QGP fluid is more viscous or

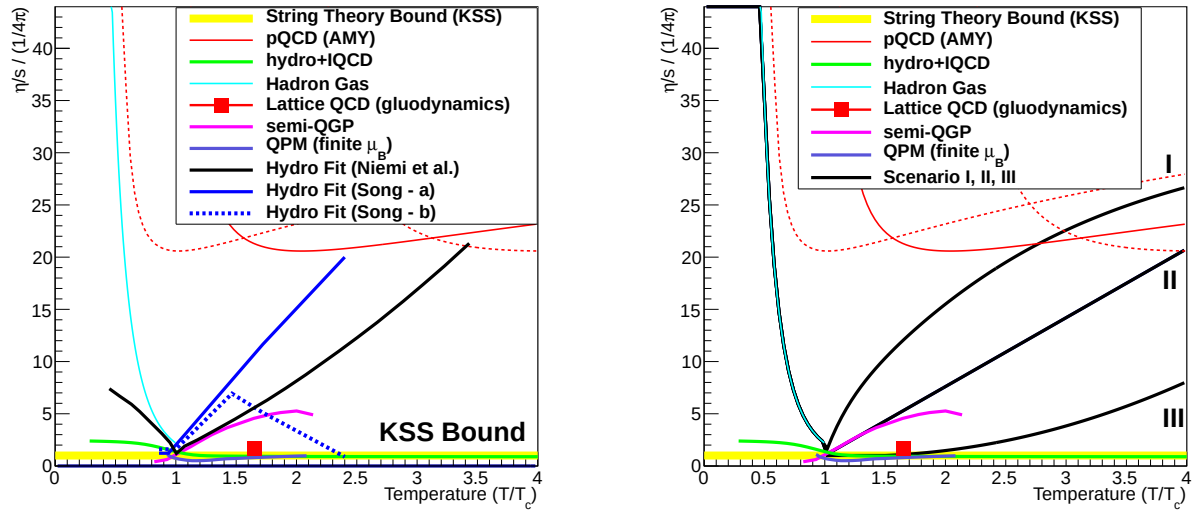

Figure 1.5: (Left) Shear Viscosity divided by entropy density, η/s, renormalized by the conjectured KSS bound as a function of the reduced temperature, T/T_c, with various calculations for the quark-gluon plasma case. See text for discussion. (Right) Figure with three conjectured scenarios for the quark-gluon plasma transitioning from the strongly coupled bound (as a near perfect fluid) to the weakly coupled case.

more perfect at LHC energy."

Shown in Figure 1.5 (right panel) are three possible scenarios for a more or less rapid modification of the medium from the strong to the weak coupling limit. Scenario I has the most rapid change in $\eta/s(T)$ following the "Song-a" parametrization and Scenario III has the least rapid change going through the lattice QCD pure glue result [24]. It is imperative to map out this region in the 'condensed matter' physics of QCD and extract the underlying reason for the change.

The above discussion has focused on η/s as the measure of the coupling strength of the quark-gluon plasma. However, both η/s and jet probe parameters such as $\hat{q}$ and $\hat{e}$ are sensitive to the underlying coupling of the matter, but in distinct ways. Establishing for example the behavior of $\hat{q}$ around the critical temperature is therefore essential to a deep understanding of the quark-gluon plasma. Hydrodynamic modeling may eventually constrain $\eta/s(T)$ very precisely, though it will not provide an answer to the question of the microscopic origin of the strong coupling (something naturally available with jet probes).

The authors of Ref [18] propose a test of the strong coupling hypothesis by measuring both η/s and $\hat{q}$. They derive a relation between the two quantities expected to hold in the weak coupling limit.

$$\hat{q} \stackrel{?}{=} \frac{1.25T^3}{\eta/s} \tag{1.1}$$

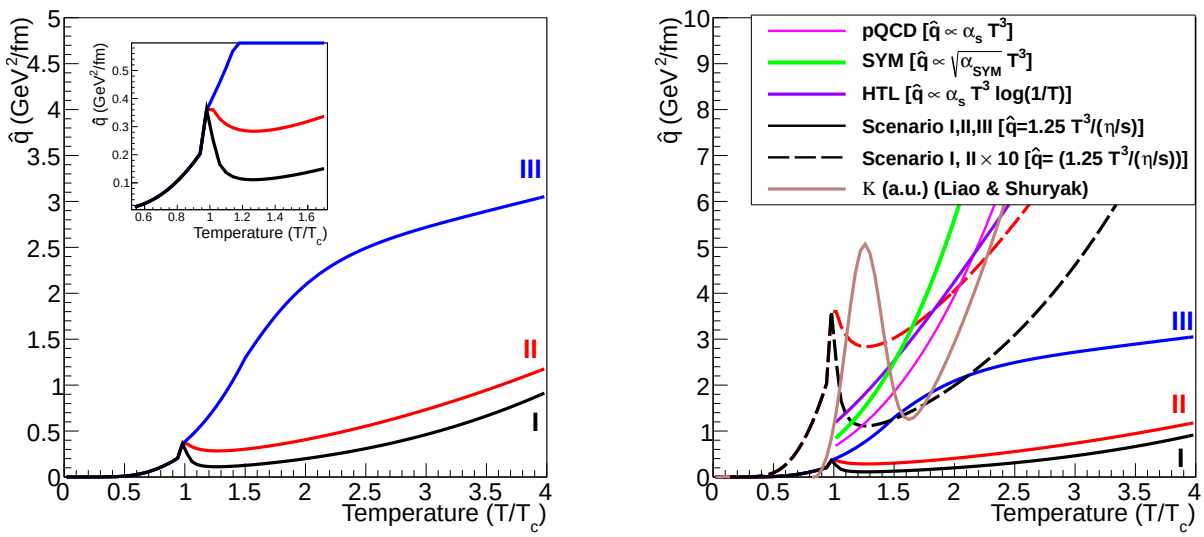

Figure 1.6: (Left) $\hat{q}$ as a function of T/T_c in the three scenarios as related with the weak-coupling calculation. (Right) Different calculations for the scaling of $\hat{q}$ under weak and strong coupling assumptions.

The authors conclude that "an unambiguous determination of both sides of [the equation] from experimental data would thus permit a model independent, quantitative assessment of the strongly coupled nature of the quark-gluon plasma produced in heavy ion collisions." For the three scenarios of $\eta/s(T)$ shown in Figure 1.5 (right panel), we calculate $\hat{q}$ as a function of temperature assuming the equivalence case in Eqn. 1.1 and the result is shown in Figure 1.6 (left panel). The inset in Figure 1.6 shows a magnified view of the region around T_c and a significant local maximum in $\hat{q}$ is observed in scenarios I and II.

Figure 1.6 (right panel) shows that for the equivalence relation of Eqn. 1.1, all three scenarios have a result that differs significantly from the simple perturbative expectation of $\alpha_s T^3$ [31]. Also shown in Figure 1.6 are the predicted temperature dependence of $\hat{q}$ in the strongly coupled AdS/CFT (supersymmetric Yang-Mills) case [19] and the Hard Thermal Loop (HTL) case [32].

Since the expected scaling of $\hat{q}$ with temperature is such a strong function of temperature, jet quenching measurements should be dominated by the earliest times and highest temperatures. In order to have sensitivity to temperatures around 1–2 T_c, measurements at RHIC are needed in contrast to the LHC where larger initial temperatures are produced. In addition, the ability of RHIC to provide high luminosity heavy-ion collisions at a variety of center of mass energies can be exploited to probe the detailed temperature dependence of quenching right in the vicinity of T_c.

In a recent paper [33], Liao and Shuryak use RHIC measurements of single hadron suppression and azimuthal anisotropy to infer that "the jet quenching is a few times stronger near

T_c relative to the quark-gluon plasma at $T > T_c$." This enhancement of $\hat{q}$ is shown in Figure 1.6 (right panel) and is the result of color magnetic monopole excitations in the plasma near T_c. A more detailed discussion of constraints from current experimental measurements is given in Section 1.5. We note that enhancements in $\hat{q}$ above the critical temperature may be a generic feature of many models, as illustrated by the three conjectured evolutions, and so underscore the need for detailed measurements of quark-gluon plasma properties near the transition temperature.

All measurements in heavy ion collisions are the result of emitted particles integrated over the entire time evolution of the reaction, covering a range of temperatures. Similar to the hydrodynamic model constraints, the theory modeling requires a consistent temperature and scale dependent model of the quark-gluon plasma and is only well constrained by precision data through different temperature evolutions, as measured at RHIC and the LHC.

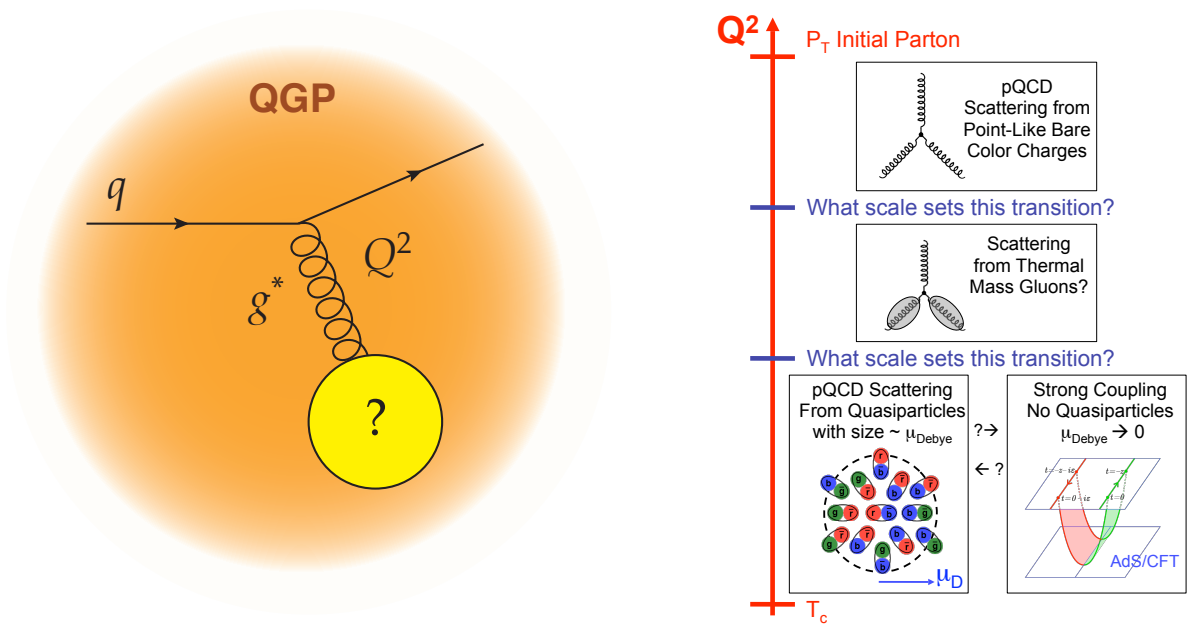

Figure 1.7: (Left) Diagram of a quark exchanging a virtual gluon with an unknown object in the QGP. This highlights the uncertainty for what sets the scale of the interaction and what objects or quasiparticles are recoiling. (Right) Diagram as a function of the Q^2 for the net interaction of the parton with the medium and the range of possibilities for the recoil objects.

1.3 What are the inner workings of the QGP?

A second axis along which one can investigate the underlying structure of the quark-gluon plasma concerns the question of what length scale of the medium is being

probed by jet quenching processes. In electron scattering, the scale is set by the virtuality of the exchanged photon, Q^2. By varying this virtuality one can obtain information over an enormous range of scales: from pictures of viruses at length scales of 10^{-5} meters, to the partonic make-up of the proton in deep inelastic electron scattering at length scales of less than 10^{-18} meters. For the case of hard scattered partons in the quark-gluon plasma, the length scale probed is related not to the virtuality of the initial hard process discussed above, but rather to the virtuality of the gluon exchanged with the color charges in the medium, as shown in the left panel of Figure 1.7. However, it is theoretically unclear whether the length scale is simply set by the individual exchange gluon virtuality or instead by the total coherent energy loss through the medium.

Figure 1.7 (right panel) shows that if the length scale probed is very small then one expects scattering directly from point-like bare color charges, most likely without any influence from quasiparticles or deconfinement. As one probes longer length scales, the scattering may be from thermal mass gluons and eventually from possible quasiparticles with size of order the Debye screening length. Rajagopal states that "at some length scale, a quasiparticulate picture of the QGP must be valid, even though on its natural length scale it is a strongly coupled fluid. It will be a challenge to see and understand how the liquid QGP emerges from short-distance quark and gluon quasiparticles. [34]"

The extension of jet measurements over a wide range of energies and with different medium temperatures again gives one the largest span along this axis. What the parton is scattering from in the medium is tied directly to the balance between radiative energy loss and inelastic collisional energy loss in the medium. In the limit that the scattering centers in the medium are infinitely massive, one only has radiative energy loss—as was assumed for nearly 10 years to be the dominant parton energy loss effect. In the model of Liao and Shuryak [33], the strong coupling near the quark-gluon plasma transition is due to the excitation of color magnetic monopoles, and this should have a significant influence on the collisional energy loss and equilibration of soft partons into the medium.

As a parton traverses the medium if it scatters from infinitely massive scattering centers, then the energy loss can only be through radiative processes. As the mass of the objects being scattered from lowers, the contributions of elastic energy loss become more significant. That is why measurements of jet observables that help disentangle these different energy loss processes are needed at both RHIC and LHC where the length scale probed and the possible coupling strength of the QGP are different.

1.4 How does the QGP evolve along with the parton shower?

The initial hard scattered parton starts out very far off-shell and in e^+e^-, $p+p$ or $p+\overline{p}$ collisions the virtuality evolves in vacuum through gluon splitting down to the scale of hadronization. In heavy ion collisions, the vacuum virtuality evolution is interrupted at some scale by scattering with the medium partons which increase the virtuality with

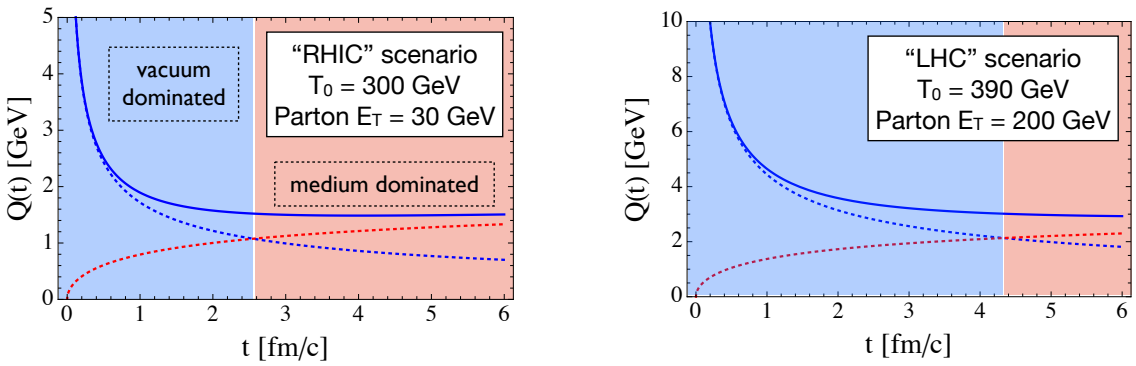

Figure 1.8: Jet virtuality evolution at RHIC (left) and LHC (right). Vacuum contributions to virtuality (blue dashed lines) decrease with time and medium induced contributions (red dashed lines) increase as the parton scatters in the medium. The total virtuality (blue solid lines) is the quadrature sum of the two contributions. At RHIC the medium induced virtuality dominates by 2.5 fm/c while at the LHC the medium term does not dominate until 4.5 fm/c. From Ref. [35].

respect to the vacuum evolution. Figure 1.8 shows the expected evolution of virtuality in vacuum, from medium contributions, and combined for a quark-gluon plasma at $T_0 = 300$ MeV with the traversal of a 30 GeV parton (left) and at $T_0 = 390$ MeV with the traversal of a 200 GeV parton (right) [35, 36]. If this picture is borne out, it "means that the very energetic parton [in the right picture] hardly notices the medium for the first 3–4 fm of its path length [36]." Spanning the largest possible range of virtuality (initial hard process Q^2) is very important, but complementary measurements at both RHIC and LHC of produced jets at the same virtuality (around 50 GeV) will test the interplay between the vacuum shower and medium scattering contributions.

1.5 Current jet probe measurements

Jet quenching (i.e., the significant loss of energy for partons traversing the QGP) was discovered via measurements at RHIC of the suppression of single hadron yields compared to expectations from $p+p$ collisions [43, 44]. Figure 1.9 [39] shows a comparison between the PHENIX π^0 R_{AA} data and the Parton Quenching Model (PQM) [37, 38] with various values of $\hat{q}$. This calculation assumes radiative energy loss only in a weakly coupled picture and with no recoil collisional energy loss with partons or quasiparticles in the medium. The coupling parameter value $\hat{q} = 13.2\,\mathrm{GeV}^2/\mathrm{fm}$ implies a very strong coupling and violates the weak coupled assumption of the model formalism.

However, as detailed in Ref. [39, 40], other formalisms also assuming weak coupling are able to achieve an equally good description of the data and with substantially smaller values of $\hat{q}$. Thus, the single high p_T hadron suppression constrains the $\hat{q}$ value within a

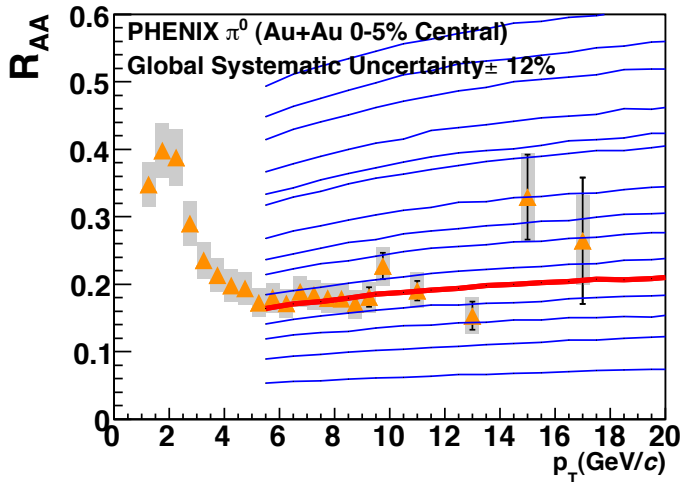

Figure 1.9: π^0 R_{AA} for central Au+Au collisions compared to PQM Model calculations [37, 38] for various values of $\langle\hat{q}\rangle$ [39]. The red line corresponds to $\langle\hat{q}\rangle = 13.2\,\mathrm{GeV}^2/\mathrm{fm}$ and is the best fit to the data.

model, but is not able to discriminate between different energy loss mechanisms and formalisms for the calculation. Two-hadron correlations measure the correlated fragmentation between hadrons from within the shower of one parton and also between the hadrons from opposing scattered partons. These measurements, often quantified in terms of a nuclear modification I_{AA} [45, 46, 47], are a challenge for models to describe simultaneously [48].

One observable that has been particularly challenging for energy loss models to reproduce is the azimuthal anisotropy of π^0 production with respect to the reaction plane. A weak dependence on the path length in the medium is expected from radiative energy loss. This translates into a small v_2 for high p_T particles (i.e., only a modest difference in parton energy loss when going through a short versus long path through the QGP). Results of π^0 v_2 are shown in Figure 1.10 [42]. Weakly coupled radiative energy loss models are compared to the R_{AA} (bottom panels) and v_2 (top panels) data. These models reproduce the R_{AA}, but they fall far short of the v_2 data in both p_T ranges measured (6–9 GeV/c and > 9 GeV/c). This large path length dependence is naturally described by strongly coupled energy loss models [49, 42]. Note that one can match the v_2 by using a stronger coupling, larger $\hat{q}$, but at the expense of over-predicting the average level of suppression.

The total energy loss of the leading parton provides information on one part of the parton-medium interaction. Key information on the nature of the particles in the medium being scattered from is contained in how the soft (lower momentum) part of the parton shower approaches equilibrium in the quark-gluon plasma. This information is only accessible through full jet reconstruction, jet-hadron correlation, and γ-jet correlation observables.

There are preliminary results on fully reconstructed jets from both STAR [50, 51, 52, 53]

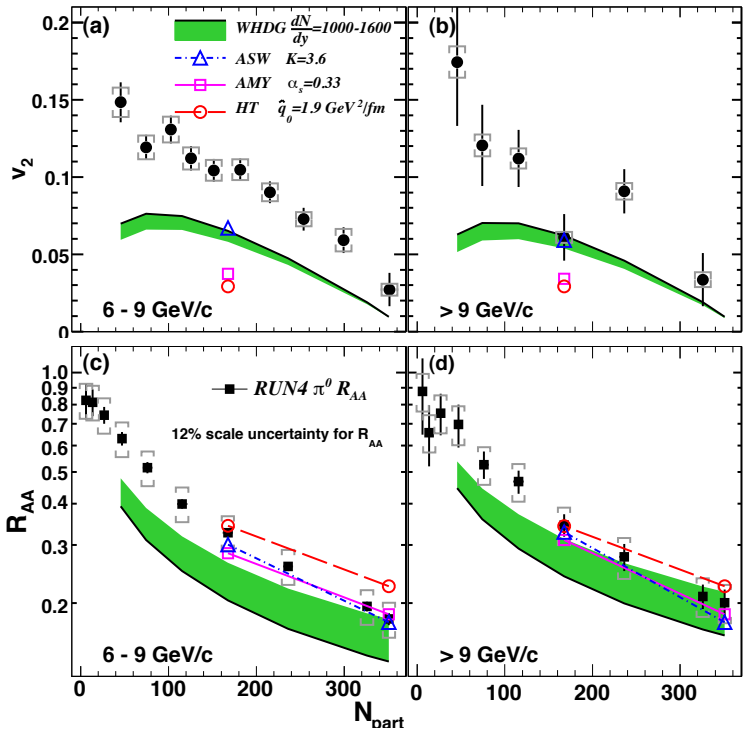

Figure 1.10: π^0 v_2 (top panels) and R_{AA} (bottom panels) for $6 < p_T < 9\,\mathrm{GeV/c}$ (left panels) and $p_T > 9\,\mathrm{GeV/c}$ (right panels). Calculations from four weakly coupled energy loss models are shown as well [40, 41]. From Ref. [42].

and PHENIX experiments [54, 55]. However, these have not proceeded to publication in part due to limitations in the measurement capabilities. In this proposal we demonstrate that a comprehensive jet detector (sPHENIX) with large, uniform acceptance and high rate capability, combined with the now completed RHIC luminosity upgrade can perform these measurements to access this key physics.

New data from the LHC experiments has significantly expanded the information on jet probes of the QGP. Figure 1.11 shows the aforementioned π^0 nuclear modification factor from the PHENIX experiment together with an energy loss calculation wherein the value of $\hat{q}$ is constrained to match the data [56]. Also shown are recent results from the ALICE experiment at the LHC [57] compared to the same energy loss calculation scaled by the expected increase in the color charge density created in the higher energy LHC collisions, shown as the light blue band. The over-prediction based on the assumption of an unchanging probe-medium coupling strength led to title of Ref. [56]: "The surprisingly transparent sQGP at the LHC." They state that "one possibility is the sQGP produced at the LHC is in fact more transparent than predicted." Similar conclusions have been reached by other authors [58, 59, 60].

The measurements of fully reconstructed jets and the particles correlated with the jet (both inside the jet and outside) are crucial to testing this hypothesis. Not only does the strong

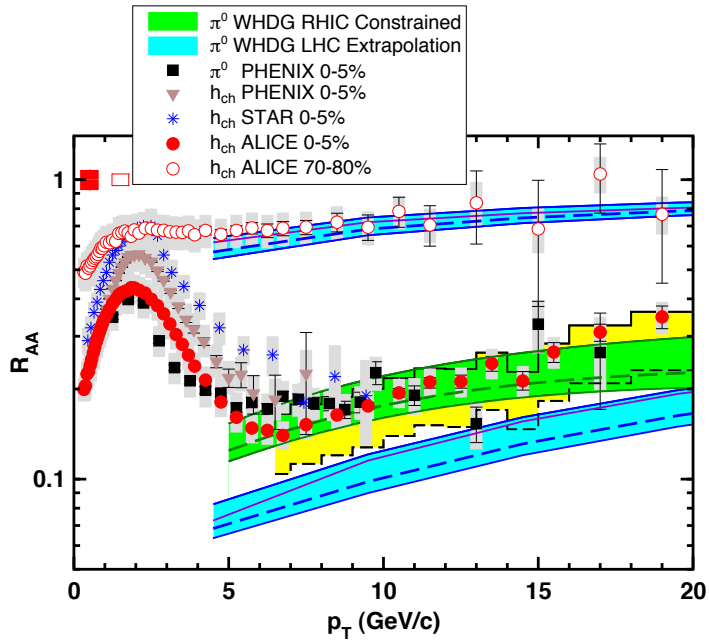

Figure 1.11: R_{AA} measurements from RHIC and the LHC compared to WHDG calculations. The parameters are constrained by the RHIC data and extrapolated to 2.76 TeV. The prediction for the LHC is shown (blue band) and lies below the ALICE data for central collisions (red circles). From Ref. [56].

coupling influence the induced radiation from the hard parton (gluon bremsstrahlung) and its inelastic collisions with the medium, but it also influences the way soft partons are transported by the medium outside of the jet cone as they fall into equilibrium with the medium. Thus, the jet observables combined with correlations get directly at the coupling of the hard parton to the medium and the parton-parton coupling for the medium partons themselves.

These jet observables are now becoming available at the LHC. The first results based on reconstructed jets in heavy ion collisions were the centrality dependent dijet asymmetries measured by ATLAS [61]. These results, shown in Figure 1.12, indicate a substantial broadening of dijet asymmetry $A_J = (E_1 - E_2)/(E_1 + E_2)$ distribution for increasingly central Pb+Pb collisions and the lack of modification to the dijet azimuthal correlations. The broadening of the A_J distribution points to substantial energy loss for jets and the unmodified azimuthal distribution shows that the opposing jet $\Delta\phi$ distribution is not broadened as it traverses the matter. Figure 1.13 shows CMS results [62] quantifying the fraction of dijets which are balanced (with $A_J < 0.15$) decreases with increasing centrality.

Direct photon-jet measurements are a powerful tool to study jet quenching. Unlike dijet measurements the photon passes through the matter without losing energy, providing a much cleaner handle on the expected jet p_T [63]. CMS has first results for photons

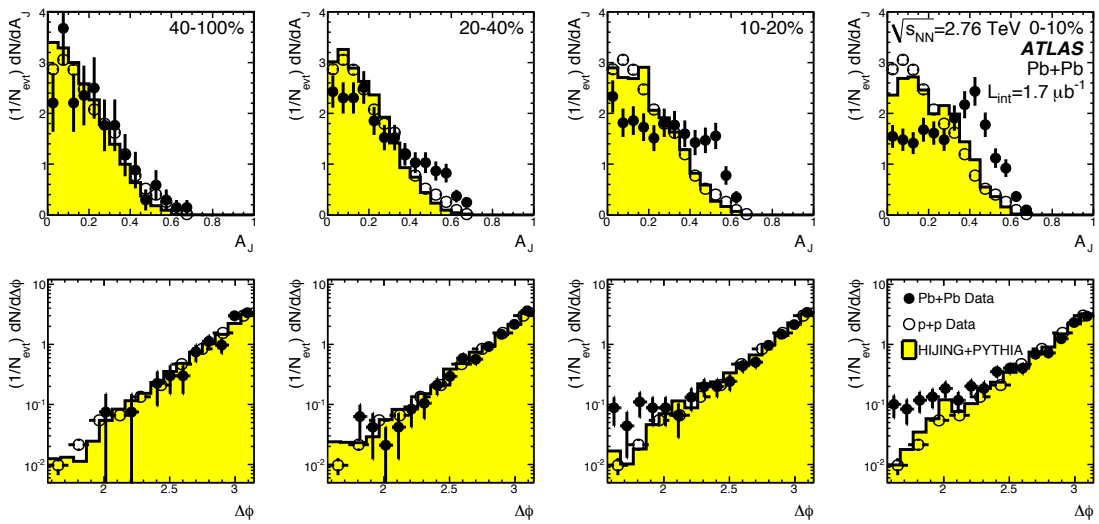

Figure 1.12: A_J (top row) and dijet $\Delta\phi$ distribution from ATLAS [61]. Jets are reconstructed with the anti-k_T algorithm with $R = 0.4$. The leading jet has $E_T > 100$ GeV and the associated jet has $E_T > 25$ GeV. Pb+Pb data (solid points), p+p data at 7 TeV (open points) and PYTHIA embedded in HIJING events and run through the ATLAS Monte Carlo (yellow histograms) are shown. From Ref. [61].

with $p_T > 60$ GeV/c correlated with jets with $p_T > 30$ GeV/c [64]. Though with modest statistical precision, the measurements indicate energy transported outside the $R = 0.3$ jet cone through medium interactions.

These and other reconstructed jet measurements have been complementary to one and two particle measurements at the LHC. Reconstructed jets have significantly extended the kinematic range for jet quenching studies at the LHC, and quenching effects are observed up to the highest reconstructed jet energies (> 300 GeV) [65]. They also provide constraints on the jet modification that are not possible with particle based measurements. For example, measurements from ATLAS constrain jet fragmentation modification from vacuum fragmentation to be small [66] and CMS results on jet-hadron correlations have shown that the lost energy is recovered in low p_T particles far from the jet cone [62]. At the LHC the lost energy is transported to very large angles and the remaining jet fragments as it would in the vacuum.

Detector upgrades to PHENIX and STAR at RHIC with micro-vertex detectors will allow the separate study of c and b quark probes of the medium, as tagged via displaced vertex single electrons and reconstructed D and Λ_c hadrons. Similar measurements at the LHC provide tagging of heavy flavor probes as well. These measurements will also provide insight on the different energy loss mechanisms, in particular because initial measurements of non-photonic electrons from RHIC challenge the radiative energy loss models.

It is clear that in addition to extending the RHIC observables to include fully reconstructed

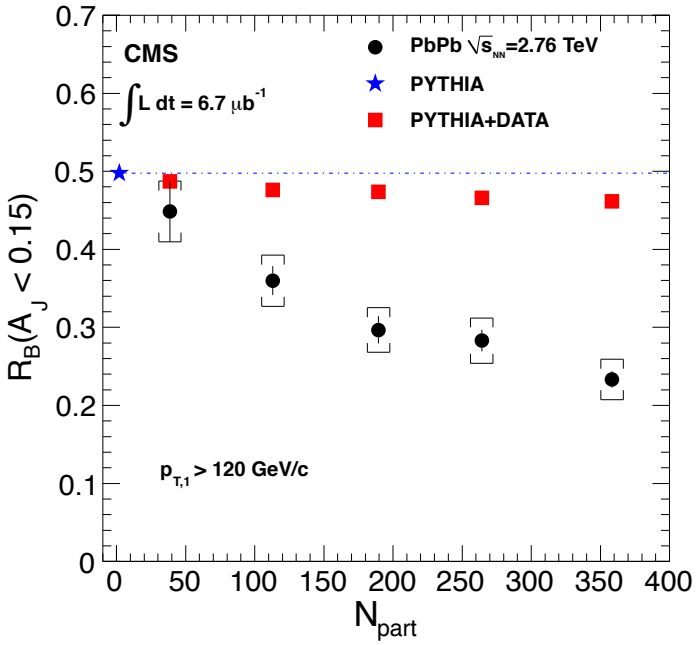

Figure 1.13: Fraction of dijets which have $A_J < 0.15$ in Pb+Pb collisions as a function of centrality. Jets are reconstructed with an iterative cone algorithm with a radius of 0.5. The leading jet is required to have an $E_T > 120\,\text{GeV}$ and the associated jet has $E_T > 50\,\text{GeV}$. Results are shown for Pb+Pb data (circles), PYTHIA (star) and PYTHIA jets embedded into real data (squares). From Ref. [62].

jets and γ-jet correlations, theoretical development work is required for converging to a coherent 'standard model' of the medium coupling strength and the nature of the probe-medium interaction. In the next section, we detail positive steps in this direction.

1.6 Theoretical calculations of jets at RHIC

Motivated in part by the new information provided by early LHC jet results and the comparison of RHIC and LHC single and di-hadron results, the theoretical community is actively working to understand the detailed probe-medium interactions. The challenge is to understand not only the lost energy of the leading parton, but how the parton shower evolves in medium and how much of the lost energy is re-distributed in the quark-gluon plasma. Theoretical calculations attempting to describe the wealth of new data from RHIC and the LHC currently have not reconciled some of the basic features, with some models including large energy transfer to the medium as heat (for example [67]) and others with mostly radiative energy loss (for example [68, 69]). None of the current calculations available has been confronted with the full set of jet probe observables from RHIC and the LHC. Measurements of jets at RHIC energies and with jets over a different

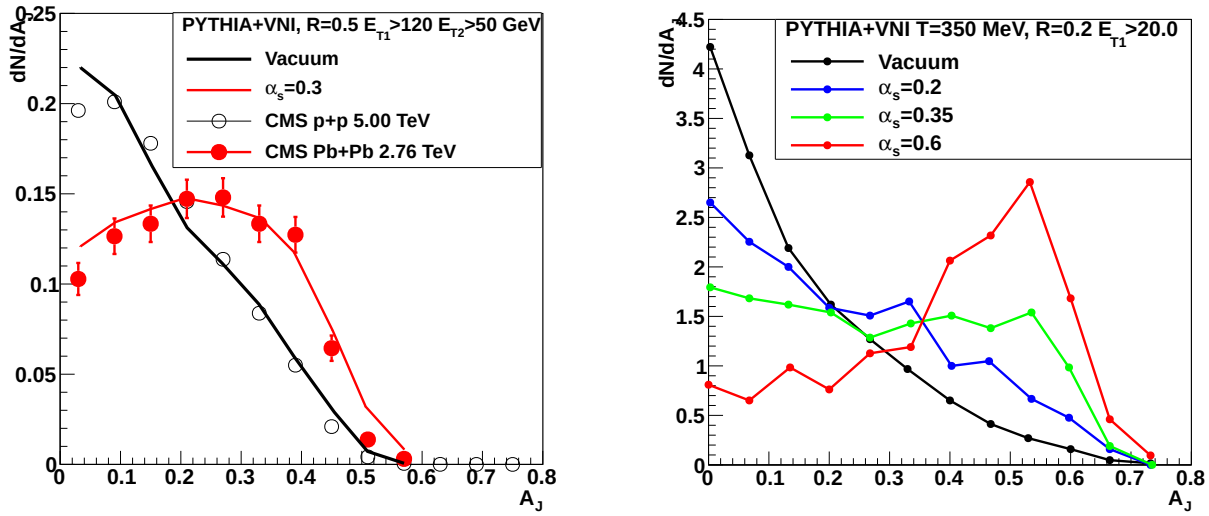

Figure 1.14: (Left) Calculation in VNI parton cascade of dijet A_J with $T = 0.35\,\text{GeV}$ and $\alpha_s = 0.3$ compared to the CMS data [77]. (Right) Calculation for RHIC jet energies, $E_{T,1} > 20\,\text{GeV}$, for a circular geometry of radius 5 fm of A_J for different values of α_s increasing to $\alpha_s = 0.6$ (red line) [78].

kinematic range allow for specific tests of these varying pictures. In this section, we give a brief review of a subset of calculations for jet observables at RHIC enabled by the sPHENIX upgrade and highlight the sensitivity of these observables to the underlying physics.

Much of this work has been carried out under the auspices of the Department of Energy Topical Collaboration on Jet and Electromagnetic Tomography of Extreme Phases of Matter in Heavy-ion Collisions [70]. A workshop was held by the JET Collaboration at Duke University in March 2012 dedicated to the topic of jet measurements at RHIC which was attended by theorists as well as experimentalists from both RHIC and the LHC. There was active participation by a number of theory groups and there has been significant continued effort, including follow up video conferences connecting theorists and experimentalists.

In order to overcome specific theoretical hurdles regarding analytic parton energy loss calculations and to couple these calculations with realistic models of the QGP space-time evolution, Monte Carlo approaches have been developed (as examples [71, 72, 73, 74, 75, 76]). Here we describe RHIC energy jet probe results from four specific theory groups utilizing different techniques for calculating the jet-medium interactions. These efforts indicate a strong theoretical interest and the potential constraining power of a comprehensive jet physics program at RHIC.

The first results are from Coleman-Smith and collaborators [77, 74] where they extract jet parton showers from PYTHIA (turning off hadronization) and then embed the partons into a deconfined quark-gluon plasma, modeled with the VNI parton cascade [79]. For

the calculations shown here, the background medium consists of a cylinder of deconfined quarks and gluons at a uniform temperature. One excellent feature of the calculation is that it provides the ability to track each individual parton and thus not only look at the full time evolution of scattered partons from the shower, but also medium partons that are kicked up and can contribute particles to the reconstructed jets.

Calculation results for the dijet asymmetry $A_J = (E_1 - E_2)/(E_1 + E_2)$ in a QGP with a temperature appropriate for LHC collisions and fixed $\alpha_s = 0.3$ are shown in Figure 1.14 (left panel) [77]. The jets in the calculation are reconstructed with the anti-k_T algorithm with radius parameter $R = 0.5$ and then smeared by a simulated jet resolution of $100\%/\sqrt{E}$, and with requirements of $E_{T1} > 120\,\text{GeV}$ and $E_{T2} > 50\,\text{GeV}$ on the leading and sub-leading jet, respectively. The calculated A_J distributions reproduce the CMS experimental data [62].

In Figure 1.14 (right panel) the calculation is repeated with a medium temperature appropriate for RHIC collisions and with RHIC observable jet energies, $E_{T1} > 20\,\text{GeV}$ and $R = 0.2$. The calculation is carried out for different coupling strengths α_s between partons in the medium themselves and the parton probe and medium partons. The variation in the value of α_s should be viewed as changing the effective coupling in the many-body environment of the QGP. It is interesting to note that in the parton cascade BAMPS, the authors find a coupling of $\alpha_s \approx 0.6$ is required to describe the bulk medium flow [80]. These results indicate sizable modification to the dijet asymmetry and thus excellent sensitivity to the effective coupling to the medium at RHIC energies.

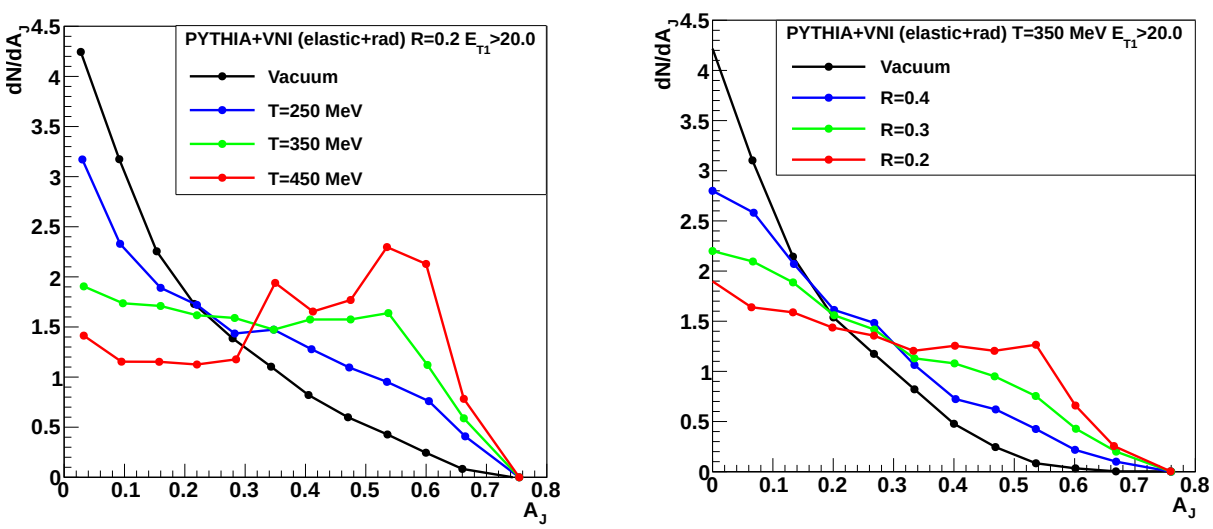

Figure 1.15: Calculations from Coleman-Smith [78] for dijets embedded into the VNI parton cascade. The dijet asymmetry A_J for leading jets with $E_T > 20\,\text{GeV}$ is shown as the medium temperature is varied (left panel) and as the jet cone radius is varied with fixed temperature $T = 350\,\text{MeV}$ (right panel).

Figure 1.15 (left panel) shows the temperature dependence of the dijet asymmetry, now

keeping the coupling α_s fixed. One observes a similar sharp drop in the fraction of energy balanced dijets with increasing temperature to that seen for increasing the effective coupling, and so combining these observations with constrained hydrodynamic models and direct photon emission measurements is important. Given that the initial temperatures of the QGP formed at RHIC and the LHC should be significantly different, this plot shows that if RHIC and LHC measure the A_J distribution at the same jet energy there should still be a sensitivity to the temperature which will lead to an observable difference. Thus, having overlap in the measured jet energy range at RHIC and the LHC is important, and this should be available for jet energies of 40–70 GeV. Figure 1.15 (right panel) shows the jet cone size, R, dependence of A_J at a fixed temperature. The narrowest jet cone $R = 0.2$ has the most modified A_J distribution, as partons are being scattered away by the medium to larger angles.

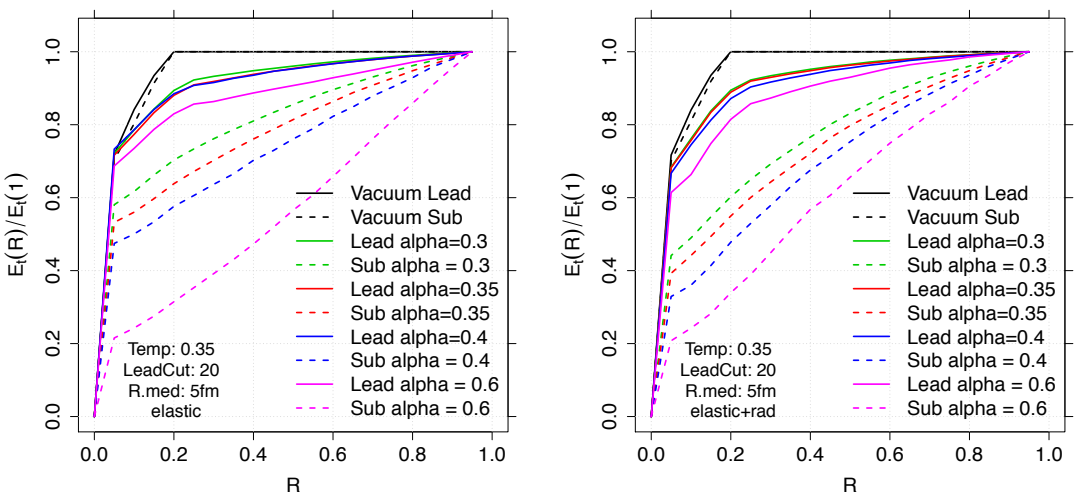

Figure 1.16: Calculations from Coleman-Smith [78] showing the jet energy profile as a function of radius for leading (solid lines) and sub-leading (dashed lines) jets. Leading jets have $E_T > 20$ GeV and sub-leading jets have $E_T > 5$ GeV. The medium temperature is 350 MeV.

Complementary to measuring jets with different radius parameters is to directly examine the profile of energy both within and outside the reconstructed jet. Results on the predicted distribution of energy as a function of radius are shown in Figure 1.16. The solid lines are for the leading jet and for different values of the medium coupling α_s. The dashed lines are for the sub-leading jet. One observes a particularly strong dependence on the coupling in the radial energy profile of the sub-leading jet, as this parton is typically biased to a longer path length through the medium. The left panel is including only elastic collisional interactions and the right panel incorporates additional radiative processes. At coupling $\alpha_s = 0.4$ for example, the fraction of energy in the sub-leading jet within $R < 0.2$ is 60% with elastic collisions only and less than 50% when including radiative energy loss. The experimental extraction of these two contributions is a critical step towards extracting a microscopic picture of the QGP.

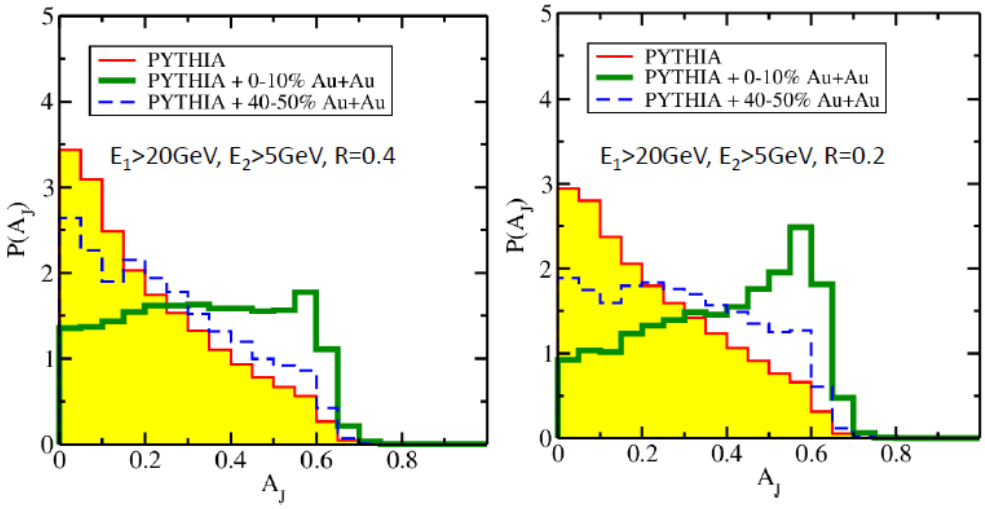

Figure 1.17: Calculations from Qin et al. [81] of dijet A_J for $E_{T,1} > 20\,\text{GeV}$ and $E_{T,2} > 5\,\text{GeV}$ for $R = 0.4$ jets (left) and $R = 0.2$ jets (right). Central (green) and mid-central (blue) distributions are shown along with the initial PYTHIA distributions (red).

The second results are from Qin and collaborators [82, 81] where they solve a differential equation that governs the evolution of the radiated gluon distribution as the jet propagates through the medium. Energy contained inside the jet cone is lost by dissipation through elastic collisions and by scattering of shower partons to larger angles. Their calculation is able to describe the LHC measured dijet asymmetry [82]. Figure 1.17 shows the predicted dijet asymmetry at RHIC for mid-central and central Au+Au collisions for leading jets $E_{T1} > 20\,\text{GeV}$ and jet radius parameter $R = 0.4$ and $R = 0.2$ in the left and right panels, respectively. Despite the calculation including a rather modest value of $\hat{q}$ and $\hat{e}$, the modification for $R = 0.2$ is as strong as the result with $\alpha_s = 0.6$ from Coleman-Smith and collaborators shown above in the right panel of Figure 1.14. Calculations of γ-jet correlations indicate similar level modifications. It is also notable that Qin and collaborators have calculated the reaction plane dependence of the dijet A_J distribution and find negligible differences. This observable will be particularly interesting to measure at RHIC since these calculations have difficultly reproducing the high p_T π^0 reaction plane dependence (v_2) as discussed in the previous section.

Figure 1.18 shows results for the inclusive jet R_{AA} as a function of p_T for jet radius parameters $R = 0.2$ and $R = 0.4$. It is striking that the modification is almost independent of p_T of the jet and there is very little jet radius dependence. The modest suppression, of order 20%, in mid-central Au+Au collisions is of great interest as previous measurements indicate modification of single hadrons and dihadron correlations for this centrality category. Measurements of jets with a broad range of radius parameters are easier in the lower multiplicity mid-central collisions.

The third results are from Young and Schenke and collaborators [73]. These calculations

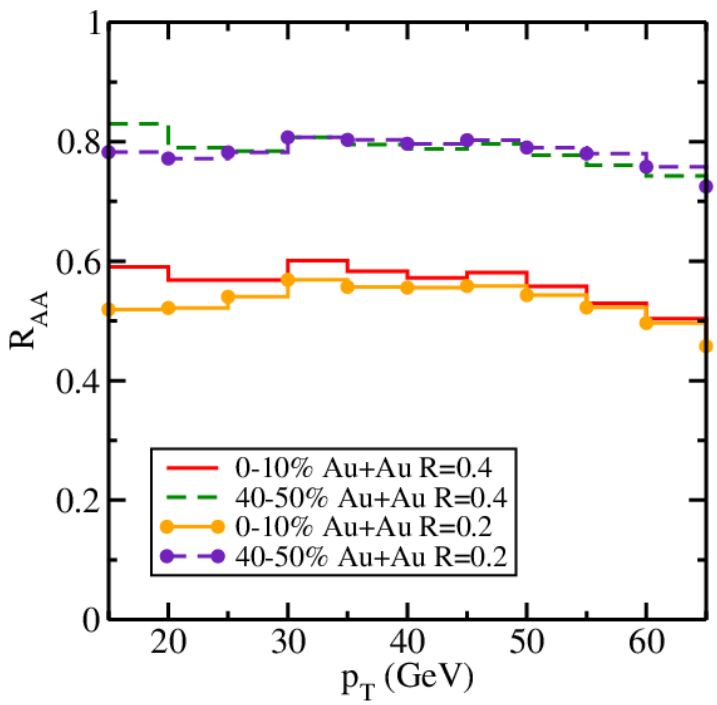

Figure 1.18: Calculations from Qin et al. [81] for jet R_{AA} for central (solid lines) and mid-central collisions (dashed lines) for $R = 0.2$ and 0.4 jets.

utilize a jet shower Monte Carlo, referred to as MARTINI [83], and embed the shower on top of a hydrodynamic space-time background, using the model referred to as MUSIC [84]. Figure 1.19 shows the jet energy dependence of A_J for RHIC energy dijets, $E_{T1} > 25\,\text{GeV}$ and $E_{T1} > 35\,\text{GeV}$ in the left and right panels, respectively. These results are directly compared to the calculations from Qin and collaborators and indicate a substantially different modification for the higher energy dijets. Interestingly, both of these approaches, when applied at the higher collision energies of the LHC, each reproduce the measured data quite well [85, 82].

Our final set of illustrative theory calculations come from Vitev and collaborators [87, 88, 89] where they utilize a Next-to-Leading-Order (NLO) calculation and consider not only final-state inelastic parton interactions in the QGP, but also initial-state cold nuclear matter effects. Figure 1.20 shows the dijet asymmetry A_J for jets with $E_{T1} > 30\,\text{GeV}$ and $R = 0.2$ (left panels) and $E_{T1} > 50\,\text{GeV}$ and $R = 0.6$ (right panels). The upper plots are for radiative energy loss only and the lower plots are including collisional energy loss as well, and then the different colors are varying the probe-medium coupling by $\pm 10\%$. There is sensitivity even to these 10% coupling modifications, and for the higher energy jets there is a dramatic difference predicted from the inclusion of collisional energy loss.

For the inclusive jet suppression, these calculations predict a significant jet radius R dependence to the modification, in contrast to the result from Qin and collaborators. In

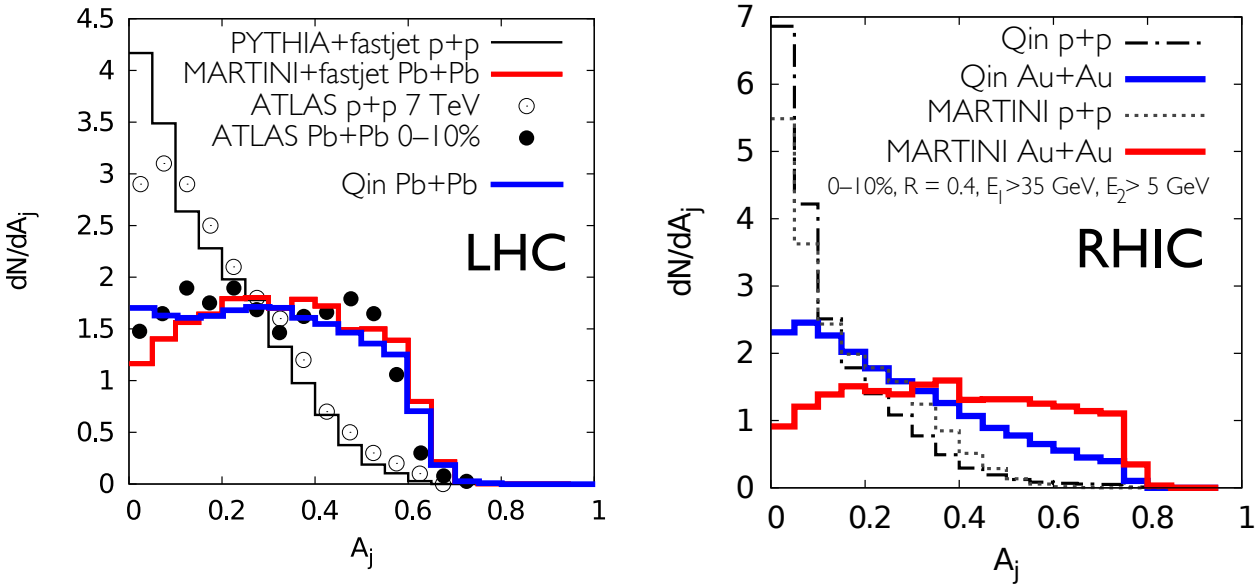

Figure 1.19: A_J distributions in MARTINI+MUSIC [86] and the model of Qin et al. [81]. (Left) Comparison of A_J calculations in MARTINI+MUSIC and by Qin et al for Pb+Pb collisions at 2.76 TeV (red line, Qin et al; blue line, MARTINI+MUSIC). Both calculations show a similar broad A_J distribution. (Right) Same as left panel, but for Au+Au collisions at 200 GeV (with leading jet $E_T > 35$ GeV). Here a difference in shape is observed between the two models with the Qin et al. model developing a peak at small A_J while the MARTINI+MUSIC calculation retains a shape in the calculation at the higher energy.

addition, Vitev and collaborators hypothesize a substantial cold nuclear matter effect of initial state parton energy loss. Because the high energy jets originate from hard scattering of high Bjorken x partons, a modest energy loss of these partons results in a reduction in the inclusive jet yields. At RHIC with d+Au running we will make cold nuclear matter measurements at the same collision energy and determine the strength of these effects as a baseline to heavy ion measurements.

1.7 Measuring jets, dijets, and γ-jet correlations at RHIC

Jet and γ-jet measurements at RHIC are particularly appealing for the reasons previously detailed. In order to make these observations, one requires both sufficient rate and acceptance for jets, dijets, and γ-jet events and a detector with large and uniform acceptance to measure them. The performance of the proposed sPHENIX detector is described in later chapters. Here we highlight the large rate of such events available at RHIC energies.

The inclusive jet yield within $|\eta| < 1.0$ in 0–20% central Au+Au collisions at 200 GeV has been calculated for p+p collisions by Vogelsang in a Next-to-Leading-Order (NLO)

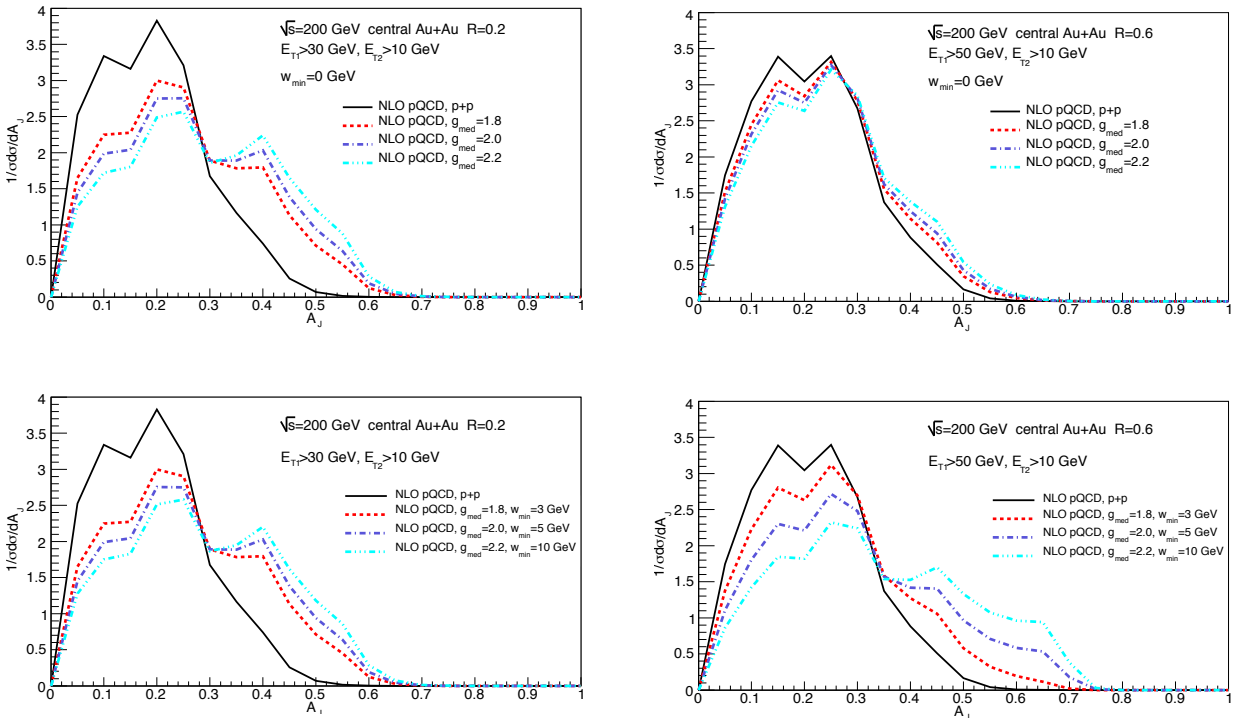

Figure 1.20: A_J distributions calculated by Vitev et al. [87, 88, 89] for two sets of kinematic cuts and jet cone radii. The upper plots are for radiative energy loss only, and the lower plots include collisional energy loss as well.

perturbative QCD formalism [90] and then scaled up by the expected number of binary collisions, as shown in Figure 1.21. Also shown are calculation results for π^0 and direct and fragmentation photons. The bands correspond to the renormalization scale uncertainty in the calculation (i.e., $\mu, \mu/2, 2\mu$).

The completion of the stochastic cooling upgrade to the RHIC accelerator [91] has been incorporated into the RHIC beam projections [92]. Utilizing these numbers and accounting for accelerator and experiment uptime and the fraction of collisions within $|z| < 10$ cm, the nominal full acceptance range for the detector, the sPHENIX detector can sample 50 billion Au+Au minimum bias collisions in a one-year 20 week run. Note that the PHENIX experiment has a nearly dead-timeless high-speed data acquisition and trigger system that has already sampled tens of billions of Au+Au minimum bias collisions, and maintaining this high rate performance with the additional sPHENIX components is an essential design feature.

Figure 1.21 shows the counts per event with p_T larger than the value on the x-axis for the most central 20% Au+Au collisions at $\sqrt{s_{NN}} = 200$ GeV. With 10 billion events per RHIC year for this centrality selection, this translates into jet samples from 20–70 GeV and direct photon statistics out to 40 GeV. The statistical sample of jets and direct photons measurable in one year with sPHENIX is shown in Table 1.1. It is notable that within the acceptance of

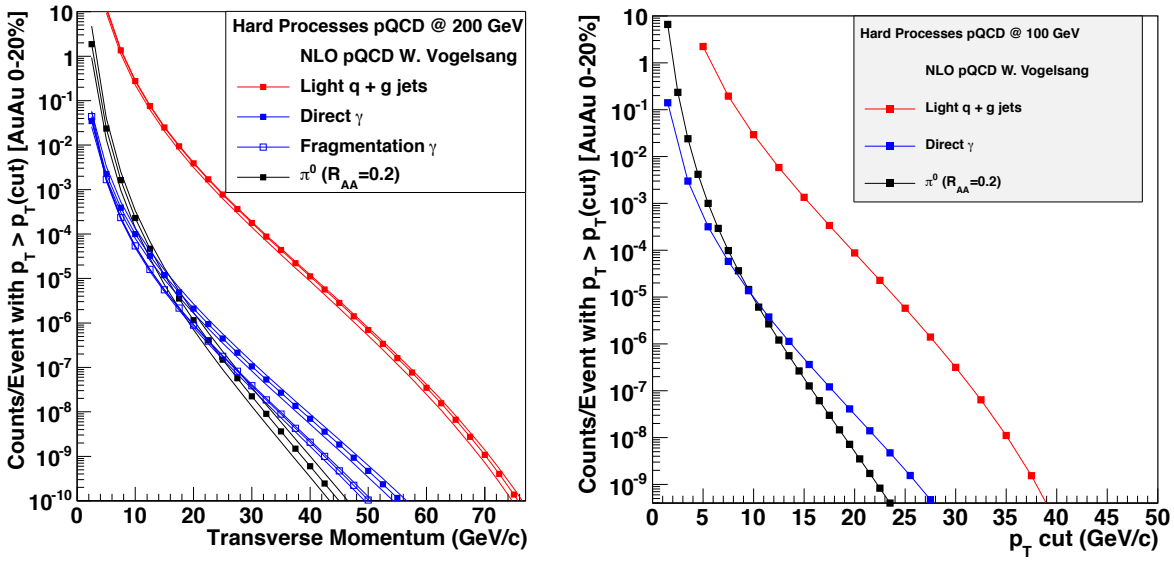

Figure 1.21: Jet, photon and π^0 rates with $|\eta| < 1.0$ from NLO pQCD [90] calculations scaled to Au+Au central collisions for $\sqrt{s_{NN}} = 200\,\text{GeV}$ (left) and $\sqrt{s_{NN}} = 100\,\text{GeV}$ (right). The scale uncertainties on the pQCD calculations are shown as additional lines. Ten billion Au+Au central collisions correspond to one count at 10^{-10} at the bottom of the y-axis range. A nominal 20 week RHIC run corresponds to 10 billion central Au+Au events at $\sqrt{s_{NN}} = 200\,\text{GeV}$ or 1.7 billion central Au+Au events at $\sqrt{s_{NN}} = 100\,\text{GeV}$.

the sPHENIX detector, over 80% of the inclusive jets will also be accepted dijet events.

In addition, the right panel of Figure 1.21 shows the same quantity, but for the most central 20% Au+Au collisions at a lower collision energy of $\sqrt{s_{NN}} = 100\,\text{GeV}$. The projected luminosity delivered by the collider is lower than in the 200 GeV case, of course, but with 1.7 billion events per RHIC year for this centrality selection, one obtains a substantial sample of jets reaching out to 35 GeV.

Shown in Table 1.1 are the jet and direct photon samples in p+p and d+Au collisions at $\sqrt{s_{NN}} = 200\,\text{GeV}$. The number of jets expected in the three systems are similar, meaning that good control measurements in p+p and d+Au events will be available on the same timescales to quantify baseline expectations and initial state effects. Additionally, new geometries can be explored with precision utilizing asymmetric heavy ion reactions, such as Cu+Au, and non-spherical geometries with U+U beams, now available with the RHIC EBIS upgrade [93]. Control measurements with different geometries with high statistics are particularly interesting since current theoretical calculations are challenged by the path length dependence of the energy lost by the parton probe.

Measurement of direct photons requires them to be separated from the other sources of inclusive photons, largely those from π^0 and η meson decay. The left panel of Figure 1.22 shows the direct photon and π^0 spectra as a function of transverse momentum for both $\sqrt{s} = 200\,\text{GeV}$ and 2.76 TeV p+p collisions. The right panels show the γ/π^0 ratio as a

	Au+Au (central 20%)	p+p	d+Au
$> 20\,\mathrm{GeV}$	10^7 jets	10^6 jets	10^7 jets
	10^4 photons	10^3 photons	10^4 photons
$> 30\,\mathrm{GeV}$	10^6 jets	10^5 jets	10^6 jets
	10^3 photons	10^2 photons	10^3 photons
$> 40\,\mathrm{GeV}$	10^5 jets	10^4 jets	10^5 jets
$> 50\,\mathrm{GeV}$	10^4 jets	10^3 jets	10^4 jets

Table 1.1: Table of jet rates for different systems. Each column shows the number of jets or direct photons that would be measured within $|\eta| < 1$ in 20 week running periods at a collision energy of 200 GeV.

function of p_T for these energies with comparison PHENIX measurements at RHIC. At the LHC, the ratio remains below 10% for $p_T < 50\,\mathrm{GeV}$ while at RHIC the ratio rises sharply and exceeds one at $p_T \approx 30\,\mathrm{GeV/c}$. In heavy ion collisions the ratio is further enhanced because the π^0s are significantly suppressed. Taking the suppression into account, the γ/π^0 ratio at RHIC exceeds one for $p_T > 15\,\mathrm{GeV/c}$. The large signal to background means that it will be possible to measure direct photons with the sPHENIX calorimeter alone, even before applying isolation cuts. Beyond measurements of inclusive direct photons, this enables measurements of γ-jet correlations and γ-hadron correlations.

1.8 Summary

Detailed information about the quark-gluon plasma properties, dynamics, time evolution, and structure at 1–2 T_c is accessible at RHIC through the extensive set of reconstructed jet measurements proposed here. The theoretical bridgework needed to connect these measurements to the interesting and unknown medium characteristics of deconfined color charges is under active construction by many theorists. Combining this work with the flexible and high luminosity RHIC accelerator facility can produce new discoveries in heavy ion collisions with an appropriate set of baseline measurements provided a suitable detector apparatus is constructed. Our proposed design for a jet detector at RHIC that is best able to make use of these opportunities is given in the following chapter.

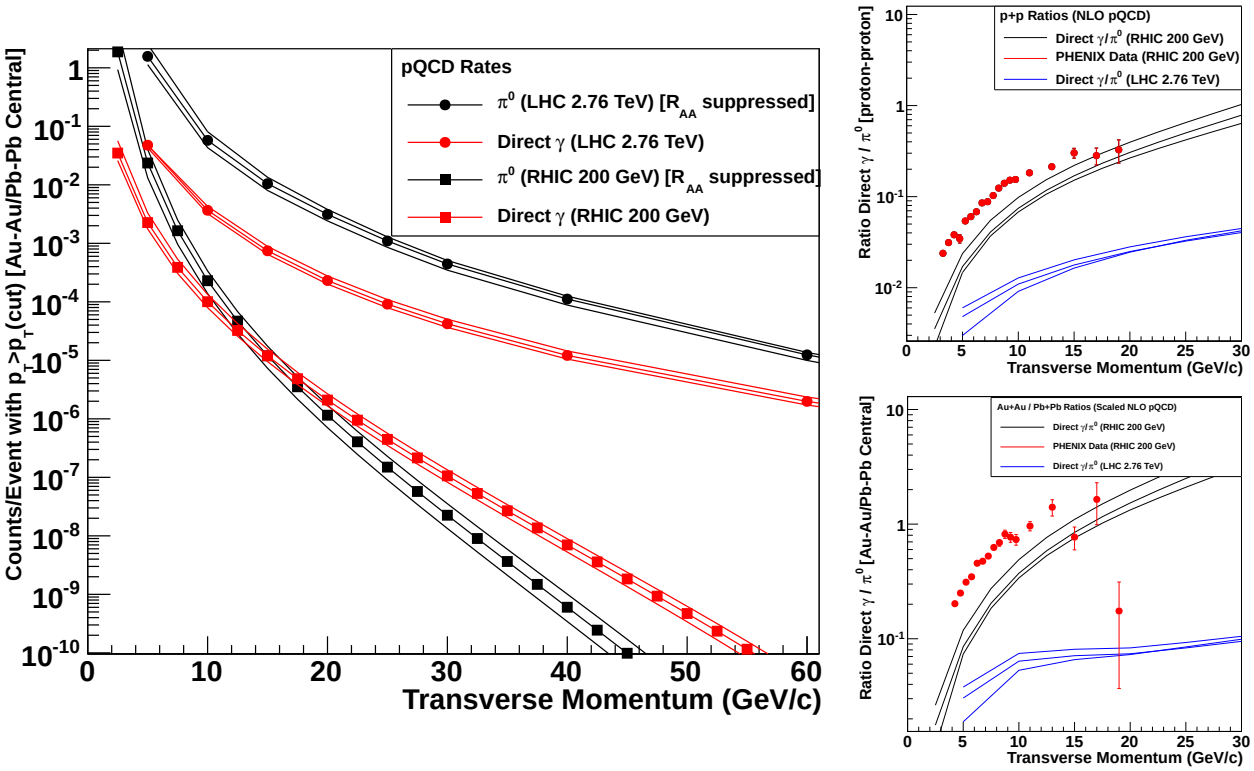

Figure 1.22: NLO pQCD calculations of direct photons and π^0 for RHIC and LHC. The plot on the left shows the counts per event in Au+Au or Pb+Pb collisions (including the measured R_{AA} suppression factor for π^0). The upper (lower) panel on the right shows the direct γ to π^0 ratio in p+p (Au+Au or Pb+Pb) collisions, in comparison with measurements from the PHENIX experiment at RHIC [94, 95].

Chapter 2

sPHENIX Detector Requirements

In order to perform the precision jet measurements outlined in Chapter 1, there is a set of detector requirements that must be met. In addition, as outlined in the Executive Summary, this sPHENIX upgrade serves as the foundation for future potential upgrades including a detector for the Electron-Ion Collider (referred to as ePHENIX), and those requirements must also be met. In this Chapter we detail the basic sPHENIX detector design and the requirements on the detector performance. Details of the specific detector and GEANT4 simulations are given in Chapter 3.

2.1 Detector Overview

Based on the physics requirements, detector constraints, and cost considerations, a baseline conceptual design has evolved. Here we describe the basic features and the key design parameters for the detector. The basic components are:

Magnetic Solenoid A thin superconducting solenoid with a 2 T field and an inner radius of 70 cm. The integrated field strength is driven by the tracking resolution requirements. The radius allows sufficient space for future upgrades with high resolution tracking and preshower detectors (as detailed in Appendix 6) and particle identification detectors for a future ePHENIX (as detailed in Appendix B). The cost of the solenoid scales approximately linearly with the inner radius [96], and thus a small radius must be maintained. This constraint is also to fit the entire detector onto the rail system in the PHENIX experiment hall. Minimizing the number of radiation lengths in the cryostat and coil allows the electromagnetic calorimeter to be placed outside the solenoid, simplifying the deployment of the electronics.

Electromagnetic Calorimeter A compact tungsten-scintillator sampling calorimeter outside the cryostat read out with silicon photo-multipliers. The small Molière radius

and short radiation length allows for a highly segmented calorimeter ($\Delta\eta \times \Delta\phi \sim 0.024 \times 0.024$) at a radius of about 100 cm from the beam axis, which results in about 25,000 electronic channels.

Hadronic Calorimeter An iron-scintillator sampling calorimeter outside the electromagnetic calorimeter. In order to minimize the mass and bulk, the calorimeter doubles as the flux return for the solenoid. A thickness of $5\lambda_{\text{int}}$ combined with the electromagnetic calorimeter in front is sufficient to fully contain the energies of interest, and provide more than enough iron for the full flux return. The hadronic calorimeter is divided into two longitudinal compartments consisting of plates running parallel to the beam axis with scintillator plates interleaved, then read out via embedded wavelength shifting fiber. The hadronic calorimeter will use the same silicon photomultiplier sensors as the electromagnetic calorimeter and similar electronics. The coarser segmentation ($\Delta\eta \times \Delta\phi \sim 0.1 \times 0.1$) results in an electronic channel count of about 10% that of the electromagnetic calorimeter.

Readout electronics Bias voltage and analog signal processing for silicon photomultipliers in physical proximity to the sensors, with a number of options for the digitization and buffering using either commercial components or integrated circuits adapted from existing experimental projects.

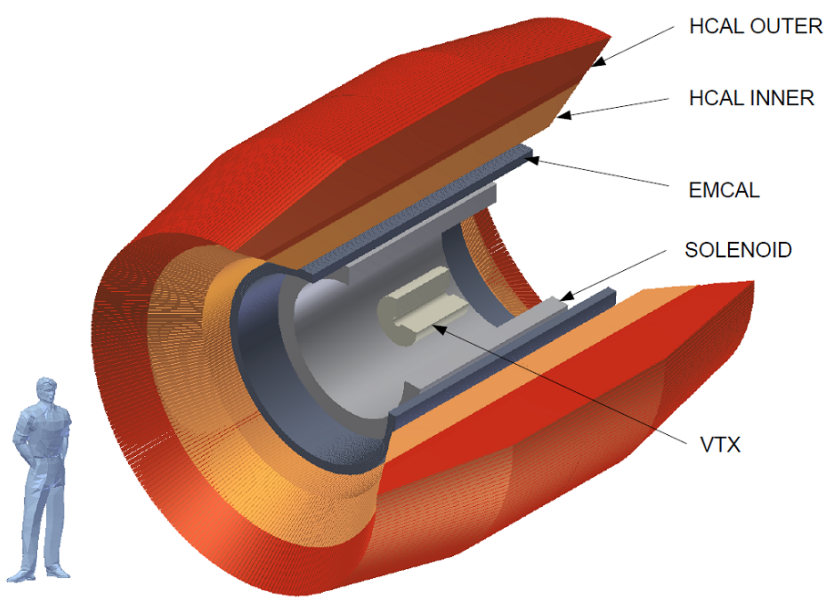

Figure 2.1: Cutway view of the detector.

The detector concept that has resulted from these considerations is shown in Figure 2.1 and Figure 2.2 and will be described in detail in Chapter 3. Taking advantage of both

Physics	Detectors	Requirements	
Full jet reconstruction	EMCal	$\sigma/E < 20\%/\sqrt{E}$	sPHENIX
	HCal	$\sigma/E < 100\%/\sqrt{E}$	
		$\Delta\eta \times \Delta\phi \sim 0.1 \times 0.1$	
		uniform within $\lvert\eta\rvert < 1$	
Direct γ, $p_T > 10\,\mathrm{GeV/c}$	EMCal	$\sigma/E \simeq 15\%/\sqrt{E}$	sPHENIX
		$\Delta\eta \times \Delta\phi \sim 0.03 \times 0.03$	
Jet-hadron	VTX 4 layers	tracking $p_T < 4\,\mathrm{GeV/c}$	Current PHENIX
	Solenoidal field		sPHENIX
High-z FFs	Jets as above	EMCal and HCal	sPHENIX
	Tracking	$\Delta p/p \simeq 2\%$	Future Option
Tagged HF jets	Jets as above	EMCal and HCal	sPHENIX
	DCA capability	Current PHENIX VTX	Current PHENIX
	Tracking	$\Delta p/p \simeq 2\%$	Future Option
Heavy quarkonia	Electron ID		
Separation of Y states	EMCal	$\sigma/E \simeq 15\%/\sqrt{E}$	sPHENIX
		$\Delta\eta \times \Delta\phi \sim 0.03 \times 0.03$	
	Preshower	e/π rejection	Future Option
		fine segmentation	
	Tracking	$B = 2T$	sPHENIX
		$\Delta p/p \simeq 2\%$	Future Option
π^0 to $p_T = 40\,\mathrm{GeV/c}$	EMCal	$\sigma/E \simeq 15\%/\sqrt{E}$	sPHENIX
		$\Delta\eta \times \Delta\phi \sim 0.03 \times 0.03$	
	Preshower	2γ separation	Future Option
		fine segmentation	

Table 2.1: Summary of detector requirements, showing the capabilities needed for various physics observables, and whether those capabilities are part of the current proposal or are possible additions to the detector through other means. Those items labeled sPHENIX are included with the detector upgrades in this proposal. Those items labeled "Future Option" are detailed in Appendix 6 and require modest additional upgrades.

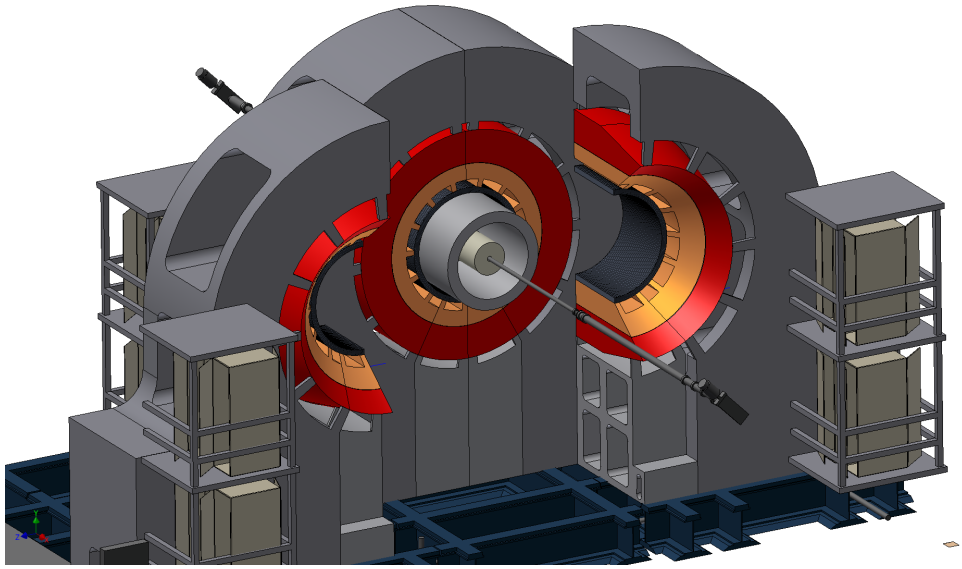

Figure 2.2: View of the sPHENIX detector in the collision hall with conceptual design for structural support.

technological developments in the era of RHIC and LHC experiments, and building on equipment already in place in PHENIX, the detector is both compact, which plays a large role in keeping costs under control, and much larger in solid angle than current PHENIX experiment. The outer radius of the hadronic calorimeter is about 200 cm and there are approximately 27,000 electronic channels for the two calorimeters combined.

The physics requirements that drive the design are summarized in Table 2.1 and will be discussed in the following section.

2.2 Design Goals

2.2.1 Coverage

The total acceptance of the detector is determined by the requirement of high statistics jet measurements and the need to fully contain both single jets and dijets. To fully contain hadronic showers in the detector requires both large solid angle coverage and a calorimeter deep enough to fully absorb the energy of hadrons up to 70 GeV.

The PYTHIA event generator has been used to generate a sample of $p+p$ at 200 GeV events which can be used to demonstrate the pseudorapidity distribution of jets. The left panel in Figure 2.3 shows the pseudorapidity distribution of jets with E_T above 20, 30, and 40 GeV. The right panel in Figure 2.3 shows the fraction of events where a trigger jet with E_T greater than a given value within a pseudorapidity range has an away side jet with

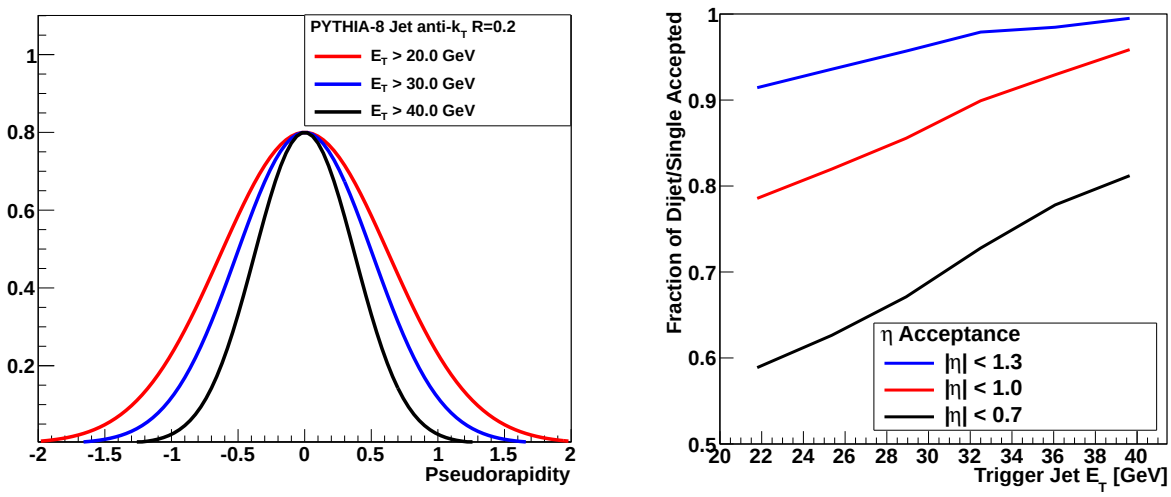

Figure 2.3: (Left) Pseudorapidity distribution of PYTHIA jets reconstructed with the FASTJET anti-k_T and R=0.2 for different transverse energy selections. (Right) The fraction of PYTHIA events where the leading jet is accepted into a given pseudorapidity range where the opposite side jet is also within the acceptance. Note that the current PHENIX acceptance of $|\eta| < 0.35$ corresponds to a fraction below 30%.

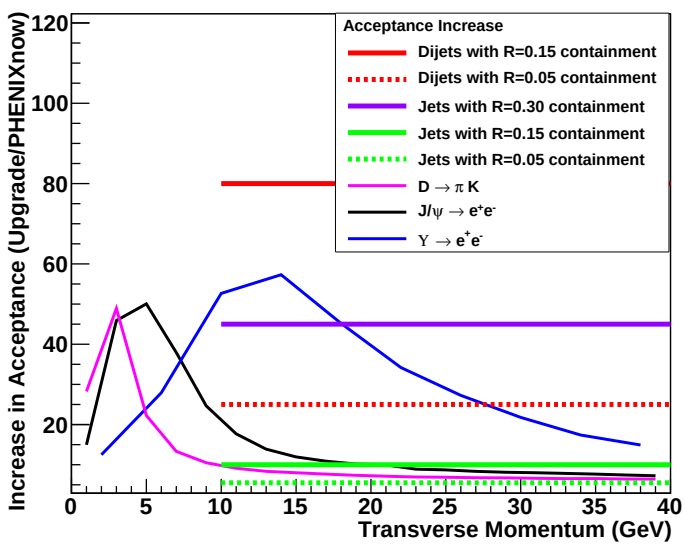

Figure 2.4: Acceptance increase for various processes (as modeled using the PYTHIA event generator) for the proposed sPHENIX barrel detector compared with the current PHENIX central arm spectrometers.

$E_T > 5\,\text{GeV}$ accepted within the same coverage. In order to efficiently capture the away side jet, the detector should cover $|\eta| < 1$, and in order to fully contain hadronic showers within this fiducial volume, the calorimetry should cover slightly more than that. Given the segmentation to be discussed below, the calorimeters are required to cover $|\eta| < 1.1$.

It should be noted that reduced acceptance for the away-side jet relative to the trigger suffers not only a reduction in statistics for the dijet asymmetry and γ-jet measurements but also results in a higher contribution of low energy fake jets (upward fluctuations in the background) in those events where the away side jet is out of the acceptance. For the latter effect, the key is that both jet axes are contained within the acceptance, and then events can be rejected where the jets are at the edge of the detector and might have partial energy capture.

Compared to the current PHENIX acceptance (the central arms cover $|\eta| < 0.35$ and $\Delta\phi = \pi$), full azimuthal coverage with $|\eta| < 1.0$ results in a very substantial increase in the acceptance of single jets and an even larger increase in the acceptance of dijets as shown in Figure 2.4. Also shown in Figure 2.4 is the substantial increase in acceptance for other observables including heavy quarkonia states. Thus, the large acceptance and high rate detector with incremental additional upgrades enables a much broader program as detailed in Appendix 6.

2.2.2 Segmentation

Jets are reconstructed from the four-vectors of the particles or measured energies in the event via different algorithms (as described in Chapter 4), and with a typical size $R = \sqrt{\Delta\phi^2 + \Delta\eta^2}$. In order to reconstruct jets down to radius parameters of $R = 0.2$ a segmentation in the hadronic calorimeter of $\Delta\eta \times \Delta\phi = 0.1 \times 0.1$ is required. The electromagnetic calorimeter segmentation should be finer as driven by the measurement of direct photons for γ-jet correlation observables. The compact electromagnetic calorimeter design being considered for sPHENIX has a Molière radius of $\sim 15\,\text{mm}$, and with a calorimeter at a radius of about 100 cm, this leads to an optimal segmentation of $\Delta\eta \times \Delta\phi = 0.024 \times 0.024$ in the electromagnetic section.

2.2.3 Energy Resolution

The requirements on the jet energy resolution are driven by considerations of the ability to reconstruct the inclusive jet spectra and dijet asymmetries and the fluctuations on the fake jet background (as detailed in Chapter 4. The total jet energy resolution is typically driven by the hadronic calorimeter resolution and many other effects including the bending of charged particles bending in the magnetic field out of the jet radius. Expectations of jet resolutions approximately 1.2 times worse than the hadronic calorimeter resolution alone are typical (see a more detailed discussion in Chapter 4).

In a central Au+Au event, the average energy within a jet cone of radius $R = 0.2$ ($R = 0.4$) is approximately 10 GeV (40 GeV) resulting in an typical RMS fluctuation of 3 GeV (6 GeV). This sets the scale for the required reconstructed jet energy resolution, as a much better resolution would be dominated by the underlying event fluctuations regardless. A measurement of the jet energy for $E = 20$ GeV with $\sigma_E = 100\% \times \sqrt{E} = 4.4$ GeV gives a comparable contribution to the underlying event fluctuation. A full study of the jet energy resolution with a GEANT4 simulation of the detector configuration is required and is presented in Chapter 4.

Different considerations set the scale of the energy resolution requirement for the EMCal. The jet physics requirement is easily met by any EMCal design. For the direct γ-jet physics, the photon energies being considered are $E_\gamma > 10$ GeV where even a modest $\sigma_E/E = 20\%/\sqrt{E}$ represents only a blurring of 0.6 GeV. In Au+Au central events, the typical energy in a 3×3 tower array is approximately 400 MeV. These values represent a negligible performance degradation for these rather clean photon showers even in central Au+Au events.

The energy resolution is driven by physics enabled by the future option upgrades to the sPHENIX detector. These future options upgrades described in Appendix 6 incorporate electron identification using a combination of a preshower detector and energy in the EMCal matching with the momentum from charged particle tracking. These set a more stringent requirement on the energy resolution of the EMCal, and the trade-off determines how low in p_T electrons can be identified without requiring additional detectors for electron identification. As detailed in Appendix 6, for the quarkonia measurements in the Upsilon family, an EMCal resolution of order $15\%/\sqrt{E}$ is required, along with the preshower for electron-pion separation. A similar EMCal resolution requirement must be met in a future ePHENIX as described in Appendix B

Most of these physics measurements require complete coverage over a large range of rapidity and azimuthal angle ($\Delta\eta \leq 1.1$ and $\Delta\phi = 2\pi$) with good uniformity and minimal dead area. The calorimeter should be projective (at least approximately) in both η and ϕ. For a compact detector design there is a trade-off in terms of thickness of the calorimeter and Molière radius versus the sampling fraction and, therefore, the energy resolution of the device. Further optimization if these effects will be required as we work towards a final design.

2.2.4 Triggering

The jet energy should be available at the Level-1 trigger as a standard part of the PHENIX dead-timeless Data Acquisition and Trigger system. This triggering ability is important as one requires high statistics measurements in proton-proton, proton-nucleus, light nucleus-light nucleus, and heavy nucleus-heavy nucleus collisions with a wide range of luminosities. It is important to have combined EMCal and HCal information available so

as to avoid a specific bias on the triggered jet sample.

2.2.5 Tracking

Tracking capabilities are critical both in the sPHENIX upgrade and for the physics enabled by future option upgrades. The sPHENIX detector with a reconfiguration of the existing PHENIX barrel silicon vertex detector will be able to track charged hadrons up to $p_T \approx 5\,\mathrm{GeV/c}$, which is important for understanding how the soft part of parton showers is modified and potentially completely equilibrated in the quark-gluon plasma. A number of physics measurements are enabled by additional tracking layers which are not part of this proposal. These are described in more detail in Appendix 6.

Chapter 3

sPHENIX Detector Concept

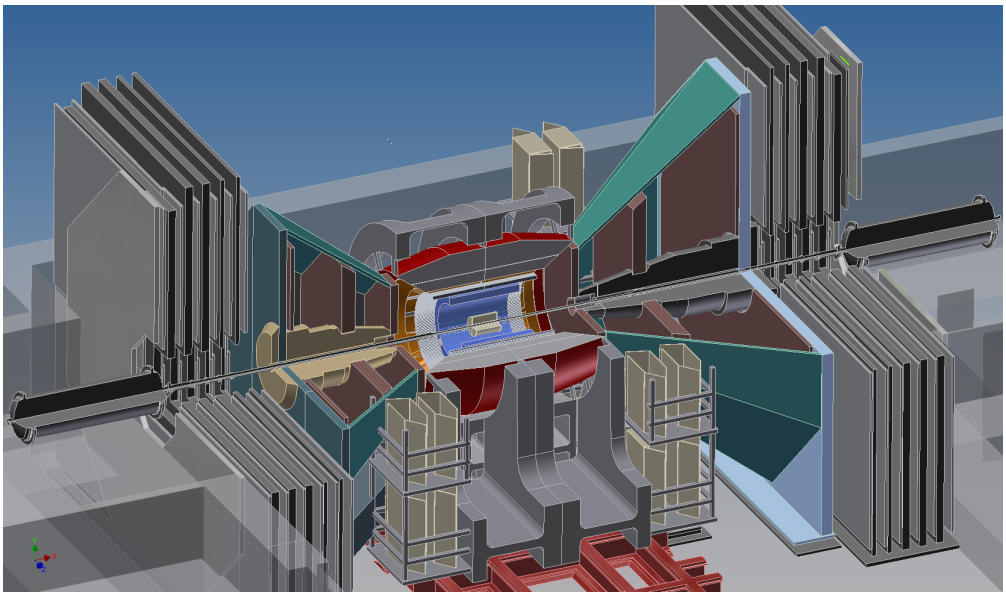

Figure 3.1: An engineering drawing of sPHENIX, showing the superconducting solenoid surrounded by electromagnetic and hadronic calorimetery, with a model of the associated support structure, as it would sit in the PHENIX IR.

In this Chapter we detail the sPHENIX detector design including the magnetic solenoid, electromagnetic and hadronic calorimeters, and readout electronics. Detector performance specifications are checked using a full GEANT4 simulation of the detector. Full physics performance measures are detailed in Chapter 4.

The sPHENIX detector concept takes advantage of technological developments to enable a compact design with excellent performance. A tungsten-scintillator electromagnetic calorimeter read out with silicon photomultipliers (SiPMs) or avalanche photodiodes (APDs) allows for a physically thin device which can operate in a magnetic field, without

the bulk of photomultiplier tubes and the need for high voltage distribution. The smaller electromagnetic calorimeter also allows the hadronic calorimeter to be less massive, and the use of solid-state sensors for the hadronic calorimeter allows for nearly identical electronic readout for the two major systems. A superconducting magnet coupled with high resolution tracking detectors provides good momentum resolution inside a compact solenoid. The detector has been designed from the beginning to minimize the number of distinct parts to be simpler to manufacture and assemble. The use of components insensitive to magnetic fields enables the hadronic calorimeter to double as the flux return for the solenoid, reducing both mass and cost. Adapting existing electronic designs for the readout allows for reduced development cost and risk, and leverages a decade and a half of experience at PHENIX. We now detail each subsystem in the following Sections.

3.1 Magnet and Tracking

The magnet and tracking system should ultimately be capable of order 1% momentum resolution at 10 GeV/c, cover the full 2π in azimuth and $|\eta| < 1.1$. Achieving this will require a central field of up to 2 T, and in order to minimize the material in front of the calorimeters, a thin superconducting solenoid is the clear choice for the magnet.

A natural question is whether or not an existing superconducting solenoid might be repurposed for use in sPHENIX. The physical constraints of the PHENIX interaction region (IR) have a strong influence on the dimensions of the sPHENIX design. The RHIC beamline is 444.8 cm above the tracks that are used to move detectors into the collision hall and 523.2 cm above the floor, and we propose to keep the track system in place for maneuvering detectors in and out. Thus, the detector should have an outer radius of no more than 400 cm in order to provide room for support. The flux return and calorimeters require a radial extent of at least 125 cm, and the support structure and rollers allowing disassembly of the detector require on the order of 50 cm. Instrumentation in the forward and backward direction is not part of this proposal (see Appendix A), but the space available is approximately the same as the present muon tracker systems. The north muon magnet was assembled in place and is fixed to the floor, while the south muon magnet is movable on the rail system. With the south muon magnet fully retracted to the muon identifier steel (also fixed to the floor), there is about 520 cm of open space available along the beam line.

We have surveyed several completed experiments that used solenoid magnets to see if their magnet would be suitable. The basic facts we uncovered in this survey are are shown in Table 3.1. The CDF and BaBar solenoids have been considered, but they are either too large or unavailable. The CLEO solenoid could be available, and is in good condition, but its size and thickness would also make for an extremely massive hadronic calorimeter. The D0 solenoid is slightly smaller in radius than is desirable to allow for high resolution tracking and other possible detectors in the future, but it would be a reasonable candidate for use in sPHENIX. However, removal of the solenoid from inside the D0 liquid

Argon calorimeter is a sizable task, and after visiting Fermilab and consulting the D0 decommissioning coordinator, it was found to be impractical. The result of this exercise drives us to consider a new magnet, the specifications of which will be discussed in the next section.

Experiment	Inner radius (cm)	Field strength (T)	Length (cm)	X/X_0
CDF	150	1.5	507	0.84
BaBar	150	1.5	346	large
CLEO	155	1.45	380	2.5
D0	55	2.0	273	0.9

Table 3.1: Existing solenoids considered for use in this proposal.

3.1.1 Solenoid Magnet Specifications

The basic features of the solenoid were determined by the present and anticipated future physics needs of sPHENIX to require an inner radius of at least 70 cm with a length of 187 cm to cover a pseudorapidity of $|\eta| < 1.1$. The thickness of the solenoid and cryostat is to be less than one radiation length at normal incidence, with a radial thickness of less than 20 cm, design parameters similar to the D0 solenoid. The design of the solenoid will be done by the vendor, and several vendors responded to a preliminary request for information prepared with Brookhaven National Laboratory's Procurement Department.

3.1.2 Magnetic Field Calculations

Magnetic field calculations of the solenoid coil and a three dimensional model of the return steel were carried out with OPERA. A field map is shown in Figure 3.2.

3.2 The Electromagnetic Calorimeter

The concept for the sPHENIX electromagnetic calorimeter follows from the physics requirements outlined earlier in this proposal. These requirements lead to a calorimeter design that is compact (i.e. has a small Molière radius and short radiation length), has a high degree of segmentation (0.024×0.024 in η and ϕ), and can be built at a reasonable cost. Since the calorimeter will be located just outside the coil of the solenoid, it will also

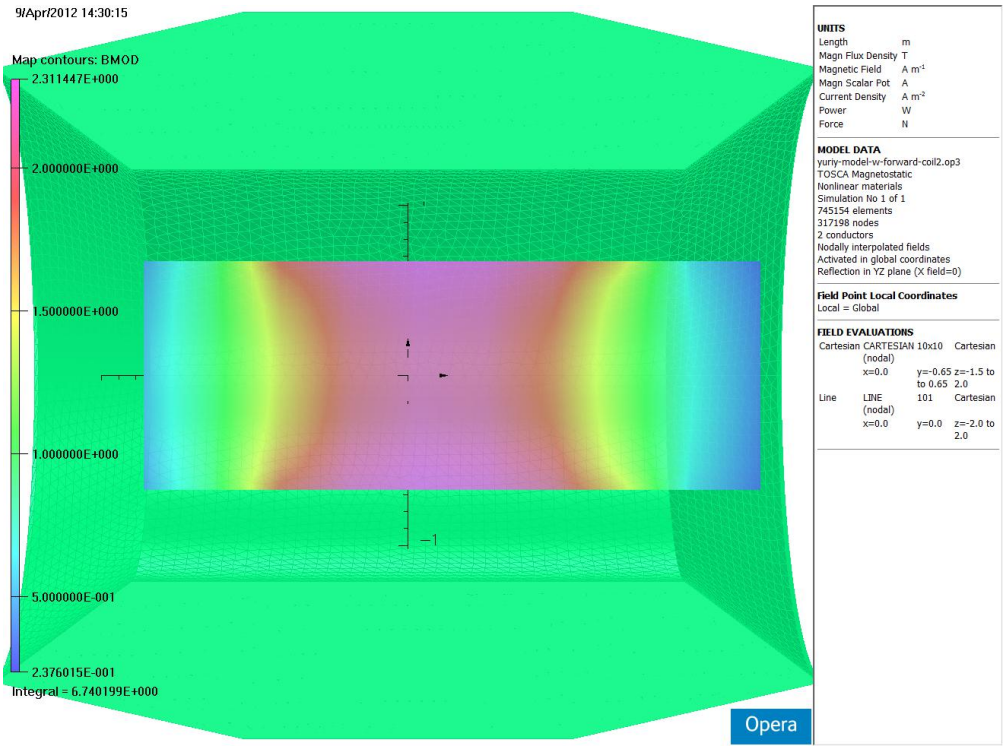

Figure 3.2: Calculation of the magnetic field from the solenoid with the iron flux return. The coil has been removed for clarity.

have to operate in the rather strong fringe field of the magnet. This has led us to a so-called optical accordion design, which is a descendant of the design of the ATLAS lead-liquid argon calorimeter [97], but uses tungsten as the absorber material and scintillating fibers as the active medium. This has the advantage of being very compact, as described below, and being able to be read out with silicon photomultipliers (SiPM's), which provide high gain, similar to conventional phototubes, but can work inside the magnetic field; avalanche photodiodes (APD's) offer many of the same advantages. It is similar to other scintillating fiber calorimeters which have been built using lead as an absorber [98]. Recently, very good resolution ($\sim$12%/$\sqrt{E}$) has been obtained with a fiber calorimeter using tungsten as an absorber [99].

The EMCal optical accordion will consist of alternating layers of thin tungsten sheets glued onto cast composite layers consisting of scintillating fibers embedded in a matrix of tungsten powder and epoxy. The basic structure is shown in Figure 3.3. The undulations, characteristic of the accordion design, provide a more uniform response for particles incident at various positions and angles by preventing channeling of particles through the calorimeter—something which could occur if the plates were flat and a particle traversed the calorimeter interacting only with scintillator. This design can be made projective in the azimuthal direction by having the thickness of the layers increase as a function of radius. It is not possible to vary the fiber thickness, so one must increase the absorber thickness,

either by increasing the thickness of the tungsten plates, or by increasing the thickness of the tungsten-epoxy layer.

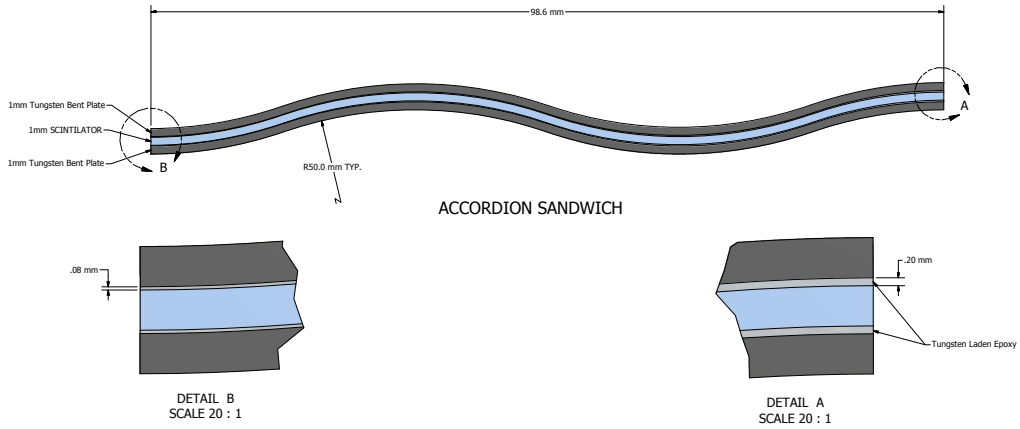

Figure 3.3: Optical accordion "sandwich" consisting of two tungsten plates in an accordion shape (1 mm thickness) and a layer of 1 mm scintillating fibers with tungsten powder and epoxy filling the gaps. The characteristic accordion-like undulations prevent channeling of particles through the scintillator layers alone.

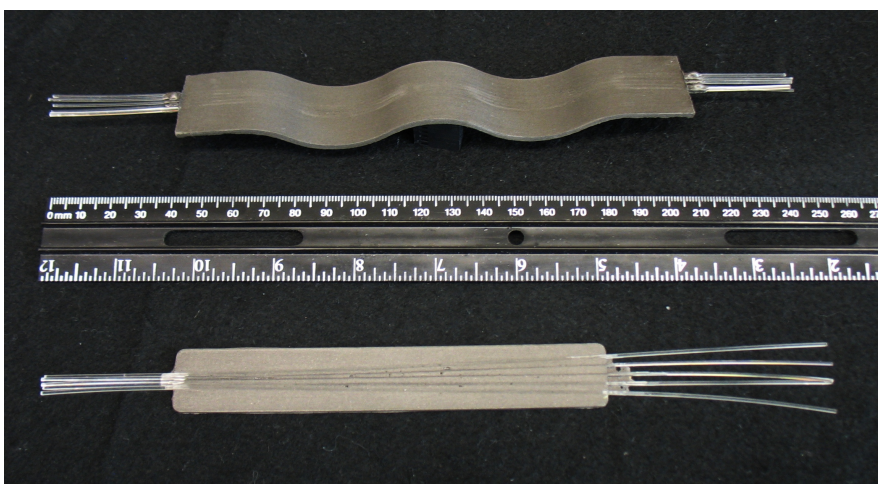

Figure 3.4: Samples of scintillating fiber embedded in a formed tungsten epoxy mixture. Produced by Tungsten Heavy Powder.

Until recently, it had only been possible to achieve an accordion shape for absorbers made of highly malleable materials such as lead. New technology now makes it possible to achieve this with tungsten, which results in a higher density, and hence more compact, calorimeter. We have been working with a company, Tungsten Heavy Powder [100], that fabricates a wide variety of tungsten components, to produce a practical, cost effective design for the calorimeter that would allow it to be manufactured in private industry. Based on our discussions with them, it appears that the simplest and most economical method to

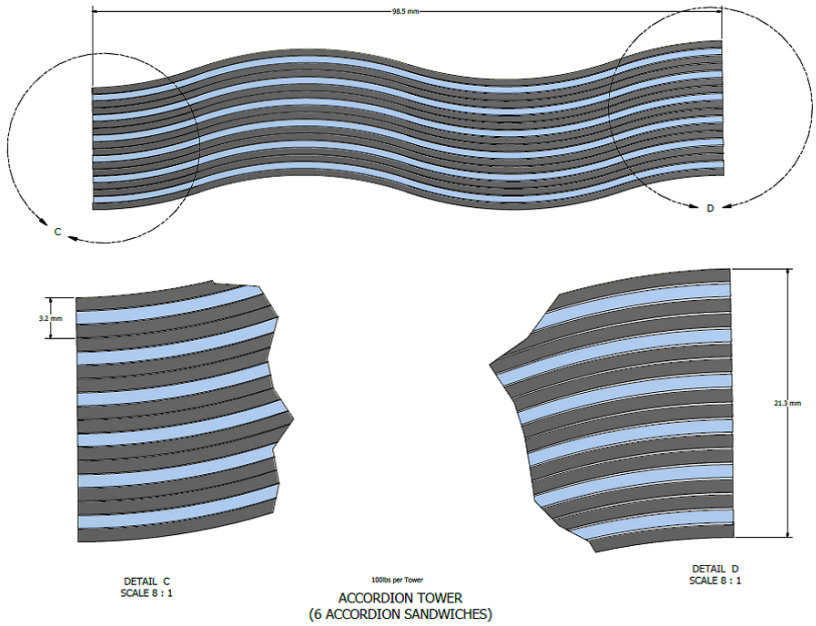

Figure 3.5: Cross section of the accordion calorimeter in the plane normal to the beam direction, showing how the single layers seen in Figure 3.3 are stacked. Scintillating fibers are embedded in tapered and undulating layers of tungsten and epoxy mixture and are approximately projective towards the interaction region, which has an extent of $\pm$ 30 cm along the beam direction.

achieve this design is to use thin, uniform thickness tungsten plates and scintillating fibers with a tungsten powder epoxy polymer to fill the gaps. In this design, shown in Figure 3.3, two uniform thickness tungsten plates with a thickness $\sim$ 1 mm would be pre-bent into the accordion shape and cast together with a layer of scintillating fibers and a mixture of tungsten powder and epoxy in a mold to form a "sandwich" with the desired shape. Figure 3.4 shows an example of scintillating fibers embedded into an epoxy layer with tungsten powder and formed into an accordion shape. Six layers of these sandwiches would be glued together to form a tower module measuring $\sim$ 2.1 cm in the ϕ dimension and half the length of the calorimeter ($\sim$ 1.39 m) along the beam direction, as shown in Figure 3.5. Four tower modules would then be combined into sections weighing about 180 kg each and arranged azimuthally to form a ring, as shown in Figure 3.6. Figure 3.7 shows a cross sectional view of the calorimeter along the beam direction. The fibers are arranged in a radial pattern projective to the vertex. The fibers are closely spaced together at the front of the calorimeter and flare out slightly towards the back in order to make the device projective. The fibers are grouped at the back into individual towers (corresponding to the η and ϕ segmentation as discussed below in the readout section) and coupled to a light mixer box that randomizes and collects the light from all of the fibers of a given tower onto a single SiPM.

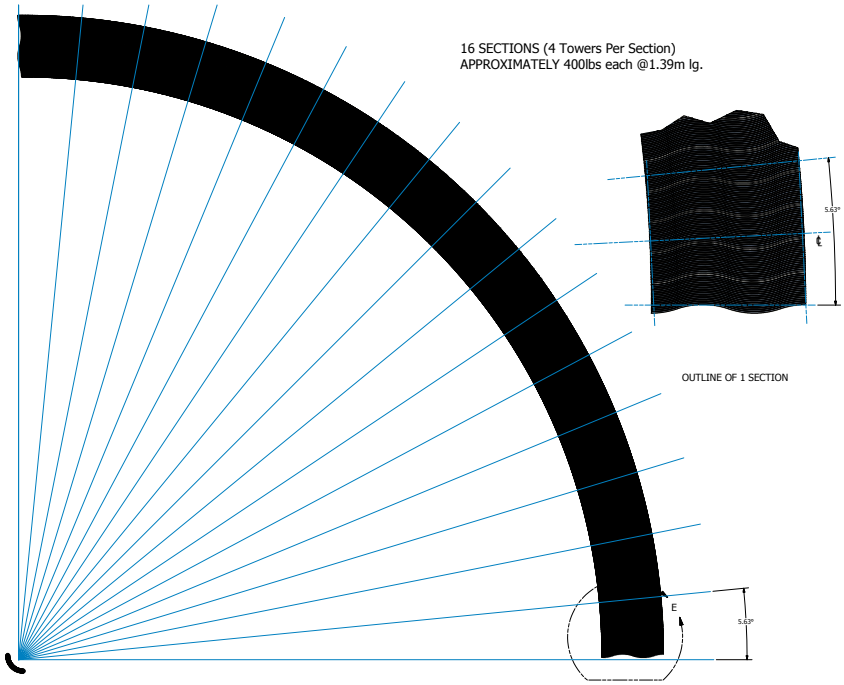

Figure 3.6: Tower modules combined into sections azimuthally to form a ring.

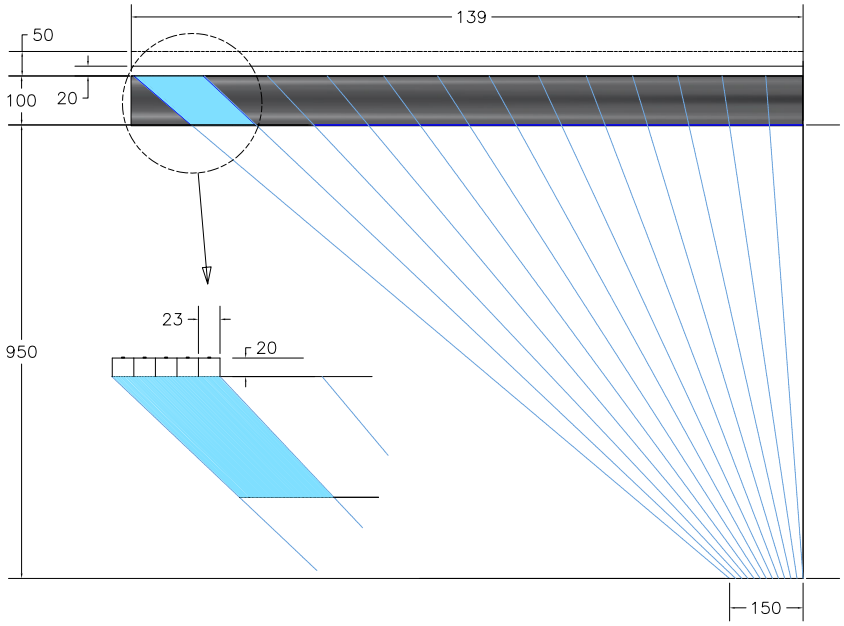

Figure 3.7: View of the calorimeter along the beam direction showing approximately projective towers back to the interaction region, which has an extent of $\sim \pm 30$ cm.

3.2.1 Segmentation and readout

The segmentation of the calorimeter is determined by a number of different requirements. One primary factor is the occupancy of the individual readout towers in heavy ion collisions, which determines the ability to resolve neighboring showers and to measure the energy in the underlying event. In addition, the degree of segmentation also determines the ability to measure the transverse shower shape, which is used in separating electrons from hadrons (e/π rejection). All of these capabilities could be improved with the addition of a finely segmented preshower detector (as detailed in Appendix 6), but we believe the segmentation chosen for the baseline detector will provide the capability to perform the physics program of this proposal.

The calorimeter will be divided into individual towers corresponding to a segmentation in η and ϕ of approximately 0.024×0.024 and would result in about 25,000 readout channels (256 in $\phi\times$ 96 in η). The fibers from the back of the calorimeter will be grouped into towers measuring $\sim$ 2$\times$2 cm where the light from $\sim$ 125 fibers will be collected and randomized using a small light mixer box and read out with a single SiPM. It has not yet been decided how this light collection and mixing will be accomplished, but a number of options are being explored. These include a small reflecting and diffusing cavity, or possibly a wavelength shifting block. We will keep the thickness of the mixer as thin as possible in order to minimize the radial space required by the mixer, SiPM and readout electronics.

The light yield resulting from the mixer configuration is of primary importance in determining the photostatistics for the readout. Fortunately, with an energy resolution of $15\%/\sqrt{E}$, the requirement on the light yield is not very severe. We have made a number of measurements with scintillating fibers that have been embedded into various mixtures of tungsten powder and epoxy to determine their light yield, and have obtained light yields $\sim$ 100 photoelectrons/MeV of energy deposit in the scintillator with a SiPM reading out the fibers directly With the thicknesses of the tungsten plates, scintillator and tungsten powder epoxy in the current design, the sampling fraction for the energy deposited in the scintillator is $\sim$ 4%, so this corresponds to $\sim$ 4000 photoelectrons/GeV of energy deposit in the calorimeter, which would have a negligible effect on the calorimeter energy resolution. This number will be reduced by the light collection efficiency of the mixer, but with this high initial light yield, it should be possible to maintain sufficient photostatistics so as not to affect the overall energy resolution of the calorimeter.

The PHENIX collaboration has been working with the company Tungsten Heavy Powder [100] on the design and fabrication of actual calorimeter components. Tungsten Heavy Powder has also recently received a Phase I Small Business Innovation Research (SBIR) grant to study and develop materials and components for compact tungsten based calorimeters for nuclear physics applications. Members of the sPHENIX group, as part of a broader collaboration, have submitted a "Joint Proposal to Develop Calorimeters for the Electron Ion Collider" for EIC research and development funds. Thus, this technology is an area of very active work and for which test beam results for the sPHENIX type design

should be available soon.

3.3 The Hadronic Calorimeter

The hadronic calorimeter is a key element of sPHENIX and many of the overall performance requirements are directly tied to performance requirements of the HCal itself. The focus on measuring jets and dijets in sPHENIX leads to a requirement on the energy resolution of the calorimeter system as a whole—the particular requirement on the HCal is that it have an energy resolution better than $\sigma_E/E = 100\%/\sqrt{E}$. The jet measurement requirements also lead to a transverse segmentation requirement of $\Delta\eta \times \Delta\phi \approx 0.1 \times 0.1$ over a rapidity range of $|\eta| < 1.1$ with minimal dead area.

The combination of the EMCal and the HCal needs to be at least $\sim 6\lambda_{\text{int}}$ deep—sufficient to absorb $\sim$ 97% of the energy of impinging hadrons with momenta below 50 GeV/c, as shown in Figure 3.8. The electromagnetic calorimeter is $\sim 1\lambda_{\text{int}}$ thick, so an iron-scintillator hadronic calorimeter should be $\sim 5\lambda_{\text{int}}$ deep. The thickness of the HCal is driven by physics needs, but these needs dictate a device of sufficient thickness that, with careful design, the hadronic calorimeter can also serve as the return yoke for the solenoid.

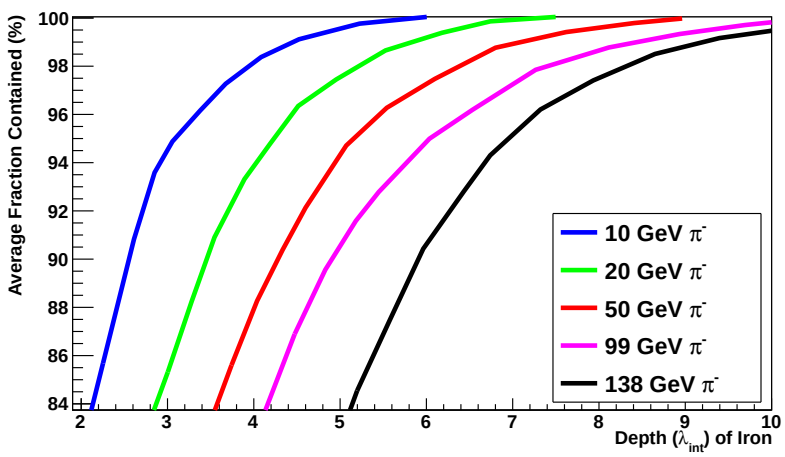

Figure 3.8: Average energy fraction contained in a block of iron with infinite transverse dimensions, as a function of the thickness of the block. Figure adapted from Ref. [101].

The hadronic calorimeter as shown in Figure 3.9 surrounds the electromagnetic calorimeter with an active volume which extends from a radius of 112 cm to 212 cm and is segmented longitudinally (i.e., along a radius vector) into two compartments of 1.5 and 3.5 interaction lengths deep (at normal incidence). The inner and outer sections share the total energy of a shower approximately equally.

Both the inner and outer longitudinal segments of the calorimeter are constructed of

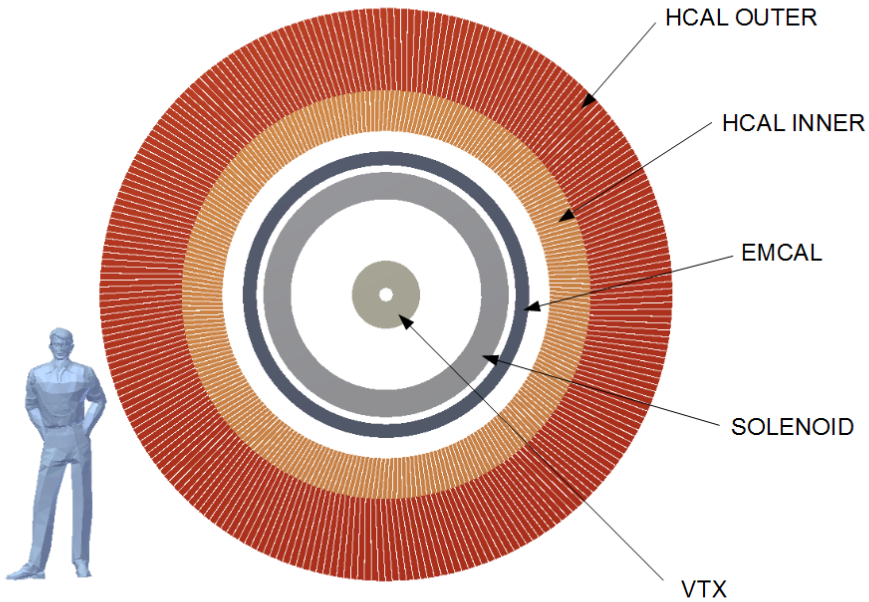

Figure 3.9: Cross section of sPHENIX, showing a typical collider detector structure. The calorimeters sit just outside the solonoid.

tapered absorber plates, creating a finned structure, with each fin oriented at an angle of $\pm 5^\circ$ with respect to a radius vector perpendicular to the beam axis. There are 256 fins in each of the inner and outer segments. The fins in the inner and outer segments are radially tilted in opposite directions resulting in a 10 degree angle with respect to each other. They are also staggered by half a fin thickness. The gaps between the iron plates are 8 mm wide and contain individually wrapped 7 mm thick scintillating tiles with a diffuse reflective coating and embedded wavelength shifting fibers following a serpentine path. The slight tilt and the azimuthal staggering of steel fins and scintillating tiles prevents particles from traversing the depth of the calorimeter without encountering the steel absorber. The benefits of two longitudinal segments include a further reduction in the channeling of particles in the scintillator, shorter scintillators with embedded fibers for collecting the light, and shower depth information.

With plates oriented as described, particles striking the calorimeter at normal incidence will, on average, cross 22.5 cm of steel in the inner and 57.5 cm of steel in the outer sections resulting in total probability for the punch through of particles with momenta above $\sim$ 2 GeV/c of only 1% as confirmed with GEANT4 simulations. This punch through probability varies from 0.93–1.07 depending on the incident angle across the sampling cell. This design has a very small number of distinct components which is designed to make it

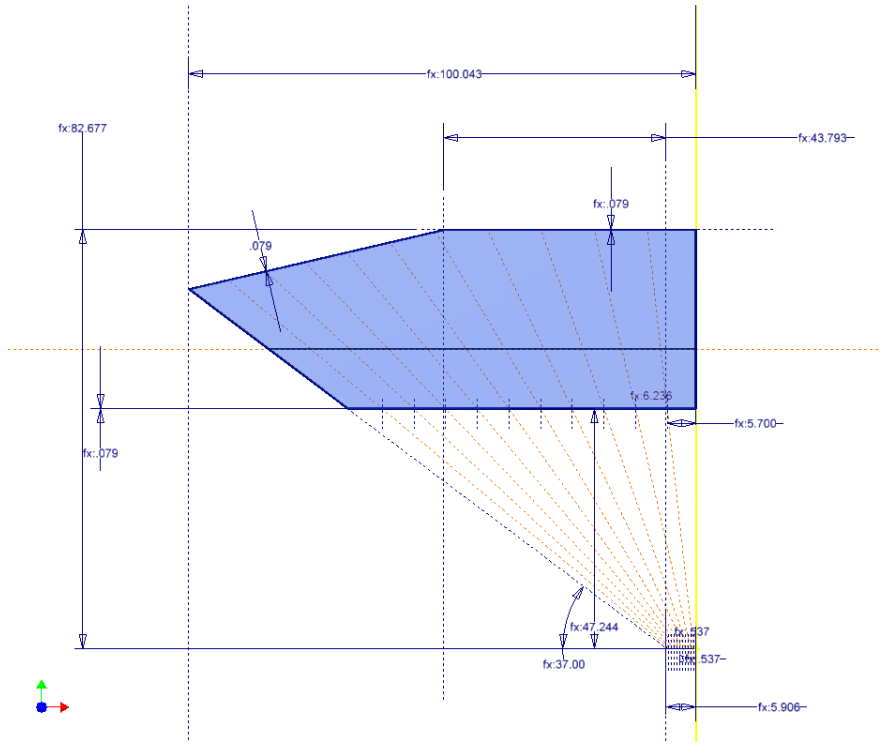

Figure 3.10: Scintillating tiles in the sampling gap of sPHENIX hadronic calorimeter, showing the transverse segmentation into element 0.1 units of pseudorapidity wide.

simple to fabricate, assemble, and to model.

Within each gap, there are 22 separate scintillator tiles of 11 different shapes, corresponding to a detector segmentation in pseudorapidity of $\Delta\eta \sim 0.1$ (see Figure 3.10). Azimuthally, the hadronic calorimeter is divided into 64 wedges ($\Delta\phi \simeq 0.1$). Each wedge is composed of four sampling cells (steel plate and scintillating tile) with the scintillating tile edges pointing towards the origin. The 22 pseudorapidity slices result in towers about 10 cm$\times$10 cm in size at the inner surface of the calorimeter. The total channel count in the calorimeter is 1408×2.

The light from the scintillating tiles between the steel fins is collected using wavelength shifting fibers laid along a serpentine path as shown in Figure 3.11. This arrangement provides relatively uniform light collection efficiency over the whole tile. We have considered two fiber manufacturers: (1) Saint-Gobain (formerly BICRON), product brand name BCF91A [102] and (2) Kuraray, product name Y11 [103]. Both vendors offer single and double clad fibers.

The calorimeter performance is determined by the sampling fraction and the light collection and readout efficiency. The readout contributes mostly to the stochastic term in calorimeter resolution through Poisson fluctuations in the number of photoelectrons on the input to the analog signal processing. Factors contributing to those fluctuations are luminous

properties of the scintillator, efficiency of the light collection and transmission, and the photon detection efficiency of the photon detector.

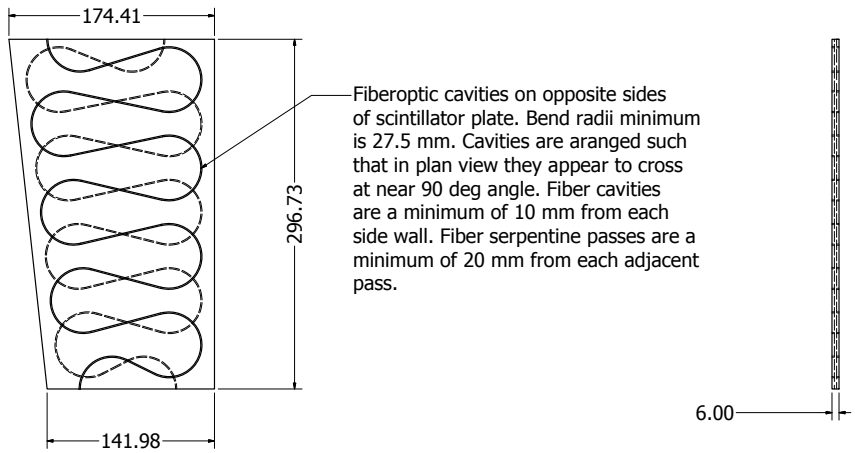

Figure 3.11: Grooved scintillating tiles for inner HCal section, showing the serpentine pathway the fiber will follow and the uniform thickness of the tiles.

The scintillating tiles are based on the design of scintillators for the T2K experiment by the INR group (Troitzk, Russia) who designed and built 875 mm long scintillation tiles with a serpentine wavelength shifting fiber readout [104]. The T2K tiles are injection molded polystyrene tiles of a geometry similar to those envisioned for sPHENIX, read out with a single serpentine fiber, with each fiber viewed by an SiPM on each end. The measured light yield value was 12 to 20 photoelectrons/MIP at 20°C [105]. With 12 p.e./MIP measured by T2K for 7 mm thick tiles (deposited energy $\sim$ 1.4 MeV) and an average sampling fraction of 4% estimated for the sPHENIX HCal we expect the light yield from the HCal to be about 400 p.e./GeV. A 40 GeV hadron will share its energy nearly equally between the inner and outer HCal segments so the upper limit of the dynamic range of the HCal can be safely set to $\sim$ 30 GeV which corresponds to a yield of 12000 p.e. on the SiPM. To avoid signal saturation and ensure uniform light collection, care will be required to both calibrate the light yield (possibly requiring some attenuation) and randomize it.

The uniformity of light collection as measured by T2K using the serpentine fiber arrangement can be judged from Figure 3.12 (data from Ref. [105]). The largest drop in the light yield is along the tile edges and in the corners farthest from the fibers.

We note that this design is optimized for simplicity of manufacturing, good light yield, and also acting as the flux return for the magnetic. As such, it has a manifestly non-uniform sampling fraction as a function of depth and is not highly compensated. However, the performance specifications are quite different from particle physics hadronic calorimeters, particularly with a limited energy measurement range (0–70 GeV). GEANT4 simulations described in the next Section indicate a performance better than the physics requirements, and full test beam results are necessary as a validation.

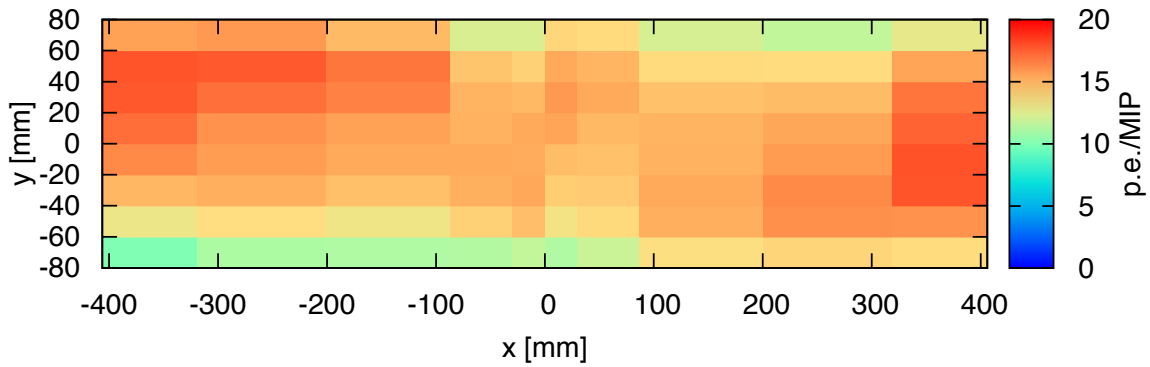

Figure 3.12: Light yield (photoelectrons) profile for the T2K scintillation tile, showing the degree of uniformity achieved using a serpentine fiber layout [105].

3.4 Simulations

We have employed the GEANT4 simulation toolkit [106] for our full detector simulations. It provides collections of physics processes suitable for different applications. We selected the QGSP_BERT list which is recommended for high energy detector simulations like the LHC experiments. We have integrated the sPHENIX simulations with the PHENIX software framework, enabling us to use other analysis tools we have developed for PHENIX.

The detectors and readout electronics and support structures are currently implemented as cylinders. The setup is highly configurable, making it easy to test various geometries and detector concepts. The simulation is run using a uniform solenoidal field of 2 T. We keep track of each particle and its descendants so every energy deposition can be traced back to the original particle from the event generator.

The existing PHENIX silicon vertex detector (VTX) consists of four inner silicon layers at a radius of 2.5 cm (200 μm), 5 cm (200 μm), 10 cm (620 μm), 14 cm (620 μm). These are followed by a one radiation thick layer of aluminum which represents the effects of the superconducting magnet. The electromagnetic and hadronic calorimeters are implemented as tungsten and iron cylinders respectively in which 1792 (EMCal) and 320 (HCal) scintillator plates of 1 mm (EMCal) and 6 mm (HCal) thickness with a configurable tilt angle (currently 5°) are embedded. The readout electronics for the EMCal is approximated by 5 mm of Teflon following the EMCal.

All tracks which reach a layer 10 cm behind the HCal are aborted to prevent particles which are curled up by the 2 T field from re-entering the detector. Adding up the energy of those aborted tracks yields an estimate of the energy which is leaked from the back of the HCal.

We have two algorithms to account for the granularity of the detectors and their readout. For the silicon layers the deposited energy is summed using a given strip or pixel size. The

dimensions for the inner 2 layers are 0.05 mm×0.425 mm, layer 3 and 4 are 0.08 mm×1 mm and layers 5 and 6 are 0.08 cm×3 cm. The energy deposited in the scintillators of the calorimeters is summed in equal sized bins of pseudorapidity and azimuthal angle. The size for the EMCal is 0.024 × 0.024, the size for the HCal is 0.1 × 0.1.

3.4.1 Electromagnetic Calorimeter Simulation

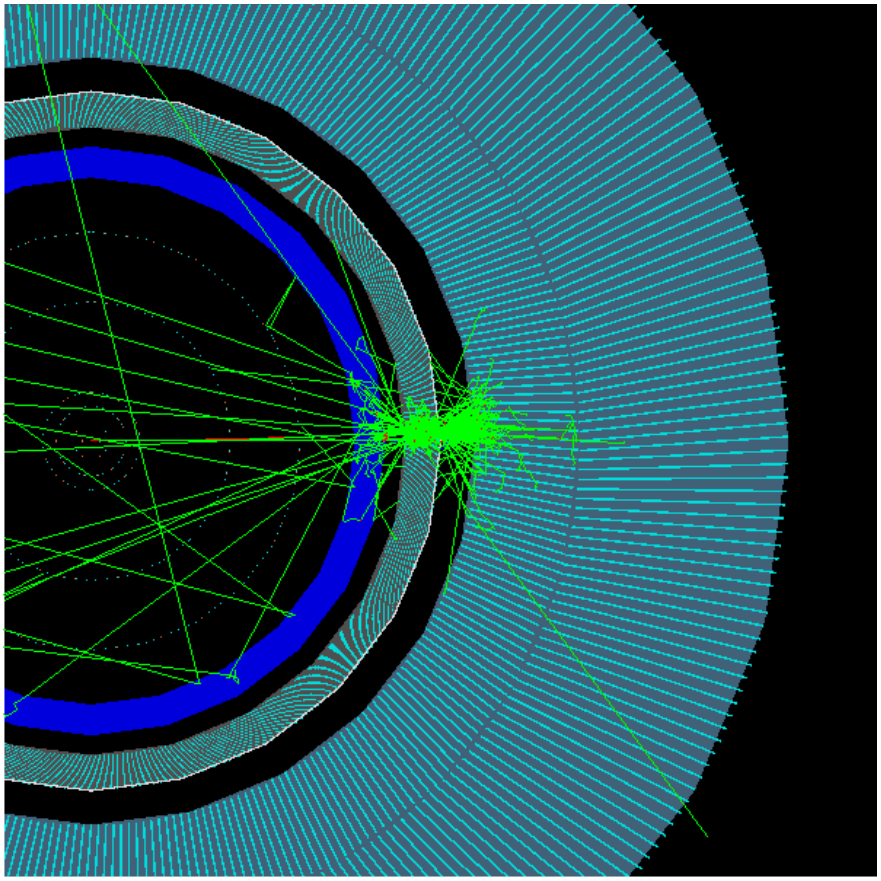

Figure 3.13: Transverse view of a 10 GeV/c electron in sPHENIX. It penetrates the magnet (blue) and showers mainly in the EMCal.

The electromagnetic calorimeter has been simulated using the GEANT4 tools described above. Figure 3.13 shows a typical GEANT4 event in which a 10 GeV/c electron hits the calorimeter. Most of the shower develops in the EMCal. The response of the electromagnetic calorimeter to electrons and protons at normal incidence is shown in Figure 3.14. The resolution of the electromagnetic calorimeter for electrons at normal incidence is summarized in Figure 3.15. The single particle energy resolution at normal incidence is determined to be $14.2\%/\sqrt{E} + 0.7\%$.

The energy deposited in the electromagnetic calorimeter in central HIJING events is shown in Figure 3.16. The mean energy deposited in any single tower is estimated to be 47 MeV. The existing PHENIX electromagnetic calorimeter cluster finding algorithm has been adapted for the sPHENIX EMCal specifications. Initial results indicate that for a 10 GeV photon there is an extra 4% of underlying event energy in the cluster and a degredation of approximately 10% in the energy resolution when embedded in a central Au+Au event (simulated with the HIJING event generator).

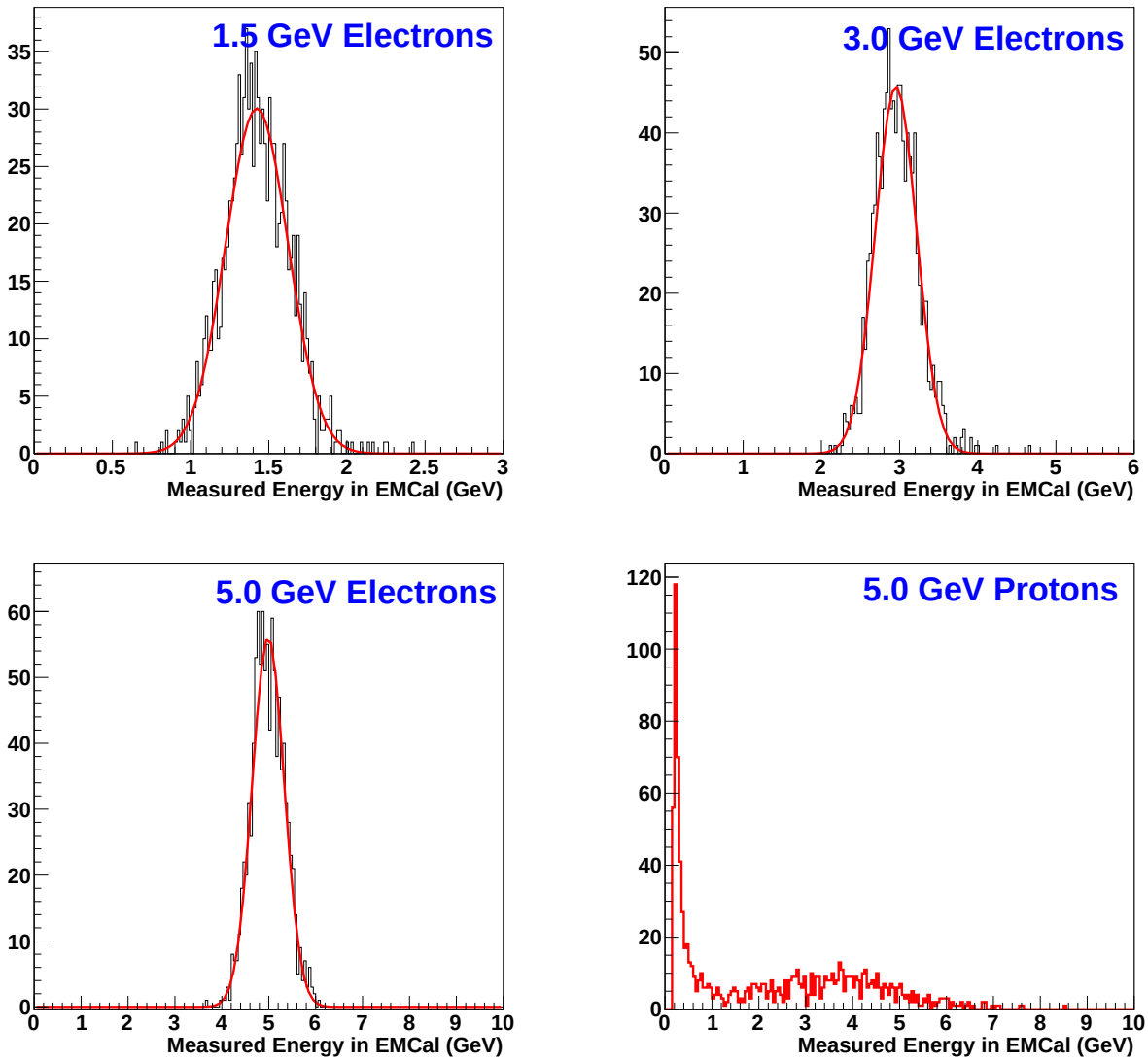

Figure 3.14: Response of the electromagnetic calorimeter to 1.5, 3, and 5 GeV electrons and 5 GeV protons. For the protons there is a large minimum ionizing particle (MIP) peak and a broad distribution corresponding to cases where the proton induces an hadronic shower at some depth into the EMCal.

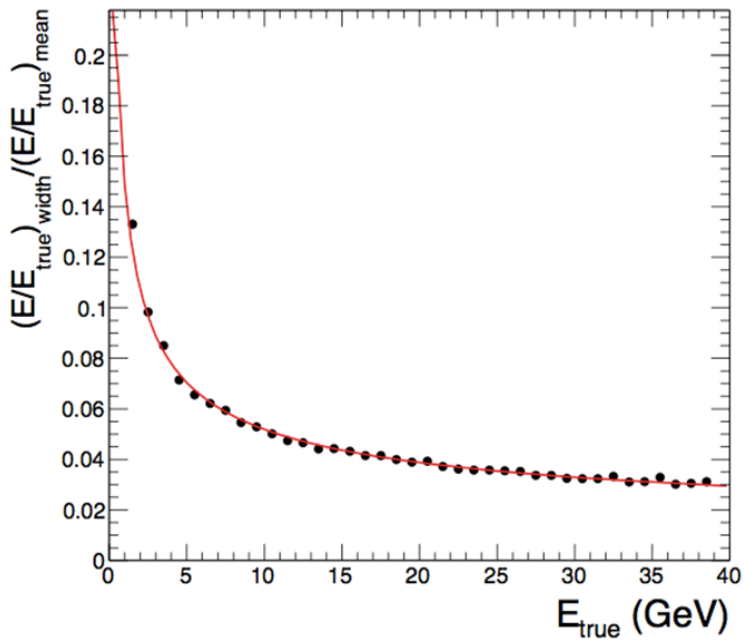

Figure 3.15: Energy resolution of a tungsten-scintillator sampling calorimeter with the same sampling fraction as the sPHENIX tungsten-scintillator accordion calorimeter. The data are obtained for electrons at normal incidence with energies indicated. The fit indicates an energy resolution of $\sigma_E/E = 14.2\%/\sqrt{E}+0.7\%$.

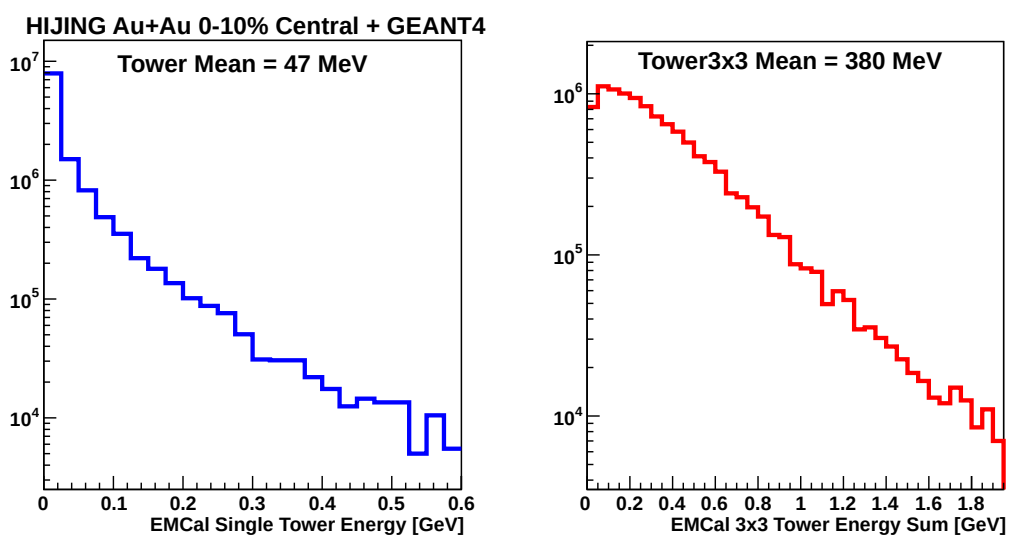

Figure 3.16: Distribution of energy deposited in the electromagnetic calorimeter for single towers (left panel) and in 3×3 arrays of towers (right panel) in central HIJING events.

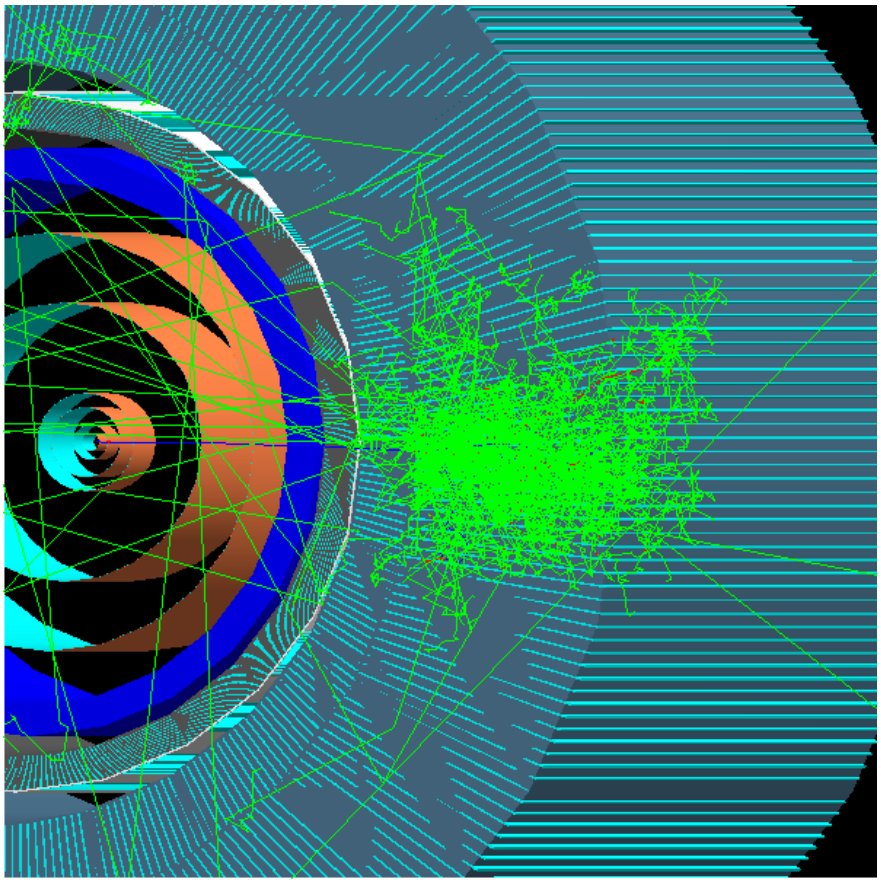

Figure 3.17: Transverse view of a 10 GeV/c π^+ in sPHENIX. It penetrates the magnet (blue) and the EMCal and showers in the first segment of the HCal.

3.4.2 Hadronic Calorimeter Simulation

The hadronic calorimeter has been simulated using the GEANT4 tools described above. Figure 3.17 shows a typical GEANT4 event in which a 10 GeV/c π^+ incident on the calorimeter showers in the Hcal.

The single particle energy resolution in the HCal has been determined using a full GEANT4 description of the calorimeters. The energy deposition in the scintillator is corrected for the average sampling fraction of the inner and outer sections separately, calculated to be 18.2% for the inner and 27% for the outer. The calorimeter response to single protons is shown in Figure 3.18. Figure 3.19 shows the resolution of just the HCal itself when illuminated by a beam of π^-. In this case, there is nothing in front of the HCal, it is just an isolated device. Figure 3.20 shows the energy resolution of the combined system of EMCal and HCal when illuminated by a beam of protons. In this case, the full GEANT4 description of sPHENIX is in place.

The mean and standard deviation from a Gaussian fit to the measured energy distri-

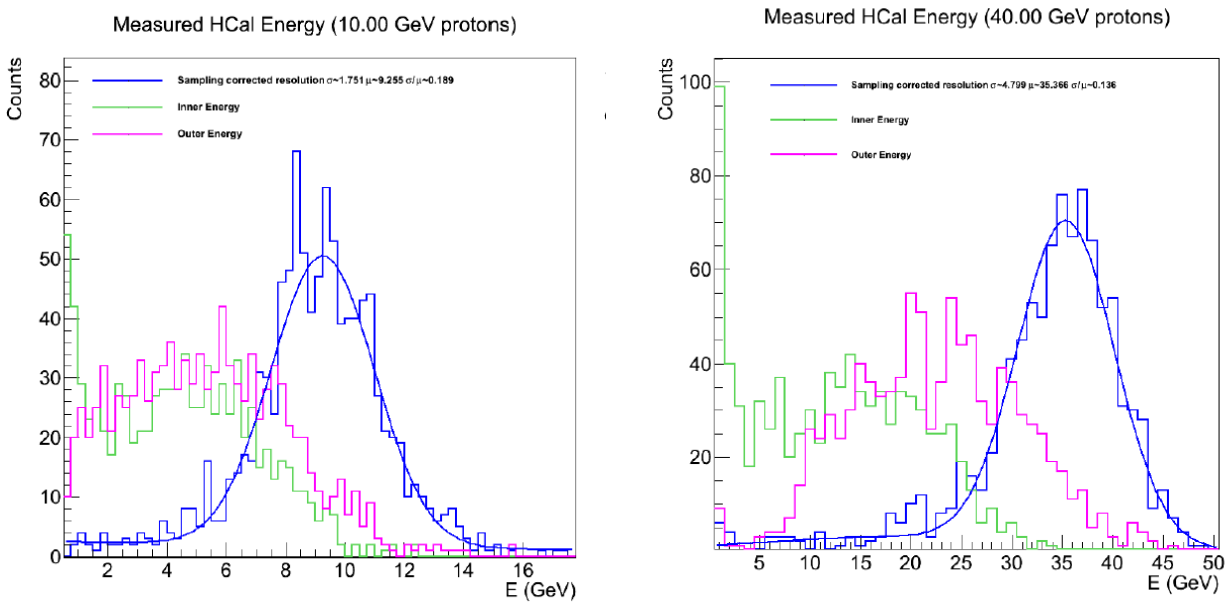

Figure 3.18: Energy deposited in the hadronic calorimeter by 10 (left panel) and 40 (right panel) GeV/c protons, showing the good containment and Gaussian response of the calorimeter.

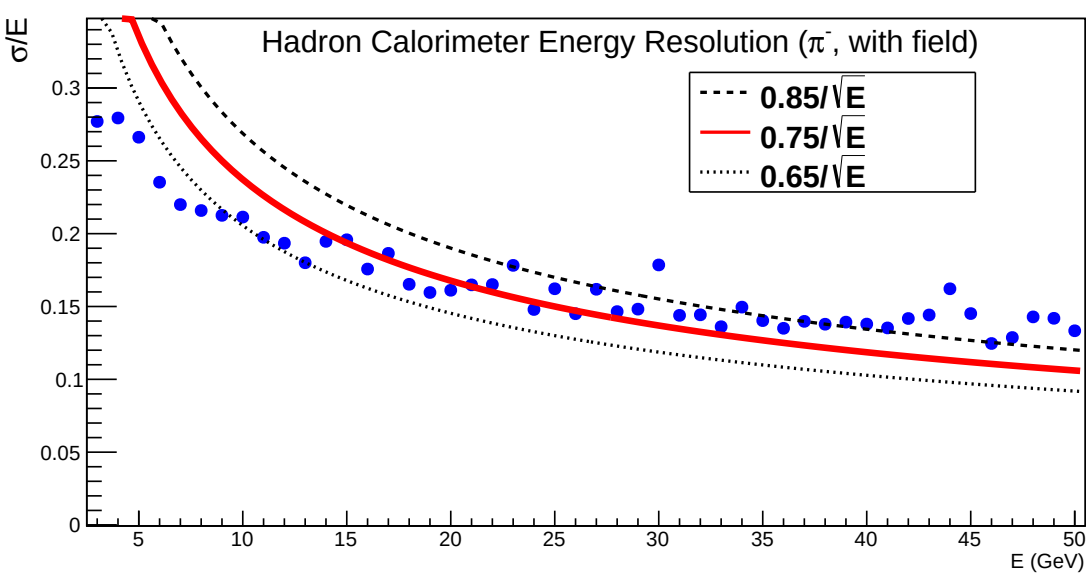

Figure 3.19: Energy resolution of the hadronic calorimeter as one might measure in a test beam. The HCal is isolated, with nothing in front of it, and is illuminated by pions.

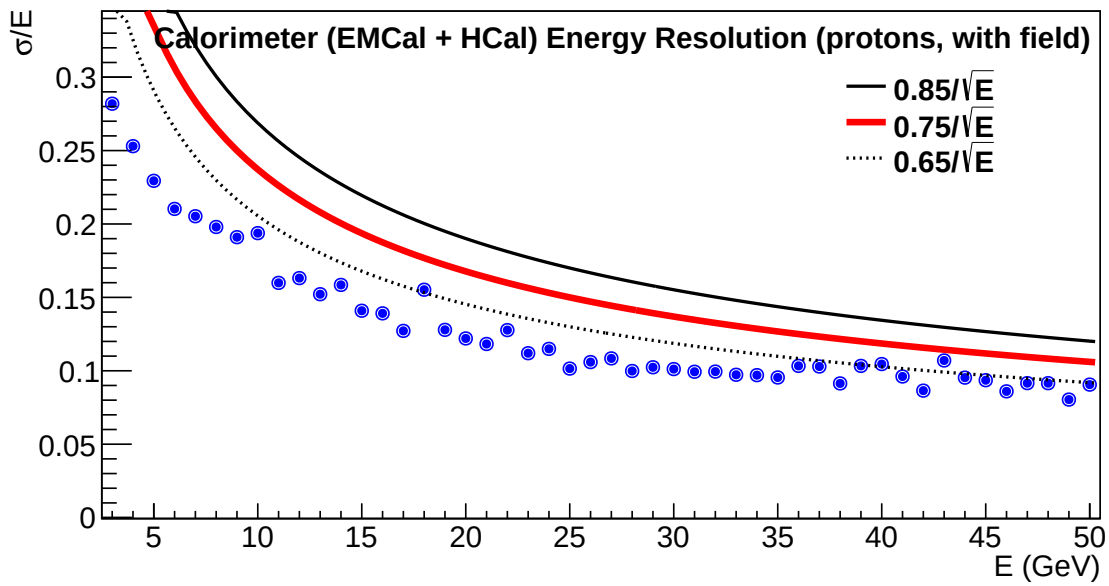

Figure 3.20: Energy resolution of the combined system of EMCal and HCal. In this case, the calorimeters sit behind the VTX and the solenoid magnet.

bution are used to calculate the nominal detector resolution. In both Figure 3.19 and Figure 3.20, the resolution determined from simulation is compared to curves of $0.85/\sqrt{E}$, $0.75/\sqrt{E}$, and $0.65/\sqrt{E}$ as reference for the simulated resolution. These indicate a GEANT4 performance level better than the physics requirements.

As mentioned above, the proposed sPHENIX calorimeter system is about $6\lambda_{int}$ deep, and one expects some leakage of energy out of calorimeter. The amount of this leakage and its energy dependence can be estimated from literature Figure 3.8 above or from simulation which is tuned to available experimental data. The probability for a proton to go through the whole depth of calorimeter without an hadronic interaction is about 0.6% (verified with full GEANT4 simulations). Energy leakage out the back is thus not expected to be a serious problem for this calorimeter.

3.5 Electronics

For the readout of both the EMCal and HCal a common electronics design will be used to reduce the overall cost and minimize the design time. Two viable alternatives for reading out the sPHENIX calorimeters have been identified. The first approach is based on electronics developed for the PHENIX Hadron Blind Detector (HBD) and Resistive Plate Chambers (RPC), and uses the current PHENIX DAQ as the backend readout. The second approach is based on the BEETLE chip developed for the LHCb experiment and the

SRS DAQ developed at CERN. The following sections describe both approaches and how they could be implemented in sPHENIX. Both approaches will be evaluated in terms of performance and cost to enable an eventual selection of a readout system for the sPHENIX calorimeters.

3.5.1 Sensors

For both the electromagnetic and hadronic calorimeters, we are currently considering as sensors 3 mm$\times$3 mm silicon photomultipliers (SiPMs), such as the Hamamatsu S10362-33-25C MultiPixel Photon Counters (MPPC). These devices have 14,400 pixels, each 25 μm$\times$ 25 μm. Any SiPM device will have an intrinsic limitation on its dynamic range due to the finite number of pixels, and with over 14K pixels, this device has a useful dynamic range of over 10^4. The saturation at the upper end of the range is correctable up to the point where all pixels have fired. The photon detection efficiency is $\sim$ 36% and it should therefore be possible to adjust the light level to the SiPM using a mixer to place the full energy range for each tower ($\sim$ 5 MeV–50 GeV) in its useful operating range. For example, if the light levels were adjusted to give 10,000 photoelectrons for 50 GeV, this would require only 200 photoelectrons/GeV, which should be easily achieved given the light level from the fibers entering the mixer.

While we believe that the SiPMs are likely the most suitable sensor for the calorimeters, we are also considering avalanche photodiodes (APDs) as an alternative. They have much lower gain ($\sim$50–100 compared to $\sim 10^5$ for SiPMs), and therefore would require lower noise and more demanding readout electronics, but they do provide better linearity over a larger dynamic range. In addition, while the gain of both SiPMs and APDs depend on temperature, SiPMs have a stronger gain variation than APDs (typically 10%/°C for SiPMs vs 2%/°C for APDs). Thus, we are considering APDs as an alternative solution as readout devices pending further tests with SiPMs and our light mixing scheme.

3.5.2 All Digital Readout [Option 1]

SiPM Preamplifier Circuitry

The requirements of the sPHENIX calorimeter preamplifier circuit board are to provide localized bias/gain control, temperature compensation, signal wave shaping and differential drive of the SiPM signal to an ADC for acquisition. Gain adjustment and temperature compensation are performed as part of the same control circuit. Signal wave shaping is performed by the differential driver to satisfy the sampling requirements of the ADC.

Temperature Compensation

The reverse breakdown voltage V_{br} for the Hamamatsu S10362-33-25C device is nominally 70 Volts. As the bias is increased over the value of V_{br} the SiPM begins to operate in Geiger mode with a gain of up to 2.75×10^5. The range of this over-voltage (V_{ov}) is typically 1–2 Volts and represents the useful gain range of the device. The V_{br} increases by 56 mV/°C linearly with temperature and must be compensated to achieve stable gain. This compensation is achieved using a closed feedback loop circuit consisting of a thermistor, ADC, logic and DAC voltage control as shown in Figure 3.21.

The thermistor is fixed to the back of the SiPM and provides a significant voltage variation over temperature when used as part of a voltage divider, thereby easing temperature measurement over a length of cable. The bias supply for an array of SiPMs is fixed nominally at $V_{br} + 2.5$V. The DAC in each SiPM circuit then outputs a subtraction voltage of 0 V to 5 V to provide a full range of gain control over the device temperature range. The SiPM gain may then be adjusted externally through an interface to the logic.

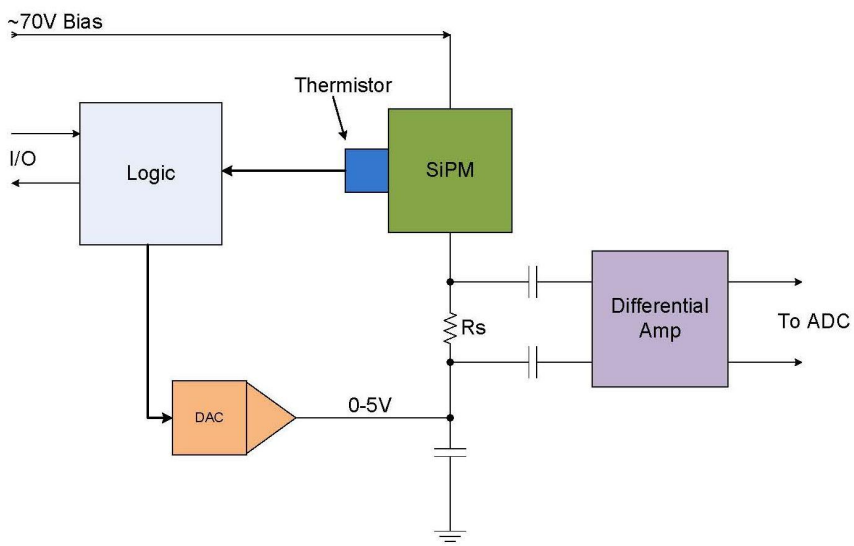

Figure 3.21: Block diagram of a temperature compensating circuit for SiPMs

Preamplifier-Shaper-Driver

The SiPM current develops a voltage across the load resistor R_s proportional to the number of pixels fired. To avoid the region of greatest non-linearity due to saturation of the SiPM, the maximum signal level is optically adjusted to 10K out of 14.4K pixels fired. Simulations of the SiPM indicate that the current could be as much as several tenths of an ampere at this maximum level. Results of a SPICE simulation are shown in Figure 3.22. Such a large current affords the use of a small value for R_s which virtually eliminates the contribution

of R_s to non-linearity. This signal voltage is sensed differentially, amplified and filtered by a low power, fully differential amplifier. For sampling by a 65MSPS ADC, a peaking time of approximately 35 ns is achieved through the use of a second order Butterworth filter implemented in the differential driver circuit.

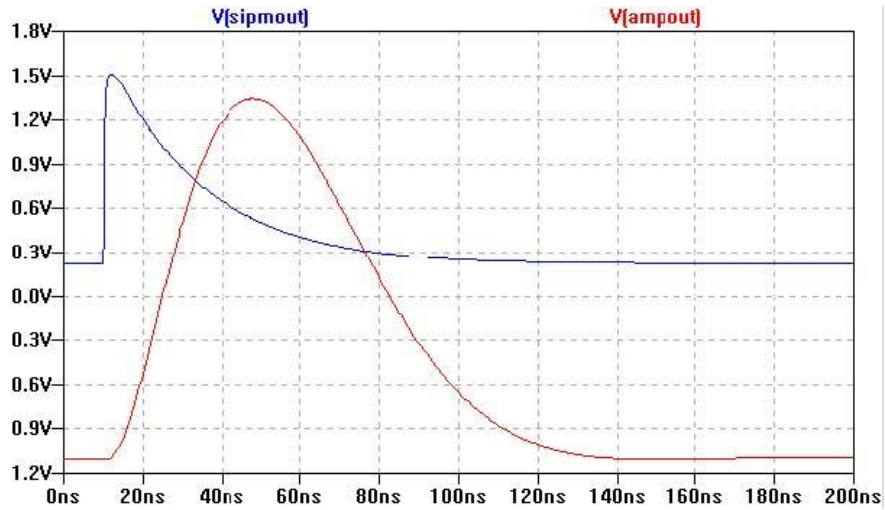

Figure 3.22: SPICE simulation of a prototype temperature compensating circuit for SiPM readout of the sPHENIX EMCal and HCal.

Signal Digitization

One solution for the readout of the EMCal and HCal detectors for sPHENIX is the direct digitization of the SiPM signal. The signals from the SiPM are shaped to match the sampling frequency, and digitized using a flash ADC. The data are stored in local memory pending a Level-1 (L1) trigger decision. After receiving an L1 trigger decision, the data are read out to PHENIX Data Collection Modules (DCM II). These second generation Data Collection Modules would be the identical design as those developed and implemented for reading out the current PHENIX silicon detectors. One advantage of direct digitization is the ability to do data processing prior to sending trigger primitives to the L1 trigger system. The data processing can include channel by channel gain and offset corrections, tower sums, etc. This provides trigger primitives that will have near offline quality, improved trigger efficiency, and provide better trigger selection.

A readout system based on this concept was implemented for the Hadron Blind Detector (HBD) for the PHENIX experiment as shown in Figure 3.23 and subsequently modified for the PHENIX Resistive Plate Chamber (RPC) system. The block diagram of the Front-End Module (FEM) is showed in Figure 3.24. In the HBD system, the discrete preamplifier-shaper is mounted on the detector and the signals are driven out differentially on a 10 meter Hard Metric cable. The signals are received by Analog Device AD8031 differential receivers which also serves as the ADC drivers. Texas Instruments ADS5272 8 channel 12

bit ADCs receive the differential signals from 8 channels and digitize them at 6x the beam crossing clock . The 8 channels of digitized data are received differentially by an Altera Stratix II 60 FPGA which provides a 40 beam crossing L1 delay and a 5 event L1 triggered event buffer.

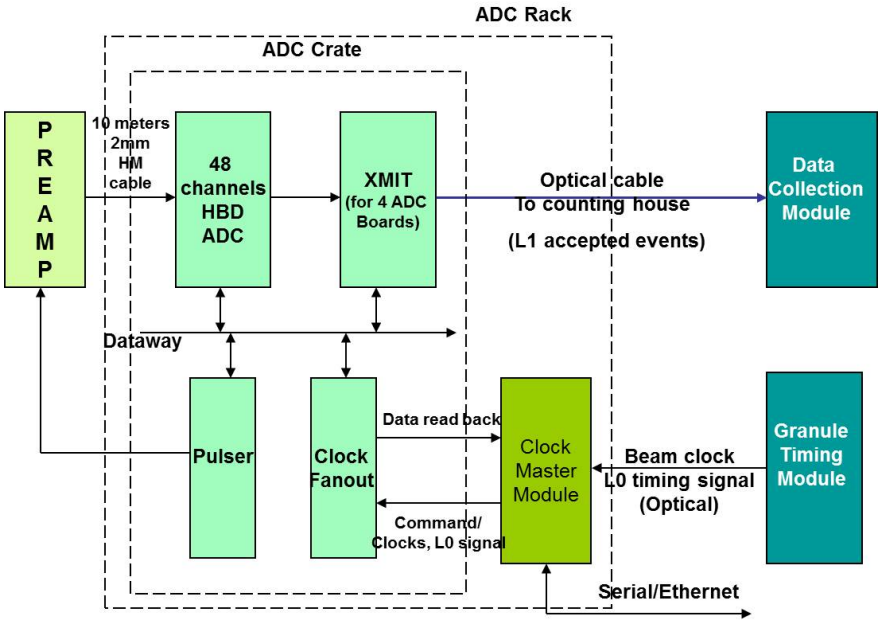

Figure 3.23: Block diagram of the HBD read out electronics

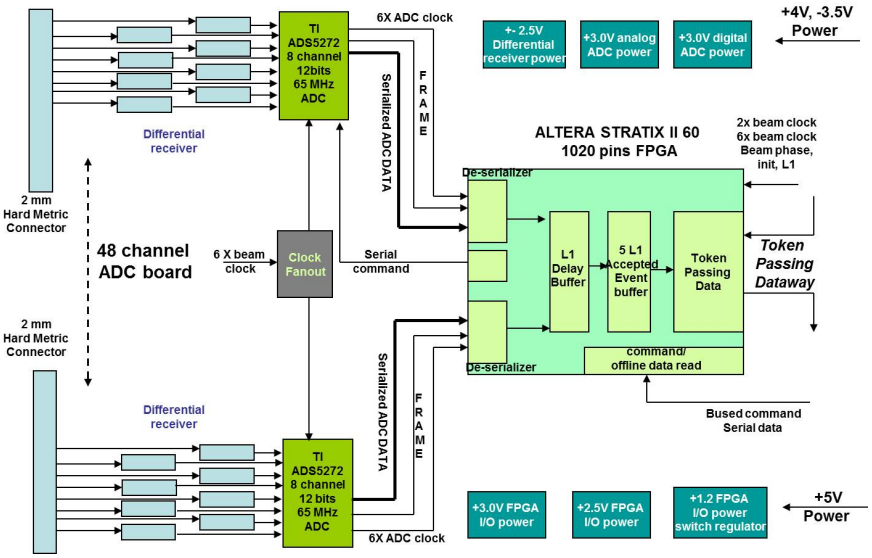

Figure 3.24: Block diagram of the HBD FEM electronics

The L1 triggered data from 4 FEMs is received by an XMIT board using token passing to control the readout of the FEMs. The data is then sent by 1.6 GBit optical links to

the PHENIX DAQ. A ClockMaster module interfaces to the PHENIX Granulate Timing Manager (GTM) system and fans out the clocks, L1 triggers and test enable signals to the FEMs and XMIT modules. The ClockMaster module also receives slow control signals for configuring the readout.

Although not shown in the block diagram, the FEM has 4 LVDS outputs that can be used to bring out L1 trigger primitives at 800 Mbits/sec. This feature was not used for the HBD readout, however it has been implemented for the RPC detector. A trigger module for the RPC system based on the Altera Arria FPGA receives the trigger primitives from the FEMs, combines them and sends them to the PHENIX L1 trigger system through two 3.125 GBit optical links.

For implementation in sPHENIX, two possible implementations are under consideration. The first design would place the analog and digital electronics directly on the detector. All control and clock signals would be brought in and L1 trigger primitives and triggered digital data transmitted out via high-speed optical fibers.

The second approach has the temperature compensating preamplifier mounted on the detectors and the shaped and amplified signals driven differentially to the digital modules located in racks near the detector using shielded differential cables. High speed fiber optic cables bring in all control and clock signals and transmit L1 trigger primitives and triggered data to the PHENIX DAQ.

3.5.3 Mixed-Mode Readout [Option 2]

Preamp ASIC

A preamp ASIC appropriate for readout of sPHENIX calorimeters has been identified. This custom ASIC is being developed at ORNL for front end readout of a new forward calorimeter (FoCal) under consideration as an upgrade for ALICE at CERN. This ASIC, or a very close variant, is appropriate for front end readout of the sPHENIX EMCal, HCal, (and possible future strip-pixel preshower as discussed in Appendix 6) detectors. The ORNL ASIC development is funded as part of a multi-disciplinary DOE SC LAB 11-450 project which is in its first year. The ORNL team is in close communication with colleagues at BNL and are working to coordinate simulation and actual testing of the ORNL ASIC with appropriate Hamamatsu silicon photomultipliers (SiPM) for the sPHENIX EMCal and HCal. The already-funded first year of LAB 11-450 work at ORNL will generate first round ASIC chips this summer for testing.

Traditional charge-sensitive preamplifiers (CSP) are commonly used for readout of capacitive detectors (silicon pads, strips, etc.) for two reasons. First, all the charge generated in a detector due to a radiation event is ultimately collected by the preamplifier irrespective of the detector capacitance. Higher detector capacitance may slow the preamplifier bandwidth such that it takes many microseconds to collect the charge but it will ultimately be

collected. Second, the ratio of the output voltage to the input charge (charge gain) is determined by the feedback capacitor used in the CSP and not the detector. Since $Q/C = V$, this will allow a small charge signal to be processed by a small feedback capacitor on the CSP instead of that same small charge on a much larger detector capacitance. This results in a proportionally larger voltage signal for subsequent processing.

Because of the large amount of charge per event available from an SiPM and the need for a fast trigger signal (fast preamplifier response), a traditional CSP is likely not ideal or needed. Therefore, a truly application-specific approach to on-chip readout is proposed. For simplicity, we can utilize a very fast high-speed follower topology similar to that used on a photomultiplier tube. This will allow us to maintain high speed, low noise, and simplicity at the front end detector. With a follower, we will have sufficient bandwidth to provide a fast trigger without having to maintain a high bandwidth closed loop CSP. Processing electronics can be placed away from the detector thus somewhat mitigating heat and power-distribution problems. The follower, shown in Figure 3.25, is very straightforward. Simulations in Figure 3.26 show that if we design the detector/follower such that our input maximum charge results in approximately 1.6 V output, we can develop a circuit which will exhibit noise of approximately 108 μV RMS, a peak/RMS ratio of 14,800. This shows that we will likely not be limited by noise, but by inter-channel crosstalk. The follower requires a buffered output, preferably differential to minimize crosstalk. The output of the differential buffer will drive the signal to an area with more available space, where it will be connected to processing electronics (shaper, trigger processor, ADC), simplifying their requirements.

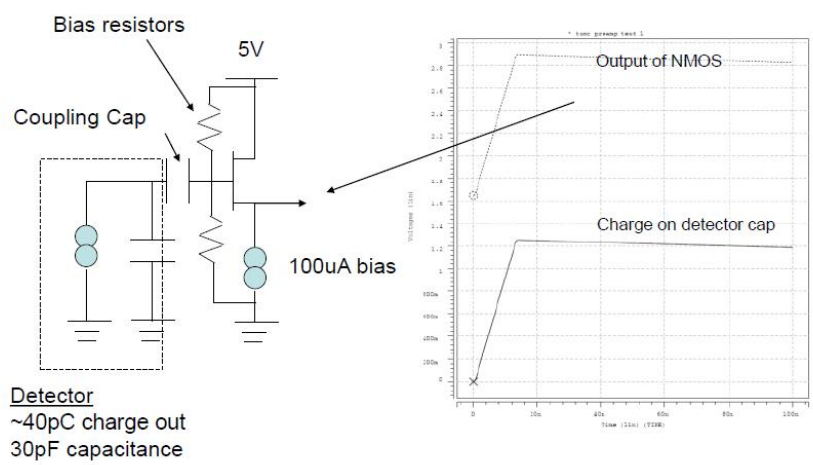

Figure 3.25: ASIC follower schematic and output signal

A block diagram for the proposed preamplifier/driver is shown in Figure 3.27. The preamplifier connects to the detector as shown in Figure 3.25 (through a coupling capacitor if needed) and can utilize either polarity of charge input. There are bias setting resistors on the chip that set the quiescent input voltage. When an event occurs, the charge is collected on the detector capacitance and the voltage output is buffered and sent to the

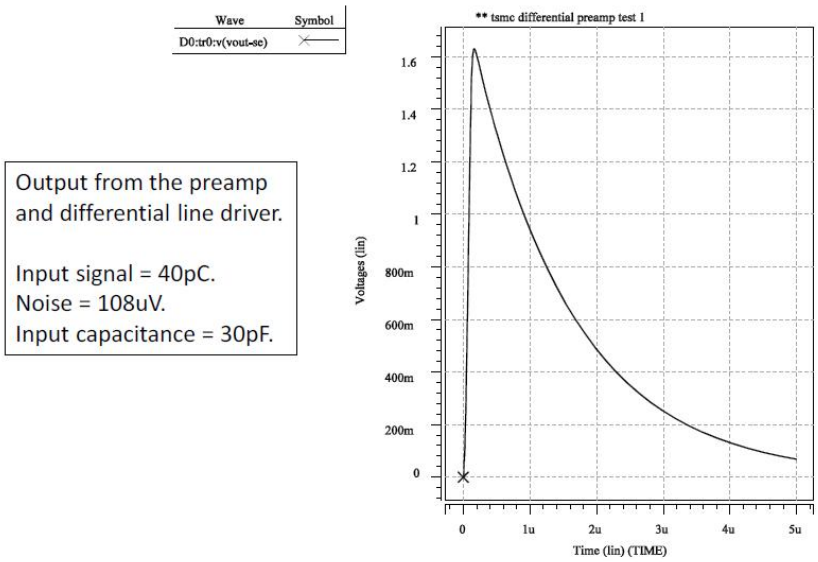

Figure 3.26: Simulation ASIC preamp output voltage versus time.

single-ended-to-differential driver. This driver is designed to drive a 100-ohm differential line. The power dissipation is currently under 10 mW for the entire circuit which operates on 2.5 V. The preamplifier is presently under design in the TSMC 0.25μm CMOS process. A layout estimate results in an expected chip area of under 2 mm$\times$2 mm for four channels.

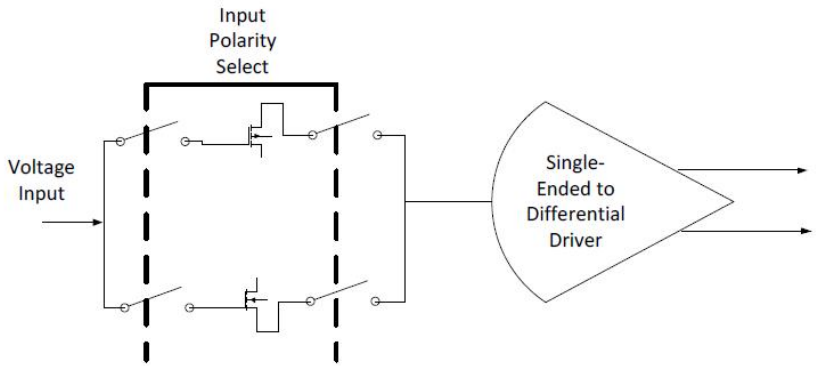

Figure 3.27: A block diagram for the proposed preamplifier/driver.

This electrical engineering design and development of the ASIC is undertaken as part of a separate ongoing DOE LAB 11-450 project. Fabrication and testing of 120 ASIC chips is scheduled for summer 2012. The chip bench testing will be performed at ORNL and include tests of basic functionality to ensure essential operation of the device such as amplification, rise time, power dissipation, channel-to-channel gain variation, noise, and chip-to-chip variations.

We have obtained a MOSIS quotation for fabrication and packaging of a sufficient number of 4-channel preamp ASICs plus spares for the sPHENIX EMCal and HCal for a cost of $2.80/channel. This price does not include the testing which can be accomplished very cost effectively by EE and physics graduate students with direct supervision by electrical engineers.

Front-End Readout Design using the CERN SRS

In this Section we present a design outline for sPHENIX calorimeter readout based on the already-existing CERN Scalable Readout System (SRS) which has been developed as part of the CERN RD51 project [107, 108].

The SRS architecture consists of three stages, as shown in Figure 3.28. Signals from the detector elements are conditioned and analog buffered on an analog FEE board (see below for more detail), which also generates trigger primitives. When an event is read out, the FEE board transmits analog levels to the front-end card (FEC), where they are digitized and assembled as sub-events. The transfer from the FEE board to the FEC is carried across commercial standard HDMI-format cables, which can accommodate a separation of several meters from a detector-mounted board to crate-mounted FECs. The FECs receive trigger primitives from the FEE boards along the same HDMI cables.

With existing implementations, each FEC can service eight FEE boards. Continuing hierarchically, up to 40 FECs can be gathered through standard network connections, to one Scalable Readout Unit (SRU) component of the SRS system. The SRU gathers the real-time trigger information from the whole system and fulfills the same function as the existing PHENIX Local Level-1 (LL1) system. The SRU also serves as the overall controller/director for the FECs and fulfills the same function as the existing the PHENIX Granule Timing Module (GTM) to pass down readout and control instructions. When an event is processed, the FECs can put out sub-event data on standard network connections directly to an Event Builder; and thus the FEC fulfills the function of both the Data Collection Module (DCM II) and Sub-Event Builder (SEB) of the PHENIX architecture.

The sPHENIX Analog FEE Board

The advantage of adopting the SRS, for any large-scale system, is that only the analog FEE board needs to be designed specifically for the detector in question, and its functionality is relatively simple. It only needs to buffer and transmit analog levels; all the ADC and digital processing functions are carried out on existing FECs.

In the SRS-based readout design, we would use an existing circuit for the analog buffering function: the BEETLE chip, designed for use in the LHCb experiment[109]. An SRS FEE card based on the BEETLE chip is being developed by a group from the Weizmann Institute for use in an ATLAS upgrade. The BEETLE has 128 analog input channels, each of which

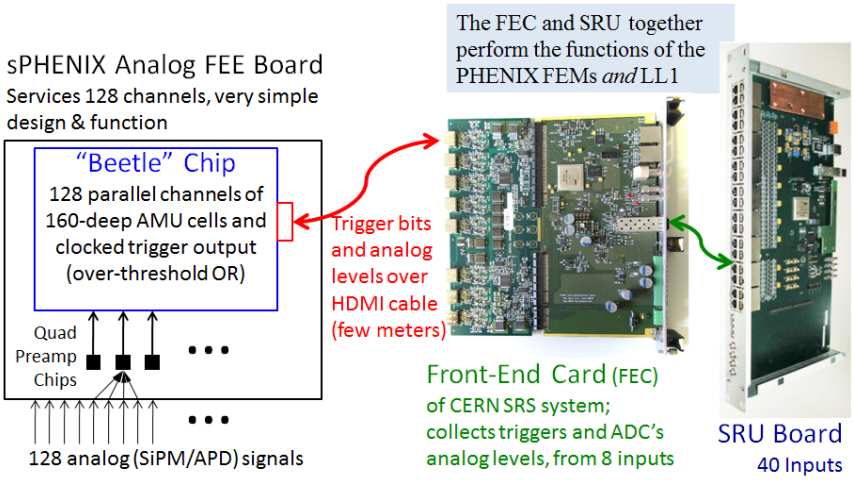

Figure 3.28: The SRS topology: The analog FEE board sits on the detector and buffers analog levels, which are then transferred to, and digitized on, the Front-End Card (FEC); the array of FECs are controlled by a Scalable Readout Unit (SRU) board. Only the analog FEE board is specific to the detector; the FEC and SRU are already-existing components of the SRS.

can be buffered at up to 40 MHz in a 160-sample analog ring buffer. On readout, the BEETLE copies the analog level from the appropriate ring cells to an on-chip buffer, so the ring operation is not interrupted; the BEETLE then multiplexes these analog levels over to the FEC for digitization. The entire complement of 128 channels for one event can be transferred and converted in slightly under one microsecond.

Figure 3.29 shows a timing diagram for the processing of one physics event, with the trigger primitive bits coming up through the FECs and the SRU to the PHENIX GL1 system, which returns the LVL-1 accept down to the FECs. Sampling at up to 40 MHz, the BEETLE analog ring has enough depth to accommodate the PHENIX-standard 4 microsecond latency between the crossing of interest and the arrival of the LVL-1 accept instruction.

Trigger primitive bits are generated within the BEETLE chip, and are continually passed up to the FECs, where they are gathered in the SRU for calorimeter-wide processing. The trigger information provided by each BEETLE chip is essentially a channel-by-channel voltage-over-threshold condition, of which groups of four channels are then OR'ed together. The simplest global condition would be a logical OR of the over-threshold for all the towers in a fiducial portion of either the EMCal or HCal layers of the calorimeter.

One advantage of adapting the SRS system for sPHENIX is the large potential savings in development time and effort and procurement costs. The only component which needs to be specifically designed for the detector is the analog FEE board; and in the scheme outlined here that board is relatively simple, interfacing the ORNL preamp ASIC to the detector and carrying the BEETLE analog buffer chips. The digitization and digital processing are all carried out on the FECs, which use multiplexing of analog levels for higher economy; and the FECs are crate-mounted up to several meters away from the detector, which would

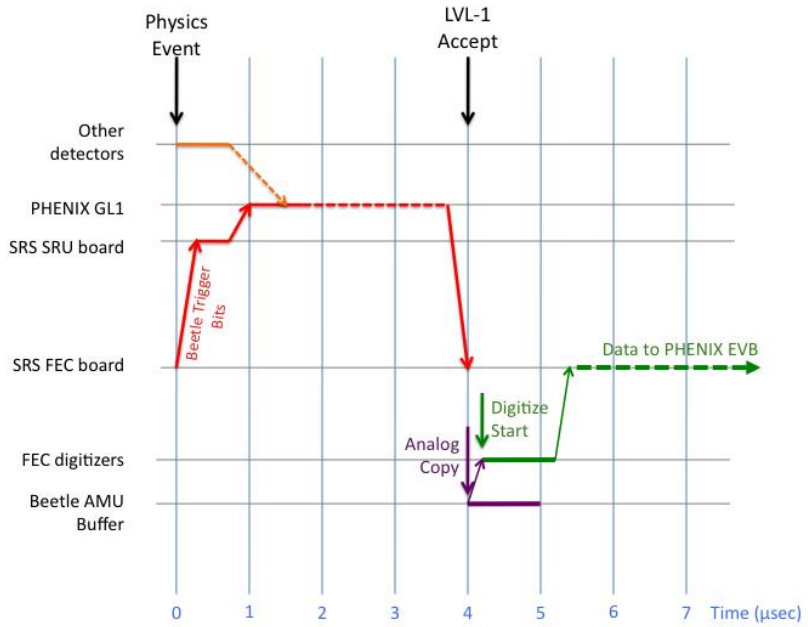

Figure 3.29: Timing diagram for processing one physics event, showing the operation of the BEETLE-based analog FEE board and the FEC and SRU components of the SRS, staying well within the PHENIX specifications for digitization and readout.

simplify the effort of deployment. All together, the FEC/SRU portions of the readout chain are estimated to be available for approximately $2/channel for large channel count systems, based on the production costs of the first prototype SRS systems including FEC and SRU modules with power supplies and SRS crates, and including also FEE boards based on the AVX chip.

3.5.4 sPHENIX DAQ

The sPHENIX DAQ will be largely based on the current PHENIX DAQ. In the PHENIX DAQ, trigger primitives from the FEMs are transferred via optical fibers to the Local Level-1 (LL1) trigger system that process the signals and generates an LL1 accept if the event meets the trigger requirements. The trigger operates in a pipeline mode with a 40 beam crossing latency, generating a trigger decisions fro each crossing. The Local Level-1 trigger can be configured to accept events with different signatures and can operate at up to 10 kHz.

The LL1 accept is transmitted to all FEMs, and the corresponding event is transferred to the DCM II modules via optical fibers. The DCM II modules zero suppress the data and transmit the zero suppressed data to the event builder which collects the data and formats it for archiving. The formatted data is buffered locally at the PHENIX experimental hall before being transferred to HPSS for archiving. The PHENIX Online Computing System

(ONCS) configures and initializes the DAQ, monitors and controls the data flow, and provides monitoring and control of axillary systems.

For the all digital approach 48 SiPMs are readout by a single FEM and data from 4 FEMs is collected and readout to a single DCM II channel. Each DCM II module has 8 channels, so based on channel count a total of 16 DCM II modules are required for the EMCal and another 2 DCM II modules are required for the HCal.

For the mix-mode approach using the SRS, the SRS replaces the DCM II modules and the data from the SRS would be transmitted directly to the event builder over high speed ethernet.

In either case, raw data manipulation, databases, logging and archiving, controls and monitoring can be adapted from the existing PHENIX architecture with minimal upgrades, taking advantage of a developed system which has been functioning for more than a decade.

3.6 Mechanical Design and Infrastructure Concept

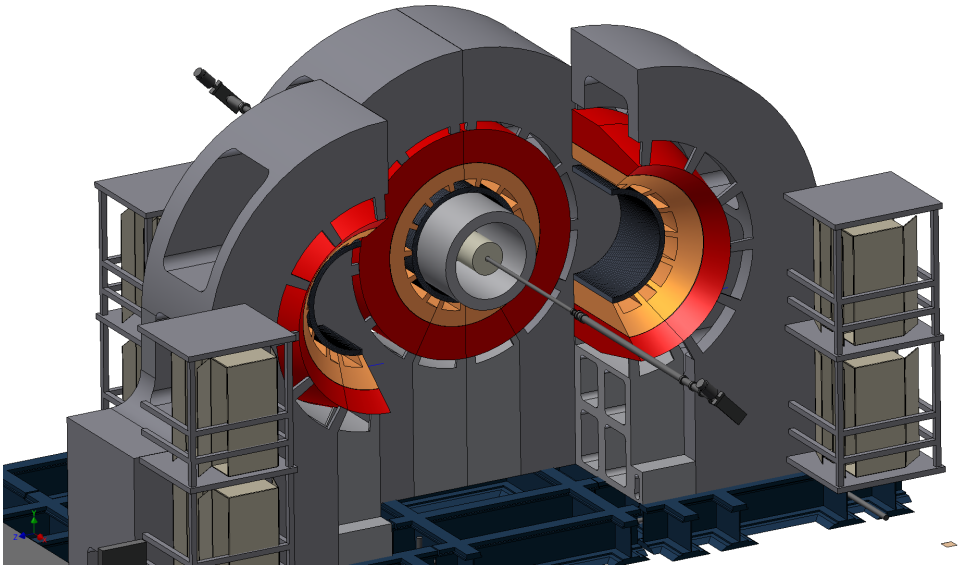

Figure 3.30: Illustration of sPHENIX underlying structural support, support equipment, overall assembly and maintenance concepts

sPHENIX has been designed to be straightforward to manufacture and assemble, but it still requires significant and well thought out infrastructure to support and service it. The overall concept for how sPHENIX will sit in the existing PHENIX IR is shown in Figure 3.30. A set of envelope dimensions and design constraint parameters for each of the major components of sPHENIX has been established and is discussed below.

3.6.1 Beampipe

The existing PHENIX beampipe will be used with minimal modification. The current beampipe has a 40 mm outside diameter in the central area, and connected on either end with transition pipe sections from 40 mm to 75 mm OD and 75 mm OD to 125 mm OD. A new support structure to support the beampipe inside the superconducting solenoid will need to be designed.

3.6.2 Silicon Vertex Tracker (VTX)

The support structure for the VTX, utilities supply and readout design will need to be modified to allow the VTX to fit within the superconducting solenoid cryostat. Existing VTX and upgrades to detector subassembly will be integrated into a new structural support design and mechanisms which will mount the VTX onto rails supported by the cryostat inner surface, allowing the VTX to be separated laterally then extracted from inside the cryostat longitudinally parallel to the beampipe for maintenance. The VTX electronics and services inside the cryostat will not be serviceable during runs. The VTX support structure will have a clamshell design to allow the east and west halves to be opened then extracted longitudinally on a rail system during long maintenance shutdowns.

3.6.3 Superconducting solenoid magnet

The magnet has a 2 Tesla solenoid field, 700 mm inner cryostat radius, 900 mm outer cryostat radius, 1870 mm cryostat length. The cryostat is not designed to be disassembled. The cryostat will incorporate two or more support mounts that will fit in the clearance between the EMCal and the outer skin of the cryostat. The cryostat will have an angled services stack at the south end to exit beyond the end of the EMCal and HCal detectors to cryogenic supply lines, power supplies and monitoring equipment. Provision will also be incorporated for transport, lifting and installation. Preliminary specifications and requirements for the solenoid and cryostat have been developed based on a recently developed solenoid in the BNL Magnet Division.

3.6.4 Electromagnetic calorimeter

The EMCal will have a 100 mm radial thickness with an inside 50 mm radial clearance from the cryostat outer radius and a 75 mm outer radial allowance for electronics and services with full 2π azimuthal coverage. The EMCal will have integral support for the Cryostat and/or clearance for support from a lower structure. The EMCal will also incorporate provision for support of itself in the fully assembled configuration, any maintenance configuration, and for assembly/disassembly and integration of component segments.

The EMCal will be constructed of tungsten (2 mm thick) and light fibers (1 mm thick). These will be grouped into 314 azimuthal segments. Details of the mechanical design of the EMCal segments is covered in Section 3.2.

3.6.5 Hadronic calorimeter

The HCal will be 900 mm in radial thickness, with full 2π azimuthal coverage, and with the calorimeter divided into an inner radial section and an outer radial section. The inner radial section will be 300 mm in radial thickness with a 75 mm inner radial allowance for readout electronics and services. The outer calorimeter will be 600 mm in radial thickness with a 75 mm outer radial allowance for readout electronics and services. The HCal will have integral support for the EMCal and Cryostat and/or clearance for support from lower structure. The HCal will also incorporate provision for support of itself in the fullys assembled configuration, any maintenance configuration and for assembly/disassembly and integration of component segments.HCal will be constructed of 256 segments of 6 mm thick scintillator sections with embedded optical fibers to accumulate the light energy. The scintillator sections will be sandwiched between tapered steel plates angled at 5 degrees from the radial direction, with the inner steel dividers angled in the opposite direction from the outer steel and offset by a half a segment thickness. Details of the mechanical design of the HCal segments is covered in Section 3.3.

3.6.6 Structural support apparatus

Structural support for the sPHENIX major components will provide appropriate structural support for all of the equipment with the following criteria:

- Appropriate structural support will be provided to all components, with integral connections and support interfaces and/or clearances for support structure designed into the comprising detector subassemblies and the superconducting solenoid.
- Components will be able to be completely assembled in the PHENIX Assembly Hall (AH) utilizing existing cranes (40 ton max.). The assembly will be mounted on the existing PHENIX rail system or a modification of the existing rail system.
- Functional tests including pressure, and magnetic tests will be able to be performed in the AH.
- The sPHENIX will have designed-in capabilities to separate into subdivisions to allow maintenance of any electronics, support services and replaceable components. This capability will be available with the full assembly in the AH or the Interaction Region (IR), with full maintenance capabilities during shutdowns between runs and with as much maintenance capabilities during a run as possible.

- The sPHENIX assembly will be relocatable from the AH to the IR using the existing rail system or a modification to the existing rail system. This relocation may be accomplished fully assembled or disassembled into subdivisions which are reassembled in the IR. Disassembly and re-assembly will use existing AH and IR cranes.
- Support equipment for the above components and the utilities supplied to the above structure including provision for electronics racks, cooling services, cryogenics, power and signal cables, and monitoring and control equipment will be provided.
- The assembled sPHENIX will allow partial disassembly during maintenance periods to provide access to all serviceable components, electronics and services. The assembled sPHENIX will provide for electronics racks and all other support components for operation and monitoring of the sPHENIX active components. Safe and efficient access to all service/monitoring components will be integrated into the design of the underlying structural support.
- Infrastructure used successfully for the past twelve years of of PHENIX operation will be adapted and expanded to support sPHENIX.

Chapter 4

Jet, Dijet, and γ-Jet Performance

In this Chapter we detail the sPHENIX jet, dijet, and γ-jet reconstruction performance and demonstrate the ability to measure key observables that can test and discriminate different quenching mechanisms and coupling strengths to the medium. The important aspects of jet performance are the ability to find jets with high efficiency and purity, and to measure the kinematic properties of jet observables with good resolution. In addition, it is necessary to discriminate between jets from parton fragmentation and fake jets caused by fluctuations in the underlying event background. For the sPHENIX physics program, there are three crucial observables that we have simulated in detail to demonstrate the jet performance: single inclusive jet yields, dijet correlations, and γ+jet correlations. There are other significant observables such as the participant plane dependence (e.g. v_2, v_3, etc.) of jets and jet-hadron correlations that are also enabled by this upgrade. The primary focus will be to demonstrate the capabilities of sPHENIX for central Au+Au collisions at $\sqrt{s_{NN}} = 200\,\text{GeV}$, and for select observables we will also show the physics performance of the detector for Au+Au collisions at $\sqrt{s_{NN}} = 100\,\text{GeV}$.

4.1 Simulations

sPHENIX will sample jet observables from 50 billion Au+Au minimum bias interactions per year at $\sqrt{s_{NN}} = 200\,\text{GeV}$ (10 billion Au+Au minimum bias interactions per year at $\sqrt{s_{NN}} = 100\,\text{GeV}$). It is not possible to simulate with full GEANT4 [106] the equivalent data sample. Thus, we perform three different levels of simulations described in detail below. The most sophisticated and computationally intensive are full GEANT4 simulations with PYTHIA [110] or HIJING [111] events where all particles are traced through the magnetic field, energy deposits in the calorimeters recorded, clustering applied, and jets are reconstructed via the FASTJET package [112]. We utilize this method to determine the jet resolution in p+p and Au+Au collisions from the combined electromagnetic and hadronic calorimeter information. We have also performed a full GEANT4 study of the

reconstruction of PYTHIA jets embedded in central Au+Au HIJING events to gauge the effect of the underlying event on jet observables.

For studies of fake jets in Au+Au central collisions, one needs to simulate hundreds of millions of events and for this we utilize a fast simulation where the particles from the event generator are parsed by their particle type, smeared by the appropriate detector resolution parametrization from GEANT4 simulations, and segmented into detector cells. As described in detail below, a full underlying event subtraction procedure is applied, and then jets reconstructed via FASTJET. This method is also utilized for embedding PYTHIA or PYQUEN [113] (a jet quenching parton shower model with parameters tuned to RHIC data) events into Au+Au HIJING events to study dijet and γ+jet observables. Finally, in order to gain a more intuitive understanding of the various effects, we run a very fast simulation where PYTHIA particles are run directly through FASTJET and then the reconstructed jet energies smeared by the parametrized resolutions and underlying event fluctuations.

The Chapter is organized as follows. First we describe the jet reconstruction and evaluate its performance in $p+p$ collisions for both an idealized detector as well as a fully simulated version. Then we describe our study of fake jet contamination, which has already been submitted for publication in Physical Review C [114]. Finally we show the expected performance for sPHENIX measurements of inclusive single jet, dijet and γ+jet processes.

4.2 Jet finding algorithm

For all of the studies presented here we use the anti-k_T jet algorithm [115] implemented as part of the FASTJET package [112]. The anti-k_T algorithm is well suited to heavy ion collisions and produces cone-like jets in an infrared and collinear safe procedure. The parameter that controls the size of the jet in this algorithm is the jet radius, R. While this is not strictly a cone size it does specify the typical extent of the jet in η-ϕ space. High energy experiments typically use large R values of 0.4–0.7 in order to come as close as possible to capturing the initial parton energy. In heavy ion collisions, the desire to measure the quenching effects on the jet profile and to minimize the effects of background fluctuations on jets has led to the use of a range of R values. Values from 0.2 to 0.5 have been used to date in Pb+Pb collisions at 2.76 TeV at the LHC [61, 65]. We note that looking at the jet properties as a function of the radius parameter is very interesting and potentially sensitive to modifications to the jet energy distribution in the medium. For the studies presented here we use R values of 0.2, 0.3, and 0.4.

4.3 Jet performance in $p+p$ collisions

We begin by exploring the performance of the detector in $p+p$ collisions. This allows us to investigate the effects of detector resolution and to investigate how well the process

of unfolding these effects in simpler collisions works before considering the additional effects of the underlying event and jet quenching in heavy-ion collisions.

The most realistic understanding of the sPHENIX jet reconstruction performance comes from a full GEANT4 simulation of the detector response. In this case, PYTHIA particles are run through a GEANT4 description of sPHENIX, the resulting energy deposition is corrected for by the sampling fraction of the relevant calorimeter, binned in cells of η-ϕ (0.024×0.024 for the EMCal and 0.1×0.1 for the HCal) and the resulting cells are used as input to FASTJET, which is used to cluster the full events into jets. Particles from PYTHIA events are put through FASTJET to determine the truth jets. The distribution of the difference between the truth and reconstructed jet energy is used to determine biases in the jet energy measurement as well as the jet energy resolution.

For the purposes of this proposal, it is important to extend this characterization to include the response of the system of calorimeters to the passage of a jet consisting of statistical ensemble of particles of a variety of particle species. This is a rather different study than for the single particle response. For example, even if one looks only at jets of a particular energy, the fraction of electromagnetic and hadronic energy will vary from jet to jet, which is found to make a strong contribution to the jet energy resolution.

From the set of matched jet pairs (i.e. truth and reconstructed jets), one next determines the difference between the energy of the reconstructed calorimeter jets, E_{reco}, and the particle-level truth jets, E_{true}. The width of this distribution, $\sigma(E)$, as a function of E_{true} is determined. Finally $\sigma(E)/E$ versus E is fit with a functional form

$$\frac{\sigma(E)}{E} = \frac{a}{\sqrt{E}} + b \tag{4.1}$$

The energy resolution for jets in $p+p$ collisions reconstructed with anti-k_T and $R = 0.2$ and $R = 0.4$ is shown in Figure 4.1 (left) and results in a resolution of $90\%/\sqrt{E}$ and a constant term of order 1%. The effect on the jet energy resolution of the underlying event in a Au+Au collision can be see in Figure 4.1 (right).

It is notable that often the jet energy resolution in collider experiments is found to be a factor of 1.2–1.3 worse than the quoted single particle resolution of the hadronic calorimeter. This factor is a balance of many effects including the better resolution for the electromagnetic part of the shower, soft particles that deflect out of the jet cone in the magnetic field, some lost energy, etc. The CMS quoted jet resolution in $p+p$ collisions at 7.0 TeV is approximately $120\%/\sqrt{E}$ which is roughly 1.2 times worse than the quoted single particle hadronic calorimeter resolution [116]. There are various methods to improve upon these resolutions, and the value for sPHENIX of $90\%/\sqrt{E}$ is consistent with this expectation given the hadronic calorimeter single particle resolutions described previously.

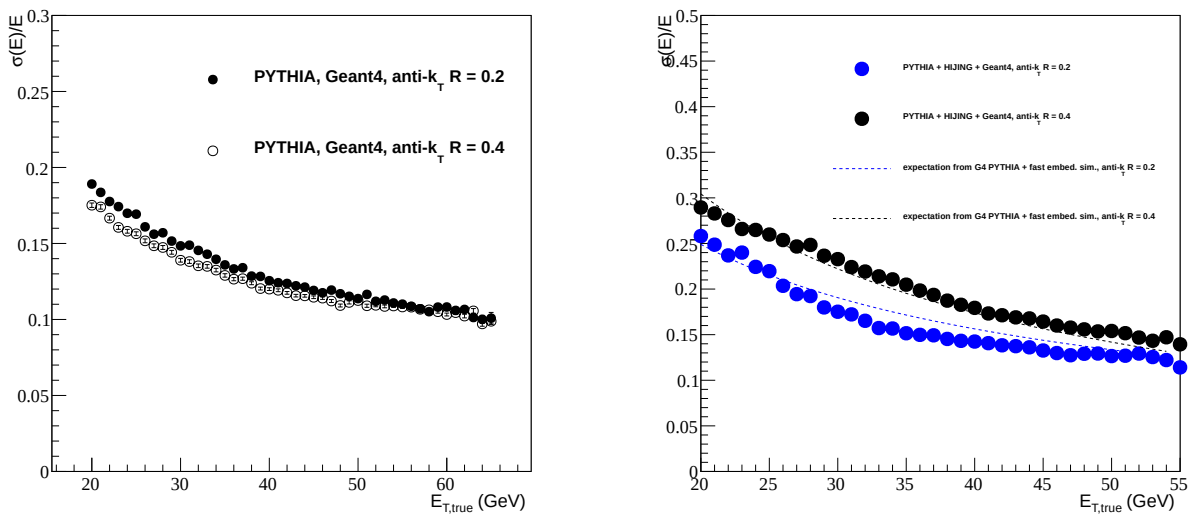

Figure 4.1: (left) The energy resolution of single jets in $p+p$ collisions reconstructed with the FASTJET anti-k_T algorithm with $R = 0.2$ and $R = 0.4$. The particles have been put through a full GEANT4 description of the apparatus. (right) The energy resolution of PYTHIA jets embedded in a Au+Au HIJING event, reconstructed using the anti-k_T algorithm with $R = 0.2$ and $R = 0.4$. The points, showing the result of the full simulation, are compared to the dotted lines, showing the result obtained using the fast simulation.

4.3.1 $p+p$ Inclusive Jet Spectra

In order to model the jet resolution effects described above on the inclusive jet spectra in $p+p$ collisions at $\sqrt{s_{NN}} = 200\,\text{GeV}$, we have used the very fast simulation. This method entails running PYTHIA, sending the resulting final state particles through FASTJET to find jets, and then blurring the energy of the reconstructed jets. We do not impose any detector response on the particles themselves. Instead, the jet energies have been smeared by an energy dependent resolution consistent with values obtained from the full GEANT4 simulation.

The truth spectrum of jets is obtained by using FASTJET to cluster the PYTHIA [110] event with the anti-k_T algorithm. Figure 4.2 shows the true jet p_T spectrum as the solid histogram. The convolution of the hard parton-parton scattering cross section and the high-x parton distribution function results in a jet cross section that falls nearly exponentially over the range 20–60 GeV, before turning steeply downward as it approaches the kinematic limit, $x = 1$.

Figure 4.2 also shows the very fast simulation result for the measured jet p_T spectrum. The main effects of the jet resolution on the jet energy spectrum are to shift it to higher energy and stiffen the slope slightly. Both of these effects can be undone reliably by a process of unfolding. We have employed the ROOUNFOLD [117] package and for this demonstration utilize the Iterative Bayes method with 4 iterations. The results of the unfolding are also

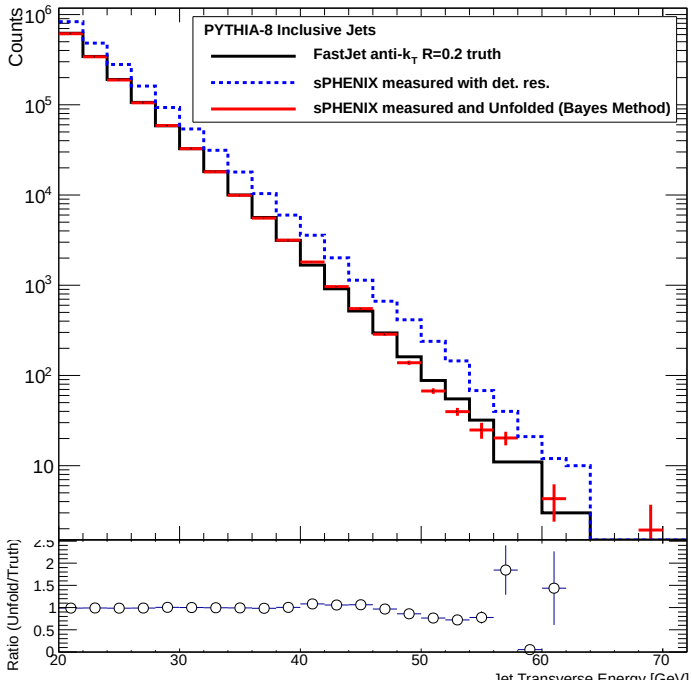

Figure 4.2: Unfolding the effect of finite detector resolution on jet reconstruction in $p+p$ events. The black histogram is the truth spectrum of jets from PYTHIA, the blue dotted histogram is the spectrum after smearing by the jet energy resolution and the red histogram shows the result of using ROOUNFOLD Iterative Bayes method to unfold the detector effects. The lower panel shows the ratio of the unfolded to the true p_T spectrum.

shown in Figure 4.2, along with the ratio of the unfolded to the true p_T spectrum, in the lower panel. The ratio of the two distributions demonstrates that the measurement provides an accurate reproduction of the true jet energy spectrum.

4.3.2 $p+p$ Dijet Asymmetry

The very fast simulation is also used to establish expectations for dijet correlations. Figure 4.3 shows the dijet correlation for PYTHIA events reconstructed using the anti-k_T algorithm with $R = 0.2$. The highest energy jet in the event is taken as the trigger jet and its transverse energy is compared to the transverse energy of the highest energy jet in the opposite hemisphere.

The jet asymmetry $A_J = (E_{T1} - E_{T2})/(E_{T1} + E_{T2})$ for the true jets, reconstructed at the particle level, is shown for leading jets with $E_{T1} > 30\,\text{GeV}$ in Figure 4.3. Also shown is the simulated measurement with the smearing due to the jet resolution included. It is notable that this results in a significant reduction in the fraction of events observed with balanced jet energies (i.e. near $A_J \approx 0$). To date, the ATLAS and CMS dijet asymmetries in Pb+Pb collisions have been published without unfolding for these detector or underlying

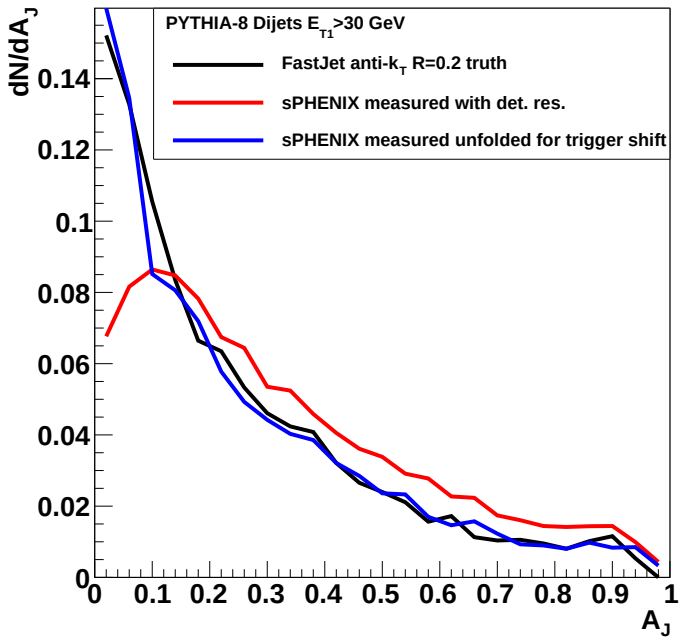

Figure 4.3: Dijet asymmetry, A_J, in p+p collisions. The truth spectrum is shown in black; the spectrum measured in PYTHIA and smeared by the jet energy resolution is shown in red. The effect of the unfolding of the trigger jet bias is also shown in blue.

event effects [61, 62]. A simultaneous two-dimensional unfolding of both the jet energies (i.e., $E_{T1}(\text{meas}), E_{T2}(\text{meas}) \rightarrow E_{T1}(\text{true}), E_{T2}(\text{true})$) is required in this case. Both ATLAS and CMS collaborations are actively working on this two-dimensional unfold, and the sPHENIX group is as well. At RHIC energies, the largest effect is that the trigger jet is being selected from a steeply falling spectrum and is biased by the resolution to be reconstructed higher than the true energy. If one simply shifts the trigger jet down by this average bias (and inverts the identity of trigger and associated jet if the trigger jet energy is then below that of the associated jet), the original dijet asymmetry distribution is recovered, as shown in Figure 4.3. This procedure is not a replacement for the eventual two-dimensional unfolding, but demonstrates the predominant effect.

4.4 Jet Performance in Au+Au collisions

Here we simulate the performance of inclusive jet and dijet observables in heavy ion collisions, where we have focused the bulk of our simulations on 0–10% central Au+Au collisions at $\sqrt{s_{NN}} = 200\,\text{GeV}$. The sPHENIX trigger and data acquisition will sample jets from the full Au+Au minimum bias centrality range, resulting in key measurements of the full centrality dependence of jet quenching effects. Finding jets and dealing with the

rate of fake jets become much easier as the multiplicity due to the underlying event drops, and so we have concentrated on showing that we have excellent performance in central Au+Au collisions (i.e., in the most challenging case).

The keen physics interest in jet observables at collision energies below the top RHIC energy has driven us to evaluate the jet performance also for central Au+Au collisions at $\sqrt{s_{NN}} = 100\,\text{GeV}$. Although the background multiplicity in these events is lower than in corresponding collisions at $\sqrt{s_{NN}} = 100\,\text{GeV}$, the true jet spectrum at the lower collision energy is steeper and we have performed simulations to demonstrate that we can reconstruct jets in this environment.

The effective jet resolution also has a significant contribution from fluctuations in the underlying event in the same angular space as the reconstructed jet. In addition, fluctuations in the underlying event can create local maxima in energy that mimic jets, and are often referred to as fake jets. While resolution effects can be accounted for in a response matrix and unfolded, significant contributions of fake jets cannot be since they appear only in the measured distribution and not in the distribution of jets from real hard processes. Thus, we first need to establish the range of jet transverse energies and jet radius parameters for which fake jet contributions are minimal. Then within that range one can benchmark measurements of the jet and dijet physics observables.

4.4.1 Jet and Fake Jet Contributions

In this section we discuss both the performance for finding true jets and estimations based on HIJING simulations for determining the contribution from fake jets. It is important to simulate very large event samples in order to evaluate the relative probabilities for reconstructing fake jets compared to the rate of true high E_T jets. Thus, we employ the fast simulation method and the HIJING simulation model for Au+Au collisions. The ATLAS collaboration has found that the energy fluctuations in the heavy ion data are well matched by HIJING at $\sqrt{s_{NN}} = 2.76\,\text{TeV}$ [118]. We have also added elliptic flow to the HIJING events used here. The fast simulation takes the particles from the event generator and parses them by their particle type. The calorimeter energies are summed into cells based on the detector segmentation and each tower is considered as a four-vector for input into FASTJET.

Any jet measurements in heavy ion collisions must remove the uncorrelated energy inside the jet cone from the underlying event. Various methodologies have been applied to this problem. The approach developed in our studies is described in detail in Ref. [114]. A schematic diagram of the algorithm (based on the ATLAS heavy ion method) is shown in Figure 4.4. Candidate jets are found and temporarily masked out of the event. The remaining event background is then characterized by the strength of its v_2 (the effect of higher Fourier coefficients was not included in this study) and overall background level in individual slices in pseudorapidity. New candidate jets are determined and the background and v_2 are recalculated. The jet finding algorithm is then re-run on the

background subtracted event to determine the collection of final reconstructed jets. This process is then run iteratively to a convergent result.

In order to distinguish true jets from fake jets we have augmented the HIJING code to run the FASTJET anti-k_T algorithm with the output of each call to the fragmentation routine (HIJFRG). In this way the true jets are identified from a single parton fragmentation without contamination from the rest of the simulated event. The reconstructed jets can then be compared to these true jets. Reconstructed jets which are within $R = \sqrt{\Delta\eta^2 + \Delta\phi^2} < 0.25$ of a true jet with $E_T > 5\,\text{GeV}$ are considered to be matched and those which are not are classified as fake jets. Other estimates of fake jet rates in heavy ion collisions have failed to take into account how the structure of the background fluctuations and the detector granularity affects the probability of any particular fluctuation being reconstructed as a jet. Note that simply blurring individual particles by a Gaussian with an underlying event fluctuation energy results in a substantial overestimate of the fake jet rate, and is not a replacement for a complete event simulation incorporating FASTJET reconstruction with a full jet and underlying event algorithm implementation. Thus, we believe these studies provide an accurate assessment of the effect of fake jets.

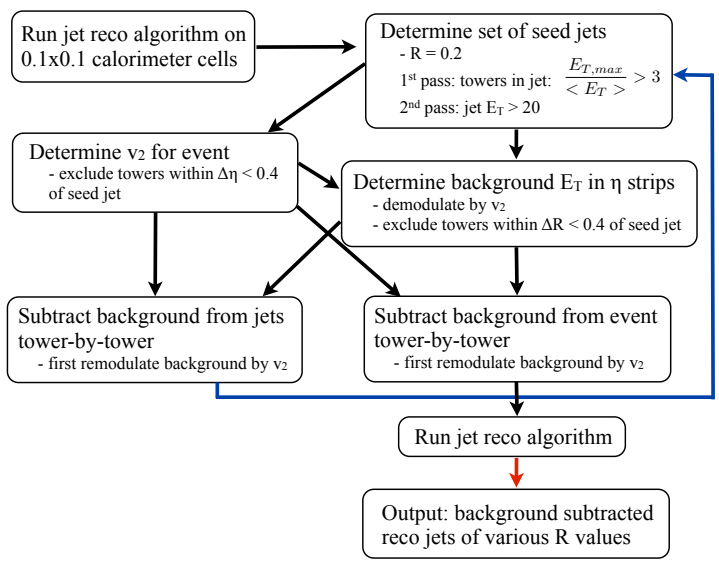

Figure 4.4: Candidate jets are found and temporarily masked out of the event. The remaining event background is then characterized by the strength of its v_2 (the effect of higher Fourier coefficients was not included in this study) and overall background level. A second set of candidate jets are determined and the background and v_2 are recalculated. The jet finding algorithm is then re-run on the background subtracted event to determine the collection of final reconstructed jets. For a detailed description see Ref. [114].

As an illustration of true and fake jets we show two calorimeter event displays in Figure 4.5. True jets at high E_T are a rare occurrence. A large energy background fluctuation at high E_T that mimics a jet is also a rare occurrence. Thus the only way to quantify the impact of fake jets on the jet performance is to run a large sample of untriggered simulated events

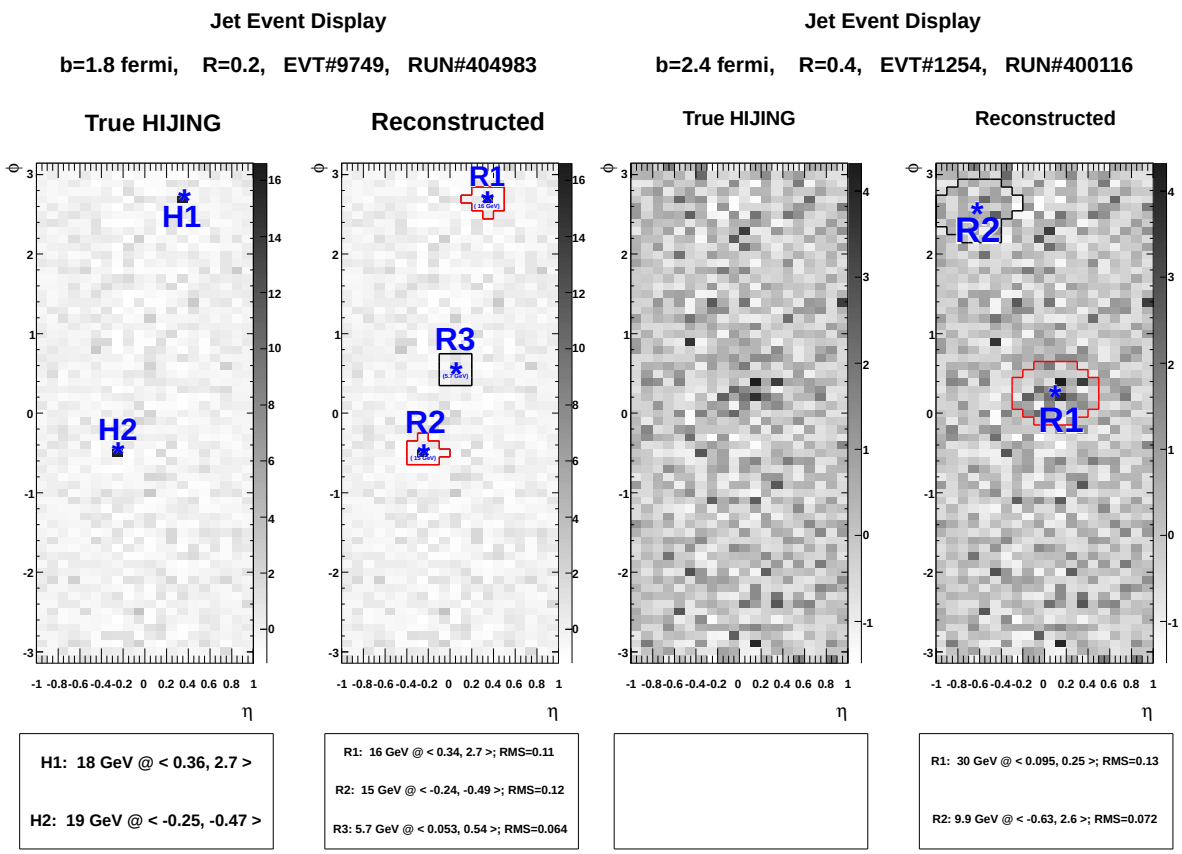

Figure 4.5: Event displays of true and reconstructed jets shown overlaid on background subtracted calorimeter towers from fast simulations. The left event shows a HIJING dijet event where both dijets (labeled H1 and H2) are reconstructed and matched (R1 and R2). A third jet, not matched to a true jet, is also reconstructed (R3). The right event shows a HIJING event with no true jets with $E_T > 5\,\text{GeV}$. Two fake jets are reconstructed, one with $E_T = 30\,\text{GeV}$. From Ref. [114].

and assess the relative probability of true and fake jets as a function of E_T and R.

A sample of over 750 million minimum bias Au+Au HIJING events at $\sqrt{s_{NN}} = 200\,\text{GeV}$ with quenching turned off was used in these studies [114]. The observable particles are binned in η-ϕ cells of size $\Delta\eta \times \Delta\phi = 0.1 \times 0.1$. In these studies [114], we have not included smearing due to detector resolution as it is expected to be a sub-dominant effect and we want to isolate the effects of the underlying event. At the end of this Section we present results including detector resolution that do not change the key conclusions of these studies. The fast simulation result for $R = 0.2$ jets without including detector-level smearing of the jet energies is shown in Figure 4.6. The full spectrum is shown on the left as solid points. The spectrum of those jets that are successfully matched to true jets is shown as a blue curve. That curve compares very well with the spectrum of true jets taken directly from HIJING. The jets which are not matched with true jets are the fake jets, and the spectrum of those jets is shown as the dashed curve. For $R = 0.2$, real jets begin to

dominate over fake jets above 20 GeV. The panels on the right of Figure 4.6 are slices in reconstructed jet energy showing the distribution and make up of the true jet energy. For reconstructed jets with E_T =25–30 GeV, a contribution of fake jets can be seen encroaching on the low energy side of the distribution. For $E_{\text{reco}} > 25$ GeV fake jets are at the 10% level and for $E_{\text{reco}} > 30$ GeV fake jets are negligible. Contributions from fake jets for larger jet cones are shown in Fig 4.7. The true jet rate becomes large compared to the fake jet rate at 30 GeV for $R = 0.3$ and 40 GeV for $R = 0.4$. We note that in one year of RHIC running, sPHENIX would measure 10^5 jets with $E_T > 30$ GeV and 10^4 jets with $E_T > 40$ GeV.

There are various algorithms for rejecting fake jets based on the jet profile or the particles within the jet. These methods applied by the ATLAS experiment significantly reduce the fake rate by an order of magnitude or more, increasing the energy and R values over which it is possible to measure jets. We are currently studying the utility of fake jet rejection, including a simple requirement that there be a charged particle track within the jet radius with $p_T > 2$ GeV/c. These methods may extend the sPHENIX jet measurements to significantly lower E_T, and also provide a tool for evaluating the extent of fake jet contributions.

The efficiency of finding true jets is shown in Figure 4.8. We find $> 95\%$ efficiency for finding jets above 20 GeV reconstructed with $R = 0.2$ or 0.3 and above 25 GeV for jets reconstructed using $R = 0.4$.

Having found the jets in Au+Au with good efficiency and having established that the rate of fake jets coming as a result of background fluctuations are understood and under control, we also need to show that we can reconstruct the kinematics of jets accurately and precisely. This is quantified by the jet energy scale, the average shift of the jet energy between reconstructed and true jets and the jet energy resolution which shows the relative width of the difference between the true and reconstructed jet energies. Results from $R = 0.2$ and 0.4 are shown in Figure 4.9. For both jet radii the jets are reconstructed within 4% of the true energy over the measured range. The jet energy resolution shown in the right panel only includes effects due to the detector segmentation applied and the underlying event resolution. In p+p collisions the resolution for $R = 0.4$ jets is better than for $R = 0.2$ jets because the segmentation can cause jet splitting with the smaller jet cones. In Au+Au collisions the order is swapped because the dominant effect is the additional smearing due to the underlying event.

The fast simulation results described above have been re-run with the inclusion of the detector resolutions as parametrized from the single particle GEANT4 results – detailed in Section 3.4. The results shown in Figures 4.6 and 4.7 remain quite similar with the detector resolution included, though with an overall shift of all the distributions to higher E_T due to the additional blurring on falling spectra. For $R = 0.2$ jets, the smearing due to detector resolution is comparable to the effect of the underlying event and for larger jet cones the effect of the underlying event is found to be much larger than detector resolution effects. Figure 4.10 shows the jet purity (i.e., $S/(S+B)$) for $R = 0.2$ jets as a function of reconstructed E_T. The solid black (red) points correspond to the cases without (with)

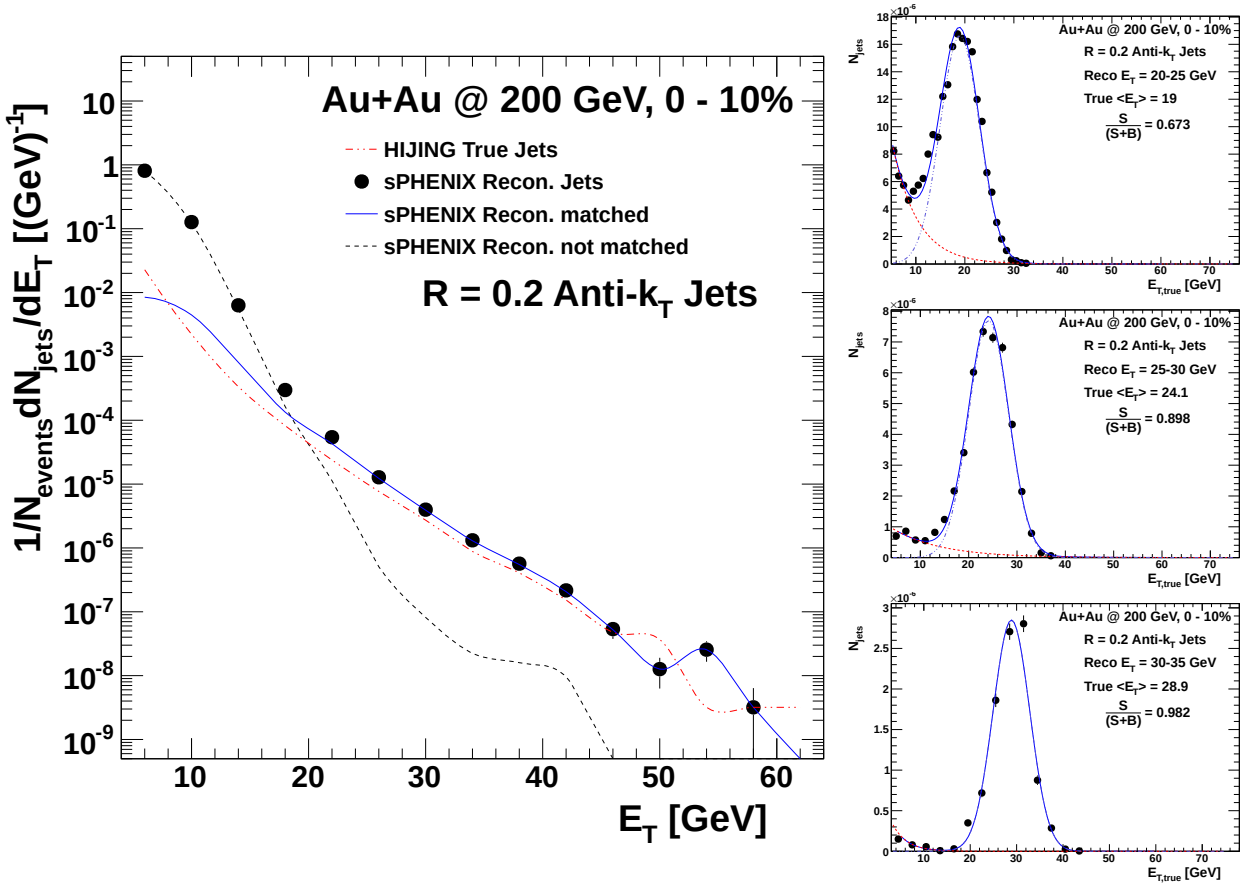

Figure 4.6: The composition of the jet spectrum in central 0-10% Au+Au based on 750M HIJING events. The full spectrum is shown in the left plot as solid points. The spectrum of those jets that are successfully matched to known real jets is shown as a blue curve. That curve compares very well with the spectrum of true jets taken directly from HIJING. The jets which are not matched with known jets are the fake jets, and the spectrum of those jets is shown as the dashed curve. For $R = 0.2$, real jets begin to dominate over fake jets above 20 GeV. The panels on the right are slices in true jet energy showing the distribution and make up of the reconstructed jet energy. At low E_{true}, fake jets can be seen encroaching on the low energy side of the distribution. For higher E_{true} the fake jets are negligible.

detector resolution effects. Also shown as open points are both results shifted down in energy by the average reconstructed energy bias as determined from the reconstructed matched jet sample. One observes that the relative true and fake jet contributions are the same for the equivalent true jet energy ranges.

Jet and Fake Jet Contributions at $\sqrt{s_{NN}} = 100$ GeV

A procedure identical to that used for evaluating the jet finding performance at the top RHIC energy was followed to evaluate the jet finding performance for Au+Au collisions

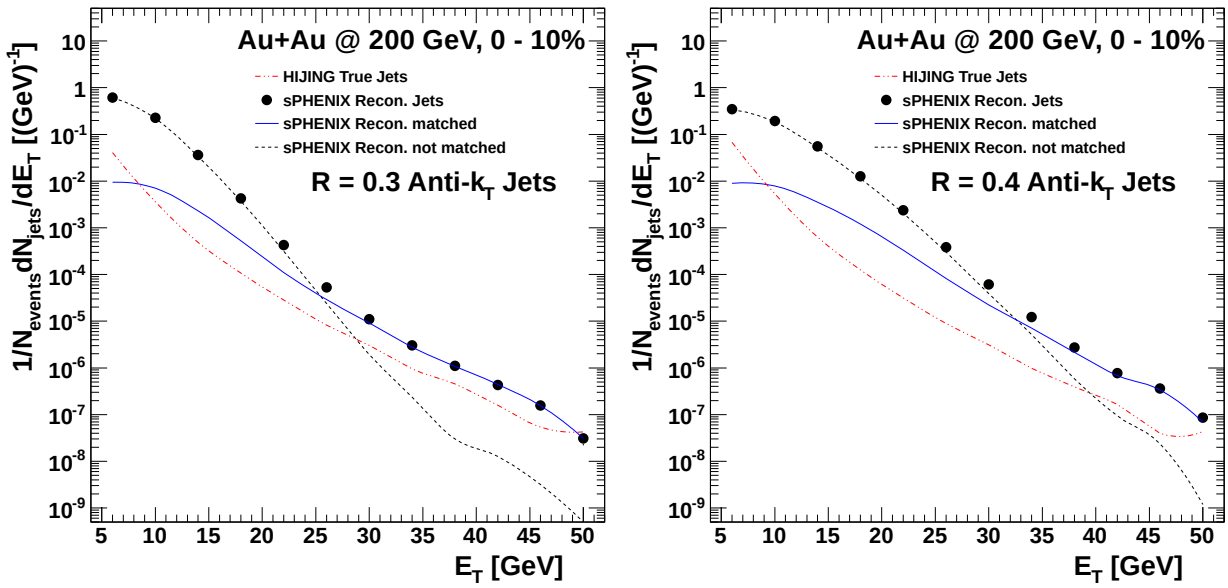

Figure 4.7: Composition of the jet spectra in central 0-10% Au+Au based on 750 million HIJING events for $R = 0.3$ (left) and $R = 0.4$ (right) jets.

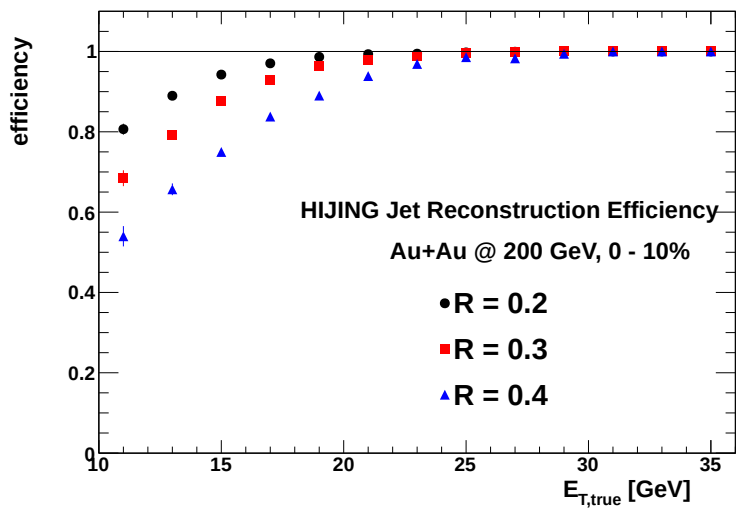

Figure 4.8: The efficiency for finding jets in central Au+Au collisions as a function of true jet energy and for $R = 0.2$, 0.3 and 0.4.

at $\sqrt{s_{NN}} = 100\,\text{GeV}$. A sample of 400 million HIJING events at the lower collision energy was generated and the procedure of Section 4.4.1 was employed. The results are shown in Figure 4.11. The effects of the steeper jet spectrum and of the reduced multiplicity at the lower collision energy work largely negate one another, and the true jet signal dominates over the background at a transverse energy quite similar to that seen for $\sqrt{s_{NN}} = 200\,\text{GeV}$.

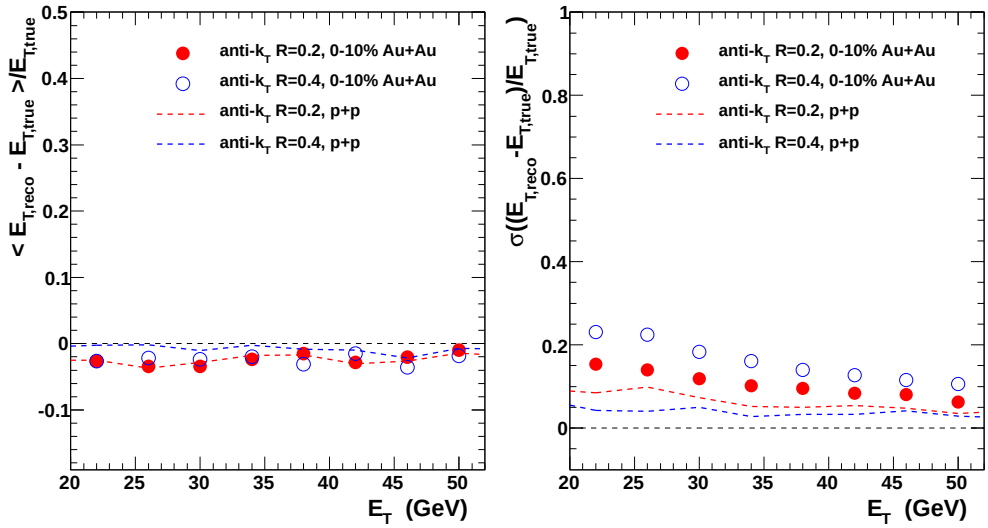

Figure 4.9: The energy scale of reconstructed jets in Au+Au collisions. The left plot shows the shift in the mean energy of the reconstructed jets compared to the true value. There is only a few percent shift in the energy and no apparent dependence on jet cone size. The right plot shows the jet energy resolution. From Ref. [114].

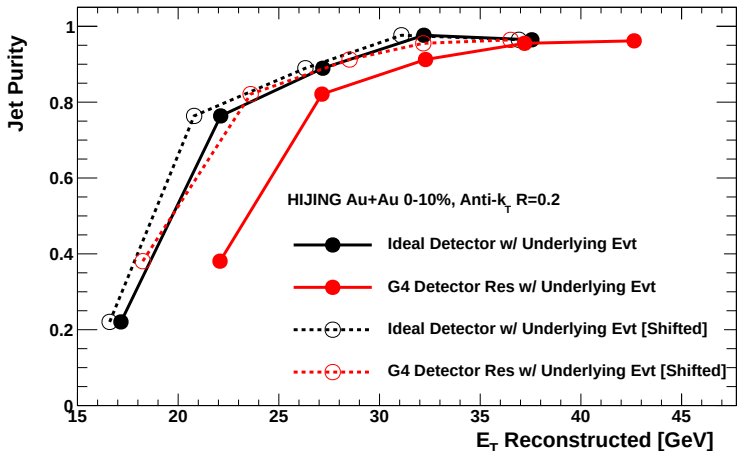

Figure 4.10: Results for the jet purity ($S/(S+B)$) in terms of matched true and fake jets in 0-10% Au+Au collisions from HIJING. The purity values are for a ideal detector (i.e, sPHENIX segmentation with perfect resolution) and then including the GEANT4 parametrized EMCal and HCal resolutions. Both results are then shifted down in E_T by the reconstructed energy bias.

4.4.2 Inclusive Jet Yield in Au+Au Collisions

The inclusive jet spectrum is the most important first measurement to assess the overall level of jet quenching in RHIC collisions. The results shown in Figure 4.12 were obtained by the very fast simulation approach described above. PYTHIA was used to generate events and the final state particles were sent to FASTJET in order to reconstruct jets. The resulting

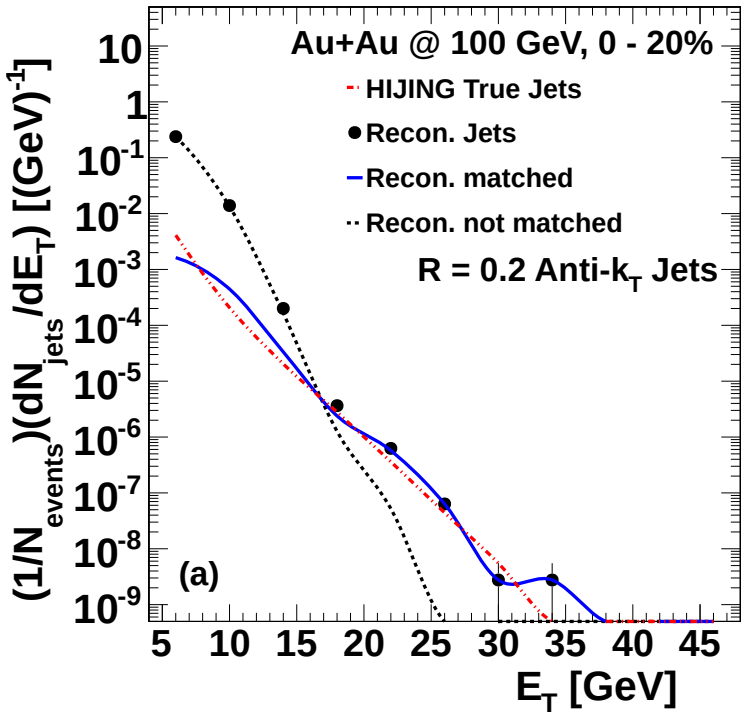

Figure 4.11: Results of a fake jet study at $\sqrt{s_{NN}} = 100\,\text{GeV}$ for the most central 20% of the cross section. The anti-k_T algorithm with $R = 0.2$ was used to reconstruct jets. True jets dominate over fake jets for $E_T > 20\,\text{GeV}$.

jet energy spectrum was smeared by the jet resolution determined for $p+p$ collisions from GEANT4, and an additional smearing by the underlying event fluctuations (determined from the full 0–10% central HIJING fast simulation). Finally, an unfolding procedure was used to recover the truth spectrum. The ratio shown at the bottom of the plot shows that the unfolding is very effective.

As an estimate of the uncertainties on a jet R_{AA} measurement from one year of RHIC running, the uncertainties from Figures 4.3 and 4.12 are propagated and shown in Figure 4.13. For $E_T < 50\,\text{GeV}$ the point to point uncertainties are very small. Also shown is an estimated systematic uncertainty including the effects from unfolding. All points are shown projected at $R_{AA} = 1$, and we show for comparison the predicted jet R_{AA} including radiative and collisional energy loss and broadening from Ref. [81].

4.4.3 Dijets in Au+Au collisions

Fake jets contaminate dijet observables much less than they do the inclusive jet measurement. In the case of inclusive jets, one is working with a sample of 10^{10} central Au+Au events in a typical RHIC year, so even if it is only a rare fluctuation in the background that will be reconstructed as a real jet, there is a huge sample of events in which to look for

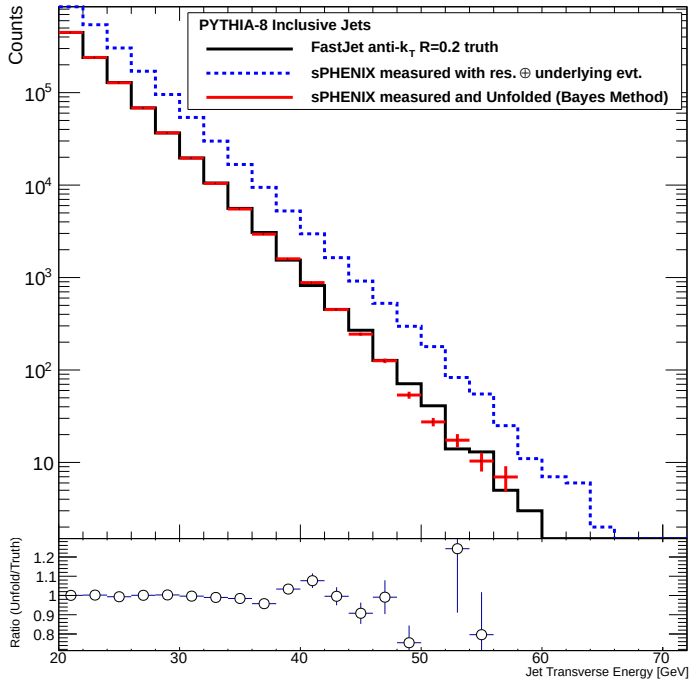

Figure 4.12: Effect of smearing the inclusive jet spectrum in Au+Au collisions. The jets found by FASTJET are smeared by the jet resolution contributions from the detector and the underlying event fluctuations. The unfolded spectrum from the Iterative Bayes method is shown and the ratio of the unfolded to the true p_T spectrum (lower panel).

such fluctuations.

The case of dijet correlations is very different. There are 10^6 clean trigger jets above $E_T = 30\,\text{GeV}$ in central Au+Au collisions in a RHIC year – detailed in Figure 1.1. This means there is a factor of 10^4 fewer chances to find the rare background fluctuation that appears to be a true jet in the opposite hemisphere. Also, the presence of a high energy jet, for which the fake rate is known to be low, tags the presence of a hard process occurring in the event, and thus dramatically reduces the probability of a jet in the opposite hemisphere being a fake. Because of these considerations, one can go to much lower p_T for the away side partner of a dijet pair. Studies presented here include away side jets down to 5 GeV, and we have found that the fake jet rate remains small for the associated jets, even at these low jet energies.

In order to address the sensitivity to modifications of the A_J distributions that might be expected at RHIC here we compare PYTHIA simulations with those from PYQUEN [113] (a jet quenching parton shower model with parameters tuned to RHIC data). All the PYQUEN events generated are for central Au+Au events with $b = 2\,\text{fm}$. Figure 4.14 shows the particle level (i.e truth) A_J distributions and how they are reconstructed after being embedded in a central Au+Au event with a parametrized detector smearing and segmentation applied. As described above, the full iterative underlying event subtraction method is applied. The simulated measured distributions (middle panel of Figure 4.14)

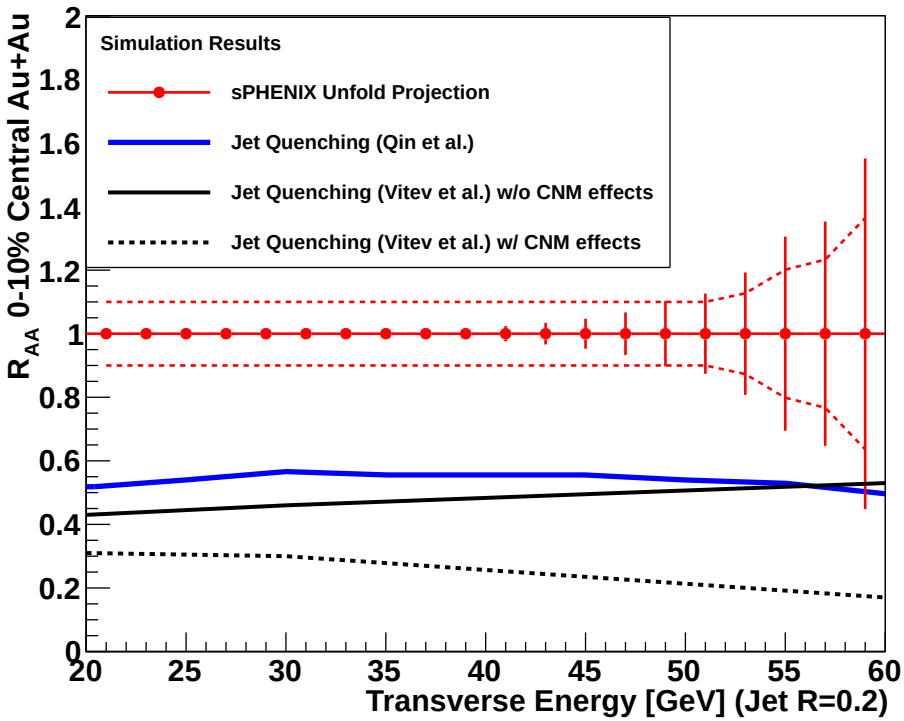

Figure 4.13: Single inclusive jet R_{AA} with $R = 0.2$ for Au+Au central events from the unfolding of the p+p and Au+Au spectra with an estimated systematic uncertainty as a multiplicative factor of approximately $\pm$ 10%. Also shown are the predictions from a calculation including radiation and collisional energy loss and broadening [81] and another with and without cold nuclear matter effects [87, 88, 89] (as discussed in Section 1.6).

show the effects of the smearing; and the distinction between the PYTHIA and PYQUEN distributions remain large. An unfolding procedure can be applied to these embedded distributions to regain the true distributions. However, as in the p+p case discussed in Section 4.3.2 this should involve a full two-dimensional unfolding. Applying the same "unfolding" applied to the p+p case where the smearing of the trigger jet is taken as the dominant effect recovers most of the original distribution, as shown in the lower panel of Figure 4.14. Again, this does not replace a full unfolding procedure, but it does show that the reconstruction is well under control and unfolding will be possible despite the presence of a large fluctuations in the underlying event, after baseline and flow subtraction.

4.4.4 γ+jets in Au+Au collisions

The rate for γ+jet events is lower than the rate for dijet events by about α_{EM}/α_s. In a canonical RHIC year of running one would expect more than 20k direct photons above 20 GeV/c. As shown earlier in Figure 1.22, at p_T = 20 GeV the fraction of direct photons

in the inclusive photon sample is large and γ-jet measurements will be possible without employing isolation cuts. The γ measurement is very clean as fake jets are not an issue for trigger photons. We show fast simulation results for 20k γ triggers embedded in central Au+Au events.

In contrast to the dijet case studied above, the γ-jet measurements do not compare two similar objects with the same effects from the underlying event. The γ is always the trigger. In this case it makes sense to measure $x \equiv E_{\text{jet}}/E_\gamma$ rather than A_J. While in a leading order QCD picture the γ and the jet should exactly balance in energy, in reality this is not the case, especially when higher-order diagrams are taken into account. For small jet sizes there is a significant probability that the away side parton shower is split into more than one jet by the reconstruction procedure, with each carrying a fraction of the energy needed to balance that of the γ. This can be seen in the PYTHIA truth curves in the top panels of Figure 4.15. The smeared and embedded results are shown in the middle panel. Again the smearing has a significant effect, but the distinction between the PYTHIA and PYQUEN results is retained.

In the γ-jet case, the unfolding is to a very good approximation one-dimensional. This is because the dominant smearing effect is on the jet energy since the γ is measured in the EMCal which has a very good energy resolution compared to the jet. We have applied a one dimensional Iterative Bayes unfolding procedure to the γ-jet x distributions for the $R = 0.3$ jets in the bottom panel of Figure 4.15. The unfolded results compare well with the particle level distributions for both PYTHIA and PYQUEN.

4.4.5 γ+hadron correlations in Au+Au collisions

sPHENIX will be able to track charged particles in addition to its calorimetric jet finding capabilities, and this can be used to construct γ+hadron and jet+hadron correlations. This is particularly appealing as a complement to the dijet measurements. At sufficiently low p_T, the background of fake jets for the away-side jet in a dijet analysis becomes problematic. At that same low p_T, one can turn to the capabilities of the existing PHENIX vertex detector tracking system (with moderate momentum resolution) to extend the measurement. Figure 4.16 shows the tracking efficiency and rejection of fake tracks that could be expected in sPHENIX with the existing four layers of the VTX, suitably reconfigured to provide full azimuthal coverage.

One can use γ+hadron correlations to study the redistribution of energy lost by the opposite going parton, and results from CMS [62] on jet+hadron correlations indicate that, at the LHC, this energy is spread over a wide angular range. Measurements at RHIC of γ+hadron correlations have not had the statistical precision or the acceptance necessary to make comparable statements about the modification to jet fragmentation. In order to recover the energy using the standard jet reconstruction, one would have to use an extremely wide jet cone, and in a heavy-ion collision this presents a problem, as it exposes the away side jet finder to a very large contamination of energy coming from the

underlying event. Precisely because of this difficulty, one could instead use correlations between a trigger γ and an away side hadron.

Figure 4.17 shows γ+hadron correlations for photons with $E_T > 20$ GeV from PYTHIA and PYQUEN in the hadron p_T range of 0.5–4.0 GeV/c. This hadron p_T range will be accessible with no additional tracking beyond the existing VTX. The PYQUEN distributions are broader and have a larger yield at lower p_T, and would be easily measured by sPHENIX.

4.5 Summary

Overall we conclude that a robust jet, dijet, and γ-jet program with high statistics is achievable with the sPHENIX detector upgrade. These observables indicate excellent discriminating ability between scenarios with different medium coupling strengths and jet quenching mechanisms.

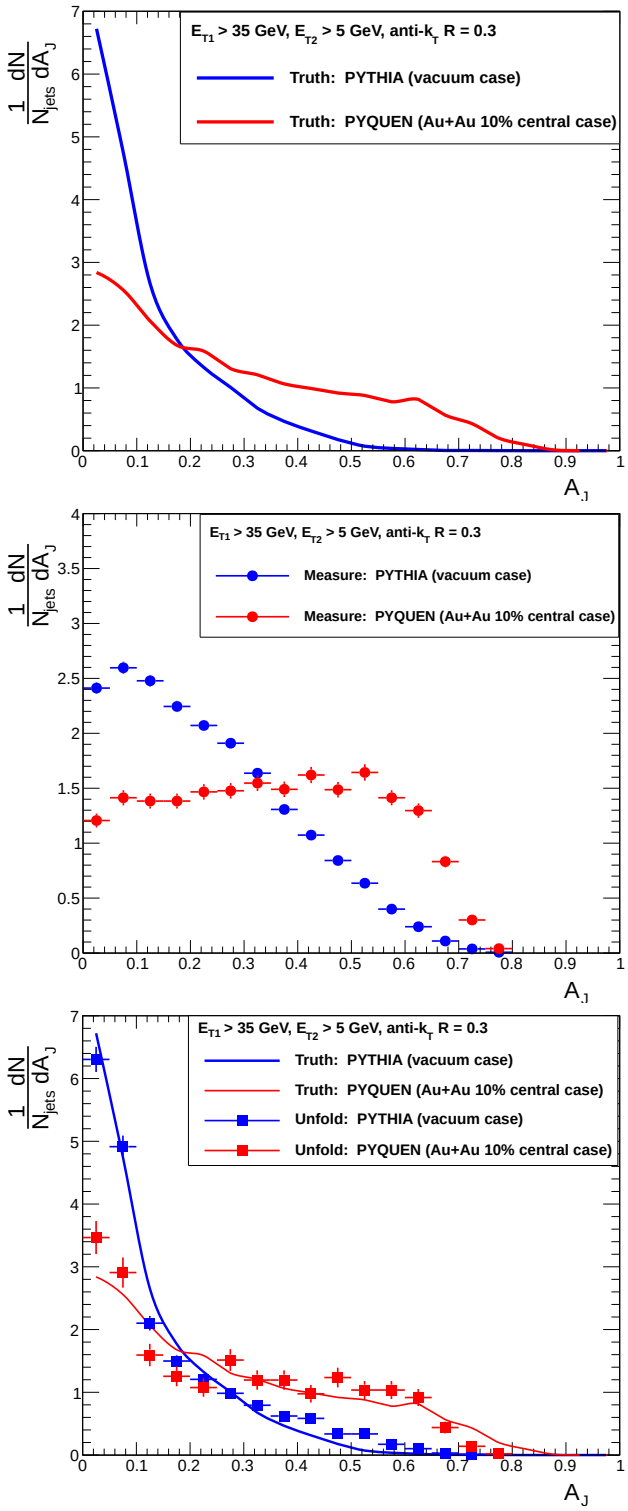

Figure 4.14: The effect of smearing on A_J for $R = 0.3$ jets. The upper panel shows the ratio expected in PYTHIA and PYQUEN, showing the effect of quenching. The middle panel shows the effect of smearing on the ratio determined from jets reconstructed after embedding in Au+Au events. Although smeared, the reconstructed data still show a distinct difference between the quenched and unquenched results. The bottom panel shows the results of the "unfolding" procedure discussed in Section 4.3.2.

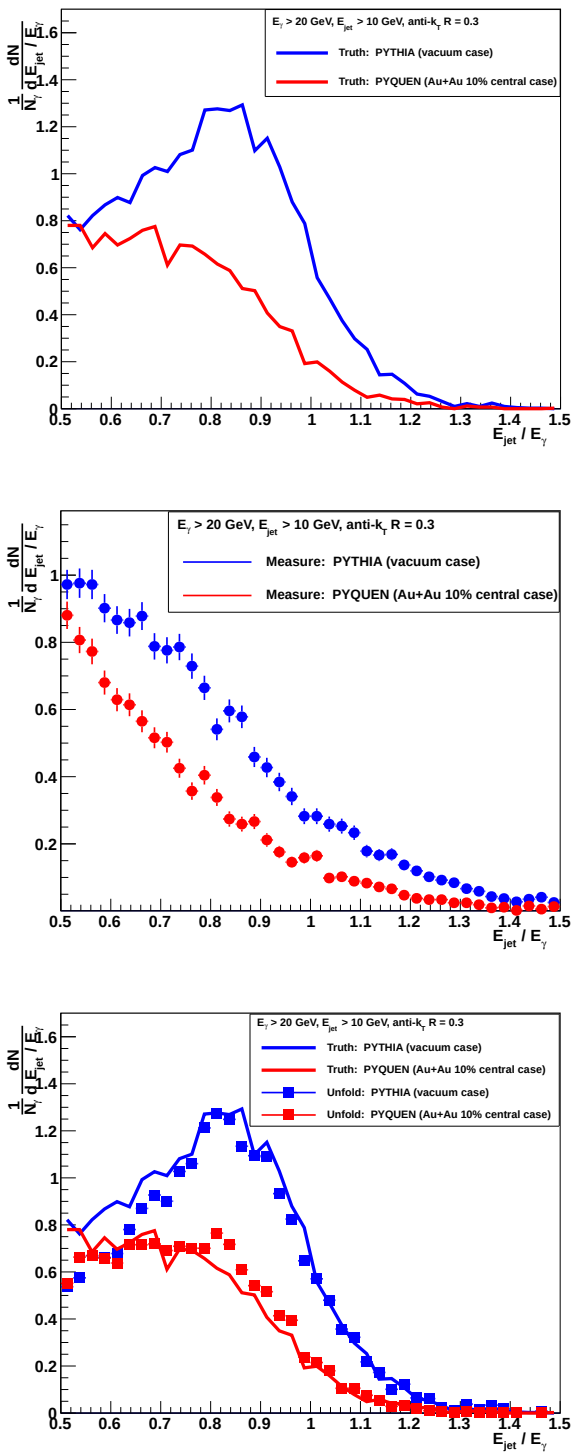

Figure 4.15: The effect of smearing on energy ratio E_{jet}/E_γ for $R = 0.3$ jets. The upper panel shows the ratio expected in PYTHIA and PYQUEN, showing the effect of quenching. The middle panel shows the effect of smearing on the ratio determined from jets reconstructed after embedding in Au+Au events. Although smeared, the reconstructed data still show a distinct difference between the quenched and unquenched results. Results of a one dimensional unfolding are compared with the truth particle level distributions in the bottom panel.

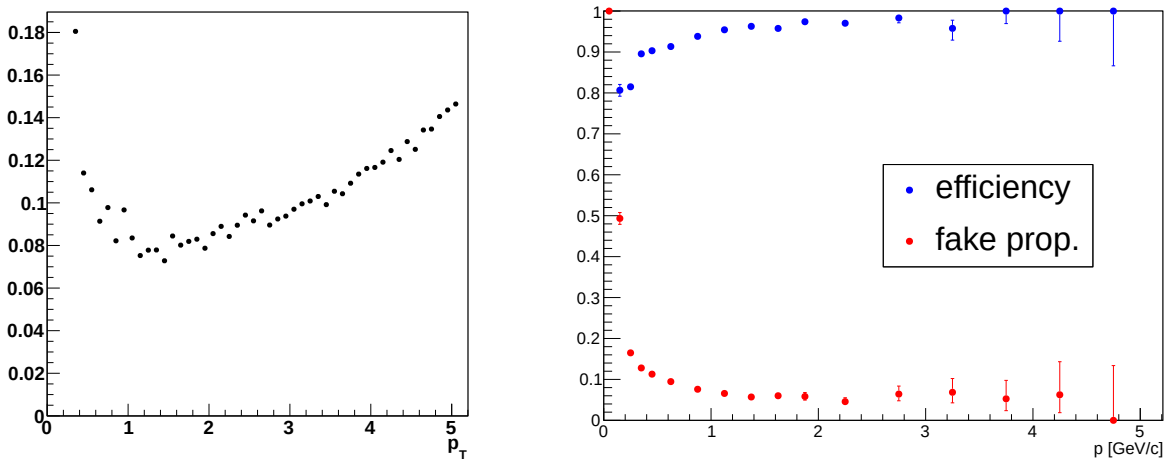

Figure 4.16: The momentum resolution, tracking efficiency and fake track rejection achievable with the existing four layers of tracking provided by the VTX in the 2 T solenoidal field of sPHENIX. The blue points are the fraction of GEANT4 tracks which are reconstructed with 3 or 4 correct hits. The red points are the proportion of reconstructed tracks for which it is not true that at least three hits belonged to the same GEANT4 track.

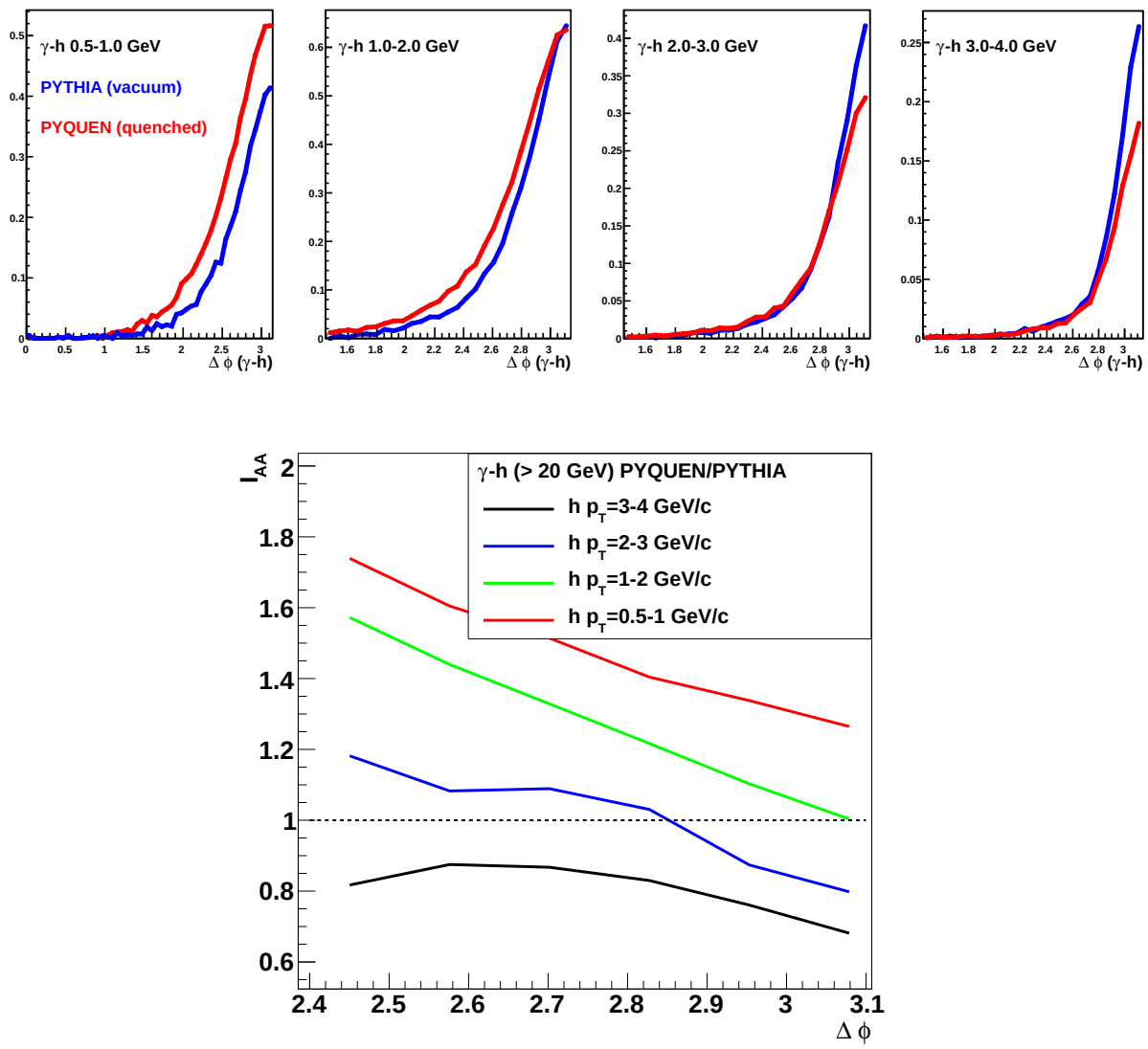

Figure 4.17: A simulation of the γ+hadron angular correlation for PYTHIA and for PYQUEN events for hadron p_T ranges shown in the Figure. These p_Ts would be accessible with the current PHENIX silicon tracker. The lower panel shows the nuclear modification I_{AA} between Au+Au central with PYQUEN and p+p with PYTHIA as a function of hadron p_T and $\Delta\phi$.

Chapter 5

Management, Cost, and Schedule

In this Chapter, we describe the organization of the project, the estimated cost of construction, and the proposed project schedule. The sPHENIX project is expected to have a Total Project Cost (TPC) that exceeds $20M which will require the project to be managed in accordance with DOE Project Management Order 413.3B. In discussion with BNL management, we have formulated a plan for managing the project consistent with the scope of work based on similar projects executed in the BNL Physics Department.

5.1 Management

The sPHENIX construction project will be managed by a project office in the BNL Physics Department. The anticipated WBS project lines and a brief summary of the scope of work are:

1 Magnet Specification and procurement of tested solenoid. Power supply, quench protection and cryogenic integration. Mapping of the magnetic field.

2 Electromagnetic Calorimeter Specification and procurement of tungsten-scintillator modules. Attachment of photosensors to bundled fibers. Testing of completed modules. Assembly into detector support structure. Connection to electronics.

3 Hadronic Calorimeter Design and procurement of steel. Specification and procurement of scintillator and fiber. Assembly of scintillator into wedges and modules. Attachment of photosensors to bundled fibers. Connection to electronics.

4 Electronics Fabrication of analog signal processing boards and bias supply. Fabrication of digitizer system. Low voltage power distribution. Integration of digitizer system with data acquisition. Cabling and cooling.

5 Integration Mechanical support structure, access platforms, electric power distribution, cable management, and modification to safety systems.

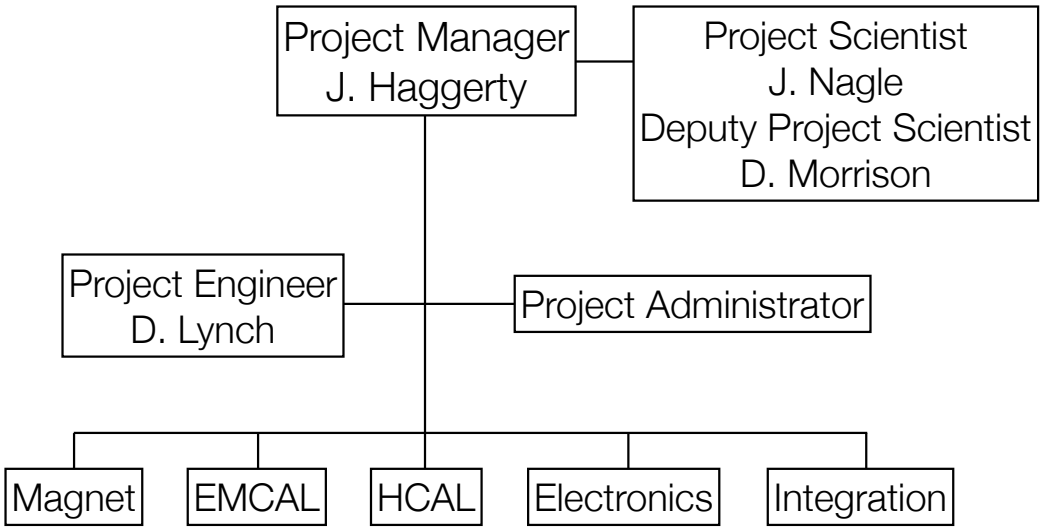

Figure 5.1: Organization chart for sPHENIX project.

The Project Manager will be assisted by the Project Engineer and a project office for administration, contracts, safety, and quality assurance. The Project Scientist and Deputy Project Scientist will advise the Project Manager on the scientific needs of the experiment. The project office will maintain the cost and schedule data to be used to track progress on the project and report to funding agencies. Each of the five major subsystems will have subsystem managers reporting to the Project Manager. An organization chart is shown in Figure 5.1.

The sPHENIX WBS is provided in Table 5.1 and shows the subsystems as currently defined. The Level 2 tasks are the starting point for the cost and schedule effort needed to develop a reviewable cost book and resource loaded schedule.

Manpower for design, engineering, testing, and assembly will come from the existing PHENIX collaboration and any new collaborators. Institutions that have directly expressed interest in participating in the sPHENIX construction project are shown in Table 5.2. Collaborators at these institutions have already participated in the preparation of this proposal, the pre-conceptual design of the detector and electronics, and in the simulation of the detector performance. As is the case in PHENIX, collaborators not directly involved in detector construction will provide a variety of support functions including maintenance, calibration, and data production.

Although not part of this proposal, future optional upgrades for sPHENIX could include additional tracking and a preshower detector as detailed in Appendix 6. RIKEN has

WBS Line	
1	sPHENIX Project
1.1	Magnet System
1.2	Electromagnetic Calorimeter System
1.3	Hadronic Calorimeter System
1.4	Electronic Systems
1.5	System Integration
1.6	Project Management

Table 5.1: WBS at Level 2.

expressed very strong interest in contributing to this effort on a scale similar to the RIKEN contribution to the existing PHENIX VTX detector.

5.2 Research and Development

Development of this proposal has been and will continue to be supported by RHIC detector R&D funding. PHENIX detector R&D funding has been used to support work at a number of institutions on the electromagnetic and hadronic calorimeter. Ohio University has constructed a testbed calorimeter that has allowed a beam test of an easily reconfigurable calorimeter module for comparison with GEANT4 simulations, and work at the University of Colorado has begun measuring light collection in scintillator with embedded wavelength shifting fiber. The Brookhaven group has initiated R&D on the electromagnetic calorimeter which is supplemented by a DOE Small Business Innovation Research (SBIR) grant. The 2012 Phase I award describing the grant states:

> "The proposed research effort would fabricate custom accordion shaped tungsten sheets. In the future, these preformed absorber plates will provide a simple and inexpensive material for the construction of large scale particle detectors in nuclear, high energy and space physics experiments, and for shielding purposes. It may also find commercial applications in x-ray instrumentation, medical imaging, baggage and container inspection, and material analysis."

	Institutions
Magnet	BNL; Los Alamos National Laboratory; Sungkyungkwan University (SKKU), Korea; Yonsei University, Korea
EMCal	Baruch College; BNL; IHEP Protvino, Russia; Oak Ridge National Laboratory; Stony Brook University; University of Tennessee
HCal	Abilene Christian University; Augustana College; BNL; Columbia University; Lawrence Livermore National Laboratory; Muhlenberg College; Ohio University; University of Colorado
Electronics	BNL; Columbia University; Iowa State University; Oak Ridge National Laboratory; University of Tennessee
Future option: additional tracking and preshower	BNL; CNS, Tokyo; Florida State University; Hiroshima; Iowa State University; KEK; RIKEN BNL Research Center; Tsukuba; University of Tokyo

Table 5.2: Institutions expressing interest in participating in the construction of sPHENIX and possible future enhancements. The future option is described in detail in Appendix 6.

Simulation of the detector response to single particles and jets is a priority, and Christopher Pinkenburg, PHENIX Simulation Coordinator, has led the development of a new simulation framework for sPHENIX based on GEANT4 which has been used in the preparation of this proposal. A wide range of institutions in the PHENIX collaboration have contributed to this effort, with notable contributions from Brookhaven, Iowa State University, Florida State University, the University of Colorado, Lawrence Livermore National Laboratory, and Stony Brook University

Since much of the proposal reuses existing PHENIX components such as power supplies, trigger, data acquisition, and the electronics concepts are designed to be compatible with PHENIX, a great deal of development has been done as part of support for PHENIX and its current upgrades. For example, electronics initially developed for the Hadron Blind Detector (HBD) has been reused by the Muon Piston Calorimeter (MPC), which uses APD's to read out $PbWO_4$ crystals in PHENIX. This electronics can be adapted for readout and testing of EMCal and HCal prototypes. The Magnet Division has assisted us by adapting the specifications for the superconducting solenoid purchased for the RHIC electron lens to the spectrometer solenoid. In this way, we plan to carry the pre-conceptual design as far as possible to minimize engineering needed to construct sPHENIX.

Internal review of the proposal resulted in a recommendation that two full sized prototype detectors be constructed. The first round of prototype detectors is already under way using R&D and SBIR funding as has been described, and a "Prototype and testing" line is meant to cover the costs of building the pre-production prototype detectors.

5.3 Cost

A preliminary cost for the project has been determined. The estimated costs for the major components of the experiment are shown in Table 5.3. The costs have been estimated from budgetary quotes as much as possible, or information based on recent acquisitions of similar equipment, as detailed in the following section. Overhead rates consistent with BNL FY12 rates have been applied to all the estimated costs, and a 40% contingency has been applied to all costs.

5.3.1 Equipment Cost

Magnet

Initially, the cost of the solenoid was estimated using a scaling law for the cost of DOE procured superconducting magnets [96]. This scaling law provided a tool to estimate the cost of the magnet based on documented costs of previously constructed superconducting solenoid spectrometer magnets procured by DOE laboratories. After simulation and evaluation of solenoids within the cost range expected for the proposal, a Request For Information was posted by the BNL Procurement and Property Management Division which resulted in several expressions of interest and one budgetary quotation. The budgetary information provided was from Ansaldo Superconducting Group (ASG), which has built many successful superconducting magnets for experiments.

The required solenoid and cryostat is of modest scale and similar in specofications to superconducting solenoids built for the D0, CDF, CLEO, and BaBar experiments. Recent difficulties with acquisitions of superconducting magnets suggest that it would be prudent to assign a 100% contingency to the cost of the solenoid, and to budget for engineering oversight from the laboratory during the specification, design, construction, and installation of the solenoid, so approximately Integration and Mechanical costs include approximately two months of on-project engineering for each year from FY14 to FY18.

Electromagnetic Calorimeter

Development of the tungsten-scintillator accordion has been funded under an SBIR with Tungsten Heavy Powder, which has produced a cost estimate for completed modules. The

total cost is dominated by the cost of tungsten and epoxy, and includes the labor costs for assembling scintillator sandwiches. A one time cost for tooling and molds is included, so the estimate is for completed calorimeter modules.

Several variations of fiber are being considered and are under test (single and double cladded, round and square fiber) and selection of the fiber will take account of the cost ramifications. A recent purchase order for small quantities of 1 mm fiber have a cost range of $1.8/m to $3.5/m. In quantities necessary for sPHENIX, we estimate a cost of approximately $1/m.

Hadronic Calorimeter

The cost of the hadronic calorimeter is dominated by the cost of the tapered steel plates. Engineering drawings of the plates were used by the vendor to estimate the cost of machining plates to meet our specifications. This vendor has produced large steel components for a number of experiments (including PHENIX) at Brookhaven and Fermilab. A number of alternative manufacturing techniques are being considered for plates which could reduce the cost, but this estimate, which amounts to approximately $4.15/lb, is in line with the expected cost of machined steel parts.

The cost of the scintillator has been estimated from a budgetary quotation for scintillator for the hadronic calorimeter by Technoplast (Vladimir, Russian Federation). The scintillator would be manufactured with a reflective coating and grooved for insertion of wavelength shifting fiber by the manufacturer. The estimated cost amounts to approximately $43/kg. The cost of the fiber is estimated to be the same as for the EMCAL.

Electronics

The cost of SiPM sensors is estimated from a budgetary quotation from Hamamatsu, and so we use the estimated cost in quantities of 30k parts for the catalog SiPM (Hamamatsu 10362-33-025C) whose performance is reasonable for the detector. An alternate readout option using Avalanche Photodiodes (APD's) has also been investigated and has been estimated to have similar or lower cost.

The cost of the front end bias supply and analog signal processing is based on either a simple design now undergoing prototype testing, or adapting an ASIC being developed for the ALICE experiment which could be available in large quantities by the time the design is finalized. The higher cost solution is selected for the purpose of estimating the cost.

The cost of the digitizer system is based on the cost of a very similar system used for the retired Hadron Blind Detector, and so the costs are well understood. Testing can be carried forward with electronics retired from that detector.

		Cost	Overhead	Contingency	Total
Magnet	solenoid	3.60	0.34	3.94	7.87
	cryo/power supply	0.20	0.10	0.12	0.43
EMCal		2.80	0.49	1.32	4.61
	tungsten	2.30			
	scintillator	0.50			
HCal		3.65	0.64	1.72	6.01
	inner steel	0.60			
	inner scintillator	0.10			
	outer steel	2.65			
	outer scintillator	0.30			
Electronics	$117/channel	3.25	0.57	1.53	5.35
Integration/Mechanical		1.80	1.14	1.17	4.11
Calibration Systems		0.10	0.05	0.06	0.21
Prototype detectors		0.25	0.13	0.15	0.53
Total Overhead					3.46
Total Contingency					10.01
Total					29.12

Table 5.3: Estimated equipment costs for the sPHENIX detector (in M$).

5.3.2 Labor Cost

The labor costs of constructing the sPHENIX detector have been estimated by assuming

	FY14	FY15	FY16	FY17	FY18	Total
Capital equipment (M$)	2	8	8	8	3.1	29.1
Redirected labor (M$)	0.3	1.1	1.1	1.8	2.00	6.3

Table 5.4: Spending profile for construction and procurement of major components, and profile for redirected labor from PHENIX operations group to construction in fully burdened at-year dollars.

	FY14	FY15	FY16	FY17	FY18	Total
Redirected labor	1.1	3.7	3.7	7.5	8.3	24.3
Collaboration labor (U.S. FTE's)	4.0	4.0	4.5	4.5	4.5	22.5
Collaboration labor (non-U.S. FTE's)	2.0	4.0	4.0	4.0	4.0	18.0

Table 5.5: Total estimated labor from domestic and foreign collaboration sources to sPHENIX construction.

that the construction tasks will largely be carried out by redirected labor by the PHENIX Operations Group. This group consists of engineers and technicians, whose effort over an assumed construction period from FY15–FY18 will gradually move from support of the existing PHENIX detector and its current upgrades to design, engineering, and assembly of the sPHENIX detector. The required fully burdened costs in at-year dollars estimated during the construction are shown in Table 5.4. The total cost of redirected labor is estimated to be approximately $6.3M. The plan assumes that this effort will be funded through a reprogramming of a fraction of PHENIX Operations labor redirected to the design and construction of sPHENIX. Approximately 40% of the $6.3M redirected labor is engineering. Since the superconducting solenoid is expected to be purchased as equipment, a substantial fraction of the cost of the solenoid is the engineering carried out by the vendor, however approximately $0.8M engineering oversight of the magnet design and construction has been allocated as part of the Integration cost line.

We show the estimated labor component of the project from all sources in Table 5.5. The first line ("Redirected labor") is the labor whose value is estimated in Table 5.4 converted to FTE's. The lines of "Collaboration labor" are an estimate of the equivalent FTE's of effort by scientists, engineers, and postdoctoral research associates in the PHENIX collaboration that would contribute to sPHENIX construction through work on assembly and testing, for example.

5.3.3 Support from Existing Infrastructure

Since the sPHENIX detector is designed to take advantage of existing infrastructure built up in the PHENIX facility over more than a decade, some costs normally expected in a project of this scope will be covered by reuse of existing facilities. Specifically, costs for electrical power distribution, safety systems, data acquisition, most of the generic trigger system, online computing, some of the modifications to the RHIC cryogenic system, and installation of the detector in the collision hall are expected to be minimized by redeployment of existing parts of the facility.

5.4 Schedule

The project Total Project Cost (TPC) is greater than $20M, so it is subject to the guidelines of DOE Project Management Order 413.3B and must obtain Critical Decisions. Based on the schedule for budget decisions in the DOE, Office of Nuclear Physics, the earliest start for construction funding would be FY15. This is an aggressive schedule, but we consider pursuit of this program of measurements an urgent scientific priority, and so we describe a schedule which leads to most timely completion. A proposed schedule for the DOE Critical Decisions is:

CD0 2QFY13 Based on review of this proposal and additional documentation deemed necessary as a result, the physics case could be approved in the spring of 2013. With CD0 approval, R&D funds can be expended and Project Engineering and Design (PED) funds can be requested. Funding from CD0 will appear as part of the Total Project Cost (TPC).

CD1 1QFY14 CD1 approval is required before expending PED funding. Upon completion of R&D funding, a Technical Design Report with a rather complete design should be available.

CD2/3 1QFY15 A year or less of engineering on the project will bring it to a baseline design which can be reviewed for CD2. CD3 approval is required to request construction funding which could then begin for some long lead time items, like the solenoid, in 2QFY15.

CD4 4QFY18 The construction project would be complete after 3.5 years of construction funding. Project completion is the assembly of all detector components to the point at which installation of the detector in the PHENIX Collision Hall can commence.

The sPHENIX detector is designed to reuse as much of the existing PHENIX infrastructure and components as possible, and develop new detectors which take advantage of technological progress to build an experiment which is well matched to the anticipated

physics program at RHIC. The calorimeters are built from components which are specified conservatively to mitigate technical and schedule risk and reduce cost. The schedule, while aggressive in order to meet the physics need, can be achieved by the experienced PHENIX collaboration and its technical support team.

Chapter 6

Midrapidity Tracking and Preshower Upgrades

The sPHENIX midrapidity magnetic solenoid with electromagnetic and hadronic calorimeters can be substantially augmented in physics capabilities through modest incremental upgrades that have been considered from the beginning of the sPHENIX design. In this Chapter we discuss two specific future option upgrades: (1) additional charged particle tracking layers outside the existing PHENIX silicon vertex detector (VTX) and (2) a preshower with fine segmentation just inside the magnetic solenoid. An engineering drawing of the location of these future option upgrades is shown in Figure 6.1. We then detail how these additions expand the sPHENIX physics program to include the following: (a) heavy quarkonia suppression via the three Y states, (b) tagging of charm and beauty jets, (c) jet fragmentation function modifications, (d) nuclear suppression of π^0 yields up to $p_T = 40\,\mathrm{GeV/c}$, and (e) a possible low to intermediate mass dilepton program.

Our goal is to have these upgrades installed and available for physics on day-one, and toward that goal we are pursuing funding through proposals to US-Japan, RIKEN and JSPS. The nature and interests of these potential funding sources is rather different, and that is reflected in the different proposals. RIKEN has expressed an interest in the tracking upgrade. A proposal is being prepared for FY'13 to US-Japan; if funded, that proposal would likely cover elements of R&D related to a pre-shower detector for the electromagnetic calorimeter and support for research. A proposal to JSPS for 5 years of funding is also being pursued.

6.1 Charged Particle Tracking Extension Upgrade

The current PHENIX silicon vertex tracker (VTX) consists of two inner layers (pixels) at radii 2.5 and 5 cm from the beamline and two outer layers (strip-pixels) at radii of 10 and

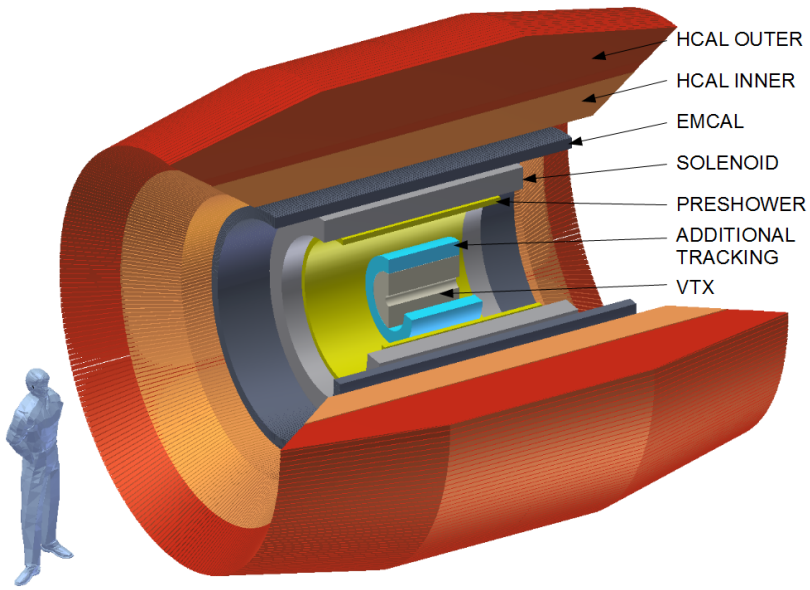

Figure 6.1: Engineering drawing of the sPHENIX upgrade including two future option upgrades (additional tracking and a preshower detector inside the magnetic solenoid and electromagnetic calorimeter).

14 cm. Currently in PHENIX standalone tracks (in the VTX only) are determined with a momentum resolution of $\Delta p/p \approx 0.1 + 0.02 \times p$ [GeV/c]. The sPHENIX magnetic field will have an appreciably larger strength (2.0 Tesla) than the current PHENIX axial field magnet (0.8 Tesla). However, simulations from the current PHENIX VTX indicate that even with the larger sPHENIX magnetic field, there will be significant fake track contributions (i.e. picking up incorrect VTX hits and thus reconstructing to the incorrect momentum vector) for $p_T > 5$ GeV/c. In addition, with only four hits, reconstructed tracks at large Distance of Closest Approach (DCA) have substantial fake track contributions. In the current PHENIX detector, these fake contributions are removed by the required matching to the outer tracking Drift Chamber and Pad Chamber hits. In the sPHENIX proposed in this document with only the VTX for tracking, one will be limited to charged particle tracks with $p_T < 5$ GeV/c and without heavy flavor tagging via displaced vertices (the VTX by itself will not be able to discriminate sufficiently against fake tracks).

Thus, the sPHENIX future option upgrade incorporates additional precision tracking in the radial space from 15–65 cm (inside the new magnetic solenoid). The technology and exact number of layers or space-points has not been determined at this time.

In order to design in this upgrade option, we have done a full GEANT4 simulation with two additional silicon tracking layers at radii of 40 and 60 cm. We have assumed a strip design with 80μm $\times$3 cm, which results in 1.0 (2.2) million channels in the inner (outer)

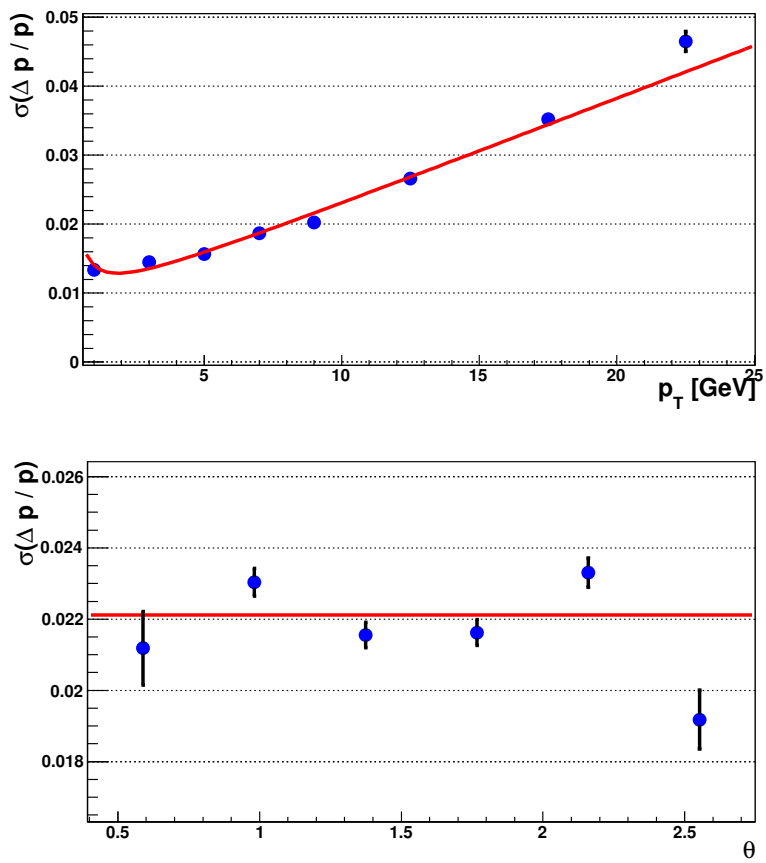

Figure 6.2: GEANT4 and track model evaluation of single particle momentum resolution. From a fit to the data in the upper panel, shown as a red line, we determine the momentum resolution to be $\Delta p/p = 0.007 + 0.0015 \times p$. The lower panel shows the momentum resolution as a function of the polar angle of the track.

layer. The material thickness of the intermediate layer at 40 cm must be thin (of order 0.03 radiation lengths) to reduce multiple scattering and deliver good momentum resolution. We have implemented a full pattern recognition algorithm and track reconstruction model based on software development for the existing VTX. The momentum resolution shown in Figure 6.2 has an RMS $\Delta p/p = 0.007 + 0.0015 \times p$ for momentum with $p_T > 1\,\mathrm{GeV/c}$. Also shown is the momentum averaged resolution as a function of polar angle θ. In order to have good separation of the three Υ states ($\Upsilon(1s), \Upsilon(2s), \Upsilon(3s)$) — crucial to the physics of the color screening length — we need the term linear in the momentum to be less than 0.002.

We have also studied the effect of the additional layers on the tracking efficiency and rejection of fake tracks that could be expected in sPHENIX. Figure 6.3 shows these aspects of the performance as a function of the transverse momentum of the embedded track. This

should be compared with Figure 4.16, which shows the performance one could expect with only the existing four layers of the VTX in place.

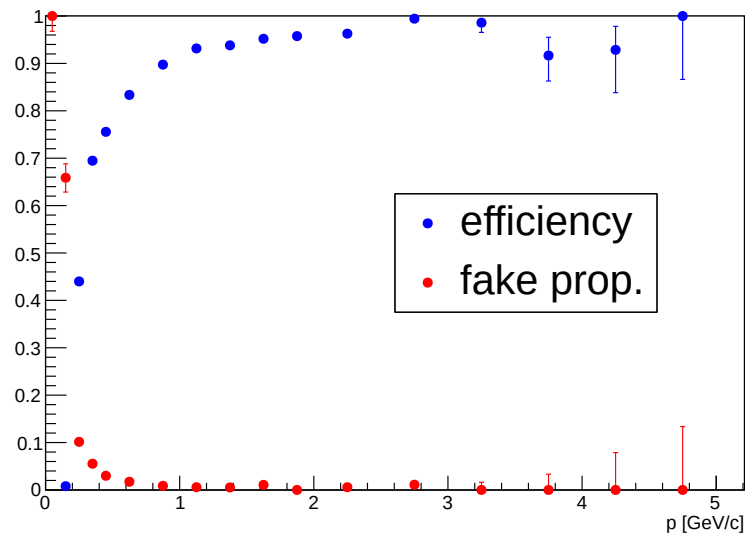

Figure 6.3: The tracking efficiency and fake track fraction that results from augmenting the existing VTX with two additional layers of tracking in the sPHENIX solenoidal field. The blue points are the proportion of the GEANT4 tracks which are reconstructed with 5 or 6 out of 6 correct hits. The red points are the proportion of reconstructed tracks for which it is not true that at least 5 hits belonged to the same GEANT4 track.

The inner four VTX layers are currently arranged without full 2π coverage, and would need to be re-configured and augmented to do so. The outer layers in principle could be a similar silicon design to the outer two VTX layers. The exact number of layers and technology choice required in terms of Au+Au central pattern recognition efficiency, fake track rates, and charm/beauty tagging via displaced vertices is currently under study.

6.2 Preshower Detector

The sPHENIX proposed electromagnetic calorimeter has a segmentation of $\Delta\eta \times \Delta\phi = 0.024 \times 0.024$ and thus has relatively good separation of single photons from $\pi^0 \to \gamma\gamma$ decays up to approximately 10 GeV. A preshower layer in front of the magnetic solenoid and the electromagnetic calorimeter can extend this separation up to $p_T > 50\,\mathrm{GeV/c}$ (essentially the entire kinematic range of measurements possible within the luminosity limits). In addition to separating single from double overlapping showers, the preshower can provide significant additional electron identification capability. As we discuss later, the combined pion rejection (i.e. electron identification) from the sPHENIX electromagnetic calorimeter and the preshower are sufficient for excellent Υ measurements.

Again, the exact design and technology for this preshower detector is under active investigation and simulation. For the purposes of understanding the basic performance and design constraints on the sPHENIX upgrade (e.g. the magnetic solenoid radius), we have implemented a GEANT4 configuration with a 2.3 radiation length thickness of tungsten backed by a silicon layer with strips 300 μm $\times$6 cm as a pre-sampler. The detector sits just after the outermost tracking layer and before the magnetic solenoid. The segmentation corresponds to $\Delta\eta \times \Delta\phi = 0.0005 \times 0.1$. We are still investigating whether two layers of perpendicular strips are necessary for the physics performance in all channels (particularly the efficiency for tagging two photons from a very high p_T π^0 decay). Shown in Figure 6.4 (left panel) is an event display of the energy deposition from a 42.8 GeV π^0 in the preshower, with clear separation of the two initiated photon showers. Shown in Figure 6.4 (right panel) is the response of the electromagnetic calorimeter total energy versus the preshower energy for electrons and charged pions. The combination of information provides a powerful discriminator for electron identification. Even if the charged pion induces a hadronic shower in the electromagnetic calorimeter, it has a much lower probability for that interaction occurring in the first layer of tungsten of the preshower. Initial studies indicate a charged pion rejection of order 100–200 with good electron efficiency for $p_T > 2$–$3\,\mathrm{GeV/c}$.

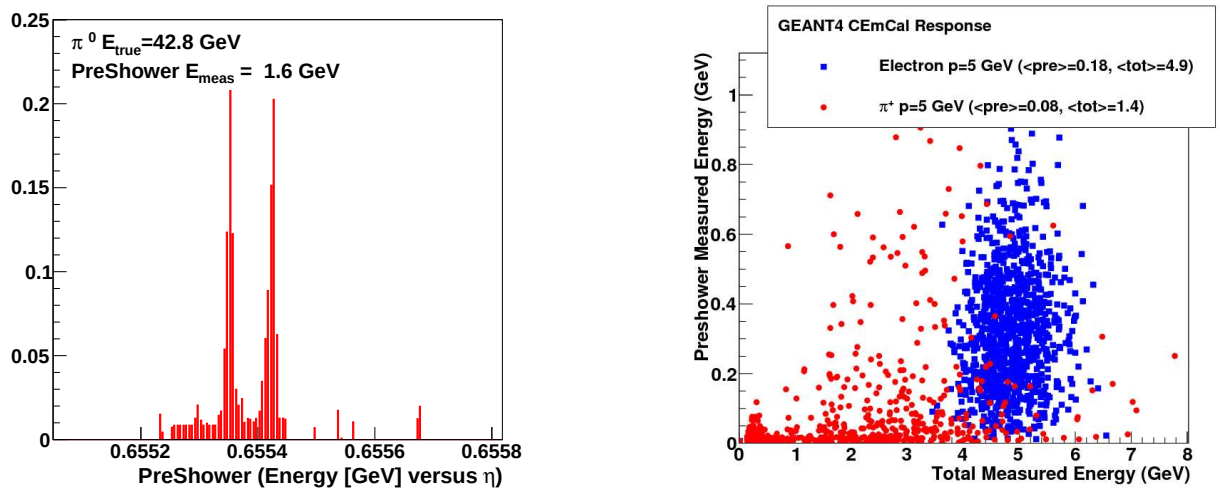

Figure 6.4: (Left Panel) GEANT4 example preshower energy distribution for a single 42.8 GeV π^0. (Right Panel) GEANT4 simulation examining the electron to π^- separation for $p_T = 5\,\mathrm{GeV/c}$.

6.3 Quarkonia Spectroscopy of the Upsilon States

We have investigated the feasibility of using the sPHENIX detector, with the addition of outer tracking layers and additional electron identification capability, to make high quality

Υ measurements at $\sqrt{s_{NN}} = 200\,\text{GeV}$. We conclude that a world class Υ measurement is possible, with separation of the three states and statistical precision comparable with that of the LHC experiments. In this section we discuss the physics motivation for these measurements, and summarize the expected performance.

6.3.1 Physics Motivation

An extensive program of J/ψ measurements in A+A collisions has been carried out at the SPS ($\sqrt{s_{NN}} = 17.3\,\text{GeV}$) and RHIC ($\sqrt{s_{NN}} = 200\,\text{GeV}$) and has now begun at the LHC ($\sqrt{s_{NN}} = 2.76\,\text{TeV}$). These measurements were motivated by a desire to observe the suppression of J/ψ production by color screening in the QGP. In fact, strong suppression is observed at all three energies, but it has become clear that the contribution of color screening to the observed modification can not be uniquely determined without a good understanding of two strong competing effects.

The first of these, the modification of the J/ψ production cross section in a nuclear target, has been addressed at RHIC and the SPS using $p(d)$+A collisions, and will soon be addressed at the LHC using p+Pb collisions. The second complicating effect arises from the possibility that previously unbound heavy quark pairs could coalesce into bound states due to interactions with the medium. This opens up the possibility that if a high enough density of heavy quark pairs is produced in a single collision, coalescence of heavy quarks formed in different hard interactions might actually increase the production cross section beyond the initial population of bound pairs [119].

Using p+Pb and d+Au data as a baseline, and under the assumption that cold nuclear matter (CNM) effects can be factorized from hot matter effects, the suppression in central collisions due to the presence of hot matter in the final state has been estimated to be about 25% for Pb+Pb at the SPS [120], and about 50% for Au+Au at RHIC [121], both measured at midrapidity. The first J/ψ data in Pb+Pb collisions at $\sqrt{s_{NN}} = 2.76\,\text{TeV}$ from ALICE [122], measured at forward rapidity, are shown alongside PHENIX data in Figure 6.5. Interestingly, the suppression in central collisions is far greater at RHIC than at the LHC. This is qualitatively consistent with a predicted [119] strong coalescence component due to the very high $c\bar{c}$ production rate in a central collision at LHC. There is great promise that, once CNM effects are estimated from p+Pb data, comparison of these data at widely spaced collision energies will lead to an understanding of the role of coalescence.

Upsilon measurements have a distinct advantage over charmonium measurements as a probe of deconfinement in the QGP. The Υ(1S), Υ(2S) and Υ(3S) states can all be observed with comparable yields via their dilepton decays. Therefore it is possible to compare the effect of the medium simultaneously on three bottomonium states—all of which have quite different radii and binding energies.

CMS has already shown first upsilon data from Pb+Pb at 2.76 GeV that strongly suggest

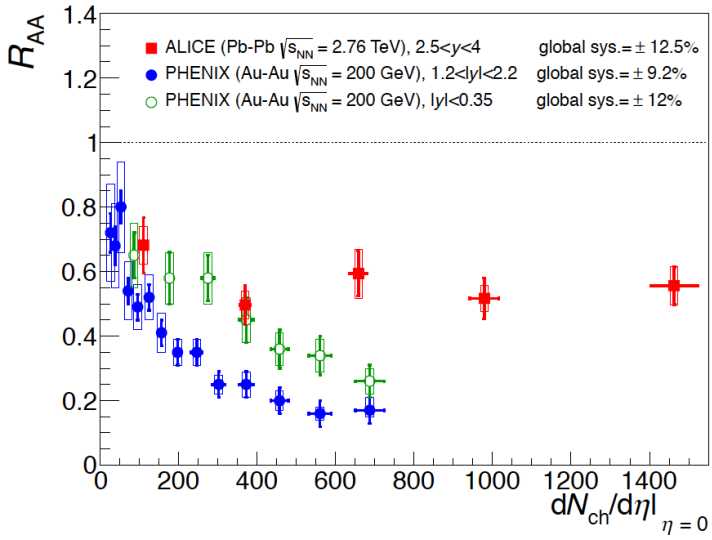

Figure 6.5: Comparison of nuclear modification measured by PHENIX and ALICE, showing that suppression is much stronger at the lower energy [122]. The modification measured by NA50 at low energy is similar to the PHENIX midrapity result.

differential suppression of the 2S and 3S states relative to the 1S state [123]. With longer Pb+Pb runs, and a p+Pb run to establish a CNM baseline, the LHC measurements will provide an excellent data set within which the suppression of the three upsilon states relative to p+Pb can be measured simultaneously at LHC energies.

At RHIC, upsilon measurements have been hampered by a combination of low cross sections and acceptance, and insufficient momentum resolution to resolve the three states. So far, there are preliminary measurements of the three states combined by PHENIX [124] and STAR [125], including in the STAR case a measurement for Au+Au. However a mass-resolved measurement of the modifications of the three upsilon states at $\sqrt{s_{NN}} = 200\,\text{GeV}$ would be extremely valuable for several reasons.

First, the core QGP temperature is approximately $2T_c$ at RHIC at $1\,\text{fm}/c$ and is at least 30% higher at the LHC (not including the fact that the system may thermalize faster) [126]. This temperature difference results in a different color screening environment. Second, the bottomonium production rate at RHIC is lower than that at the LHC by ~ 100 [121]. As a result, the average number of $b\bar{b}$ pairs in a central Au+Au collision at RHIC is ~ 0.05 versus ~ 5 in central Pb+Pb at the LHC. Qualitatively, one would expect this to effectively remove at RHIC any contributions from coalescence of bottom quarks from different hard processes, making the upsilon suppression at RHIC dependent primarily on color screening and CNM effects. This seems to be supported by recent theoretical calculations [127] where, in the favored scenario, coalescence for the upsilon is predicted to be significant at the LHC and small at RHIC.

The luminosity at RHIC for Au+Au collisions is ~ 30 times that at the LHC for Pb+Pb collisions, and running cycles for heavy ions are longer at RHIC. Therefore, with large acceptance and good momentum resolution, it is possible in one year of running to make upsilon measurements in the sPHENIX acceptance with yields comparable to those at the LHC.

STAR is constructing a Muon Telescope Detector (MTD) to measure muons at midrapidity [128]. Scheduled for completion in 2014, it will have a coverage of $|\eta| < 0.5$, with about 45% effective azimuthal coverage. The MTD will have a muon to pion enhancement factor of 50–100, and the mass resolution will provide a clean separation of the Υ(1S) from the Υ(2S+3S), and likely the ability to separate the Υ(2S) and Υ(3S) by fitting. While STAR will already have made upsilon measurements with the MTD at RHIC before the upgrade to sPHENIX proposed here would be available, the upgrade to sPHENIX would provide better mass resolution and approximately 10 times higher yields per run for upsilon measurements. This would substantially enhance the ability of RHIC to provide upsilon data of comparable quality to the LHC data.

6.3.2 Detector Performance

We report first the expected yield and line shape of the Υ(1S), Υ(2S) and Υ(3S) signal from decays to dielectrons. The results were obtained with single simulated Υ events in a GEANT 4 simulation containing the VTX detector and two additional tracking layers at 40 and 60 cm radius. The magnetic field was 2 tesla. The sPHENIX acceptance times tracking efficiency for $\Upsilon(1S+2S+3S) \rightarrow e^+e^-$ decays was found to be 0.34, in the mass window 7–11 GeV/c^2.

The baseline p+p cross section for $\Upsilon(1S+2S+3S)$ of $B_{ee}d\sigma/dy_{|y=0} = 114 \pm 40$ pb is taken from a PHENIX central arm measurement [124]. The rapidity dependence was taken from PYTHIA. The relative yields of the three Υ states were taken from CDF measurements at 1.8 TeV [129]. Estimates of the $p+p$ yields in sPHENIX are shown in Table 6.1, along with projected yields of the three Υ states for a Au+Au run. These assume binary scaling, and no suppression of any of the Υ states.

A critical question is whether the proposed tracking system, with a magnetic field of 2 tesla, is capable of adequately resolving the Υ(1S) from the Υ(2S) and Υ(3S) states.

The reconstructed mass spectrum for dielectron decays is shown in the left panel of Figure 6.6. That spectrum contains the number of Upsilons expected in the 0–10% centrality bin if there is no suppression. It can be seen that there are significant low mass tails on the Upsilon mass peaks due to radiative energy loss in the material of the VTX and outer tracking layers of sPHENIX. The radiative tails are found to be significantly (and helpfully) suppressed by the drop in tracking efficiency with increasing energy loss, due to the use of a circular track algorithm, as shown in the right panel of Figure 6.6.

The background under the Upsilon peaks consists of an irreducible (physics) background

Species	$\int \mathbf{L\,dt}$	Events	$\langle N_{coll} \rangle$	Y(1S)	Y(2S)	Y(3S)	Y(1S+2S+3S)
p+p	18 pb^{-1}	756 B	1	805	202	106	1113
Au+Au (MB)		50 B	240.4	12794	3217	1687	17698
Au+Au (0–10%)		5 B	962	5121	1288	675	7084

Table 6.1: The yield of different Y states obtained in one year of p+p or Au+Au RHIC running. The numbers for Au+Au in this table are calculated assuming no suppression of any of the Y state yields.

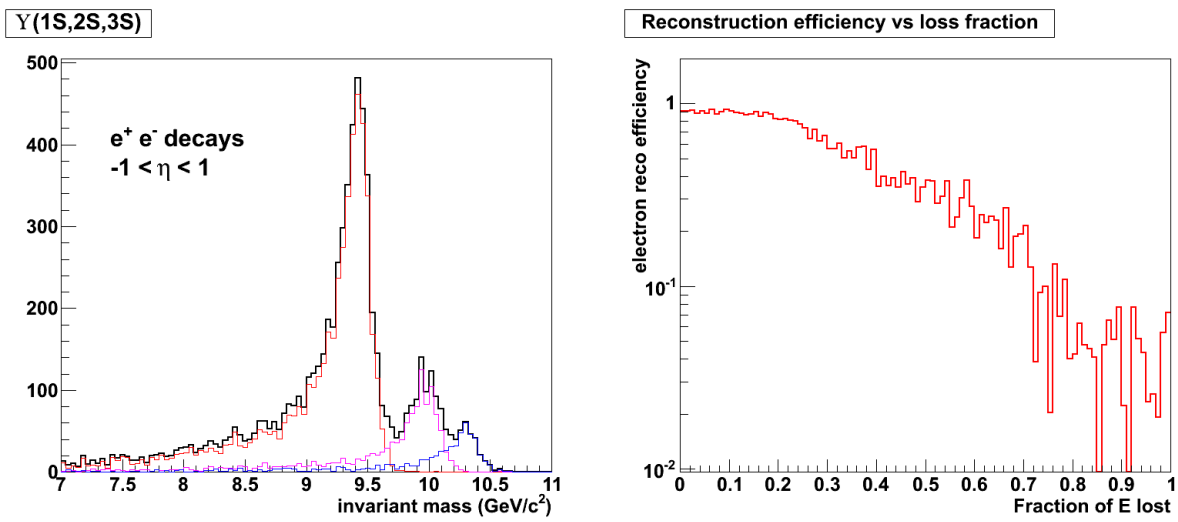

Figure 6.6: Left panel: The mass spectrum from reconstructed electron decay tracks for the three Upsilon states combined. The yield corresponds roughly to that for the 0–10% centrality bin from 50B minimum bias events, assuming no suppression in Au+Au collisions. Right panel: The electron track reconstruction efficiency for reconstructed electrons from Y decays versus the radiative energy loss of the electron as it exits the last tracking layer.

due to dileptons from correlated charm, correlated bottom and Drell Yan. There is also combinatorial background from misidentified charged pions. The latter can be estimated and removed by like sign subtraction, or by the mixed event method.

To study the physics background, correlated charm and bottom di-electron invariant mass distributions predicted by PYTHIA were normalized to the measured charm and bottom cross-sections in Au+Au collisions. The PYTHIA Drell-Yan di-electron invariant mass distribution was normalized to the theoretical prediction by Vogelsang.

The combinatorial background was studied by generating events with fake electrons due

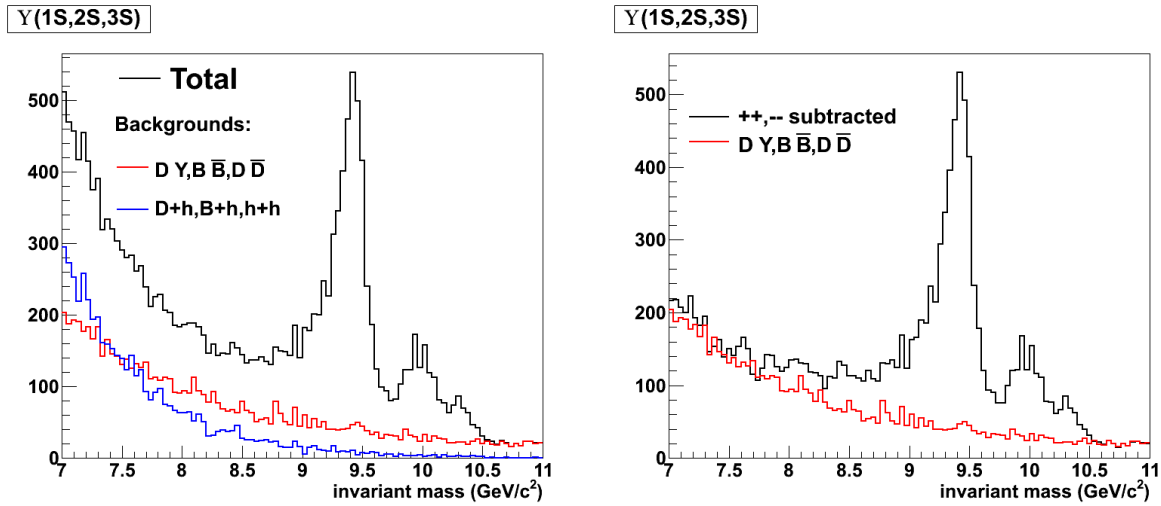

Figure 6.7: (Left) The signal plus background in the Upsilon mass region for 5B 0–10% central Au+Au events, assuming a pion rejection factor of 200. The combined backgrounds due to correlated bottom, correlated charm, and Drell Yan are shown as the red curve. The combined backgrounds due to fake electrons combining with themselves, bottom, and charm are shown as the blue line. (Right) The expected invariant mass distribution for 5B 0–10% central Au+Au events, after subtraction of combinatorial background using the like-sign method. The remaining background from correlated bottom, charm and Drell Yan is not removed by like sign subtraction. It must be estimated and subtracted.

to misidentified pions, using input pion distributions taken from measured π^0 spectra in Au+Au collisions. A p_T-independent rejection factor was applied to the π^0 spectra to imitate fake electron spectra. In the results presented here a rejection factor of 200 was used.

All combinations of fake electrons from misidentified pions were made with each other, and with high p_T electrons from physics sources. The latter turned out to be the least important source of background. The results are summarized in Figure 6.7(left), which shows the signal + background in the Υ mass region for the 5B 0–10% most central events, along with our estimates of the total correlated (physics) background and the total uncorrelated (combinatoric) backgrounds. In Figure 6.7 (right) we show the di-electron invariant mass distribution for 5B 0–10% central Au+Au events after the combinatorial background has been removed by subtracting all like-sign pairs.

From Figure 6.7 (left) we estimate that without Υ suppression the S/B ratios are Υ(1S): 2.4, Υ(2S): 1.4, and Υ(3S): 0.67. Using these estimates as the unsuppressed baseline, we show in Figure 6.8 the expected statistical precision of the measured R_{AA} for 50B recorded Au+Au events . For illustrative purposes, we take the measured suppression for each state to be equal to that from a recent theory calculation [130]. For each state, at each value of N_{part}, both the Υ yield and the S/B ratio were reduced together by the predicted suppression level.

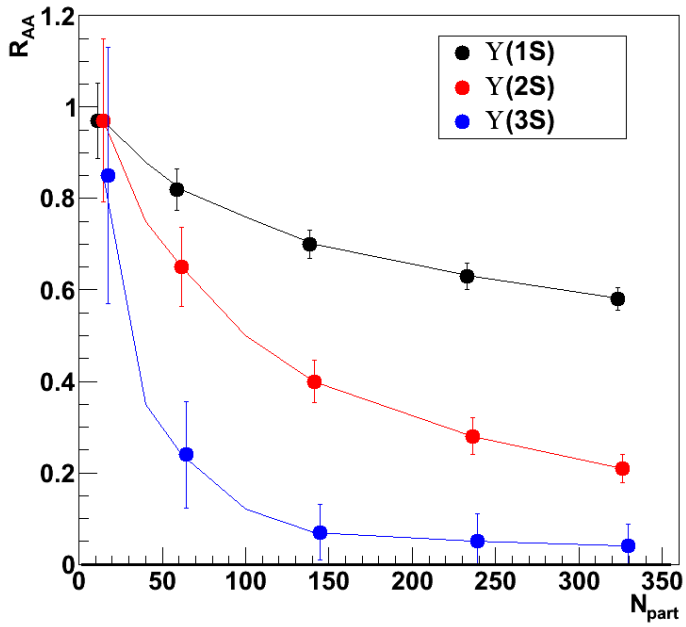

Figure 6.8: Estimate of the statistical precision of a measurement of the Υ states using sPHENIX, assuming that the measured R_{AA} is equal to the results of a recent theory calculation [130]. The yields assume 50B recorded Au+Au events.

We conclude from these results that the proposed upgrade to the sPHENIX detector would provide a good Υ measurement in one future RHIC Au+Au run, and would have the required mass resolution and S/B to separate the Υ(1S) state from the Υ(2S) and Υ(3S) states. Further, we expect that by fitting a line shape—which could be determined very well from the Υ(1S) peak—we could extract the Υ(2S) and Υ(3S) yields separately with reasonable precision.

6.4 Tagging Charm / Beauty Jets

A main motivation for studying heavy flavor jets in heavy ion collisions is to understand the mechanism for parton-medium interactions and to further explore the issue of *strong versus weak* coupling [131]. There are crucial measurements of single electrons from semileptonic D and B decays and direct D meson reconstruction with the current PHENIX VTX and the soon to come STAR Heavy Flavor Tracker (HFT) upgrade. The sPHENIX program can significantly expand the experimental acceptance and physics reach by having the ability to reconstruct full jets with a heavy flavor tag. The rates for heavy flavor production from perturbative QCD calculations [132] are shown in Figure 6.9.

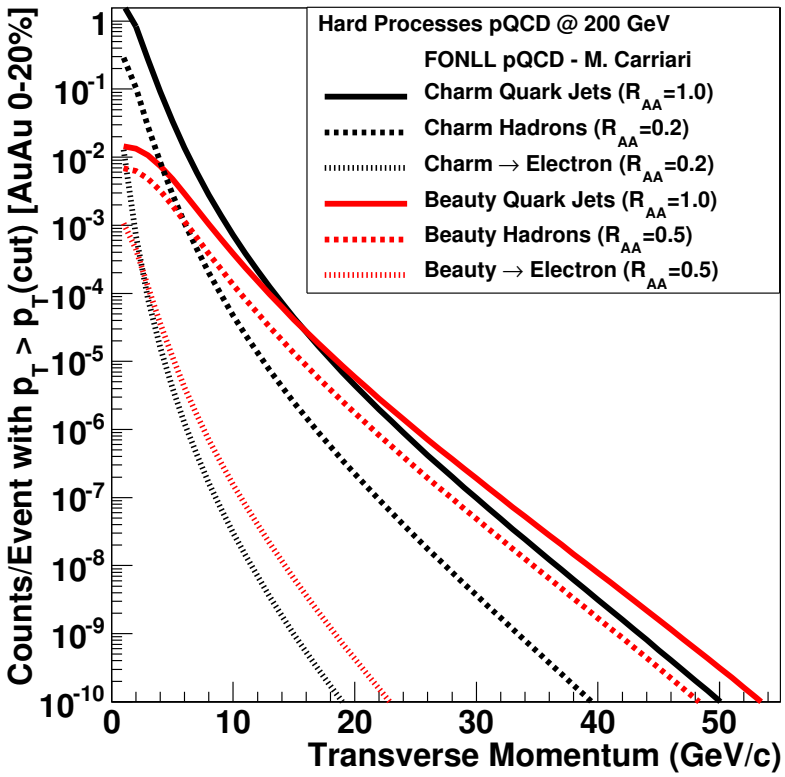

Figure 6.9: FONLL calculations [132] for heavy flavor (charm and beauty) jets, fragmentation hadrons (D, B mesons primarily), and decay electrons as a function of transverse momentum. The rates have been scaled to correspond to counts with $p_T > p_T(cut)$ for Au+Au 0–20% central collisions.

One promising tool is the study of heavy flavor jet-shape modification in Au+Au relative to $p+p$ collisions. Different mechanisms of energy loss (radiative versus collisional) predict different re-distributions of the jet fragments both inside and outside the jet cone. There are also scenarios where the heavy meson forms inside the medium and is dissociated in the matter [133, 134]. This would lead to a nearly unmodified jet shape relative to $p+p$ collisions and a much softer fragmentation function for the leading heavy meson. Figure 6.10 shows the D meson fragmentation function in PYTHIA and Q-PYTHIA for 20 GeV charm jets. The peak of the fragmentation function is shifted in Q-PYTHIA from $z \approx 0.7$ to $z \approx 0.5$. Thus, for a given p_T, D mesons are more suppressed than charm jets.

The tagging of charm and beauty jets has an extensive history in particle physics experiments. Detailed studies for this tagging within the sPHENIX upgrade with the additional tracking and electron identification described above are underway. There are three ways to tag heavy flavor jets. First is the method of tagging via the selection of a high p_T

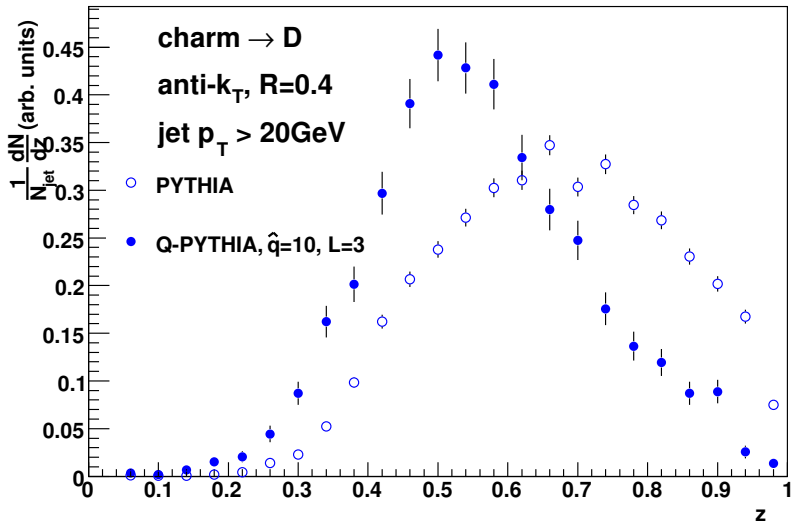

Figure 6.10: D meson fragmentation function in PYTHIA (open points) and Q-PYTHIA (solid points) for anti-k_T jets with $R = 0.4$ and $E_T(jet) > 20\,\text{GeV}$ as a function of z, the fractional momentum of the D meson relative to the charm quark.

electron with a displaced vertex inside the jet. In minimum bias Au+Au collisions at $\sqrt{s_{NN}} = 200\,\text{GeV}$, the fraction of inclusive electrons from D and B meson decays is already greater than 50% for $p_T > 2\,\text{GeV/c}$. The VTX in combination with the additional tracking layers can confirm the displaced vertex of the electron from the collision point, further enhancing the signal. Since the semileptonic branching fraction of D and B mesons is approximately 10%, this method provides a reasonable tagging efficiency. Also, the relative angle of the lepton with respect to the jet axis provides a useful discriminator for beauty jets as well, due to the decay kinematics. Second, the direct reconstruction of D and B mesons is possible within sPHENIX, with the additional tracking. The current PHENIX VTX is limited in its acceptance for D decays by the need to also reconstruct the track in the existing PHENIX central arm outer spectrometer, which has $|\eta| < 0.35$ and $\Delta\phi = 2 \times \pi/2$. The sPHENIX acceptance will yield a much higher (order of magnitude) yield of D mesons. The third method utilizes jets with many tracks that do not point back to the primary vertex. This technique is used by the $D0$ collaboration to identify beauty jets at the Tevatron [135]. This method exploits the fact that most hadrons with a beauty quark decay into multiple charged particles all with a displaced vertex. The detailed performance metrics for tagged heavy flavor jets are being developed in conjunction with converging on a design for the additional tracking layers.

6.5 Extending π^0 R_{AA} to 40 GeV/c

The preshower detector will allow separation of single photon and two photon (from π^0 decay) showers and thus substantially extend the high p_T measurement of the π^0 R_{AA}. As shown in Figure 1.21, with 50 billion Au+Au minimum bias collisions and the very large acceptance increase for sPHENIX, that would permit R_{AA} measurements out to $p_T \approx 40\,\mathrm{GeV/c}$. With this extended range it would be particularly interesting to see if one observes the predicted rise in R_{AA} that is a common feature of all perturbative radiative energy loss models. Shown in Figure 6.11 (left panel) is the calculation from Ref. [136] for collisional energy loss only (blue), radiative energy loss only (green), and both (red). One sees good agreement with the measured PHENIX π^0 data, but then no rise at higher p_T and instead a modest decrease. In fact, the initial rise at lower p_T may be from switching from the predominance of gluon to quark jets and then the almost exponentially falling spectra leads to a slow decrease in the predicted R_{AA}.

In Ref. [137] the authors utilize a simplified analytic "polytrop" jet energy-loss model that is used to test different jet-energy, path length, and temperature-power dependencies. They conclude that the experimental data indicate an approximate 60% reduction of the coupling κ from RHIC to LHC. The results from three calculations are shown in Figure 6.11 (right panel) and they note that "future higher statistics measurements at RHIC in the range $5 < p_T < 30\,\mathrm{GeV/c}$ are obviously needed to differentiate between the energy-loss models." sPHENIX will make just such a set of precision measurements.

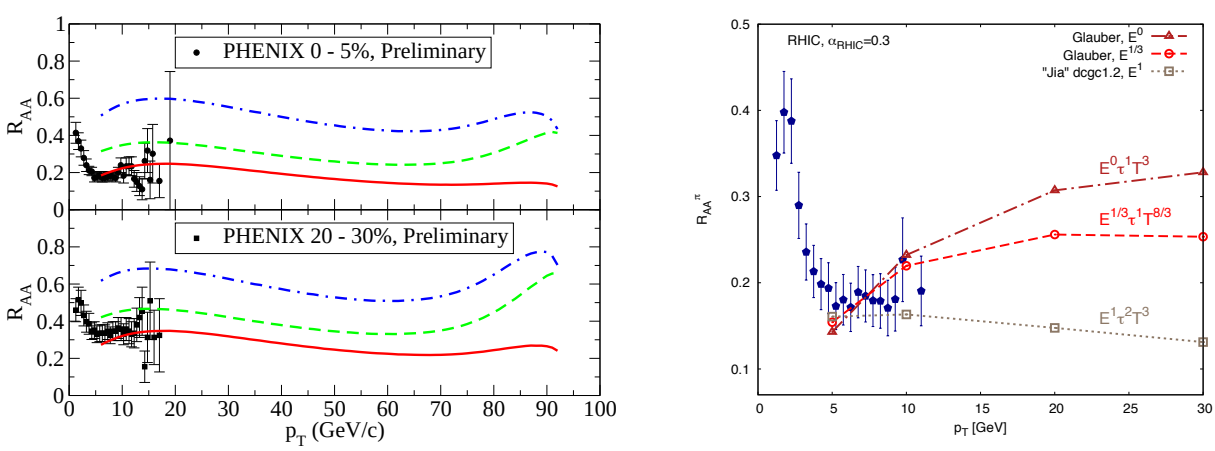

Figure 6.11: (Left) Calculations for π^0 show a clear modification of R_{AA} in Au+Au collisions at $\sqrt{s_{NN}} = 200\,\mathrm{GeV}$ that include collisional (blue), radiative (green), and both (red) energy loss mechanisms. Also shown are PHENIX measured π^0 results. (Right) Three different parameterized energy loss calculation results using the simplified analytic "polytrop" jet energy-loss model [137].

6.6 High z Jet Fragmentation Functions

The original predictions of jet quenching in terms of induced forward radiation had the strongest modification in the longitudinal distribution of hadrons from the shower (i.e. a substantial softening of the fragmentation function). One may infer from the nuclear suppression of π^0 in central Au+Au collisions $R_{AA} \approx 0.2$ that the high z (large momentum fraction carried by the hadron) showers are suppressed. However, a direct measurement with reconstructed jets and γ-jet events provides significantly more information. Shown in Figure 6.12 is the fragmentation function for 40 GeV jets in vacuum (PYTHIA) compared with the case of substantial jet quenching (Q-PYTHIA with $\hat{q} = 10\,\mathrm{GeV}^2/\mathrm{fm}$. In the sPHENIX upgrade, fragmentation functions via charged hadron measurements will be limited to the soft region ($p_T \lesssim 5\,\mathrm{GeV/c}$). The additional tracking extends these measurements over the full range for jets of 20–30 GeV (with the highest p_T reach currently being evaluated). Also, the independent measurement of jet energy (via calorimetry) and the hadron p_T via tracking is crucial. This independent determination also dramatically reduces the fake track contribution by the required coincidence with a high energy jet.

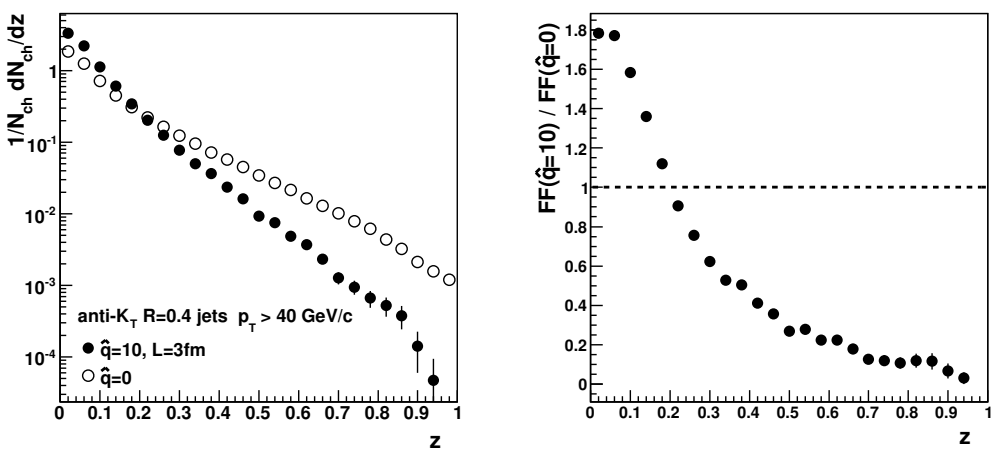

Figure 6.12: Q-PYTHIA simulation with quenching parameter $\hat{q} = 0$ (i.e., in vacuum) and $\hat{q} = 10\,\mathrm{GeV/c^2}$ for the fragmentation function of light quark and gluon jets as a function of z.

Preliminary measurements of fragmentation functions from the CMS and ATLAS experiments in Pb+Pb collisions show no modification within uncertainties . Although one explanation is that the jets that are reconstructed are from near the surface and thus not modified, with a nuclear modification factor for inclusive jets $R_{AA} \approx 0.5$ that explanation is challenged. Similar measurements at RHIC energies significantly augment the sPHENIX detector deliverables.

6.7 Low and Intermediate Mass Dileptons

Ever since the formation of quark-gluon plasma in heavy ion collisions was postulated, photons and dileptons have been considered among the most important probes to study the QGP [138]. This is because electromagnetic radiation is generated at every stage of the collision and, once created, escapes the collision volume without any strong interactions.

The energy spectra of photons and dileptons reflect the energy density and collective velocity of the strongly interacting matter from which they are emitted. For matter in local equilibrium, electromagnetic radiation provides information about the space-time evolution of temperature and collective motion. In this sense electromagnetic radiation can be considered "thermal" radiation, though strictly speaking it is not in equilibrium with the matter. Even if the matter is not in local equilibrium, the electromagnetic radiation emitted will still carry information about the energy density.

For both real and virtual photons the temperature and collective motion affect the momentum spectrum and it is difficult to unravel the two contributions. However, the mass of the virtual photons is Lorentz invariant and thus the mass distribution must be frame independent. Consequently, the mass distribution of the virtual photons will only be sensitive to the temperature. Measuring the virtual photon yield as a function of mass and momentum is the next step beyond existing data to separate temperature and flow velocity and map out the space-time evolution of the system.

Isolating thermal radiation requires subtracting lepton pairs from decays of pseudoscalar, vector, and heavy flavor carrying mesons. The CERN-SPS experiment NA60 pioneered this technique with high precision [139]. NA60 results give detailed insights into the space-time evolution of matter produced at low energies, where the emission is dominated by π-π annihilation from the hot hadronic phase. At RHIC a larger fraction of the radiation is emitted earlier in the collision; recent results bring into question some of the current ideas about the space-time evolution.

PHENIX developed a method using virtual photons at low mass but at $p_T \gg m$ to extrapolate back to the real photon point [2]. The p_T spectrum is nearly exponential, with an inverse slope of approximately 220 MeV. Since the yield of thermal radiation is expected to scale with the temperature to the fourth power, the yield and inverse slope suggest emission from early times. Hydrodynamic models that reproduce the data indicate that the initial temperature must be between 300 and 600 MeV, depending on choice of time after the collision begins at which the system is equilibrated.

Another important measurement established the elliptic flow (v_2) of direct photons [140], which was found to be very similar in the thermal region to that of hadrons. The observation is now confirmed with real photons which are converted in the detector material and detected as e^+e^- pairs. In hydrodynamical models, large anisotropies of momentum distributions are the consequence of collective motion driven by pressure gradients with respect to the reaction plane. Initial conditions for hydrodynamic expansions gener-

ally assume that matter has no transverse velocity at the time of equilibration, thus any anisotropies due to pressure gradients build up with time and are strongest very late in the collision. In such models, the large azimuthal momentum anisotropy of thermal photons suggests a late emission, apparently inconsistent with the large yields and high inverse slope. Indeed, models have difficulty describing thermal photon spectra and elliptic flow consistently [141].

PHENIX has reported excess production of di-electrons at low mass and low p_T [142], which is not consistent with theories that successfully describe the NA60 data from CERN. The p_T distributions show two components. One has a slope of approximately 250 MeV, and yields the real photon spectrum when extrapolated to zero mass. The other component is much softer, and has a much higher yield. The combination of high yield and small slope is not consistent with early emission, yet these di-leptons are absent in models of the hadronic medium. The NA60 spectra show hints of a component with a similar slope, but smaller yield. Higher quality data are needed to provide constraints on possible explanations of these soft dielectrons.

It will also be extremely interesting to measure v_2 and higher harmonic flow for dileptons. Recently it has been suggested that the angular distribution of dileptons as a function of mass can provide information on the degree of local equilibration [143]. The p_T-dependent ratio of dileptons to real photons in a certain mass window is sensitive to the value of η/s, particularly at higher dielectron masses [144]. It will be crucial, however, to measure di-leptons in the intermediate mass region, tagging on displaced vertices to pick out heavy flavor decays.

The PHENIX Hadron Blind Detector improves the signal to background ratios over that in the published data. Analysis of these data is under way. However, even with the anticipated improved sensitivity, the precision of the dilepton data is likely to be insufficient for a good determination of the flow higher moments.

Further progress in understanding the electromagnetic probes will require even higher precision data. Significantly reduced systematic uncertainties are needed; for di-electrons this can be achieved through Dalitz rejection via identified low momentum electrons. Unraveling the intermediate mass spectrum requires secondary vertex measurement, which will be provided by the silicon vertex detector at the center of sPHENIX.

Our approach would be to measure both real and virtual photons in the e^+e^- channel - in one case requiring the collision vertex as the di-electron source, and in the other utilizing detector material as the conversion point. The detector should be sensitive to (at least) 0.5–5 GeV/c transverse momentum and 0–2.0 GeV/c^2 pair mass, preferably higher. Qualitatively, both the real photon (via external conversions) and the dielectron measurements require high resolution ($\delta p/p \approx 1\%$ or better) tracking and precise determination of the dielectron vertex - compatible with sPHENIX requirements for heavy flavor tagging. Electron identification (e/π rejection) should be in the range of 1/500 to 1/1000. This typically requires more than one detector. We will study how well sPHENIX with the preshower upgrade can satisfy the electron ID requirements. It may be possible that

additional electron identification will be needed. R&D efforts underway for low mass tracking and for electron ID at forward angles for ePHENIX study technology of potential applicability for dielectron measurements. However, full specification of the requirements beyond the broad-brush estimates above will require careful simulation study.

Appendix A

Forward Upgrades and Physics

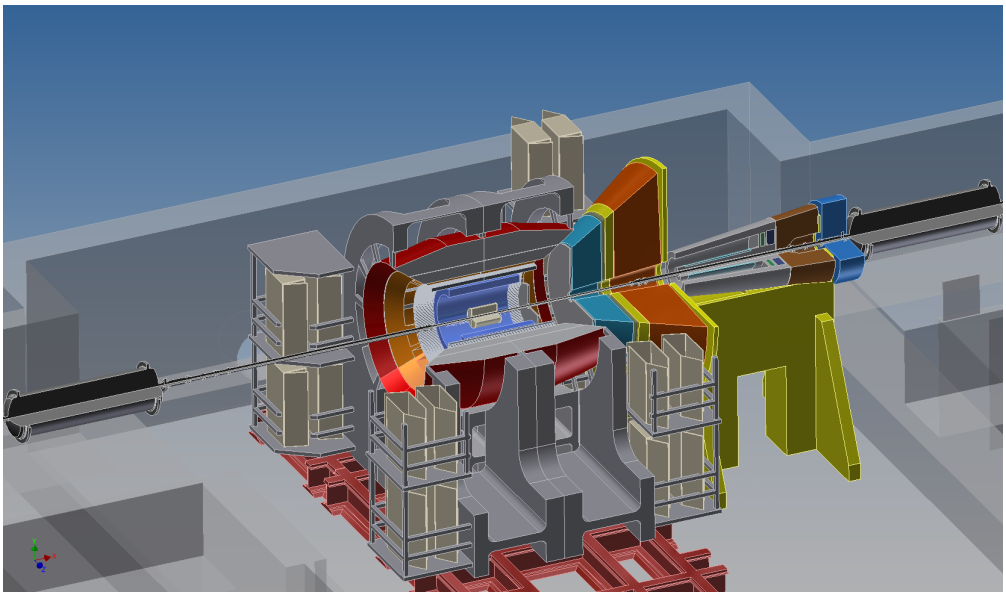

Figure A.1: An engineering drawing of fsPHENIX, showing the additional components along the direction of the beam, which provide exciting new capabilities at forward rapidities.

The sPHENIX detector described earlier in this proposal replaces the current PHENIX spectrometer arms at mid-rapidity. The upgrade will remove the central magnet including the massive iron yoke that currently provides the hadron absorber located upstream of the PHENIX muon detectors at forward rapidity. The sPHENIX open geometry will allow for the addition of spectrometers at forward and backward scattering angles capable of measuring hadrons, electrons, and photons. Such a forward detector is being designed for the study of cold nuclear matter effects in proton- and deuteron-nucleus collisions, precision measurements of single transverse spin asymmetries for the Drell-Yan process, and measurements of novel observables in jet production in transversely polarized $p+p$ collisions. A subsequent upgrade adding an electron detector in the opposite direction

would further evolve sPHENIX into a detector for inclusive, semi-inclusive and exclusive processes in deep inelastic electron-proton and electron-nucleus scattering, referred to as ePHENIX, utilizing a future high intensity electron beam at RHIC, as discussed in Appendix B.

This Appendix highlights selected physics channels that are presently being explored by the forward upgrade study group in PHENIX and provides a brief discussion of the detector design used in these studies.

A.1 Transverse Momentum Dependent Phenomena in Nucleon Structure

Over the past 10 years, RHIC experiments have studied the gluon helicity distribution, $\Delta g(x)$, in the proton through the measurement of longitudinal double spin asymmetries in inclusive hadron and jet production [145, 146, 147, 148, 149, 150]. PHENIX and STAR have completed instrumentation upgrades that will be used to measure quark and anti-quark helicity distributions through W production with high luminosity polarized $p+p$ collisions at $\sqrt{s} = 500\,\text{GeV}$. The additional high statistics data samples taken for W measurements will also be used to significantly improve the precision of the double spin asymmetries constraining $\Delta g(x)$. RHIC is on course to complete its measurements of $\Delta q(x)$ and $\Delta\overline{q}(x)$ in W production over the next few years. RHIC measurements, in combination with polarized deep inelastic lepton-nucleon scattering, will provide significant constraints for quark and gluon helicity distributions for $0.01 < x_{q,g} < 0.3$. On the theoretical side, the physics of the helicity structure of the nucleon in hard scattering processes has been described successfully at leading twist in the Operator Product Expansion (OPE) in collinear approximations of hard scattering processes ignoring parton momentum components transverse to the direction of the relativistic probe particles.

In addition to measurements constraining quark and gluon helicity distributions, the BRAHMS, STAR and PHENIX collaborations have carried out precise measurements of single transverse spin asymmetries, A_N, at center of mass energies of $\sqrt{s} = 62.4$, 200 and 500 GeV. It was observed that the large single transverse spin asymmetries found at $\sqrt{s} \sim 20$ GeV in fixed target experiments at FNAL persist to the higher center of mass energies at RHIC. Despite intense effort over the past decade, a quantitative theoretical understanding of the single transverse spin asymmetries observed in polarized proton-proton collisions remains elusive. However, the theoretical interest in these asymmetries remains high as transverse spin observables are related to the orbital angular momentum structure of hadrons [151], and as such holds promise for understanding these dynamics as well as the complex dynamics of confinement and chiral symmetry breaking in hadrons [152].

In parallel to the measurements of transverse spin asymmetries at RHIC, deep inelastic scattering experiments at DESY, CERN, and Jefferson Laboratory have confirmed the existence of two transverse momentum dependent mechanisms that were proposed by

Sivers and Collins some 20 years ago to explain the large non-zero transverse single spin asymmetries in polarized proton-proton scattering. These measurements have been of an exploratory nature with significant statistical uncertainties and limited coverage in x and Q^2.

A consistent theoretical framework has been developed to describe transverse momentum dependent observables in hard scattering processes. At large transverse momenta the Qiu-Sterman mechanism describes Transverse Momentum Distribution (TMD) observables [153]. Spin dependent transverse momentum components can be generated through multi-gluon correlations at higher orders in the OPE. At smaller transverse momentum, corresponding to the intrinsic transverse momentum of partons in hadrons, the Sivers and Collins mechanisms are applicable. Correlations between the transverse spin of the target proton and intrinsic transverse momentum of quarks in the initial state (Sivers [154]) or correlations between quark spin and the transverse momentum of hadrons in the final state (Collins [155]) give rise to anisotropic distributions of hadrons in the final state with respect to the proton spin.

In an important result, it has been demonstrated by Ji, Qiu, Vogelsang and Yuan [156] that the Qiu-Sterman and Sivers mechanisms lead to identical results in the region of intermediate transverse momenta. The departure from the collinear approximation and the description of transverse momentum dependent processes requires the correct treatment of the exchange of soft (non-collinear) gluons in the initial and final states of high energy scattering reactions. This has been accomplished through the inclusion of gauge link integrals that sum over initial and final state soft gluon exchange. The inclusion of the gauge link integrals in the hard scattering matrix elements can give rise to Sivers correlations between transverse proton spin and quark transverse momentum. Gauge link integrals have been found to be process dependent. For example, at leading order the final state gauge link relevant for the Sivers effect in semi-inclusive deep-inelastic scattering is equal in magnitude but opposite in sign to the initial state gauge link relevant for the Sivers mechanism in Drell-Yan. The test of the TMD framework through observation of the predicted sign change of Sivers asymmetry observables in Drell-Yan compared to SIDIS is the subject of a NSAC milestone for hadron physics, HP13.

Significant theoretical progress has been made recently in the derivation of evolution equations for TMD parton distributions and fragmentation functions. The knowledge of TMD evolution equations will make it possible to carry out a rigorous QCD analysis of TMD observables measured at collider energies by experiments at RHIC and future SIDIS experiments using polarized fixed targets at Jefferson Laboratory and at CERN. Recent theoretical work [157, 158] suggests that the correct evolution may lead to significantly smaller Sivers asymmetries at large Q^2. However, the final theoretical analysis of the evolution for Sivers asymmetries will require additional input from experiment.

Single transverse Spin Asymmetries (SSA) in Drell-Yan production of electron-positron pairs at forward rapidity will uniquely test the process dependence of the Sivers mechanism (sign change compared to SIDIS). Similar tests are possible through the observation

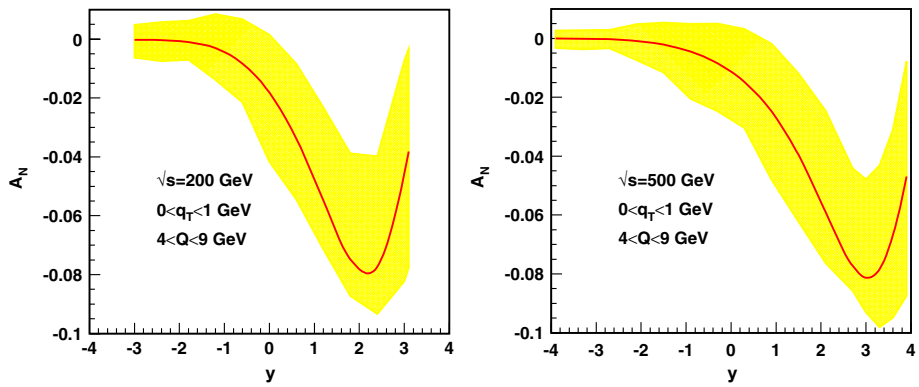

Figure A.2: The expected A_N for Drell-Yan dilepton production at RHIC for $\sqrt{s} = 200\,\text{GeV}$ and $\sqrt{s} = 500\,\text{GeV}$ [159]. The uncertainties shown as yellow bands are a result of the uncertainties from the Sivers function extracted from SIDIS data.

of SSAs in jet-photon production in polarized $p+p$ scattering at RHIC. A comparison of the asymmetries measured in proton induced Drell-Yan at RHIC with SSAs measured in pion induced Drell-Yan processes at fixed target energies provides a unique test of TMD evolution. The predicted Drell-Yan asymmetries at $\sqrt{s} = 200$ and $500\,\text{GeV}$ are shown in Figure A.2 [159]. The precise measurement of SSAs in Drell-Yan in the forward rapidity region probes the Sivers quark distributions at large x and measurements in the backward region provide unique access to the Sivers distributions for sea quarks [160].

The Collins effect manifests itself through an azimuthal anisotropy in the distribution of hadrons in final state jets with respect to the proton spin component normal to the scattering plane. Precision measurements of single transverse spin asymmetries for single identified charged pions (Collins effect) and for identified hadron pairs (Interference Fragmentation Function, IFF) will lead to the first measurement of quark transversity distributions at large $x > 0.35$. This measurement will make possible a data based determination of the tensor charge of the nucleon thus testing Lattice QCD predictions for the tensor charge [161]. A comparison of quark transversity extracted from TMD Collins observables and from collinear IFF asymmetries will provide a powerful test of the TMD framework and evolution.

In the intervening time between the current PHENIX and the sPHENIX forward upgrade, the MPC-EX upgrade [162] will add a silicon preshower detector to the current PHENIX forward calorimeters, the Muon Piston Calorimeter (MPC) [163]. Two goals of this upgrade are a measurement of the A_N of direct photons (Sivers) and an exploratory measurement of π^0s in jets to extract the Collins asymmetry contribution to the forward A_N of π^0. Because of the lack of a full jet reconstruction, the Collins asymmetry measurement will not be able to determine the asymmetry as a function of the π^0 fraction of the total jet energy. This measurement will give important guidance in the design of the sPHENIX forward upgrade by indicating how much of the forward A_N for π^0 is derived from transversity and a Collins fragmentation function, but any attempt to extract transversity from the

MPC-EX data would be model dependent. Ultimately the full sPHENIX forward upgrade will be required for a complete survey of this important physics.

A.2 Cold Nuclear Matter Effects

Our quest to understand QCD processes in Cold Nuclear Matter (CNM) centers on the following fundamental questions:

- What are the dynamics of partons at very small and very large momentum fraction (x) in nuclei, and at high gluon density what are the nonlinear evolution effects (i.e., saturation)?
- What are the pQCD mechanisms that cause energy loss of partons in CNM, and is this intimately related to transverse momentum broadening?
- What are the detailed hadronization mechanisms and time scales and how are they modified in the nuclear environment?

Various aspects of these questions are being attacked by numerous experiments and facilities around the world. Deep inelastic scattering on nuclei addresses many of these questions with results from HERMES at DESY [164, 165], CLAS at JLab [166], and in the future at the JLab 12 GeV upgrade and eventually an Electron-Ion Collider [167]. This program is complemented with hadron-nucleus reactions in fixed target p+A experiments at Fermilab (E772, E886, and soon E906) [168] and at the CERN-SPS. RHIC has significantly extended this program to d+A reactions at much higher colliding energies, and also with the key augmentation of being able to tag impact-parameter categories of the collisions.

The RHIC program has already played a major role in addressing the fundamental question of low-x partons in nuclei. It has been known for many years that the population of small momentum fraction (small x) partons in a nucleon embedded in a nucleus is depleted compared to that for a free nucleon. Evidence for this phenomenon has come largely from deep-inelastic scattering (DIS) measurements [169, 170] and from Drell-Yan [171, 168] measurements. Quarks and anti-quarks are both depleted for $x < 10^{-2}$. For gluons the evidence is mostly indirect and relies on the Q^2 scaling violations observed in lepton DIS measurements. The state of the art for gluons is embodied in the EPS09 gluon nuclear parton distribution functions (nPDFs) of Eskola *et al.* [172]. These modifications are extremely uncertain in the Q^2 range relevant at RHIC energies, with depletion factors ranging from $\simeq 10\%$ to nearly no gluons at $x \simeq 5 \times 10^{-3}$. Recent gluon saturation models assert that a novel semi-classical state—the color glass condensate (CGC)—is formed above a critical saturation scale, Q^2, at low enough momentum [173]. A universal and quantitative description of cold nuclear matter effects in nucleon structure for different collision systems is currently not available.

The PHENIX experiment has explored these cold nuclear matter effects with measurements of J/ψ and hadron-hadron correlations over a broad range of rapidity [174, 175, 176] which are sensitive to an extended range in Bjorken x. These results cannot be explained within the parametrized nuclear modified parton distribution functions [172], and hint at new physics of gluon saturation and possibly initial-state parton energy loss. The PHENIX forward silicon tracker (FVTX) has been installed in 2012 and will enable detailed measurements of open heavy flavor, multiple quarkonia states, and a first look at Drell-Yan at forward rapidity ($1.2 < y < 2.4$). This provides crucial comparison data to the J/ψ nuclear modification with precision open heavy flavor and Drell-Yan, the latter of which has no final state interactions to disentangle. In the future, the MPC-EX upgrade [162] will measure prompt photon production in p(d)+A collisions as another channel to constrain the nuclear gluon distribution at low-x.

The sPHENIX forward upgrade discussed here will build upon these current upgrades and substantially extend their kinematic reach and channels of measurement. It is a central goal of the sPHENIX forward upgrade to systematically survey the cold nuclear matter effects in high energy nuclear collisions with small statistical and systematic uncertainties. Important experimental observables will include the cross sections for quarkonia, vertex tagged open charm and bottom quarks, inclusive hadrons and jets, as well jet-jet correlation measurements, over a broad range of rapidity intervals between the reconstructed jets. These data sets will serve as input to the development of a universal and quantitative description of cold nuclear matter effects in nucleon structure and the initial state of high energy heavy ion collisions.

The high luminosity in deuteron-ion and proton-ion collisions achievable at RHIC will make it possible to carry out measurements for several nuclei at different collision energies, still with small statistical uncertainties. The high luminosity will also allow for the comparison of results from proton- and deuteron-ion collisions enabling the systematic analysis of the large effects expected from multiple parton interactions (MPI) in nuclear collisions at forward rapidity. These effects are expected to be large and need to be carefully accounted for in quantitative theoretical analysis [177]. Further, in order to keep experimental systematic uncertainties and model uncertainties in the theoretical analysis small the sPHENIX forward detector will be able to fully reconstruct jets and to carry out low background heavy quark and Drell-Yan measurements.

A.3 Detector Considerations

Precision Drell-Yan measurements require excellent dilepton identification and the ability to reduce backgrounds from correlated charm and beauty decays. The current PHENIX forward silicon vertex tracker (FVTX) combined with the muon spectrometer measure dimuons over rapidity $1.2 < |y| < 2.4$ and with the ability to tag heavy flavor decays. Drell-Yan measurements via dimuons will give a first look at this transverse spin physics, and the forward sPHENIX upgrade presented in this Appendix will substantially advance

this program to precision measurements over a much wider rapidity range. The forward sPHENIX Drell-Yan measurements will be via dielectrons, and will require an electromagnetic calorimeter and charged particle tracking as well as heavy flavor tagging for background rejection.

The forward sPHENIX detector will greatly extend our ability to measure the Collins and Sivers asymmetries at forward rapidities by performing full jet reconstruction. Experimentally, the measurement of transverse spin effects within jets will require electromagnetic and hadronic calorimetry for jet reconstruction, particle tracking to determine the fractional momentum of hadrons or hadron pairs in the jet and particle ID to avoid canceling of transverse spin effects in the fragmentation of different hadrons. Precise studies of the Sivers and Collins effects in different channels with the sPHENIX forward upgrade will make it possible to decompose the large transverse single spin asymmetries that historically have been observed in polarized proton-proton collisions and to identify and quantify the contributions from different spin effects.

The forward sPHENIX study group has been investigating the exact detector performance design requirements for these physics channels. The currently envisioned sPHENIX forward detector will have an acceptance from a pseudorapidity of $1.2 < \eta < 4$. The acceptances of the mid-rapidity upgrade and the forward upgrade will be matched closely in order to minimize the missing energy in the event reconstruction. Currently, a "straw man" design is being used for the purpose of sensitivity studies. This design divides forward sPHENIX into a forward section, $1.2 < \eta < 3$ and very forward region, $3 < \eta < 4$. Currently it is thought that there will be two sources of magnetic field. For the forward region an extension or modification of the central solenoid could provide a sufficiently strong tracking field. For the high momenta in the very forward region an additional forward coil is foreseen to be able to reach acceptable momentum resolution. Gas Electron Multiplier (GEM) detectors will provide charged particle tracking. Particle identification is based on a Ring Imaging Cherenkov Detector. It believed that a hadronic calorimeter with a modest energy resolution will energy smearing for Collins measurements in jets within acceptable limits. The forward electromagnetic calorimeter may consist of a re-stack of the current PHENIX electromagnetic calorimeters (EMCal) and the MPC-EX towers. Early simulation results indicate that the performance of the EMCal will be sufficient. The "straw man" design will form the basis of GEANT4 studies to better define and demonstrate the capability of an sPHENIX forward upgrade to address the physics discussed in the previous sections. It is anticipated that the details of the detector design and configuration will undergo significant evolution during this process.

Finally, PHENIX will host a workshop sponsored by the RIKEN BNL Research Center with the goal to further develop the physics case for future forward upgrades at RHIC from July 30th to August 1st. The experimental feasibility of the proposed forward physics case will be studied through GEANT4 based simulations and a final report with detailed results from the study group will be available by the end of November 2012. Institutions that are presently participating in the forward upgrades are Abilene Christian University; Brookhaven National Laboratory; University of California, Riverside; CIAE, Beijing, China;

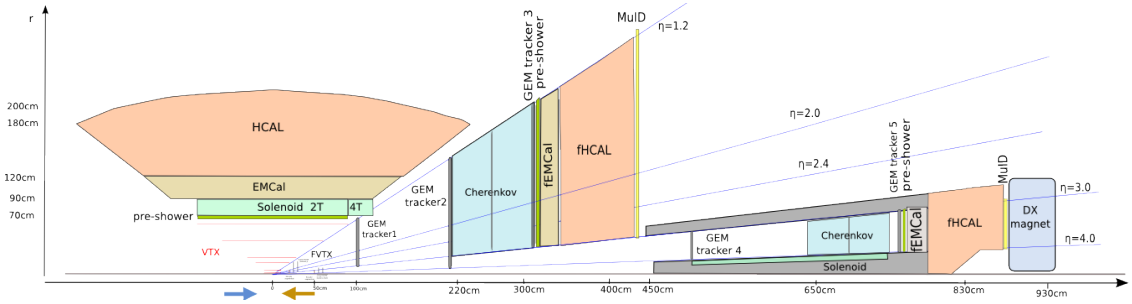

Figure A.3: A straw man layout of a possible detector for a future forward upgrade to sPHENIX.

Georgia State University; Hanyang University, Seoul, Korea; University of Illinois, Urbana; Iowa State University; KEK, Tsukuba, Japan; Korea University, Seoul, Korea; Los Alamos National Laboratory; Muhlenberg College; New Mexico State University; University of New Mexico; RIKEN Brookhaven Research Center; RIKEN Institute; Rikkyo University, Tokyo, Japan; Seoul National University, Seoul, Korea; Stony Brook University; and the University of Michigan.

Appendix B

Evolution to ePHENIX

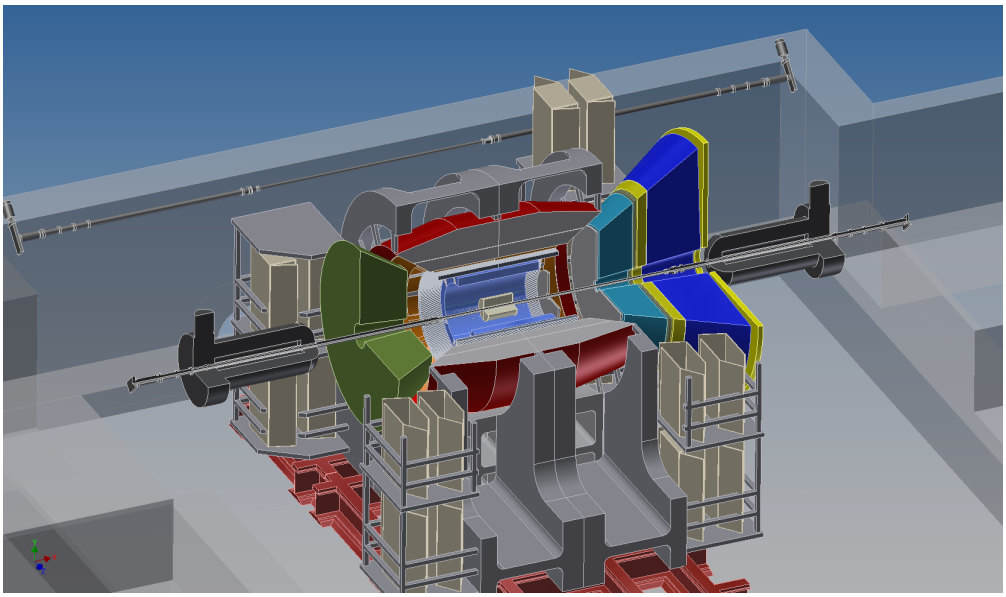

Figure B.1: An engineering drawing of ePHENIX, a detector extending the core elements of sPHENIX and fsPHENIX into an apparatus capable of world-class measurements with an electron-ion collider

One realization of a future Electron Ion Collider (EIC) consists of adding a 5–30 GeV electron beam to the current RHIC hadron and nuclear beam capabilities. The proposed initial construction would consist of a 5–10 GeV electron beam, referred to as Phase 1 of eRHIC. Given the large capital investment and expertise in the current PHENIX experiment, it is logical to determine if the sPHENIX upgrade proposal presented in this document can serve as the foundation for a future EIC detector, referred to as ePHENIX. In designing the sPHENIX upgrade (covering $|\eta| < 1.0$), we want to make sure that this is compatible with a world-class EIC program in multiple measurement channels when combined with future upgrades in the backward ($\eta < -1.0$) and forward ($\eta > 1.0$) regions (enabled by

the open geometry of the magnetic solenoid). Thus, in this Appendix, we first describe the key physics that ePHENIX can access, and then how the sPHENIX upgrade at midrapidity enables measurements in terms of the magnetic field strength, tracking resolution, calorimeter resolutions, and physical radial space for additional particle identification detectors. We conclude that the sPHENIX upgrade serves as an excellent platform for this exciting future ePHENIX project.

B.1 ePHENIX at eRHIC

Quantum Chromodyanmics (QCD) is the Standard Model of strong interactions, and yet our knowledge and understanding of it remains incomplete. The properties of visible matter in the universe are greatly influenced by the strong interactions. The investigations of the quark-gluon plasma described in this document explore one such phase of QCD matter at high temperature. In contrast, quark-gluon interactions of cold QCD matter are optimally studied using the well established technique of Deep Inelastic Scattering (DIS). Many questions remain unanswered in the regime where the gluons and sea quarks dominate the landscape of hadrons and nuclei. The US nuclear science community is considering a high-energy, high-luminosity, polarized electron-proton and electron-ion collider [178] to study and understand the structure and the properties of cold QCD matter. In particular, it aims to understand the role of gluons and sea quarks in QCD through precision measurements of the structure of protons and nuclei and the dynamics of the partons inside them [179].

Two possible realizations of the future DIS facility, the Electron Ion Collider, are under consideration. One realization, eRHIC, proposes to add a 5–30 GeV electron beam facility to the existing RHIC facility at BNL to collide with one of its hadron (polarized nucleons and nuclei) beams. The other option proposes colliding electrons from the 12 GeV CEBAF with a new hadron beam facility to be built at Jefferson Laboratory. This document will focus on the potential physics program with a future evolved/upgraded PHENIX detector (ePHENIX) to utilize collisions at eRHIC.

The construction proposal for eRHIC includes an initial beam of 5 GeV electrons colliding with an existing hadron beam of RHIC with 100–250 GeV polarized protons, and a wide range in nuclei from deuterium to uranium with energies from 100 GeV/nucleon. Figure B.2 shows the x and Q^2 kinematic region accessible with 5 GeV electrons colliding with 100 GeV protons ($\sqrt{s} = \sqrt{4E_eE_p} = 45$ GeV) in red hatches. It is envisioned that the electron beam energy could gradually go up to 10 GeV ($\sqrt{s}$ up to 100 GeV) in the following few years after construction completion. The luminosities anticipated for Phase 1 of eRHIC, with 5–10 GeV electrons, range from 0.6–10×10^{33} cm^{-2}sec^{-1}, dependent only on the proton beam energy for $E_e \leq 20$ GeV [179]. Similarly, for the nuclei (in particular Au) the luminosity ranges from 0.5–3.9×10^{33} cm^{-2} sec^{-1}, dependent on the energy of the nucleus, for $E_e \leq 20$ GeV. This is the kinematic region and luminosity reach for which ePHENIX is being designed to perform world class measurements. We envision full use of

the sPHENIX detector discussed in this document at midrapidity $|\eta| < 1.0$, followed by a sPHENIX-Forward upgrade, and then additional modifications specific to ePHENIX.

B.1.1 Kinematics

Due to the large imbalance between the electron and hadron beam energies in eRHIC collisions, the center of mass of such a collision is moving in the incoming proton direction: this is *defined* as the positive z axis, and all angles will be measured with respect to it. For a fixed center of mass energy, inclusive scattering $e + p \rightarrow eX$ is described by two independent variables x and Q^2, which are the Bjorken scaling variable, and the square of the four momentum transfer in a DIS event. These variables describe the lowest order process where the electron scatters elastically on a free constituent of the proton/nucleus. For neutral current events, which are the primary concern for this Appendix, these variables can be determined from the energy and angle of the scattered electron or from the final state hadron system, or from a mixture of both. The measurement of the scattered electron, or the hadronic final state when the measurement of scattered electron becomes difficult, yields:

$$y = 1 - (E'_e/2E_e) \cdot (1 - \cos\theta'_e) = (E_j/2E_e)(1 - \cos\theta_j) \tag{B.1}$$

$$Q^2 = 2E_eE'_e(1 + \cos\theta'_e) = E_j^2 \sin^2\theta_j/(1 - y) \tag{B.2}$$

$$x = E'_e(1 + \cos\theta'_e)/(2yE_p) = E_j(1 + \cos\theta_j)/[(1 - y)(2E_p)] \tag{B.3}$$

where y is a measure of inelasticity in $e+p$ scattering, $E_{e,p}$ are the initial energies of the electron and proton beam, and E'_e (E_j), θ'_e (θ_j) are the energy and angle of the scattered electron (hadronic final state).

B.2 Physics Goals of the EIC

There are three areas of nuclear physics where the EIC will greatly expand our current knowledge: nucleon structure, QCD in nuclei, and searches beyond the Standard Model. In Phase 1 of eRHIC, ePHENIX will be able to make important measurements in the first two, whereas the third will require the larger electron beam energies available only in a later phase. The goals presented in [179] that ePHENIX can measure are:

- Three dimensional structure of the nucleon, including its spin:
  - The gluon and sea quark helicity contributions to the nucleon helicity
  - Quark and gluon transverse momentum distributions
  - The spatial distribution of gluons and sea quarks in the nucleon

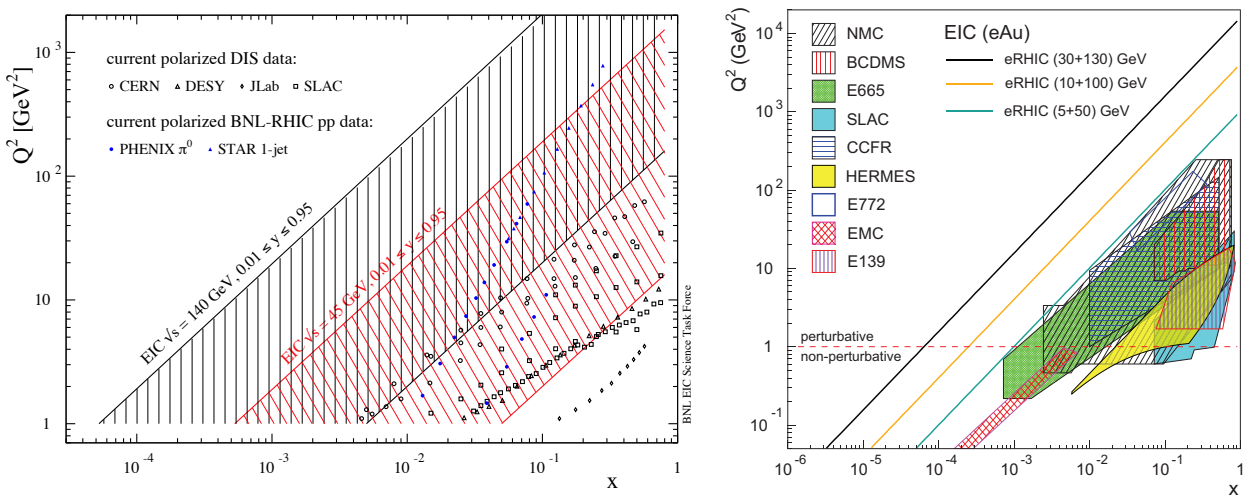

Figure B.2: (Left) The x-Q^2 region covered by eRHIC and previous experiments for e+p collisions in (red) Phase 1 and (black) at full energy, courtesy of Marco Stratmann. (Right) Same for e+A, with the Phase 1 maximum x-Q^2 coverage given by the yellow line, courtesy of Thomas Ulrich.

- QCD in nuclei
  - Nuclear modification of parton distributions
  - Parton propagation in cold nuclear matter

Here we briefly describe the physics we will measure with ePHENIX.

B.2.1 Polarized and 3d structure of the nucleon

Helicity structure

The golden physics channels to study the helicity structure of the nucleon are detailed in the INT report [179]. Two key channels are within reach during Phase 1 of eRHIC with moderate electron energies (5–10 GeV). The first is the gluon polarization to low x via the scaling of the structure function g_1 obtained from inclusive DIS. The second is the quark and antiquark helicity distributions, especially $\Delta\overline{u}(x) - \Delta\overline{d}(x)$ and $\Delta s(x) - \Delta\overline{s}(x)$, via the semi-inclusive measurement of final state pions and kaons. The last golden channel, via electroweak measurements, will require the highest electron energies as well as a more hermetic detector (for charged current reactions) than what is currently being discussed and is therefore not considered here.

Inclusive DIS is the simplest $e + p$ process in which only the scattered electron is reconstructed. In polarized DIS one is able to access the structure function $g_1(x, Q^2)$ in double spin asymmetries of the spin orientations of the lepton and nucleon. The structure function

g_1 is, at leading order in the strong coupling α_S, the charge-squared-weighted sum of the quark and antiquark helicities: $g_1(x, Q^2) = \sum_q e_q^2[\Delta q(x, Q^2) + \Delta\overline{q}(x, Q^2)]$. At next-to-leading order, the gluon helicity contribution $\Delta g(x, Q^2)$, enters via the splitting functions. It is therefore possible to extract the gluon helicity via the scaling violations by measuring g_1 over a large x-Q^2 range. While for the limited initial electron beam energies the lowest x will not yet be accessible, a large Q^2 range will still be covered for x as small as 10^{-3} and especially at intermediate x (0.01–0.1) where fixed target measurements exist but only at very low Q^2.

In semi-inclusive DIS (SIDIS), one additionally detects at least one final-state hadron fragmenting from the struck quark. It is then possible to perform a flavor decomposition of the semi-inclusive double spin asymmetries to arrive at the individual quark and antiquark helicity distribution functions, $\Delta q(x, Q^2)$ and $\Delta\overline{q}(x, Q^2)$. This relies on the fragmentation function, which describes the hadronization of an initial parton into a final-state hadron, and on the existing knowledge of the unpolarized parton distribution functions (PDFs). While the valence quark helicity distributions at intermediate to high x were already reasonably well determined, the sea quark helicities and in particular difference between $\Delta\overline{u}(x, Q^2)$ and $\Delta\overline{d}(x, Q^2)$ as well as $\Delta\overline{s}(x, Q^2)$ and $\Delta s(x, Q^2)$ are not well determined to date. The knowledge on the former difference is expected to improve with the RHIC W program at $x \sim 0.1 - 0.4$, and the data from fixed target SIDIS below that is insufficient [180]. As the fragmentation functions for favored and disfavored fragmentation become similar at lower fractional energies $z = E_h/E_q$, it is important to cover the higher z ranges to maintain flavor discrimination power. While the strange sea helicity is of interest from high to low x, the $SU(2)_F$ sea asymmetry is expected to be broken at x of 0.01–0.1 in some models.

3D structure of hadrons: Transverse momentum dependent distributions

While the previous section deals only with parton distributions integrated over transverse momenta, recent theoretical and experimental developments started to allow us also to study the transverse momentum dependence (TMD) of partons in hadrons. When the relevant transverse momentum is sufficiently smaller than the hard scale, Q, the so-called TMD framework can be applied where PDFs depend not only on the longitudinal momentum fraction x, but also on the transverse momentum, $k_\perp$. At leading twist, eight functions exist for the nucleon, which originate from the possible combinations of parton and nucleon spin and transverse momentum orientations. From this it becomes evident that orbital motion of partons is required and that spin-orbit correlations of partons in the nucleon can be studied via TMDs.

Three of the eight TMDs return to the previously defined collinear PDFs upon integration of the transverse momentum: the unpolarized distribution function, the helicity distribution and the quark transversity distribution. The quark transversity distribution function is in itself of interest as it directly connects to the tensor charge of the nucleon for which

lattice QCD and model predictions exist. Due to its chiral-odd nature, it can only be accessed via another chiral-odd function; this only became possible with the measurement of the Collins and the interference fragmentation functions in recent years. Consequently, the knowledge of this last leading twist distribution function is rather limited compared to its unpolarized and helicity counterparts. With additional chiral-odd fragmentation function measurements from e^+e^- annihilation, it will become possible to perform a flavor decomposition similar to the helicity case when several hadronic final states can be detected and identified in SIDIS. As transversity is expected to be a valence dominated object, the intermediate x range is of interest. As a detailed understanding of the evolution of the relevant fragmentation functions is still lacking, overlap in x with the fixed target experiments but at higher virtualities is important.

In recent years, increased interest has developed in the Sivers function and the Boer-Mulders function, which both are spin-orbit correlations: in the case of the Sivers function between the nucleon spin and the parton's transverse momentum and in the case of the Boer-Mulders function between the parton's transverse spin and momentum. Accessing these correlations requires a phase interference which originates in the gauge link structure of QCD. Again, in Phase 1 of eRHIC, there is overlap in x coverage with previous measurements but critically at higher scales. In addition, abundant heavy flavor production will access the unmeasured gluon Sivers distribution function.

3D structure of hadrons: Spatial imaging

Another important goal in Phase 1 of eRHIC is the spatial imaging of the nucleon. Instead of using transverse momentum dependence, the impact parameter dependence is studied via exclusive processes, in particular deeply virtual compton scattering (DVCS) and meson production. Generalized Parton Distributions (GPDs) describe the correlation between parton momentum and (transverse) position within the nucleon, and in certain limits simplify to the Form Factors and the PDFs. One important aspect of these measurements is the connection of GPDs to the total quark and gluon angular momentum through the Ji sum rule [181]. Luminosities at the $\sqrt{s}$ available in Phase 1 of eRHIC will allow measurements of GPDs with good precision over a wider x-Q^2 range than at previous high luminosity fixed target experiments.

B.2.2 QCD in nuclei

One of the fundamental goals of nuclear physics is the understanding of the structure of hadrons and nuclei in terms of the degrees of freedom in the QCD Lagrangian, quarks and gluons. More than two decades ago it was discovered that quarks and gluons in bound nucleons have markedly different distributions from those in the free nucleon, as illustrated in Figure B.3. Such differences can arise through various mechanisms, for example modification of the free nucleon structure, the presence of nonnucleonic degrees

of freedom, and quantum mechanical interference of the quark and gluon fields of multiple nucleons at small x (shadowing). At even smaller x, the gluon density increases to the point where gluon fields overlap, leading to a strong field regime of non-linear QCD evolution called saturation. This regime is argued to have universal properties for any hadronic system, but its onset is enhanced in nuclear targets due to the superposition of the gluon field of many nucleons. Measurements at ePHENIX will extend the x-Q^2 range beyond that in the fixed target data, shown in Figure B.2, and initiate the first systematic study of non-linear QCD evolution.

e+A collisions offer a clean probe of nuclear PDFs (nPDFs), complementing knowledge to be gained by p+A collisions. Detailed studies with an electroweak probe provide precision measurements without the complications of strong interactions and with full access to the scattering kinematics at the partonic level. Precise knowledge of nPDFs not only provides a deeper understanding of nuclei in terms of partonic degrees of freedom, but is also crucial input for the theoretical interpretation of a variety of ongoing and future high energy physics experiments, such as heavy ion and proton-nucleus collisions at RHIC and the LHC, or neutrino-nucleus interactions in long baseline neutrino experiments. High statistics inclusive measurements of F_2^A enabled by a 5–10 GeV electron beam would greatly improve constraints on quark nPDFs, with access to gluons made possible by examining the Q^2 dependence of F_2^A or by measuring F_L^A. Semi-inclusive DIS measurements with identified hadrons could provide flavor-separated information on the quark nPDFs.

There is great interest in understanding various features of gluon distributions in nuclei, such as their $k_\perp$ and impact parameter dependencies. While the x dependence can be accessed via F_2^A and F_L^A as described above, the simplest process to extract the gluon TMD distributions is SIDIS. The impact parameter dependence of gluon distributions in nuclei can be measured via exclusive J/ψ production [182]. Furthermore, measurements of dihadrons will allow access to multi-gluon correlations in nuclei.

e+A collisions will also enable clean measurements of transport coefficients in cold nuclear matter. Novel observables, namely open heavy flavors, charmonium, bottomonium, and jets, will be available due to the high energy reach compared to earlier fixed-target e+A experiments, greatly expanding the sensitivity to various nuclear effects.

B.2.3 Hadronization

Closely linked to the propagation of color charges in nuclear matter is the study of how these color charges neutralize into hadrons. The unique feature of eRHIC compared to previous fixed target experiments in studying the space-time evolution of hadronization is its large energy range, allowing one to experimentally boost the hadronization process in and out of the nuclear medium. This permits isolation of in-medium parton propagation effects from color neutralization and hadron formation times. Subsequent comparison to nuclear Drell-Yan data, which are free from hadronization effects, will further isolate initial-state parton energy loss from nuclear wave function effects. The energies at eRHIC

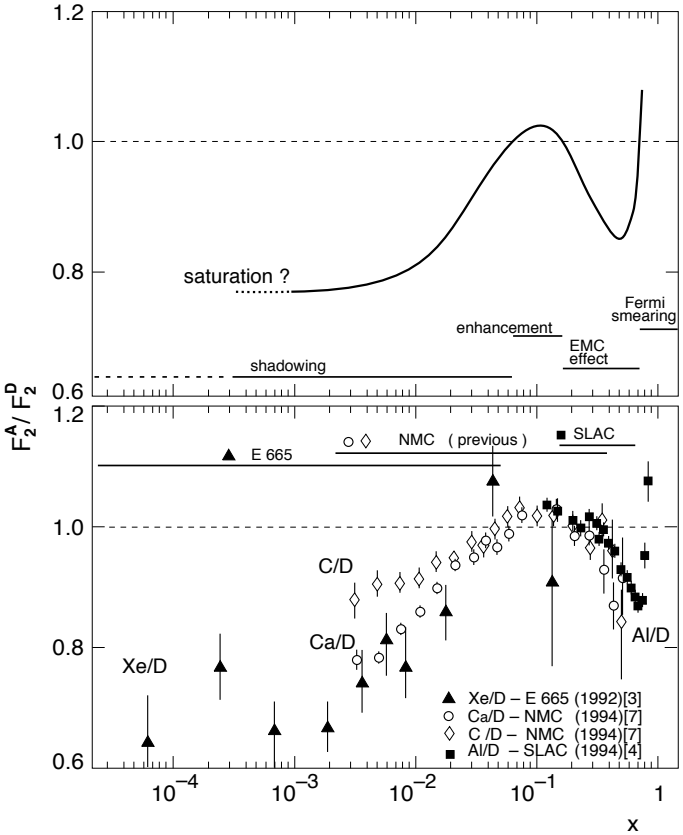

Figure B.3: (Top) Idealized depiction of the ratio of the structure function of a nucleus, $F_2^A(x, Q^2)$ per nucleon to $F_2^d(x, Q^2)$ of deuterium. Lower: Measured $F_2(x, Q^2)$ structure functions for C, Ca, and Xe relative to deuterium. Figure taken from [183].

will enable the study of hadronization of charm and bottom quarks in e+A collisions for the first time.

The collider mode will also make it feasible to study in detail for the first time target fragmentation and its correlation to current fragmentation through multi-particle correlations. Hadronization data from $e + p$ and e+A at eRHIC spanning from the current to the target fragmentation region will offer many opportunities to study the dynamics of color confinement mechanisms.

B.3 Detector Considerations

We now turn to the detector requirements to make the above described physics measurements in terms of momentum and angular resolution for the scattered electron and particle identification needs for the electron and hadrons. The key is understanding the kinematics for the various measurements and the precision required. We find that the current sPHENIX proposal at midrapidity is enabling of these measurements when augmented

with additional hadron identification fitting into the spatial envelope allowed, in addition to forward and backward future upgrade spectrometers.

B.3.1 Tracking: Momentum and Angular Resolution

Measuring F_L is challenging to the physics program as a whole since it requires a well-devised long term run plan and excellent control of systematics across a long time period. Furthermore, as the beam kinematics are varied, the scattered electrons at any given (x, Q^2) will utilize different parts of the detector.

The desired detector resolution can be solved for analytically. To determine a limit on the detector performance we require that uncertainties on the yield due to bin migration be held below some acceptable level. We take as an ansatz that 1% yield measurements are possible when the total yield uncertainty due to bin shifts is held below 20%.

Using the MRST2002 (NLO) parameterization for the structure functions, we calculated the resolution requirements necessary to satisfy the 20% ansatz for a variety of beam kinematics. Shown below in Figure B.4 (top) is the required momentum resolution as a function of lab angle θ and lab momentum p for different Phase 1 eRHIC beam energy combinations. Figure B.4 (bottom) shows the required angular resolution in the same manner.

These plots can be used as guidelines for evaluating spectrometer designs and whether they will provide the necessary performance. For the beam energies in eRHIC Phase 1, the detector performance requirements are not excessively stringent and are satisfied by the sPHENIX magnetic field strength and next stage additional tracking update, as detailed in Appendix 6.

B.3.2 Scattered Electron Energy and Angular Resolution

In collider geometry the DIS electrons are scattered mainly in backward and central rapidities. Central rapidity selects scattering with higher Q^2 and higher x (due to its correlation with Q^2); see Figure B.5. The higher electron beam energy the more scattering in the backward (electron beam) direction. The energy of the scattered electron varies in the range from zero to the electron beam energy and even to higher values for electrons detected at midrapidity $|\eta| < 1.0$, as shown in Figure B.5.

Collider kinematics allows us to clearly separate scattered electrons from other DIS fragments - hadrons and their decay products, which are detected preferably in the forward region, leaving much softer spectra in central and backward rapidities. Figure B.6 shows the scattered electron momentum spectrum along with photon (mainly from hadron decays) and charged pion spectra. Reasonable tracking and electromagnetic calorimetry will provide enough rejection through E/p matching and shower profile analysis to allow us

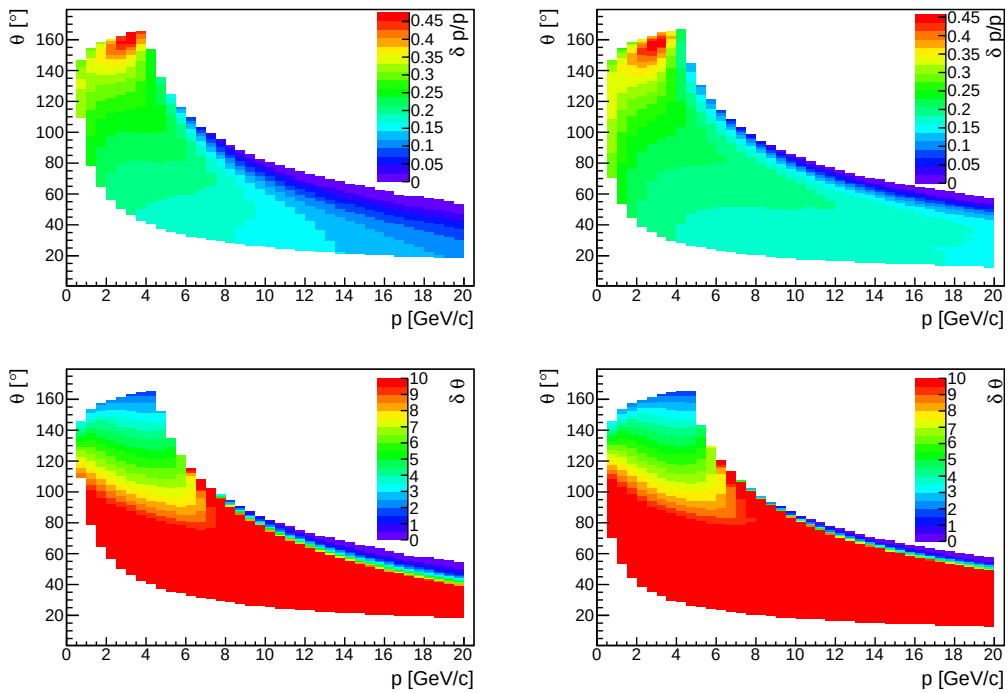

Figure B.4: Momentum resolution (top) and angular resolution (bottom) requirements for eRHIC Phase 1 with a 5 GeV electron beam colliding with a (left) 100 GeV and (right) 250 GeV proton beam. The color scale indicates the required specifications for (top) $\frac{\delta p}{p}$ and (bottom) $\delta\theta$ (in degrees).

to reliably identify electrons down to momentum at least 1 GeV/c. Photon conversion in material before the EMCal of up to 10% of a radiation length is not expected to contribute sizable background except for very low momenta ($<$ 1 GeV/c). Lower momentum electrons ($<$ 1 GeV/c) only modestly extend the x-Q^2 phase space of DIS kinematics. In addition, these events are more contaminated by radiative effects, so other approaches (e.g. Jacquet-Blondel method with hadronic final states) should be used for DIS kinematics reconstruction.

The simplest approach to reconstruct DIS kinematics is from the scattered electron. While the scattered angle is expected to be measured with good precision with tracking (see Section B.3.1), the energy resolution will limit the precision of x-Q^2 reconstruction. The energy resolution σ_E is directly propagated to σ_{Q^2}, so that $\sigma_{Q^2}/Q^2 = \sigma_E/E$, and energy resolution of ∼15–20% in the range of scattered electron kinematics (0.04–0.06 in $\log_{10}(Q^2)$ binning) is acceptable. However, the x resolution, σ_x, increases proportionally to $1/y$: $\sigma_x/x = (1/y) \cdot (\sigma_E/E)$, so the energy resolution effectively defines the reach of the kinematic region at low y. For the first eRHIC stage with a 5 GeV electron beam, the electron momentum measurements will be defined by tracking. Including an EMCal with energy resolution of $\sigma_E/E \sim 10\%/\sqrt{E}$ does not improve measurements if the tracking momentum resolution is $\sigma_p/p \sim 1\% \cdot p$ or better. RHIC/eRHIC flexibility to vary beam energy offers

another way to improve the resolutions, where lowering $\sqrt{s}$ allows access to a given x-Q^2 bin at higher y with better x-resolution.

QED radiative effects (radiation of real or virtual photons) are another source of smearing which is usually corrected with an unfolding technique. Unlike energy-momentum resolution which introduces gausian-like smearing, radiative corrections introduce a tail toward higher x. At higher y they dominate over energy-momentum smearing. Jacquet-Blondel method using hadronic final states is considered as an alternative approach to reconstruct DIS kinematics, which is free of radiative smearing effects.

It is also important to measure photons in DVCS. The produced DVCS photon energy versus pseudorapidity distribution is shown in Figure B.7 (left panel). For a 5 GeV electron beam, nearly half of all photons are detected in $|\eta| < 1$. For higher electron beam energy more photons scatter in the backward direction, still leaving about a third of photons scattered in $|\eta| < 1$ at an electron beam energy of 20 GeV. The photon momentum in central rapidity varies in the range ∼1–4 GeV/c nearly independent of beam energy in the range considered for eRHIC. Photons in the backward rapidity are more correlated with electron beam and have energy from 1 GeV/c to electron beam energy. Figure B.7 shows the x-Q^2 range covered by DVCS measurements in different rapidity ranges, emphasizing the importance of the measurements in both backward and central regions.

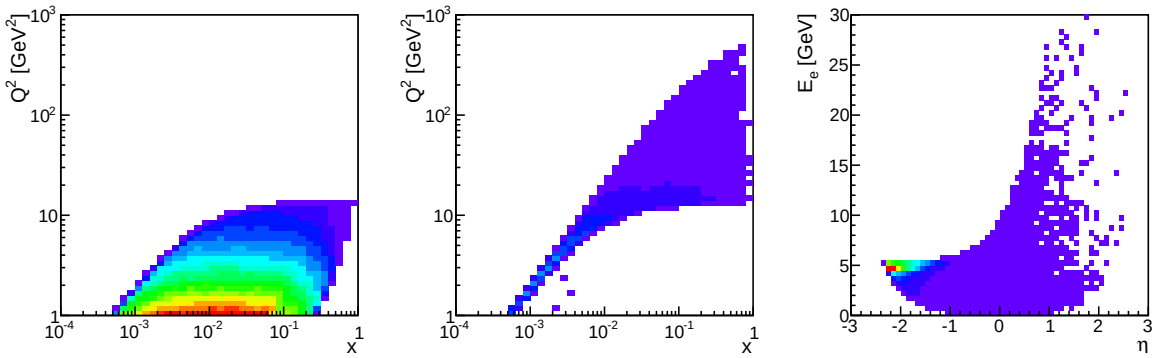

Figure B.5: For 5 GeV × 100 GeV beam energy configuration: x-Q^2 coverage of DIS for scattered electron detected in backward rapidities, $\eta < -1$ (left) and midrapidity, $|\eta| < 1$ (middle). (Right) Scattered electron energy vs pseudorapidity distribution.

B.3.3 Particle Identification Needs

Particle Identification (PID) is a requirement of several of the physics goals of ePHENIX. Pion and kaon identification are required for the SIDIS program, both for tagging kaons to extract Δs, and for tagging pions and kaons to study the transverse spin structure of the proton as well as the flavor dependence of nuclear PDFs. In addition, PID is essential for a comprehensive program to study hadronization. Electron identification is needed

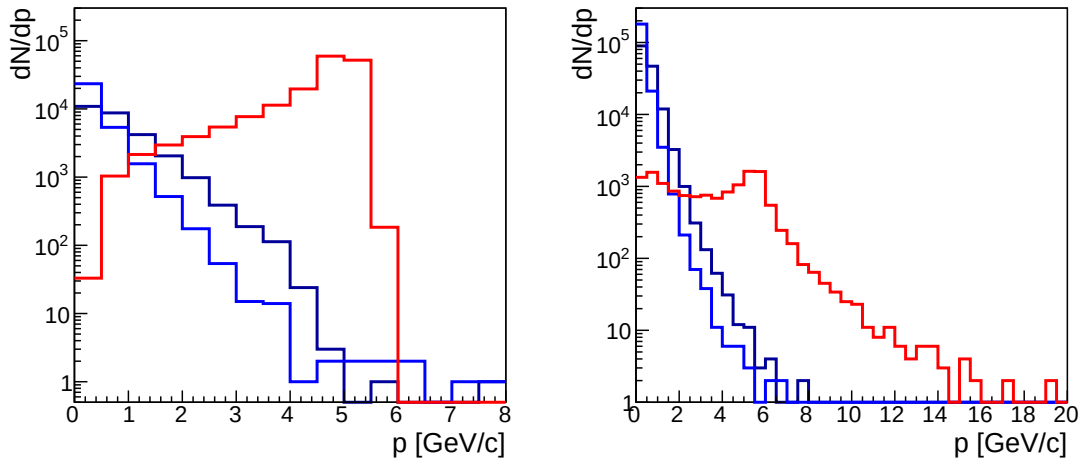

Figure B.6: For 5 GeV $\times$ 100 GeV beam energy configuration: Momentum spectra for scattered electron (red), charged pions (black) and photons (blue) detected in backward rapidities, $\eta < -1$ (left) and in central rapidities, $|\eta| < 1$ (right).

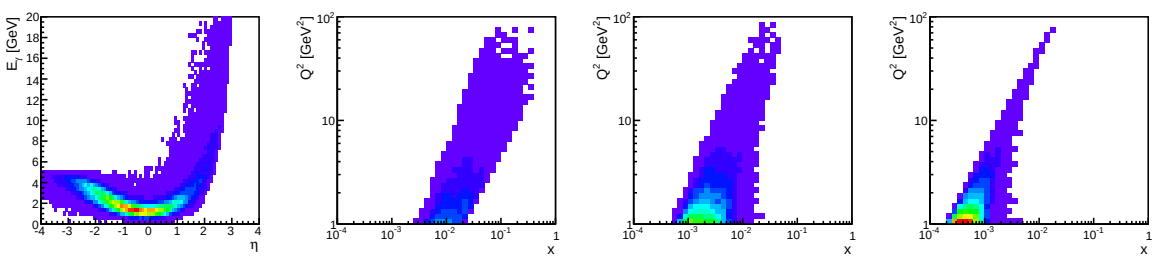

Figure B.7: For 5 GeV x 250 GeV beam energy configuration: (Left) DVCS photon energy vs pseudorapidity distribution. x-Q^2 coverage for DVCS events with photon detected in forward rapidities, $\eta > 1$ (middle left), central rapidities, $|\eta| < 1$ (middle right) and backward rapidities, $\eta < -1$ (right).

to properly reconstruct event kinematics. In the case of DVCS, it is important to tag the minimally scattered proton, which remains in the beam pipe. In this section, we will briefly discuss how we plan to meet these requirements, with the main focus on the central region, which is most relevant to the proposed detector.

Figure B.8 shows the π^+ momentum vs pseudorapidity distribution for two electron beam energy configurations relevant for the first stage of eRHIC. Minimal standard cuts have been applied: $Q^2 > 1\,\mathrm{GeV}^2$ and $W^2 > 4\ (\mathrm{GeV}/c^2)^2$. The fractional momentum of the scattered parton carried by the pion, z, is required to be above 0.2 to remove target fragmentation and below 0.85 to suppress exclusive processes. For these energies, the majority of hadrons are in the $-1 < \eta < 4$ range, which will be covered by the central ($-1 < \eta < 1$) or forward sPHENIX detector ($1 < \eta < 4$). Though hadrons in the forward

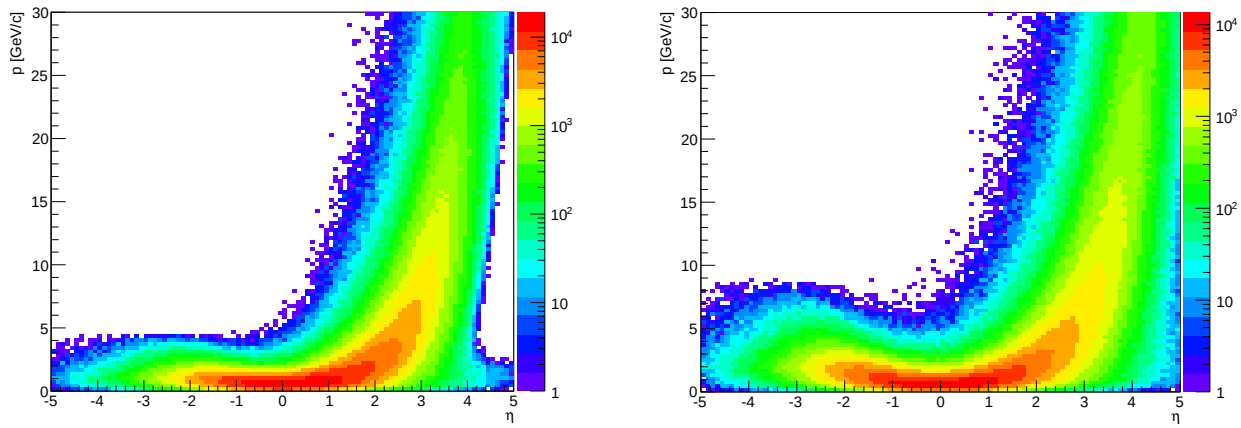

Figure B.8: Distribution of π^+ momentum vs pseudorapidity for (left) 5 GeV $\times$ 100 GeV and (right) 10 GeV $\times$ 250 GeV beam energy configurations.

direction have the highest momentum due to the boost of the system center of mass, those in the central and backward region reach higher Q^2 at a given x. Hadrons scattered in the forward direction sample events with $xE_p > E_e$, i.e. events with relatively higher x and lower to moderate Q^2. In the midrapidity region, $xE_p \simeq E_e$ with a maximum transverse momentum of $\sqrt{xE_pE_e}$ which for a 5 and 10 GeV electron beam on a 250 GeV proton can be as high as $35.4\sqrt{x}$ GeV$/c^2$ and $50\sqrt{x}$ GeV$/c^2$ respectively. Hadrons in the backwards direction cover a subset of the range covered by the midrapidity region.

The conceptual design for the forward sPHENIX detector (See Appendix A) covers $1 < \eta < 4$ and includes RICH based PID with $\pi-$K separation up to sufficiently high momentum. As the forward sPHENIX design moves ahead, all ePHENIX requirements will be considered.

In the central barrel region ($|\eta| < 1$), standard RICH-based PID is not possible due to the large radial space required, and the need for light collection in the acceptance of the planned forward spectrometer. However, we can use other Čerenkov based detectors, as is discussed in the next section, which have $\pi-$K separation up to $p \sim 4$ GeV$/c$. As stated above, a minimum z cut of 0.2 is required in SIDIS, therefore limiting the selection to events in which the scattered parton has $E < 20$ GeV. The impact of this can be seen in Figure B.9, where, assuming simple $2 \rightarrow 2$ kinematics, the maximum z accessible when imposing a $p < 4$ GeV$/c$ cut is plotted for the x-Q^2 ranges sampled in the midrapidity region. The dark blue regions coincide with $z < 0.2$, and would be inaccessible. At the beam energies available in the first stage of eRHIC, this limitation is minimal.

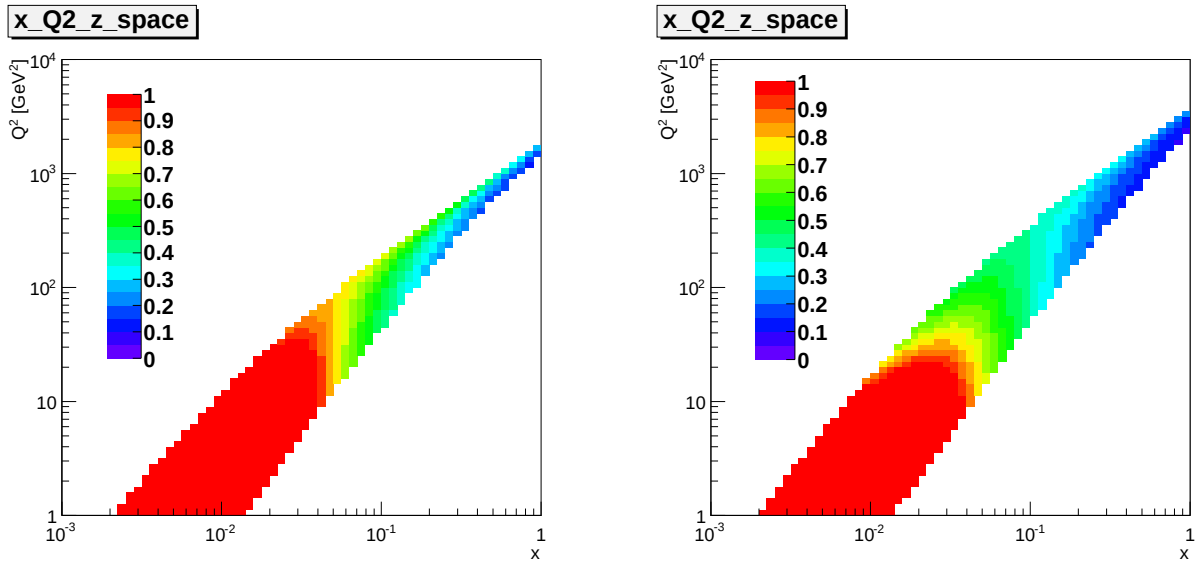

Figure B.9: (Left) 5 GeV $\times$ 100 GeV and (right) 10 GeV $\times$ 100 GeV beam energy configurations. Maximum z accessible (color scale) in $|\eta| < 1$ at given x-Q^2 assuming a $p < 4\,\mathrm{GeV}/c$ cut is imposed.

Technologies

Particle identification in ePHENIX will be accomplished using the existing sPHENIX central and forward detectors, augmented by additional ePHENIX specific detectors. In the midrapidity region, the electromagnetic calorimeter will provide the principal means for electron identification. It was shown above that with a calorimeter energy resolution $\sim$15–20%$/\sqrt{E}$ and a momentum resolution of $\sigma_p/p \sim 1\%p$ in the central tracking system, good electron identification can be achieved over the entire kinematic range of the scattered electron. It is also assumed that a preshower detector as detailed in Appendix 6 will be installed in the central sPHENIX detector by the time ePHENIX is running, which will provide significant electron-hadron separation.

Identification of pions, kaons and protons will require additional detectors both for central and forward regions. In the central region, one is limited by the space available inside the solenoid magnet, and therefore requires a compact detector that takes up the minimal amount of radial space. In order to achieve PID above 5 GeV/c, we have considered a dual radiator gas RICH. This could use a proximity focused configuration [184] and a photosensitive gas detector, such as a CsI photocathode GEM detector, similar to what was used in the PHENIX HBD [185], only with a more highly segmented readout that would allow complete ring imaging. This technology is already being studied by as part of the EIC detector R&D program.

Two other technologies being explored for PID are a DIRC (Detection of Internally Reflected Cherenkov Light) [186] and a Time of Propagation (TOP) detector [187], as is being

developed for BELLE II. A DIRC would have the advantage of a very thin radiator ($\sim$5 cm), but would have limited PID capabilities above $\sim$ 3.5 GeV/c. A TOP detector may extend this somewhat, but would still not cover the full momentum range of particles at central rapidity. However, it may be possible to extend the capabilities of either a DIRC or TOP detector using silicon photomultipliers as photodetectors, which can provide very good position and timing resolution. Currently, silicon photomultipliers provide position resolutions $\sim$ 1 mm and time resolutions $\sim$ 200 ps, but it is in principal possible to achieve $\sim$50 μm and $\sim$50 ps with these devices. This could greatly enhance the capabilities of either a DIRC or TOP counter, and also provide the ability to construct such a detector in a much more compact arrangement.

Appendix C

The PHENIX Collaboration

Abilene Christian University, *Abilene, Texas 79699, USA*
M.S. Daugherity, K. Gainey, D. Isenhower, H. Qu, A. Tate, R. Towell, R.S. Towell*, T.S. Watson

Department of Physics, *Banaras Hindu University, Varanasi 221005, India*
P. Garg, P.K. Khandai, B.K. Singh, C.P. Singh*, V. Singh

Bhabha Atomic Research Centre, *Bombay 400 085, India*
D.K. Mishra, A.K. Mohanty*, P.K. Netrakanti, P. Sett, P. Shukla

Baruch College, *City University of New York, New York, New York, 10010 USA*
S. Bathe*, J. Bryslawskyj

Collider-Accelerator Department, *Brookhaven National Laboratory, Upton, New York 11973-5000, USA*
M. Bai, K.A. Drees, S. Edwards, Y.I. Makdisi*, A. Zelenski

Physics Department, *Brookhaven National Laboratory, Upton, New York 11973-5000, USA*
B. Azmoun, A. Bazilevsky, S. Boose, M. Chiu, G. David, E.J. Desmond, K.O. Eyser, A. Franz, P. Giannotti, J.S. Haggerty, J. Jia, B.M. Johnson, H.-J. Kehayias, E. Kistenev, D. Lynch, E. Mannel, J.T. Mitchell, D.P. Morrison, R. Nouicer, E. O'Brien, R. Pak, C. Pinkenburg, R.P. Pisani, M.L. Purschke, T. Sakaguchi, A. Sickles, I.V. Sourikova, P. Steinberg, S.P. Stoll, A. Sukhanov, M.J. Tannenbaum*, C.L. Woody

University of California - Riverside, *Riverside, California 92521, USA*
K.N. Barish*, M. Beaumier, D. Black, K.O. Eyser, T. Hester, R.S. Hollis, A. Iordanova, D. Kleinjan, M. Mendoza, S.D. Rolnick, K. Sedgwick, R. Seto

Charles University, *Ovocný trh 5, Praha 1, 116 36, Prague, Czech Republic*
M. Finger Jr., M. Finger*, M. Slunečka, V. Slunečkova

Chonbuk National University, *Jeonju, 561-756, Korea*
J.B. Choi, E.-J. Kim*, K.-B. Kim, G.H. Lee

Science and Technology on Nuclear Data Laboratory, *China Institute of Atomic Energy, Beijing 102413, P. R. China*
X. Bai, X. Li*, S. Zhou

Center for Nuclear Study, *Graduate School of Science, University of Tokyo, 7-3-1 Hongo, Bunkyo, Tokyo 113-0033, Japan*
R. Akimoto, T. Gunji, H. Hamagaki*, R. Hayano, S. Hayashi, Y. Hori, Y. Komatsu, S. Masumoto, A. Nukariya, H. Oide, K. Ozawa, Y. Sekiguchi, A. Takahara, H. Torii, T. Tsuji, Y.S. Watanabe, Y.L. Yamaguchi

University of Colorado, *Boulder, Colorado 80309, USA*
A. Adare, T. Koblesky, M. McCumber, J.L. Nagle*, M.R. Stone,

Columbia University, *New York, New York 10027 and Nevis Laboratories, Irvington, New York 10533, USA*
C.Y. Chi*, B.A. Cole, T. Engelmore, N. Grau, Y.S. Lai, D. Perepelitsa, F.W. Sippach, E. Vazquez-Zambrano, A. Veicht, D. Winter, W.A. Zajc, L. Zhang

Czech Technical University, *Zikova 4, 166 36 Prague 6, Czech Republic*
T. Liška, M. Tomášek, M. Virius*, V. Vrba

Debrecen University, *H-4010 Debrecen, Egyetem tér 1, Hungary*
J. Imrek, P. Tarján*

ELTE, *Eötvös Loránd University, H - 1117 Budapest, Pázmány P. s. 1/A, Hungary*
M. Csanád*, Á. Kiss, M. Kofarago, M.I. Nagy, M. Vargyas

Ewha Womans University, *Seoul 120-750, Korea*
K.I. Hahn*, S.Y. Han, D.H. Kim, J. Lee, I.H. Park

Florida State University, *Tallahassee, Florida 32306, USA*
A.D. Frawley*, J.R. Hutchins, J. Klatsky, D. McGlinchey

Georgia State University, *Atlanta, Georgia 30303, USA*
C. Butler, H. Guragain, X. He*, M. Jezghani, L. Patel, M. Sarsour, A. Sen

Hanyang University, *Seoul 133-792, Korea*
B.H. Kang, J.S. Kang, Y.K. Kim*, M.S. Ryu

Hiroshima University, *Kagamiyama, Higashi-Hiroshima 739-8526, Japan*
K. Homma, T. Hoshino, K.M. Kijima, Y. Nakamiya, M. Nihashi, K. Shigaki, T. Sugitate*, D. Watanabe

IHEP Protvino, *State Research Center of Russian Federation, Institute for High Energy Physics, Protvino, 142281, Russia*
V. Babintsev, V. Bumazhnov, S. Chernichenko, A. Denisov*, A. Durum, I. Shein, A. Soldatov, A. Yanovich

University of Illinois at Urbana-Champaign, *Urbana, Illinois 61801, USA*
J. Blackburn, I.J. Choi, L. Eberle, F. Giordarno, M. Grosse Perdekamp*, D.S. Jumper, Y.-J. Kim, M. Leitgab, C. McKinney, B. Meredith, D. Northacker, J.-C. Peng, E. Thorsland, S. Wolin, R. Yang, E. Zarndt

Institute for Nuclear Research of the Russian Academy of Sciences, *prospekt 60-letiya Oktyabrya 7a, Moscow 117312, Russia*
V. Pantuev*

Institute of Physics, *Academy of Sciences of the Czech Republic, Na Slovance 2, 182 21 Prague 8, Czech Republic*
J. Popule, P. Sicho, L. Tomášek, M. Tomášek, V. Vrba*

Iowa State University, *Ames, Iowa 50011, USA*
S. Campbell, L. Ding, J.C. Hill*, J.G. Lajoie, A. Lebedev, R. McKay, C.A. Ogilvie, J. Perry, M. Rosati, A. Shaver, M. Shimomura, A. Timilsina, S. Whitaker

Advanced Science Research Center, *Japan Atomic Energy Agency, 2-4 Shirakata Shirane, Tokai-mura, Naka-gun, Ibaraki-ken 319-1195, Japan*
K. Imai*, T. Maruyama, H. Sako, S. Sato

Joint Institute for Nuclear Research, *141980 Dubna, Moscow Region, Russia*
S. Afanasiev, A. Isupov, A. Litvinenko*, A. Malakhov, V. Peresedov, P. Rukoyatkin, L. Zolin

Helsinki Institute of Physics and University of Jyväskylä, *P.O.Box 35, FI-40014 Jyväskylä, Finland*
D.J. Kim, F. Krizek, N. Novitzky, J. Rak*

KEK, *High Energy Accelerator Research Organization, Tsukuba, Ibaraki 305-0801, Japan*
Y. Fukao, S. Kanda, M. Makek, T. Mibe, S. Nagamiya, K. Ozawa, N. Saito, S. Sawada*, Y.S. Watanabe

Korea University, *Seoul, 136-701, Korea*
B. Hong*, C. Kim, K.S. Lee, S.K. Park,

Russian Research Center "Kurchatov Institute", *Moscow, 123098 Russia*
D.S. Blau, S.L. Fokin, A.V. Kazantsev, V.I. Manko*, T.V. Moukhanova, A.S. Nyanin, D.Yu. Peressounko, I.E. Yushmanov

Kyoto University, *Kyoto 606-8502, Japan*
H. Asano, S. Dairaku, K. Karatsu, T. Murakami*, T. Nagae, K.R. Nakamura

Laboratoire Leprince-Ringuet, *Ecole Polytechnique, CNRS-IN2P3, Route de Saclay, F-91128, Palaiseau, France*
S. Chollet, A. Debraine, O. Drapier, F. Fleuret*, F. Gastaldi, M. Gonin, R. Granier de Cassagnac

Lawrence Livermore National Laboratory, *Livermore, California 94550, USA*
I. Garishvili, A. Glenn, R.A. Soltz*

Los Alamos National Laboratory, *Los Alamos, New Mexico 87545, USA*
C. Aidala, M.L. Brooks, J.M. Durham, J. Huang, X. Jiang, J. Kapustinsky, K.B. Lee, M.J. Leitch, M.X. Liu*, P.L. McGaughey, C.L. Silva, W.E. Sondheim, H.W. van Hecke

Department of Physics, *Lund University, Box 118, SE-221 00 Lund, Sweden*
P. Christiansen, A. Oskarsson*, L. Österman, E. Stenlund

University of Maryland, *College Park, Maryland 20742, USA*
O. Baron, L. D'Orazio, A.C. Mignerey*, E. Richardson, L. Stevens

Department of Physics, *University of Massachusetts, Amherst, Massachusetts 01003-9337, USA*
N. Bandara, D. Kawall*, M. Stepanov

Muhlenberg College, *Allentown, Pennsylvania 18104-5586, USA*
G. Benjamin, A. Carollo, N. Cronin, N. Crossett, B. Fadem*, A. Isinhue, M. Moskowitz, S. Motschwiller, A. Nederlof, M. Skolnik, S. Solano, A. Tullo, M. Young, C. Zumberge

Myongji University, *Yongin, Kyonggido 449-728, Korea*
S.J. Jeon, K.S. Joo*

Nagasaki Institute of Applied Science, *Nagasaki-shi, Nagasaki 851-0193, Japan*
T. Fusayasu*, Y. Tanaka

University of New Mexico, *Albuquerque, New Mexico 87131, USA*
B. Bassalleck, J. Bok, S. Butsyk, A. Datta, K. DeBlasio, D.E. Fields*, M. Hoefferkamp, J.A. Key, I. Younus

New Mexico State University, *Las Cruces, New Mexico 88003, USA*
J. Bok, A. Meles, V. Papavassiliou, S.F. Pate*, G.D.N. Perera, E. Tennant, X.R. Wang, F. Wei

Department of Physics and Astronomy, *Ohio University, Athens, Ohio 45701, USA*
X. Bing, J.E. Frantz*, D. Kotchetkov, N. Riveli

Oak Ridge National Laboratory, *Oak Ridge, Tennessee 37831, USA*
T.C. Awes, M. Bobrek, C.L. Britton,Jr., V. Cianciolo, Y.V. Efremenko, K.F. Read, D. Silvermyr, P.W. Stankus*, M. Wysocki

IPN-Orsay, *Universite Paris Sud, CNRS-IN2P3, BP1, F-91406, Orsay, France*
D. Jouan*

PNPI, *Petersburg Nuclear Physics Institute, Gatchina, Leningrad region, 188300, Russia*
V. Baublis, D. Ivanischev, V. Ivanov, A. Khanzadeev, L. Kochenda, B. Komkov, P. Kravtsov, V. Riabov, Y. Riabov, E. Roschin, V. Samsonov*, V. Trofimov, E. Vznuzdaev

RIKEN Nishina Center for Accelerator-Based Science, *Wako, Saitama 351-0198, Japan*
Y. Akiba, K. Aoki, H. Asano, S. Baumgart, S. Dairaku, A. Enokizono, Y. Fukao, Y. Goto, K. Hashimoto, T. Ichihara, Y. Ikeda, Y. Imazu, K. Karatsu, M. Kurosawa, S. Miyasaka, T. Murakami, J. Murata, I. Nakagawa, K.R. Nakamura, T. Nakamura, K. Nakano, M. Nihashi, K. Ninomiya, R. Seidl, T.-A. Shibata, K. Shoji, A. Taketani, T. Todoroki, K. Watanabe, Y. Watanabe*, S. Yokkaichi

RIKEN BNL Research Center, *Brookhaven National Laboratory, Upton, New York 11973-5000, USA*
Y. Akiba*, S. Bathe, K. Boyle, C.-H. Chen, A. Deshpande, Y. Goto, T. Ichihara, J. Koster, M. Kurosawa, I. Nakagawa, R. Nouicer, K. Okada, J. Seele, R. Seidl, A. Taketani, K. Tanida, Y. Watanabe, S. Yokkaichi

Physics Department, *Rikkyo University, 3-34-1 Nishi-Ikebukuro, Toshima, Tokyo 171-8501, Japan*
K. Hashimoto, K. Kurita*, J. Murata, K. Ninomiya, K. Watanabe

Saint Petersburg State Polytechnic University, *St. Petersburg, 195251 Russia*
A. Berdnikov, Y. Berdnikov*, D. Kotov, A. Safonov

Universidade de São Paulo, *Instituto de Física, Caixa Postal 66318, São Paulo CEP05315-970, Brazil*
O. Dietzsch*, M. Donadelli, M. Kuriyama, M.A.L. Leite, R. Menegasso, E.M. Takagui

Department of Physics and Astronomy, *Seoul National University, Seoul, Korea*
S. Choi, S. Park, K. Tanida, I. Yoon

Chemistry Department, *Stony Brook University, SUNY, Stony Brook, New York 11794-3400, USA*
N.N. Ajitanand, J. Alexander, X. Gong, Y. Gu, J. Jia, R. Lacey*, A. Mwai, M. Soumya, S. Radhakrishnan, R. Reynolds, A. Taranenko, R. Wei

Department of Physics and Astronomy, *Stony Brook University, SUNY, Stony Brook, New York 11794-3400, USA*
N. Apadula, E.T. Atomssa, B. Bannier, K. Dehmelt, A. Deshpande*, A. Dion, A. Drees, H. Ge, C. Gal, J. Hanks, T.K. Hemmick, B.V. Jacak, J. Kamin, V. Khachatryan, P. Kline, S.H. Lee, R. Lefferts, B. Lewis, A. Lipski, M. Lynch, A. Manion, C. Pancake, R. Petti, B. Sahlmueller, E. Shafto, D. Sharma, J. Sun

Accelerator and Medical Instrumentation Engineering Lab, *SungKyunKwan University, 53 Myeongnyun-dong, 3-ga, Jongno-gu, Seoul, South Korea*
J.-S. Chai*

University of Tennessee, *Knoxville, Tennessee 37996, USA*
A. Garishvili, C. Nattrass, K.F. Read, S.P. Sorensen*, E. Tennant

Department of Physics, *Tokyo Institute of Technology, Oh-okayama, Meguro, Tokyo 152-8551, Japan*
S. Miyasaka, K. Nakano, T.-A. Shibata*

Institute of Physics, *University of Tsukuba, Tsukuba, Ibaraki 305, Japan*
T. Chujo, S. Esumi*, M. Inaba, Y. Miake, S. Mizuno, T. Niida, M. Sano, T. Todoroki, K. Watanabe

Vanderbilt University, *Nashville, Tennessee 37235, USA*
R. Belmont, S.V. Greene*, S. Huang, B. Love, C.F. Maguire, D. Roach, B. Schaefer, J. Velkovska

Weizmann Institute, *Rehovot 76100, Israel*
M. Makek, A. Milov, I. Ravinovich, I. Tserruya*

Institute for Particle and Nuclear Physics, *Wigner Research Centre for Physics, Hungarian Academy of Sciences (Wigner RCP, RMKI) H-1525 Budapest 114, POBox 49, Budapest, Hungary*
T. Csörgő*, M.I. Nagy, T. Novak, A. Ster, J. Sziklai, R. Vértesi

Yonsei University, *IPAP, Seoul 120-749, Korea*
J.H. Do, J.H. Kang*, H.J. Kim, Y. Kwon, S.H. Lim

*PHENIX Institutional Board member

Co-Spokesperson	David Morrison *Brookhaven National Laboratory*
Co-Spokesperson	Jamie Nagle *University of Colorado*
Deputy Spokesperson	Yasuyuki Akiba *RIKEN Nishina Center for Accelerator-Based Science*
Deputy Spokesperson	John Lajoie *Iowa State University*
Operations Director	Ed O'Brien *Brookhaven National Laboratory*
Deputy Operations Director for Upgrades	Mike Leitch *Los Alamos National Laboratory*
Deputy Operations Director for Operations	John Haggerty *Brookhaven National Laboratory*

Bibliography

[1] A. Bazavov, T. Bhattacharya, M. Cheng, N. H. Christ, C. DeTar, S. Ejiri, S. Gottlieb, R. Gupta, U. M. Heller, K. Huebner, C. Jung, F. Karsch, E. Laermann, L. Levkova, C. Miao, R. D. Mawhinney, P. Petreczky, C. Schmidt, R. A. Soltz, W. Soeldner, R. Sugar, D. Toussaint, and P. Vranas. Equation of state and qcd transition at finite temperature. *Phys. Rev. D*, 80:014504, Jul 2009. URL: `http://link.aps.org/doi/10.1103/PhysRevD.80.014504`, `doi:10.1103/PhysRevD.80.014504`. 1, 1.1

[2] A. Adare et al. Enhanced production of direct photons in Au+Au collisions at $\sqrt{s_{NN}} = 200\,\mathrm{GeV}$ and implications for the initial temperature. *Phys. Rev. Lett.*, 104:132301, 2010. `arXiv:0804.4168`, `doi:10.1103/PhysRevLett.104.132301`. 1, 6.7

[3] M. Luzum and P. Romatschke. Viscous hydrodynamic predictions for nuclear collisions at the LHC. *Phys. Rev. Lett.*, 103:262302, 2009. `arXiv:0901.4588`, `doi:10.1103/PhysRevLett.103.262302`. 1

[4] A. Adams, L. D. Carr, T. Schaefer, P. Steinberg, and J. E. Thomas. Strongly correlated quantum fluids: ultracold quantum gases, quantum chromodynamic plasmas, and holographic duality. 2012. `arXiv:1205.5180`. 1

[5] S. S. Gubser. Using string theory to study the quark-gluon plasma: Progress and perils. *Nucl. Phys.*, A830:657C–664C, 2009. `arXiv:0907.4808`. 1

[6] S. S. Gubser, I. R. Klebanov, and A. W. Peet. Entropy and temperature of black 3-branes. *Phys. Rev.*, D54:3915–3919, 1996. `arXiv:hep-th/9602135`, `doi:10.1103/PhysRevD.54.3915`. 1

[7] U. A. Wiedemann. Stepping outside the neighborhood of T(c) at LHC. *Nucl.Phys.*, A830:74C–80C, 2009. `arXiv:0908.2294`. 1

[8] K. Adcox et al. Formation of dense partonic matter in relativistic nucleus nucleus collisions at RHIC: Experimental evaluation by the PHENIX collaboration. *Nucl. Phys.*, A757:184–283, 2005. `arXiv:nucl-ex/0410003`, `doi:10.1016/j.nuclphysa.2005.03.086`. 1.1

[9] M. Luzum and P. Romatschke. Conformal relativistic viscous hydrodynamics: Applications to RHIC results at $\sqrt{s_{NN}} = 200\,\mathrm{GeV}$. *Phys. Rev.*, C78:034915, 2008. arXiv:0804.4015, doi:10.1103/PhysRevC.78.034915. 1.1

[10] P. Danielewicz and M. Gyulassy. Dissipative phenomena in quark gluon plasmas. *Phys. Rev.*, D31:53–62, 1985. doi:10.1103/PhysRevD.31.53. 1.1

[11] P. Kovtun, D. Son, and A. Starinets. Viscosity in strongly interacting quantum field theories from black hole physics. *Phys. Rev. Lett.*, 94:111601, 2005. arXiv:hep-th/0405231, doi:10.1103/PhysRevLett.94.111601. 1.1, 1.2

[12] H. Song and U. W. Heinz. Causal viscous hydrodynamics in 2+1 dimensions for relativistic heavy-ion collisions. *Phys. Rev.*, C77:064901, 2008. arXiv:0712.3715, doi:10.1103/PhysRevC.77.064901. 1.1

[13] B. Alver, C. Gombeaud, M. Luzum, and J.-Y. Ollitrault. Triangular flow in hydrodynamics and transport theory. *Phys. Rev.*, C82:034913, 2010. arXiv:1007.5469, doi:10.1103/PhysRevC.82.034913. 1.1

[14] D. A. Teaney. Viscous Hydrodynamics and the Quark Gluon Plasma. 2009. arXiv:0905.2433. 1.1

[15] B. Schenke, S. Jeon, and C. Gale. Elliptic and triangular flows in 3 + 1D viscous hydrodynamics with fluctuating initial conditions. *J. Phys. G*, G38:124169, 2011. 1.1

[16] A. Adare et al. Measurements of Higher-Order Flow Harmonics in Au+Au Collisions at $\sqrt{s_{NN}} = 200$ GeV. *Phys. Rev. Lett.*, 107:252301, 2011. 384 authors, 6 pages, and 3 figures. Submitted to Phys. Rev. Lett. Plain text data tables for the points plotted in figures for this and previous PHENIX publications are (or will be) publicly available at http://www.phenix.bnl.gov/papers.html. arXiv:1105.3928, doi:10.1103/PhysRevLett.107.252301. 1.1

[17] A. Adare et al. Energy loss and flow of heavy quarks in Au+Au collisions at $\sqrt{s_{NN}} = 200\,\mathrm{GeV}$. *Phys. Rev. Lett.*, 98:172301, 2007. arXiv:nucl-ex/0611018, doi:10.1103/PhysRevLett.98.172301. 1.1

[18] A. Majumder, B. Muller, and X.-N. Wang. Small shear viscosity of a quark-gluon plasma implies strong jet quenching. *Phys. Rev. Lett.*, 99:192301, 2007. arXiv:hep-ph/0703082, doi:10.1103/PhysRevLett.99.192301. 1.1, 1.2, 1.2

[19] H. Liu, K. Rajagopal, and U. Wiedemann. Calculating the jet quenching parameter from AdS/CFT. *Phys. Rev. Lett.*, 97:182301, 2006. arXiv:hep-ph/0605178, doi:10.1103/PhysRevLett.97.182301. 1.1, 1.2

[20] L. Csernai, J. Kapusta, and L. McLerran. On the strongly-interacting low-viscosity matter created in relativistic nuclear collisions. *Phys. Rev. Lett.*, 97:152303, 2006. arXiv:nucl-th/0604032, doi:10.1103/PhysRevLett.97.152303. 1.2

[21] P. B. Arnold, G. D. Moore, and L. G. Yaffe. Transport coefficients in high temperature gauge theories. 2. Beyond leading log. *JHEP*, 0305:051, 2003. arXiv:hep-ph/0302165. 1.2

[22] M. Prakash, M. Prakash, R. Venugopalan, and G. Welke. Nonequilibrium properties of hadronic mixtures. *Phys. Rept.*, 227:321–366, 1993. doi:10.1016/0370-1573(93)90092-R. 1.2

[23] N. Demir and S. A. Bass. Shear-viscosity to entropy-density ratio of a relativistic hadron gas. *Phys. Rev. Lett.*, 102:172302, 2009. arXiv:0812.2422, doi:10.1103/PhysRevLett.102.172302. 1.2

[24] H. B. Meyer. A calculation of the shear viscosity in SU(3) gluodynamics. *Phys. Rev.*, D76:101701, 2007. arXiv:0704.1801, doi:10.1103/PhysRevD.76.101701. 1.2

[25] Y. Hidaka and R. D. Pisarski. Small shear viscosity in the semi quark gluon plasma. *Phys. Rev.*, D81:076002, 2010. arXiv:0912.0940, doi:10.1103/PhysRevD.81.076002. 1.2

[26] P. K. Srivastava and C. P. Singh. Critical Point on the QCD Deconfining Phase Boundary. 2012. 15 pages, 4 figures. arXiv:1201.0445. 1.2

[27] P. Kovtun, G. D. Moore, and P. Romatschke. The stickiness of sound: An absolute lower limit on viscosity and the breakdown of second order relativistic hydrodynamics. *Phys. Rev.*, D84:025006, 2011. arXiv:1104.1586, doi:10.1103/PhysRevD.84.025006. 1.2

[28] H. Song, S. A. Bass, and U. Heinz. Elliptic flow in 200 A GeV Au+Au collisions and 2.76 A TeV Pb+Pb collisions: insights from viscous hydrodynamics + hadron cascade hybrid model. *Phys. Rev.*, C83:054912, 2011. arXiv:1103.2380, doi:10.1103/PhysRevC.83.054912. 1.2

[29] J. L. Nagle, I. G. Bearden, and W. A. Zajc. Quark-gluon plasma at RHIC and the LHC: perfect fluid too perfect? *New J. Phys.*, 13:075004, 2011. arXiv:1102.0680, doi:10.1088/1367-2630/13/7/075004. 1.2

[30] H. Niemi, G. S. Denicol, P. Huovinen, E. Molnar, and D. H. Rischke. Influence of the shear viscosity of the quark-gluon plasma on elliptic flow in ultrarelativistic heavy-ion collisions. *Phys. Rev. Lett.*, 106:212302, 2011. arXiv:1101.2442, doi:10.1103/PhysRevLett.106.212302. 1.2

[31] N. Armesto, B. Cole, C. Gale, W. A. Horowitz, P. Jacobs, et al. Comparison of Jet Quenching Formalisms for a Quark-Gluon Plasma 'Brick'. 2011. arXiv:1106.1106. 1.2

[32] P. B. Arnold, G. D. Moore, and L. G. Yaffe. Transport coefficients in high temperature gauge theories. 1. Leading log results. *JHEP*, 0011:001, 2000. arXiv:hep-ph/0010177. 1.2

[33] J. Liao and E. Shuryak. Angular Dependence of Jet Quenching Indicates Its Strong Enhancement Near the QCD Phase Transition. *Phys. Rev. Lett.*, 102:202302, 2009. arXiv:0810.4116, doi:10.1103/PhysRevLett.102.202302. 1.2, 1.3

[34] K. Rajagopal. International Quark Matter presentation (2011). URL: http://qm2011.in2p3.fr/node/12. 1.3

[35] B. Muller. Talk given at RHIC/AGS Users' Meeting, June 2011". 1.8, 1.4

[36] B. Muller. Parton energy loss in strongly coupled AdS/CFT. *Nucl. Phys.*, A855:74–82, 2011. arXiv:1010.4258, doi:10.1016/j.nuclphysa.2011.02.022. 1.4

[37] A. Dainese, C. Loizides, and G. Paic. Leading-particle suppression in high energy nucleus-nucleus collisions. *Eur. Phys. J.*, C38:461–474, 2005. arXiv:hep-ph/0406201, doi:10.1140/epjc/s2004-02077-x. 1.5, 1.9

[38] C. Loizides. High transverse momentum suppression and surface effects in Cu+Cu and Au+Au collisions within the PQM model. *Eur. Phys. J.*, C49:339–345, 2007. arXiv:hep-ph/0608133, doi:10.1140/epjc/s10052-006-0059-8. 1.5, 1.9

[39] A. Adare et al. Quantitative constraints on the opacity of hot partonic matter from semi-inclusive single high transverse momentum pion suppression in Au+Au collisions at $\sqrt{s_{NN}} = 200\,\mathrm{GeV}$. *Phys. Rev.*, C77:064907, 2008. arXiv:0801.1665, doi:10.1103/PhysRevC.77.064907. 1.5, 1.9

[40] S. Bass et al. Systematic comparison of jet energy-loss schemes in a realistic hydrodynamic medium. *Phys. Rev.*, C79:024901, 2009. arXiv:0808.0908, doi:10.1103/PhysRevC.79.024901. 1.5, 1.10

[41] S. Wicks, W. Horowitz, M. Djordjevic, and M. Gyulassy. Elastic, inelastic, and path length fluctuations in jet tomography. *Nucl. Phys.*, A784:426–442, 2007. arXiv:nucl-th/0512076, doi:10.1016/j.nuclphysa.2006.12.048. 1.10

[42] A. Adare et al. Azimuthal anisotropy of neutral pion production in Au+Au collisions at $\sqrt{s_{NN}} = 200GeV$: Path-length dependence of jet quenching and the role of initial geometry. 2010. arXiv:1006.3740. 1.5, 1.10

[43] K. Adcox et al. Suppression of hadrons with large transverse momentum in central Au+Au collisions at $\sqrt{s_{NN}} = 130\,\mathrm{GeV}$. *Phys. Rev. Lett.*, 88:022301, 2002. arXiv:nucl-ex/0109003, doi:10.1103/PhysRevLett.88.022301. 1.5

[44] C. Adler et al. Centrality dependence of high p_T hadron suppression in Au+Au collisions at $\sqrt{s}_{NN} = 130\,\mathrm{GeV}$. *Phys. Rev. Lett.*, 89:202301, 2002. arXiv:nucl-ex/0206011. 1.5

[45] A. Adare et al. Trends in yield and azimuthal shape modification in dihadron correlations in relativistic heavy ion collisions. *Phys. Rev. Lett.*, 104:252301, 2010. arXiv:1002.1077, doi:10.1103/PhysRevLett.104.252301. 1.5

[46] A. Adare et al. Suppression of away-side jet fragments with respect to the reaction plane in Au+Au collisions at $\sqrt{s_{NN}} = 200\,\mathrm{GeV}$. *Phys. Rev.*, C84:024904, 2011. arXiv:1010.1521, doi:10.1103/PhysRevC.84.024904. 1.5

[47] J. Adams et al. Distributions of charged hadrons associated with high transverse momentum particles in $p+p$ and Au+Au collisions at $\sqrt{s_{NN}} = 200\,\mathrm{GeV}$. *Phys. Rev. Lett.*, 95:152301, 2005. arXiv:nucl-ex/0501016. 1.5

[48] J. L. Nagle. Ridge, bulk, and medium response: how to kill models and learn something in the process. *Nucl. Phys.*, A830:147C–154C, 2009. arXiv:0907.2707. 1.5

[49] C. Marquet and T. Renk. Jet quenching in the strongly-interacting quark-gluon plasma. *Phys. Lett.*, B685:270–276, 2010. arXiv:0908.0880, doi:10.1016/j.physletb.2010.01.076. 1.5

[50] H. Caines. Jets and jet-like Correlations at RHIC. 2011. arXiv:1110.1878. 1.5

[51] J. Putschke. STAR: Jet reconstruction, direct gamma and multi-hadron correlations: Hard probes of the initial and final state. *Nucl. Phys.*, A855:83–91, 2011. 1.5

[52] J. Putschke. First fragmentation function measurements from full jet reconstruction in heavy-ion collisions at $\sqrt{s_{NN}} = 200\,\mathrm{GeV}$ by STAR. *Eur. Phys. J.*, C61:629–635, 2009. arXiv:0809.1419. 1.5

[53] P. M. Jacobs. Background fluctuations in heavy ion jet reconstruction. 2010. arXiv:1012.2406. 1.5

[54] Y.-S. Lai. Direct jet reconstruction in $p+p$ and Cu+Cu collisions at PHENIX. *Nucl. Phys.*, A855:295–298, 2011. 1.5

[55] Y.-S. Lai. Probing medium-induced energy loss with direct jet reconstruction in $p+p$ and Cu+Cu collisions at PHENIX. *Nucl. Phys.*, A830:251C–254C, 2009. arXiv:0907.4725. 1.5

[56] W. A. Horowitz and M. Gyulassy. The Surprising Transparency of the sQGP at LHC. *Nucl. Phys.*, A872:265–285, 2011. arXiv:1104.4958. 1.5, 1.11

[57] K. Aamodt and C. A. Loizides. Suppression of charged particle production at large transverse momentum in central Pb–Pb collisions at $\sqrt{s_{NN}} = 2.76\,\mathrm{TeV}$. *Phys. Lett.*, B696:30–39, 2011. arXiv:1012.1004. 1.5

[58] X.-F. Chen, T. Hirano, E. Wang, X.-N. Wang, and H. Zhang. Suppression of high p_T hadrons in $Pb + Pb$ Collisions at LHC. *Phys. Rev.*, C84:034902, 2011. arXiv:1102.5614, doi:10.1103/PhysRevC.84.034902. 1.5

[59] B. G. Zakharov. Variation of jet quenching from RHIC to LHC and thermal suppression of QCD coupling constant. *JETP Lett.*, 93:683–687, 2011. arXiv:1105.2028, doi:10.1134/S0021364011120162. 1.5

[60] A. Buzzatti and M. Gyulassy. Jet Flavor Tomography of Quark Gluon Plasmas at RHIC and LHC. *Phys. Rev. Lett.*, 108:022301, 2012. 4 pages, 3 eps figures. arXiv:1106.3061, doi:10.1103/PhysRevLett.108.022301. 1.5

[61] G. Aad et al. Observation of a centrality-dependent dijet asymmetry in lead-lead collisions at $\sqrt{s_{NN}} = 2.76$ TeV with the ATLAS detector at the LHC. *Phys. Rev. Lett.*, 105:252303, 2010. Accepted for publication at Physical Review Letters. arXiv:1011.6182, doi:10.1103/PhysRevLett.105.252303. 1.5, 1.12, 4.2, 4.3.2

[62] S. Chatrchyan et al. Observation and studies of jet quenching in PbPb collisions at nucleon-nucleon center-of-mass energy = 2.76 TeV. *Phys. Rev.*, C84:024906, 2011. arXiv:1102.1957, doi:10.1103/PhysRevC.84.024906. 1.5, 1.13, 1.6, 4.3.2, 4.4.5

[63] X.-N. Wang, Z. Huang, and I. Sarcevic. Jet quenching in the opposite direction of a tagged photon in high-energy heavy ion collisions. *Phys. Rev. Lett.*, 77:231–234, 1996. arXiv:hep-ph/9605213, doi:10.1103/PhysRevLett.77.231. 1.5

[64] S. Chatrchyan et al. Studies of jet quenching using isolated-photon+jet correlations in PbPb and pp collisions at sqrt(s[NN]) = 2.76 TeV. 2012. Submitted to Physics Letters B. arXiv:1205.0206. 1.5

[65] S. Chatrchyan et al. Jet momentum dependence of jet quenching in PbPb collisions at sqrt(sNN)=2.76 TeV. 2012. Long author list - awaiting processing. arXiv:1202.5022. 1.5, 4.2

[66] P. Steinberg. Recent Heavy Ion Results with the ATLAS Detector at the LHC. 2011. arXiv:1110.3352. 1.5

[67] J. Casalderrey-Solana, J. G. Milhano, and U. Wiedemann. Jet quenching via jet collimation. *J. Phys. G*, G38:124086, 2011. arXiv:1107.1964. 1.6

[68] T. Renk. Energy dependence of the dijet imbalance in Pb-Pb collisions at 2.76 ATeV. 2012. arXiv:1204.5572. 1.6

[69] T. Renk. Jets in medium: What RHIC and LHC measurements of R_{AA} and I_{AA} can teach about the parton-medium interaction. 2011. arXiv:1111.0769. 1.6

[70] JET Topical Collaboration [online]. URL: http://jet.lbl.gov. 1.6

[71] K. C. Zapp, J. Stachel, and U. Wiedemann. LPM-effect in Monte Carlo models of radiative energy loss. *Nucl. Phys.*, A830:171C–174C, 2009. arXiv:0907.4304. 1.6

[72] T. Renk. YaJEM: a Monte Carlo code for in-medium shower evolution. *Int. J. Mod. Phys.*, E20:1594–1599, 2011. arXiv:1009.3740, doi:10.1142/S0218301311019933. 1.6

[73] C. Young, S. Jeon, C. Gale, and B. Schenke. Monte-Carlo simulation of jets in heavy-ion collisions. 2011. arXiv:1109.5992. 1.6, 1.6

[74] C. E. Coleman-Smith, S. A. Bass, and D. K. Srivastava. Implementing the LPM effect in a parton cascade model. *Nucl. Phys.*, A862-863:275–278, 2011. arXiv:1101.4895, doi:10.1016/j.nuclphysa.2011.05.071. 1.6, 1.6

[75] I. P. Lokhtin, A. V. Belyaev, and A. M. Snigirev. Jet quenching pattern at LHC in PYQUEN model. *Eur. Phys. J.*, C71:1650, 2011. arXiv:1103.1853, doi:10.1140/epjc/s10052-011-1650-1. 1.6

[76] N. Armesto, L. Cunqueiro, and C. A. Salgado. Monte Carlo for jet showers in the medium. *Nucl. Phys.*, A830:271C–274C, 2009. arXiv:0907.4706. 1.6

[77] C. E. Coleman-Smith, G.-Y. Qin, S. A. Bass, and B. Muller. Jet modification in a brick of QGP matter. 2011. arXiv:1108.5662. 1.14, 1.6

[78] C. E Coleman-Smith and B. Muller. What can we learn from Dijet suppression at RHIC? 2012. arXiv:1205.6781. 1.14, 1.15, 1.16

[79] K. Geiger and B. Muller. Dynamics of parton cascades in highly relativistic nuclear collisions. *Nucl. Phys.*, B369:600–654, 1992. doi:10.1016/0550-3213(92)90280-0. 1.6

[80] C. Wesp, A. El, F. Reining, Z. Xu, I. Bouras, et al. Calculation of shear viscosity using Green-Kubo relations within a parton cascade. *Phys. Rev.*, C84:054911, 2011. arXiv:1106.4306, doi:10.1103/PhysRevC.84.054911. 1.6

[81] G.-Y. Qin and B. Muller. private communication. 1.17, 1.6, 1.18, 1.19, 4.4.2, 4.13

[82] G.-Y. Qin and B. Muller. Explanation of Di-jet asymmetry in Pb+Pb collisions at the Large Hadron Collider. *Phys. Rev. Lett.*, 106:162302, 2011. 4 pages, 3 figures, made corrections for numerical inaccuracies, qualitative conclusions unaffected. arXiv:1012.5280, doi:10.1103/PhysRevLett.106.162302. 1.6, 1.6

[83] B. Schenke, C. Gale, and S. Jeon. MARTINI: Monte Carlo simulation of jet evolution. *Acta Phys. Polon. Supp.*, 3:765–770, 2010. arXiv:0911.4470. 1.6

[84] B. Schenke, S. Jeon, and C. Gale. (3+1)D hydrodynamic simulation of relativistic heavy-ion collisions. *Phys. Rev.*, C82:014903, 2010. arXiv:1004.1408, doi:10.1103/PhysRevC.82.014903. 1.6

[85] Clint Young, Bjorn Schenke, Sangyong Jeon, and Charles Gale. Dijet asymmetry at the energies available at the CERN Large Hadron Collider. *Phys.Rev.*, C84:024907, 2011. arXiv:1103.5769, doi:10.1103/PhysRevC.84.024907. 1.6

[86] C. Young and B. Schenke. private communication. 1.19

[87] Y. He, I. Vitev, and B.-W. Zhang. Next-to-leading order analysis of inclusive jet and di-jet production in heavy ion reactions at the Large Hadron Collider. 2011. arXiv:1105.2566. 1.6, 1.20, 4.13

[88] R. B. Neufeld and I. Vitev. Parton showers as sources of energy-momentum deposition in the QGP and their implication for shockwave formation at RHIC and at the LHC. 2011. 8 pages, 4 figures. arXiv:1105.2067. 1.6, 1.20, 4.13

[89] I. Vitev and B.-W. Zhang. Jet tomography of high-energy nucleus-nucleus collisions at next-to-leading order. *Phys. Rev. Lett.*, 104:132001, 2010. arXiv:0910.1090, doi:10.1103/PhysRevLett.104.132001. 1.6, 1.20, 4.13

[90] W. Vogelsang. private communication. 1.7, 1.21

[91] W. Fischer. RHIC Luminosity Upgrade Program. *Conf.Proc.*, C100523:TUXMH01, 2010. 1.7

[92] RHIC Beam Projections [online] [online]. URL: http://www.rhichome.bnl.gov/RHIC/Runs/RhicProjections.pdf. 1.7

[93] A. Pikin, J.G. Alessi, E.N. Beebe, A. Kponou, R. Lambiase, et al. RHIC EBIS: Basics of design and status of commissioning. *JINST*, 5:C09003, 2010. 1.7

[94] S. Afanasiev et al. Measurement of Direct Photons in Au+Au Collisions at $\sqrt{s_{NN}} =$ 200 GeV. 2012. arXiv:1205.5759. 1.22

[95] A. Adare et al. Direct-Photon Production in $p + p$ Collisions at $\sqrt{s} = 200$ GeV at Midrapidity. 2012. arXiv:1205.5533. 1.22

[96] M. A. Green and B. P. Strauss. The cost of superconducting magnets as a function of stored energy and design magnetic induction. *IEEE Transactions on Applied Superconductivity*, 18:248–251, 2008. 2.1, 5.3.1

[97] G. Aad et al. The ATLAS experiment at CERN. *Journal of Instrumentation*, 3, 2008. doi:10.1088/1748-0221/3/08/S08003. 3.2

[98] M. Adinolfi, F. Ambrosino, A. Antonelli, M. Antonelli, F. Anulli, et al. The KLOE electromagnetic calorimeter. *Nucl. Instrum. Meth.*, A482:364–386, 2002. doi:10.1016/S0168-9002(01)01502-9. 3.2

[99] R. McNabb, J. Blackburn, J. D. Crnkovic, D. W. Hertzog, B. Kiburg, et al. A Tungsten / Scintillating Fiber Electromagnetic Calorimeter Prototype for a High-Rate Muon g-2 Experiment. *Nucl. Instrum. Meth.*, A602:396–402, 2009. arXiv:0910.0818, doi:10.1016/j.nima.2009.01.007. 3.2

[100] Tungsten Heavy Powder [online]. URL: http://www.tungstenheavypowder.com. 3.2, 3.2.1

[101] R. Wigmans. Calorimetry: Energy measurement in particle physics. *Int. Ser. Monogr. Phys.*, 107:1–726, 2000. 3.8

[102] Inc. Saint-Gobain Ceramics & Plastics. Scintillating optical fibers. 3.3

[103] Kuraray Co. Ltd. Scintillation materials catalogue. 3.3

[104] A. Izmaylov, S. Aoki, J. Blocki, J. Brinson, A. Dabrowska, et al. Scintillator counters with WLS fiber/MPPC readout for the side muon range detector (SMRD)of the T2K experiment. *Nucl. Instrum. Meth.*, A623:382–384, 2010. arXiv:0904.4545, doi:10.1016/j.nima.2010.03.009. 3.3

[105] O. Mineev, A. Afanasjev, G. Bondarenko, V. Golovin, E. Gushchin, et al. Scintillator counters with multi-pixel avalanche photodiode readout for the ND280 detector of the T2K experiment. *Nucl. Instrum. Meth.*, A577:540–551, 2007. arXiv:physics/0606037, doi:10.1016/j.nima.2007.04.161. 3.3, 3.12

[106] S. Agostinelli et al. GEANT4: A Simulation toolkit. *Nucl. Instrum. Meth.*, A506:250–303, 2003. doi:10.1016/S0168-9002(03)01368-8. 3.4, 4.1

[107] CERN SRS Home Page. https://espace.cern.ch/rd51-wg5/srs/default.aspx. 3.5.3

[108] RD51 Collaboration Meeting. https://indico.cern.ch/conferenceTimeTable.py?confId=176664, Feb. 2012. 3.5.3

[109] S. Lochner. Development, optimisation and characterisation of a radiation hard mixed-signal readout chip for LHCb. 2006. 3.5.3

[110] T. Sjostrand, P. Eden, C. Friberg, L. Lonnblad, G. Miu, et al. High-energy physics event generation with PYTHIA 6.1. *Comput. Phys. Commun.*, 135:238–259, 2001. arXiv:hep-ph/0010017, doi:10.1016/S0010-4655(00)00236-8. 4.1, 4.3.1

[111] M. Gyulassy and X. Wang. HIJING 1.0: A Monte Carlo program for parton and particle production in high-energy hadronic and nuclear collisions. *Comput. Phys. Commun.*, 83:307, 1994. arXiv:nucl-th/9502021, doi:10.1016/0010-4655(94)90057-4. 4.1

[112] M. Cacciari and G. P. Salam. Dispelling the N^3 myth for the k_t jet-finder. *Phys. Lett.*, B641:57–61, 2006. arXiv:hep-ph/0512210, doi:10.1016/j.physletb.2006.08.037. 4.1, 4.2

[113] I. P. Lokhtin and A. M. Snigirev. A Model of jet quenching in ultrarelativistic heavy ion collisions and high-p(T) hadron spectra at RHIC. *Eur. Phys. J.*, C45:211–217, 2006. arXiv:hep-ph/0506189, doi:10.1140/epjc/s2005-02426-3. 4.1, 4.4.3

[114] J. A. Hanks, A. M. Sickles, B. A. Cole, A. Franz, M. P. McCumber, et al. Jet-Underlying Event Separation Method for Heavy Ion Collisions at the Relativistic Heavy Ion Collider. 2012. arXiv:1203.1353. 4.1, 4.4.1, 4.4, 4.5, 4.4.1, 4.9

[115] M. Cacciari, G. Salam, and G. Soyez. The anti-k_t jet clustering algorithm. *JHEP*, 0804:063, 2008. arXiv:0802.1189, doi:10.1088/1126-6708/2008/04/063. 4.2

[116] Jet Performance in pp Collisions at 7 TeV. URL: http://cdsweb.cern.ch/record/1279362. 4.3

[117] T. Adye. Unfolding algorithms and tests using RooUnfold. 2011. arXiv:1105.1160. 4.3.1

[118] B. A. Cole. Jet probes of $\sqrt{s_{NN}} = 2.76$ TeV Pb+Pb collisions with the ATLAS detector. *J. Phys. G*, G38:124021, 2011. 4.4.1

[119] X. Zhao and R. Rapp. Medium Modifications and Production of Charmonia at LHC. *Nucl. Phys.*, A859:114–125, 2011. 7 pages, 9 eps figures. arXiv:1102.2194, doi:10.1016/j.nuclphysa.2011.05.001. 6.3.1

[120] R. Arnaldi. J/ψ production in p+A and A+A collisions at fixed target experiments. *Nucl. Phys.*, A830:345c–352c, 2009. arXiv:0907.5004, doi:10.1016/j.nuclphysa.2009.10.030. 6.3.1

[121] N. Brambilla, S. Eidelman, B. K. Heltsley, R. Vogt, G. T. Bodwin, et al. Heavy quarkonium: progress, puzzles, and opportunities. 2010. arXiv:arXiv:1010.5827. 6.3.1

[122] B. Abelev et al. J/psi production at low transverse momentum in Pb-Pb collisions at sqrt(sNN) = 2.76 TeV. 2012. Long author list - awaiting processing. arXiv:1202.1383. 6.3.1, 6.5

[123] M. Calderón de la Barca Sánchez. Dimuon results in PbPb and pp collisions in CMS. 2011. arXiv:1109.1850. 6.3.1

[124] C. L. da Silva. Recent heavy flavour and quarkonia measurements by the PHENIX experiment. *J. Phys. G*, G38:124031, 2011. 6.3.1, 6.3.2

[125] R. Reed. Measuring the upsilon nuclear modification factor at STAR. *J. Phys. G*, G38:124185, 2011. arXiv:1109.3891, doi:10.1088/0954-3899/38/12/124185. 6.3.1

[126] B. Muller, J. Schukraft, and B. Wyslouch. First results from Pb+Pb collisions at the LHC. 2012. arXiv:1202.3233. 6.3.1

[127] A. Emerick, X. Zhao, and R. Rapp. Bottomonia in the quark-gluon plasma and their production at RHIC and LHC. 2011. arXiv:1111.6537. 6.3.1

[128] L. Ruan, G. Lin, Z. Xu, K. Asselta, H. F. Chen, et al. Perspectives of a midrapidity dimuon program at RHIC: a novel and compact muon telescope detector. *J. Phys. G*, G36:095001, 2009. arXiv:0904.3774, doi:10.1088/0954-3899/36/9/095001. 6.3.1

[129] D. Acosta et al. Υ production and polarization in $p\overline{p}$ collisions at $\sqrt{s} = 1.8$ TeV. *Phys. Rev. Lett.*, 88:161802, 2002. doi:10.1103/PhysRevLett.88.161802. 6.3.2

[130] M. Strickland and D. Bazow. Thermal bottomonium suppression at RHIC and LHC. *Nucl. Phys.*, A879:25–58, 2012. arXiv:1112.2761, doi:10.1016/j.nuclphysa.2012.02.003. 6.3.2, 6.8

[131] W. Horowitz and M. Gyulassy. Heavy quark jet tomography of Pb+Pb at LHC: AdS/CFT drag or pQCD energy loss? *Phys. Lett.*, B666:320–323, 2008. arXiv:0706.2336, doi:10.1016/j.physletb.2008.04.065. 6.4

[132] M. Cacciari. private communication. 6.4, 6.9

[133] A. Adil and I. Vitev. Collisional dissociation of heavy mesons in dense QCD matter. *Phys. Lett.*, B649:139–146, 2007. arXiv:hep-ph/0611109, doi:10.1016/j.physletb.2007.03.050. 6.4

[134] R. Sharma, I. Vitev, and B.-W. Zhang. Light-cone wave function approach to open heavy flavor dynamics in QCD matter. *Phys. Rev.*, C80:054902, 2009. arXiv:0904.0032, doi:10.1103/PhysRevC.80.054902. 6.4

[135] V. Abazov et al. *b*-Jet Identification in the D0 Experiment. *Nucl. Instrum. Meth.*, A620:490–517, 2010. arXiv:1002.4224, doi:10.1016/j.nima.2010.03.118. 6.4

[136] G.-Y. Qin, J. Ruppert, C. Gale, S. Jeon, G. D. Moore, et al. Radiative and collisional jet energy loss in the quark-gluon plasma at RHIC. *Phys. Rev. Lett.*, 100:072301, 2008. arXiv:0710.0605, doi:10.1103/PhysRevLett.100.072301. 6.5

[137] Barbara Betz and Miklos Gyulassy. The reduced jet-medium coupling in Pb+Pb collisions at the Large Hadron Collider. 2012. arXiv:1201.0281. 6.5, 6.11

[138] E. V. Shuryak. Quark-gluon plasma and hadronic production of leptons, photons and psions. *Phys. Lett.*, B78:150, 1978. doi:10.1016/0370-2693(78)90370-2,10.1016/0370-2693(78)90370-2. 6.7

[139] R. Arnaldi et al. NA60 results on thermal dimuons. *Eur. Phys. J.*, C61:711–720, 2009. arXiv:0812.3053, doi:10.1140/epjc/s10052-009-0878-5. 6.7

[140] A. Adare et al. Observation of direct-photon collective flow in $\sqrt{s_{NN}} = 200\,\mathrm{GeV}$ Au+Au collisions. 2011. arXiv:1105.4126. 6.7

[141] H. van Hees, C. Gale, and R. Rapp. Thermal photons and collective flow at energies available at the bnl relativistic heavy-ion collider. *Phys. Rev. C*, 84:054906, Nov 2011. URL: http://link.aps.org/doi/10.1103/PhysRevC.84.054906, doi:10.1103/PhysRevC.84.054906. 6.7

[142] A. Adare et al. Detailed measurement of the e^+e^- pair continuum in p+p and Au+Au collisions at $\sqrt{s_{NN}} = 200\,\mathrm{GeV}$ and implications for direct photon production. *Phys. Rev.*, C81:034911, 2010. arXiv:0912.0244, doi:10.1103/PhysRevC.81.034911. 6.7

[143] E. Shuryak. Monitoring parton equilibration in heavy ion collisions via dilepton polarization. 2012. arXiv:1203.1012. 6.7

[144] A. K. Chaudhuri and B. Sinha. Dilepton to photon ratio, a viscometer of QGP. 2012. 7 pages, 7 figures. arXiv:1201.0569. 6.7

[145] S.S. Adler et al. Double helicity asymmetry in inclusive mid-rapidity π^0 production for polarized $p+p$ collisions at $\sqrt{s} = 200\,\mathrm{GeV}$. *Phys. Rev. Lett.*, 93:202002, 2004. arXiv:hep-ex/0404027. A.1

[146] S.S. Adler et al. Improved measurement of double helicity asymmetry in inclusive midrapidity π^0 production for polarized $p+p$ collisions at $\sqrt{s} = 200\,\mathrm{GeV}$. *Phys. Rev.*, D73:091102, 2006. arXiv:hep-ex/0602004. A.1

[147] B.I. Abelev et al. Longitudinal double-spin asymmetry and cross section for inclusive neutral pion production at midrapidity in polarized proton collisions at $\sqrt{s} = 200\,\mathrm{GeV}$. *Phys.Rev.*, D80:111108, 2009. arXiv:0911.2773. A.1

[148] A. Adare et al. Inclusive cross-section and double helicity asymmetry for π^0 production in $p+p$ collisions at $\sqrt{s} = 200\,\mathrm{GeV}$: Implications for the polarized gluon distribution in the proton. *Phys. Rev.*, D76:051106, 2007. arXiv:0704.3599. A.1

[149] A. Adare et al. The polarized gluon contribution to the proton spin from the double helicity asymmetry in inclusive π^0 production in polarized $p+p$ collisions at $\sqrt{s} = 200\,\mathrm{GeV}$. *Phys. Rev. Lett.*, 103:012003, 2009. arXiv:0810.0694, doi:10.1103/PhysRevLett.103.012003. A.1

[150] A. Adare et al. Event structure and double helicity asymmetry in jet production from polarized $p+p$ collisions at $\sqrt{s} = 200\,\mathrm{GeV}$. *Phys. Rev.*, D84:012006, 2011. arXiv:1009.4921, doi:10.1103/PhysRevD.84.012006. A.1

[151] M. Burkardt. Parton orbital angular momentum. 2012. arXiv:1205.2916. A.1

[152] D. Sivers. The adventure and the Prize. 2011. arXiv:1109.2521. A.1

[153] J. Qiu and G. Sterman. Single transverse-spin asymmetries in hadronic pion production. *Phys. Rev.*, D59:014004, 1999. arXiv:hep-ph/9806356, doi:10.1103/PhysRevD.59.014004. A.1

[154] D. W. Sivers. Single spin production asymmetries from the hard scattering of point-like constituents. *Phys. Rev.*, D41:83, 1990. doi:10.1103/PhysRevD.41.83. A.1

[155] J. Collins. Fragmentation of transversely polarized quarks probed in transverse momentum distributions. *Nucl. Phys.*, B396:161–182, 1993. arXiv:hep-ph/9208213, doi:10.1016/0550-3213(93)90262-N. A.1

[156] X. Ji, J. Qiu, W. Vogelsang, and F. Yuan. A unified picture for single transverse-spin asymmetries in hard processes. *Phys. Rev. Lett.*, 97:082002, 2006. arXiv:hep-ph/0602239, doi:10.1103/PhysRevLett.97.082002. A.1

[157] Zhong-Bo Kang and Jian-Wei Qiu. QCD evolution of naive-time-reversal-odd parton distribution functions. 2012. arXiv:1205.1019. A.1

[158] S. Mert Aybat, Alexei Prokudin, and Ted C. Rogers. Calculation of TMD Evolution for Transverse Single Spin Asymmetry Measurements. 2011. arXiv:1112.4423. A.1

[159] Z. Kang and J. Qiu. Single transverse spin asymmetry of dilepton production near Z^0 pole. *Phys. Rev.*, D81:054020, 2010. arXiv:0912.1319, doi:10.1103/PhysRevD.81.054020. A.2, A.1

[160] J.C. Collins, A.V. Efremov, K. Goeke, M. Grosse Perdekamp, S. Menzel, et al. Sivers effect in Drell Yan at RHIC. *Phys. Rev.*, D73:094023, 2006. arXiv:hep-ph/0511272, doi:10.1103/PhysRevD.73.094023. A.1

[161] B. U. Musch, P. Hagler, J. W. Negele, and A. Schafer. Exploring quark transverse momentum distributions with lattice QCD. *Phys. Rev.*, D83:094507, 2011. arXiv:1011.1213, doi:10.1103/PhysRevD.83.094507. A.1

[162] PHENIX Collaboration. Mpc-ex proposal, 2012. URL: http://www.phenix.bnl.gov/phenix/WWW/publish/lajoie/MPC-EX/MPC-EX_BNL_03032012.pdf. A.1, A.2

[163] M. Chiu. Calorimetry upgrade at forward rapidities for the PHENIX detector. *AIP Conf.Proc.*, 842:1091–1093, 2006. A.1

[164] A. Airapetian et al. Transverse momentum broadening of hadrons produced in semi-inclusive deep-inelastic scattering on nuclei. *Phys. Lett.*, B684:114–118, 2010. arXiv:0906.2478, doi:10.1016/j.physletb.2010.01.020. A.2

[165] A. Airapetian et al. Quark fragmentation to $\pi^{\pm}$, π^0, $K^{\pm}$, p and $\overline{p}$ in the nuclear environment. *Phys. Lett.*, B577:37–46, 2003. arXiv:hep-ex/0307023, doi:10.1016/j.physletb.2003.10.026. A.2

[166] W. Brooks and H. Hakobyan. Experimental studies of hadronization and parton propagation in the space-time domain. *Nucl. Phys.*, A830:361c–368c, 2009. arXiv:0907.4606, doi:10.1016/j.nuclphysa.2009.10.031. A.2

[167] W. Brooks. Physics with nuclei at an Electron Ion Collider. 2010. arXiv:1008.0131. A.2

[168] M. Vasilev et al. Parton energy loss limits and shadowing in Drell-Yan dimuon production. *Phys. Rev. Lett.*, 83:2304–2307, 1999. arXiv:hep-ex/9906010, doi:10.1103/PhysRevLett.83.2304. A.2

[169] D. Geesaman, K. Saito, and A. Thomas. The nuclear EMC effect. *Ann. Rev. Nucl. Part. Sci.*, 45:337–390, 1995. doi:10.1146/annurev.ns.45.120195.002005. A.2

[170] E. Berger and F. Coester. Nuclear effects in deep inelastic lepton scattering. *Ann. Rev. Nucl. Part. Sci.*, 37(1):463–491, 1987. doi:10.1146/annurev.ns.37.120187.002335. A.2

[171] D. Alde et al. Nuclear dependence of dimuon production at 800 GeV. FNAL- 772 experiment. *Phys. Rev. Lett.*, 64:2479–2482, 1990. doi:10.1103/PhysRevLett.64.2479. A.2

[172] K. Eskola, H. Paukkunen, and C. Salgado. EPS09: a new generation of NLO and LO nuclear parton distribution functions. *JHEP*, 04:065, 2009. arXiv:0902.4154, doi:10.1088/1126-6708/2009/04/065. A.2

[173] F. Gelis, E. Iancu, J. Jalilian-Marian, and R. Venugopalan. The color glass condensate. 2010. arXiv:1002.0333. A.2

[174] A. Adare et al. Cold nuclear matter effects on J/ψ as constrained by deuteron-gold measurements at $\sqrt{s_{NN}} = 200$ GeV. *Phys. Rev.*, C77:024912, 2008. arXiv:0711.3917, doi:10.1103/PhysRevC.77.024912. A.2

[175] A. Adare et al. Suppression of back-to-back hadron pairs at forward rapidity in d+Au Collisions at $\sqrt{s_{NN}} = 200$ GeV. *Phys.Rev.Lett.*, 107:172301, 2011. arXiv:1105.5112, doi:10.1103/PhysRevLett.107.172301. A.2

[176] A. Adare, S. Afanasiev, C. Aidala, N.N. Ajitanand, Y. Akiba, et al. Transverse-Momentum Dependence of the J/ψ Nuclear Modification in d+Au Collisions at $\sqrt{s_{NN}}$=200 GeV. 2012. arXiv:1204.0777. A.2

[177] Mark Strikman and Werner Vogelsang. Multiple parton interactions and forward double pion production in pp and dA scattering. *Phys.Rev.*, D83:034029, 2011. arXiv:1009.6123, doi:10.1103/PhysRevD.83.034029. A.2

[178] Nuclear science advisory council long range planning report (2007). URL: http://science.energy.gov/~/media/np/nsac/pdf/docs/nuclear_science_low_res.pdf. B.1

[179] D. Boer, M. Diehl, R. Milner, R. Venugopalan, W. Vogelsang, et al. Gluons and the quark sea at high energies: Distributions, polarization, tomography. 2011. arXiv:1108.1713. B.1, B.2, B.2.1

[180] D. de Florian, R. Sassot, M. Stratmann, and W. Vogelsang. Extraction of Spin-Dependent Parton Densities and Their Uncertainties. *Phys. Rev.*, D80:034030, 2009. arXiv:0904.3821, doi:10.1103/PhysRevD.80.034030. B.2.1

[181] X.-D. Ji. Gauge invariant decomposition of nucleon spin and its spin - off. *Phys. Rev. Lett.*, 78:610–613, 1997. arXiv:hep-ph/9603249, doi:10.1103/PhysRevLett.78.610. B.2.1

[182] A. Caldwell and H. Kowalski. Investigating the gluonic structure of nuclei via j/ψ scattering. *Phys. Rev.*, C81:025203, 2010. doi:10.1103/PhysRevC.81.025203. B.2.2

[183] M. Arneodo et al. The structure function ratios $F_2^{\mathrm{Li}}/F_2^{\mathrm{D}}$ and $F_2^{\mathrm{C}}/F_2^{\mathrm{D}}$ at small x. *Nucl. Phys.*, B441:12–30, 1995. arXiv:hep-ex/9504002. B.3

[184] F. Barile. First results from the HMPID detector in the ALICE experiment at LHC. *AIP Conf. Proc.*, 1317:71–76, 2011. B.3.3

[185] W. Anderson, B. Azmoun, A. Cherlin, C. Y. Chi, Z. Citron, et al. Design, Construction, Operation and Performance of a Hadron Blind Detector for the PHENIX Experiment. *Nucl. Instrum. Meth.*, A646:35–58, 2011. arXiv:1103.4277, doi:10.1016/j.nima.2011.04.015. B.3.3

[186] I. Adam et al. The DIRC particle identification system for the BaBar experiment. *Nucl. Instrum. Meth.*, A538:281–357, 2005. doi:10.1016/j.nima.2004.08.129. B.3.3

[187] K. Nishimura. The Time-of-propagation counter for Belle II. *Nucl. Instrum. Meth.*, A639:177–180, 2011. arXiv:1009.0876. B.3.3